JREE

Journal of Renewable Energy and Environment

Journal of Renewable Energy and Environment

Materials and Energy
Research Center

Iranian Association of
Chemical Engineers

CONTENTS

AIMS AND SCOPE

Journal of Renewable Energy and Environment (JREE) publishes original papers, review articles, short communications and technical notes in the field of science and technology of renewable energies and environmental-related issues including:

- Generation
- Storage
- Conversion
- Distribution
- Management (economics, policies and planning)
- Environmental Sustainability

INSTRUCTIONS FOR AUTHORS

Submission of manuscript represents that it had neither been published nor submitted for publication elsewhere and is result of research carried out by author(s). Only the extended and upgraded articles presented in a conference and/or appeared in a symposium proceedings could be evaluated for publication.

Authors are required to include a list describing all the symbols and abbreviations in the paper. Use of the international system of measurement units is mandatory.

- On-line submission of manuscripts results in faster publication process and is recommended. Instructions are given in the JREE web sites: www.jree.ir
- References should be numbered in brackets and appear in sequence through the text. List of references should be given at the end of the paper. All journal articles listed in the References section must follow with article doi.
- Figure captions are to be indicated under the illustrations. They should sufficiently explain the figures.
- Illustrations should appear in their appropriate places in the text.
- Tables and diagrams should be submitted in a form suitable for reproduction.
- Photographs should be of high quality saved as jpg files.
- Tables' illustrations, figures and diagrams will be normally printed in single column width (8 cm). Exceptionally large ones may be printed across two columns (17 cm).

Estimation of Solar Radiation Energy in the Paraw Mountain of Kermanshah Province as a Rugged Topography

Somayeh Naserpour[a], Hasan Zolfaghari[a*], Parviz Zeaiean Firouzabadi[b]

a *Department of Geography, Razi University, P. O. Box: 67144-14971, Kermanshah, Kermanshah, Iran.*
b *Department of Remote Sensing and GIS, Faculty of Geographical Sciences, University of Kharazmi, P. O. Box: 15719-14911, Tehran, Tehran, Iran.*

ABSTRACT

One of the most important characteristics of site selection for solar energy system installations and optimum solar energy harvesting in the hilly or mountainous terrains is knowledge about the amount and duration of solar radiation within such topographic terrains. Solar radiation data are not readily available for most mountain terrains because of their rugged topography. For these areas, solar radiation data can be obtained through alternative methods such as the Hemispherical Viewshed Algorithm in which spatial and temporal variations of radiation are calculated in terms of elevation, slope, and terrain. In this study, this algorithm was used to estimate and model solar radiation in the Paraw Mountain in Kermanshah. The inputs for this method were ASTER Digital Elevation Model (DEM) with a spatial resolution of 30 m and meteorological parameters that affect solar radiation. The slope and aspect maps were created from ASTER DEM and layers for monthly direct, diffuse, global, and radiation periods were generated for the year 2016. The results showed that in the Paraw Mountain, the amount of solar radiation received was dependent on the slope orientation, as the north and northeast-facing slopes received the lowest and the south and southwest-facing slopes and the flat areas received the highest direct and global radiation (i.e., in terms of this factor, these landscapes can be recommended as the best site for solar energy system installations and optimum solar energy harvesting). The sum annual radiation period varies from 382.67 to 4310.9 hours, the total radiation received annually varies between 1005.56 and 7467.3 MJ/m^2, and the sum monthly solar radiation is the highest in July (181.49-842.26 MJ/m^2) and lowest in December (25.42-319.90 MJ/m^2). Statistical error comparisons between station-based measurements and model-based estimates were performed via R^2, measures. As a result, this model was recommended for solar radiation estimation with acceptable accuracy, especially in high areas with rugged topography where solar radiation data are not readily available.

1. INTRODUCTION

The sun is the main source of life and energy on earth and biological organisms cannot survive without its light and thermal energy. Solar energy is a renewable and clean energy source and environmental phenomena have been and are exposed to its benefit for a long time. The earth receives only about one-millionth of the sun's energy and the rest of this energy mostly scatters into the solar system and beyond. The sun's surface temperature is about 6,000 °C and this temperature rises toward its inner core. The inner core of the sun is estimated to have a temperature of about 20 million degrees Celsius. On average, the sun releases about 2×10^{27} calories of thermal energy into space every minute, of which the earth receives about 2×10^{18} calories. Given the current volume of the sun, which is 2×10^{33} grams, it can maintain its current state for millions of years [1].

The installation of solar power systems in mountainous terrains should be done according to the temporal and spatial distribution of solar radiation. This distribution of energy received from the sun is to some extent dependent on astronomical, geographical, geometric, physical, and meteorological factors. Knowing the variations of solar radiation received on surfaces with different slopes and orientations is the basic requirement in several fields of industry and science, including meteorology, agriculture, photobiology, animal husbandry, lighting, architecture, and solar energy generation. In general, meteorological stations only measure the diffuse and global radiation received on the horizontal surface. Therefore, the solar radiation data for sloping surfaces are not readily available and must be calculated based on the values given for horizontal surfaces [2]. The intensity of solar radiation received on the surface is determined by three factors: 1- solar incidence angle, which depends on the slope and season, 2- cloudiness and pollution, which depend on the region's climate and meteorological conditions, and 3- topography, which depends on elevation, ground slope angle and aspect, and dominant gradient of the area. Elevation, zenith angle, and horizontal barriers to radiation (due to adjacent topography) can significantly impact the amount of radiation reaching the ground surface

*Corresponding Author's Email: h.zolfaghari@razi.ac.ir (H. Zolfaghari)
URL: http://www.jree.ir/article_122116.html

[3]. Total solar radiation received on a sloping surface consists of three components: direct solar radiation, diffuse solar radiation (solar radiation arriving indirectly on the surface after having been scattered in the atmosphere), and reflected solar radiation (reflected from the earth's surface). Some researchers have used empirical models (Including Liu and Jordan [4], Hay [5], Steven and Unsworth [6], Reindl et al. [7], and Tian et al. [8]). In addition to these models, this estimation can be carried out using the Solar Analyst as an ArcView GIS extension, which allows researchers to compute total radiation and its components including direct, diffuse, and reflected radiation for different topographies. Topography has a great impact on the received solar radiation, particularly because the angle and aspect of ground slopes can be such that the site receives reduced direct sunlight. Changes in the angle and aspect of slopes can determine the radiation angle and the amount of thermal energy received in different landscapes [9]. The solar radiation analysis tool is the spatial analysis program that can estimate, analyze, and visualize this parameter in any part of the globe at any time. Using this tool, one can determine the effects of atmospheric conditions, longitude and latitude, altitude, angle, and aspect of slopes, daily and seasonal changes in solar angles, and shading of heights on the amount of solar radiation that reaches the earth's surface. Therefore, this tool can be used to facilitate analyses in many studies that involve solar radiation calculations [10]. For instance, Hofierka and Suri [11] developed a flexible GIS-based model called r.sun for solar radiation modeling, which is fully integrated into the open-source GIS environment. This model can calculate all solar radiation components (e.g., direct, diffuse, and reflected radiation) for clear and cloudy skies and is especially suitable for modeling large areas with complex terrains. This model can be easily used in long-term solar radiation calculations on different scales and also in the estimation of temporal variations of solar radiation (over a day or a year). Dozier and Frew [12] proposed rapid algorithms by which the Digital Elevation Model (DEM) can be used for quick calculation of terrain parameters to estimate the incoming solar and longwave radiation in surface climate models so as to reduce the computation times of these models. In another study, Geographic Information System (GIS) was used to estimate the solar energy potential in Karnataka state, India and identify suitable areas for using solar energy. This study found that the coastal parts of Karnataka were more suitable for using solar energy [13]. Pons and Ninyerola [14] also proposed a GIS-based model for the estimation of solar radiation based on astronomical, atmospheric, and geographic factors with DEM used as input. In another study, Battles et al. [15] used the radiation analysis tool of the ArcGIS software to estimate the amount of solar radiation in areas with complex topography. The results of this study showed that the software provided a more accurate estimate of solar radiation in the summer months than in the winter months. Other researchers have also used this tool to estimate solar radiation potential in their areas of interest. These include Gastli and Charabi [16] who used this tool to determine the potential for harvesting solar energy in Oman. The results of this study showed that this region had a very high solar radiation potential throughout the year. This study estimated that implementing CSP technology in only 10 percent of Oman's flat terrain (land with a slope of less than 1 percent) would result in the annual generation of 7.6 million gigawatts

of electricity, which is 680 times more than the existing electricity generation capacity of this country (in 2007, this capacity was about 11,189 (GWh)). In the end, these researchers produced an annual solar radiation map for the studied area. Several studies have used the Solar Analyst to evaluate the potential of harvesting solar energy and identify suitable areas for the installation of solar systems. For example, this approach was used in a study in Hong Kong to estimate the region's solar energy potential and identify suitable areas for solar panels. This study claimed that its methods and findings provided an accurate estimate of solar energy potential throughout Hong Kong, thereby facilitating renewable energy production in this area [17]. Also, radiation modeling using GIS-based models was carried out by Zhang et al. [18] for the Qilian Mountains, Northwest China, Zhang et al. [19] for Northwest China, and Moren et al. [20] for the upper Green River basin in Wyoming, U.S. The GIS-based solar radiation models can provide spatial data, planning, and design of solar energy systems, preparing radiation maps of specific areas for different periods and estimating the potential of the point or area [21]. Potential solar radiation modeling, site selection for solar energy systems installations, and thus electricity generation allow one to generate different scenarios for future sustainable planning powered by smart distribution grids with integrated energy storage [22]. PV systems are used for different purposes [23, 24, 25]. The number of solar lighting systems in the top five countries, to End-2014, is given below: solar lighting systems in India (960,000), Tanzania (790,038), Kenya (764,900), Ethiopia (661,630), and Uganda (84,352). The number of solar home systems in top five countries to end-2014 is as follows: solar home systems in Bangladesh (3,600,000), India (1,100,000), China (500,000), Nepal (500,000), and Kenya (320,000) [26]. Installing these systems is very suitable for meeting the electrical needs of areas without a national electricity grid (including rugged terrains). Many rural areas of Iran are situated on mountainous terrains with rugged topography. One of the main problems of highly remote rural areas is the lack of access to electricity, as it is difficult and expensive to construct and maintain long transmission lines over rugged terrains. The most appropriate solution for supplying electricity in these areas is the use of solar energy technology. Therefore, the electricity of off-grid photovoltaic systems is technically and economically convenient for these rural settlements than connecting them to the national grid. Therefore, for appropriate utilization of solar radiation energy in these mountain villages, modeling of spatial and temporal variations of radiation and site selection (due to topographic characteristics) for installing the photovoltaic (PV) is critically important. Solar radiation data are not available for many of these areas. These data need to be obtained using alternative methods. In the present study, the Solar Analyst (as an ArcView GIS extension) was used to model the solar radiation condition and its components in the Paraw Mountain (Kermanshah, Iran), which has a complex topography, to estimate the solar radiation received in this mountain and its temporal-spatial variations and also evaluate the performance of this approach in estimating radiation in complex topographies and sloping terrains. Applying this method can help evaluate the solar radiation condition and its components in mountainous terrain and suggest the best site for installing solar energy systems in mountain villages, mountain shelters, nomadic tents, and mountain roads.

2. MATERIALS AND METHODS

2.1. Study area and data

This study was focused on the solar radiation condition and its components in the Paraw Mountain in Kermanshah, Iran. The geographical location of the Paraw Mountain is shown in Figure 1 (34^0 25′ 05 N latitude 47^0 14′ 34 E longitude). This mountain stretches from the northwest to the northeast of the city of Kermanshah and is part of the Zagros mountain range in western Iran. The highest peak of this mountain is the Paraw peak in the northeast of Kermanshah, which has a height of 3386 meters above sea level. However, this mountain has two other peaks called Bisotun and Taq-e Bostan, which are more widely known because of their historical significance. The daily solar radiation measurements made at Kermanshah Meteorological Station in 2016 were collected from Iran Meteorological Organization [27]. These measurements were subjected to a quality control process before they could be used in analyses. The digital elevation model of the study area was extracted from the DEM derived from the Advanced Spaceborne Thermal Emission and Reflection Radiometer (ASTER) with a spatial resolution of 30 meters, which were downloaded from the USGS earth explorer website [28].
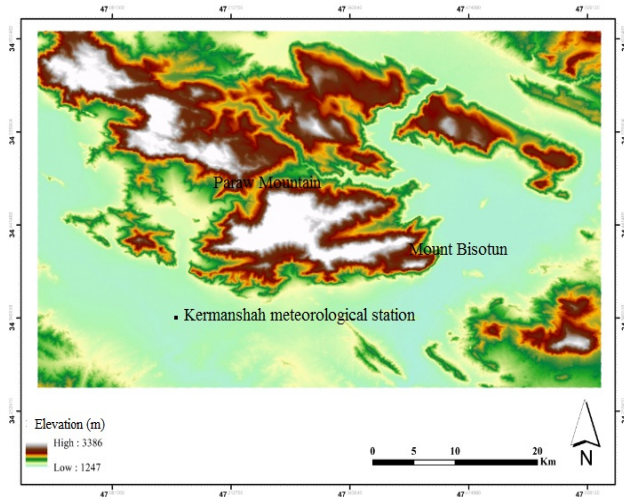

Figure 1. Digital elevation model of the study area (Paraw Mountain and Kermanshah synoptic station)

2.2. METHOD

2.2.1. The solar analyst tools in Arc Map

One way to estimate the amount of radiation received in complex terrains is to use the Solar Analyst tools in Arc Map. This tool operates based on methods from the hemispherical viewshed algorithm and performs calculations through four steps:

1. The calculation of an upward-looking hemispherical viewshed based on topography.
2. Overlay of the viewshed on a direct sun map to estimate direct radiation.
3. Overlay of the viewshed on a diffuse sky map to estimate diffuse radiation.
4. Repeating the process for every location of interest to produce an insolation map [29].

This algorithm is used to calculate the solar radiation for each site and produce an accurate radiation map, and its inputs are for calculating solar radiation are elevation, latitude, slope angle, slope aspect, and the angle of incidence, all of which affect the incoming radiation. Using this tool, one can estimate the total solar radiation and its components, including direct, diffuse, and reflected radiation for different topographies.

2.2.2. Global solar radiation calculation

The sum of direct and diffuse radiation that reaches the earth's surface in a unit of time (minute, day, month, and year) is called global radiation. Therefore, global radiation on a given surface can be obtained by summing the direct and diffuse shortwave radiations [30]. The analyses of this step were implemented using the following equations given by Rich et al. [31]; Rich and Fu [32]; Fu [33]; Fu and Rich [34]; Fu and Rich [35]:

Global solar radiation or $Global_{sum}$ is calculated as the sum of direct radiation (Dir_{sum}) and diffuse radiation (Dif_{sum}) of all sun map and sky map sectors, respectively.

$$Global_{sum} = Dir_{sum} + Dif_{sum}$$

2.2.3. Direct solar radiation calculation

The sum of direct radiation (Dir_{sum}) for a given site is the sum of the direct incoming solar radiation ($Dir_{\theta,\alpha}$) from all sun map sectors Eq. (1). The direct solar radiation from the sun map sector ($Dir_{\theta,\alpha}$) with a centroid at zenith angle (θ) and azimuth angle (α) is calculated using Eqs. (2-3). The angle of incidence ($AngInSky_{\theta,\alpha}$) is calculated using Eq. (4). Equations (1) to (4) are shown in Table 1.

Table 1. The equations of direct solar radiation calculation

Direct solar radiation calculation	Equations No.
$Dir_{sum} = \Sigma\ Dir_{\theta,\alpha}$	(1)
$Dir_{\theta,\alpha} = S_{Const} * \beta^{m(\theta)} * SunDur_{\theta,\alpha} *$ $SunGap_{\theta,\alpha} * cos(AngIn_{\theta,\alpha})$	(2)
$m(\theta) = EXP(-0.000118 * Elev - 1.638*10^{-9} * Elev^2) / cos(\theta)$	(3)
$AngIn_{\theta,\alpha} = acos(\ Cos(\theta) * Cos(G_z) +$ $Sin(\theta) * Sin(G_z) * Cos(\alpha - G_a)\ )$	(4)

2.2.4. Diffuse solar radiation calculation

The sum of diffuse radiation was calculated by the gap fraction and angle of incidence using Eqs. (5-6) and for the uniform sky diffuse model, $Weight_{\theta,\alpha}$ was calculated by Eq. (7). For the standard overcast sky model, $Weight_{\theta,\alpha}$ was calculated by Eq. (8). The sum of diffuse radiation for the location (Dif_{sum}) was calculated as the sum of the diffuse solar radiation (Dif) from all the sky map sectors using Eq. (9). Equations (5) to (9) are shown in Table 2.

Table 2. The equations of diffuse solar radiation calculation

Diffuse solar radiation calculation	Equations No.
$Dif_{\theta,\alpha} = R_{glb} * P_{dif} * Dur * SkyGap_{\theta,\alpha} *$ $Weight_{\theta,\alpha} * cos(AngIn_{\theta,\alpha})$	(5)
$R_{glb} = (S_{Const}\ \Sigma(\beta^{m(\theta)})) / (1 - P_{dif})$	(6)
$Weight_{\theta,\alpha} = (cos\theta_2 - cos\theta_1) / Div_{azi}$	(7)
$Weight_{\theta,\alpha} = (2cos\theta_2 + cos2\theta_2 - 2cos\theta_1 - cos2\theta_1) / 4 * Div_{azi}$	(8)
$Dif_{sum} = \Sigma\ Dif_{\theta,\alpha}$	(9)

2.2.5. Error evaluation test

To validate results, the available data were used to compute daily global solar radiation for the first days of each month, solstices, and equinoxes. Then, the results were compared with the total solar radiation measurements made at Kermanshah meteorological station. This comparison was made using the coefficient of determination (R^2) statistic, which is defined as follows [36, 37, 38]:

$$R^2 = \frac{\sum_{i=1}^{N}(G_i - G_m)^2}{\sum_{i=1}^{N}(G_i - \overline{G_m})^2} \qquad (10)$$

where n is the number of observations, G_i is the estimated daily global solar radiation, G_m is the measured daily global solar radiation, and $\overline{G_m}$ is the mean of daily global solar radiation measurements. The closer the R^2 value is to 1, the better the model performance will be.

3. RESULTS AND DISCUSSION

This section presents the results of solar radiation calculations implemented based on Equations 1 to 9. The duration or daylength, which is controlled by the rotation of the earth around its axis [39]. The longer the radiation duration is, the greater is the sum amount of solar radiation energy reaching the surface [30]. Calculations related to the duration in the study area are shown in Figure A1 (see Fig. A1 in Appendix). As shown in this figure, the monthly total radiation duration for January varies from 0 to 284.90 hours. The figure is 0-300.18 for February, 0-352.72 for March, 1.01-374.02 for April, 92.90-409.75 for May, 91.27-412 for June, 101.97-418.74 for July, 20.45-396.91 for August, 0-350.13 for September, 0-327.09 for October, 0-288.36 for November, and 0-236.52 hours for December. The highest monthly sum radiation durations are for May, June, and July (with very close values) and the lowest is for December. Comparing the radiation duration maps of the study area with the slope aspect map (Figure 2) shows that the south (with aspect between 157.5–202.5) and southwest-facing slopes (with aspect between 202.5–247.5) and the flat areas have the longest radiation durations and the north and northeast-facing slopes have the lowest radiation durations.
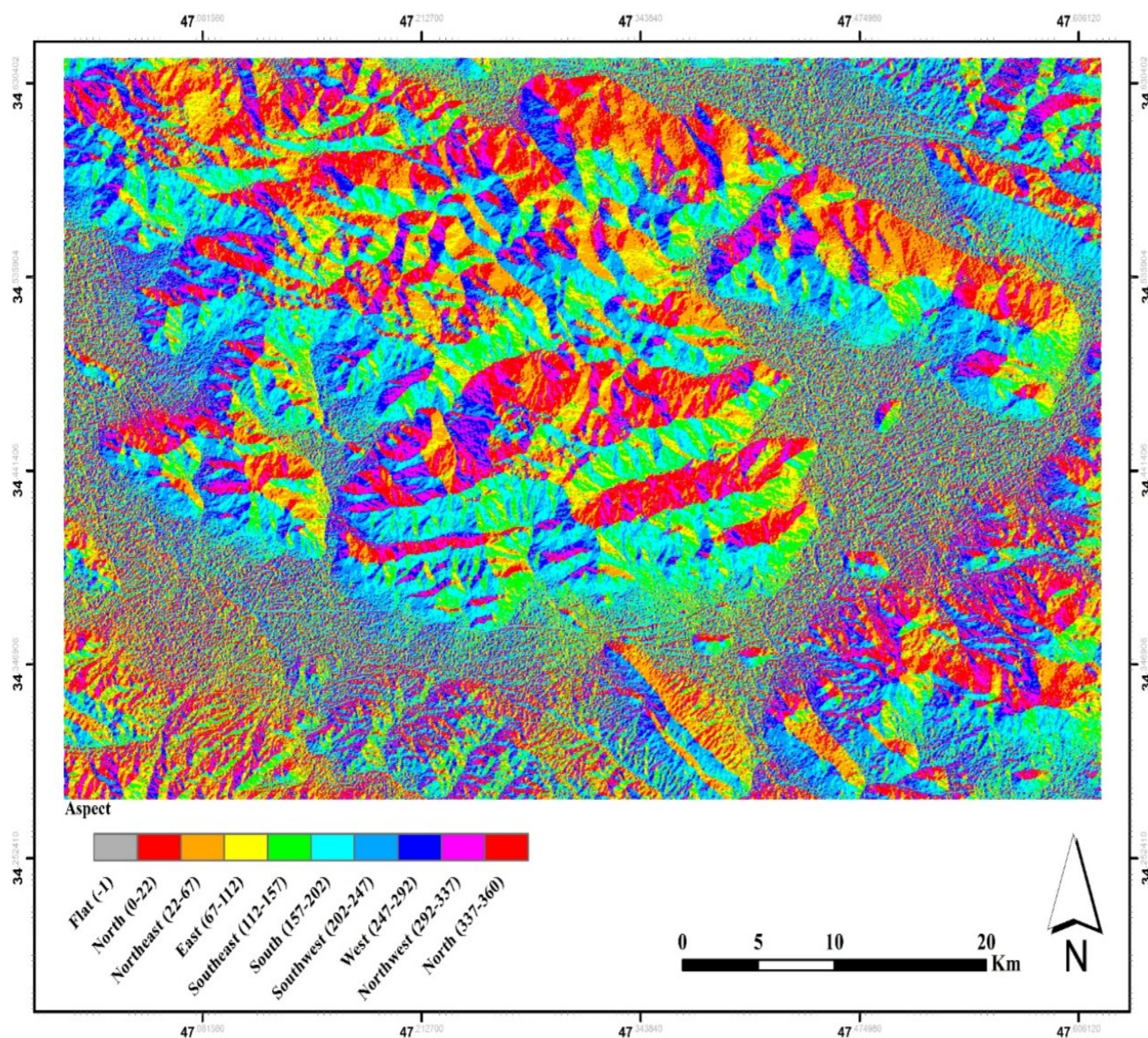

Figure 2. Map of aspect in the study area

The estimations made for direct, diffuse, and global solar radiations in the study area are provided in Table 3. As this table shows, the total direct radiation is the highest in July and the lowest in December (from 100,935 to 655.1568 MJ/m^2 for July and from 0 to 255.9125 MJ/m^2 for December). Comparing the total direct radiation maps with the aspect map as one of the important criteria for installing PV systems (Figure 2) shows that the south, southwest, and west-facing slopes and the flat areas (plains) receive the highest amount of direct radiation and the north, northeast and to some extent, northwest-facing slopes receive the lowest direct radiation. The maps of direct solar radiation estimates for the study area are shown in Figure A2 (see Fig. A2 in Appendix). The share of diffuse solar radiation in the total monthly radiation is the highest in July and the lowest in December. The diffuse solar radiation estimates obtained for the area vary from 68.4104 to 187.1345 MJ/m^2 for July and from 25.4205 to 77.2614 MJ/m^2 for December. However, comparing the diffuse solar radiation maps with the aspect map shows that the diffuse radiation has not the same distribution in the area as direct and global radiation, because the north and northeast-facing slopes receive the highest amounts of diffuse radiation, and the south and southwest-facing slopes and the flat areas have the lowest amounts of diffuse radiation. The maps of diffuse solar radiation estimates for the study area are shown in Figure A3.

The estimations of global solar radiation in the study area indicate that as in the above cases, July has the highest and December has the lowest monthly global radiation. For July, this estimate ranges from 181, 4857 to 842, 2632 MJ/m^2, and for December, it varies from 25, 4205 to 319,901 MJ/m^2. Comparing the monthly global radiation maps with the aspect map shows that the global radiation is the lowest in the north and northeast-facing slopes and the highest in the south and southwest-facing slopes and the flat areas. The maps of global radiation estimates for the study area are presented in Figure A4 (see Fig. A4 in Appendix).

Comparing the radiation received in flat areas with the radiation received in sloped areas, especially at higher elevations, shows that the amount of radiation received increases with altitude. At higher altitudes, thickness of the atmosphere is lower and thinner because air molecules can spread out more and air density decreases. Therefore, these areas have the highest potential for receiving solar radiation [40]. According to the maps of total annual radiation duration in the study area (2016), this parameter ranges from a minimum of 382.674 hours to a maximum of 4310.9 hours. The minimum and maximum diffuse radiations, direct radiation, and global radiation received annually are 606.4596 and 1702.984 MJ/m^2, 336.8423, and 5840.674 MJ/m^2, and 1005.556 and 7467.3 MJ/m^2 (per year), respectively.

Table 3. The sum of, direct, diffuse, global and duration radiations estimated at Kermanshah station by The Solar Analyst in 12 months

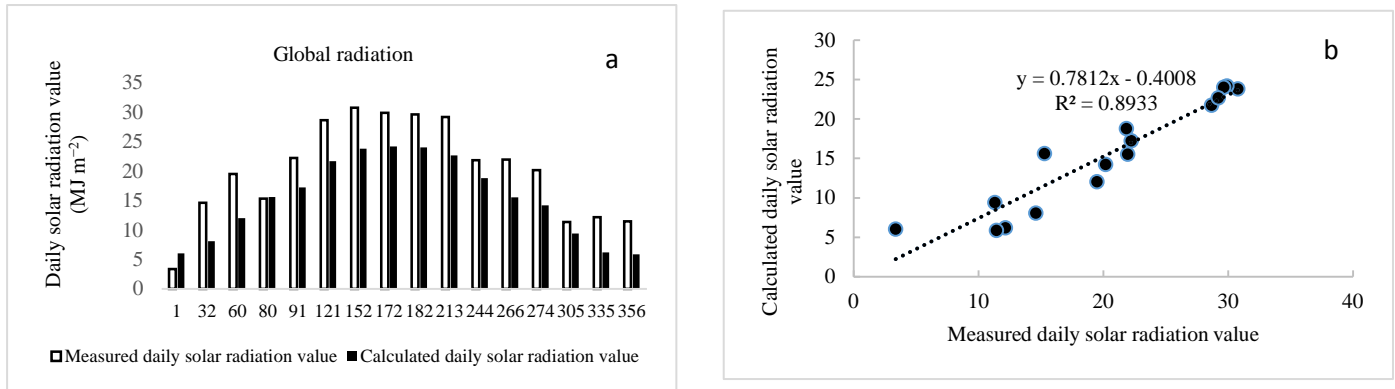| Month	Maximum diffuse radiation (MJ m^{-2})	Minimum diffuse radiation (MJ m^{-2})	Maximum direct radiation (MJ m^{-2})	Minimum direct radiation (MJ m^{-2})	Maximum global radiation (MJ m^{-2})	Minimum global radiation (MJ m^{-2})
Jan.	84.09	28.03	337.08	0.00	406.76	28.03
Feb.	103.20	35.63	402.91	0.00	488.51	35.63
Mar.	139.87	49.78	515.92	0.00	642.82	51.21
Apr.	160.62	58.21	571.50	0.65	725.13	63.00
May	183.71	67.09	649.05	74.97	831.41	148.98
Jun.	184.49	67.51	644.43	125.70	828.89	211.94
Jul.	187.13	68.41	655.16	100.94	842.26	181.49
Aug.	172.31	62.64	608.68	13.30	777.01	80.33
Sep.	143.34	51.36	521.46	0.00	654.11	53.87
Oct.	118.75	41.40	451.64	0.00	553.67	41.40
Nov.	89.13	29.98	353.14	0.00	427.01	29.98
Dec.	77.26	25.42	255.91	0.00	319.90	25.42
Annual total	1702.98	606.46	5840.68	336.84	7467.30	1005.56

Figure 3. Comparison of measured daily global solar radiation and calculated daily global solar radiation by Solar Analyst (a) and its determination coefficient (b)

To measure the accuracy and performance of the Solar Analyst, the method was used to estimate the global solar radiation in Kermanshah meteorological station for the first day of each month and solstices and equinoxes, and the results were compared with the measured data. The coefficient of determination (R^2) was then computed so that the accuracy of the software in estimating radiation could be evaluated. According to Figure 3, this model was recommended for solar radiation estimation with acceptable accuracy, especially in high areas with complex topography where solar radiation data are not available.

4. CONCLUSIONS

The Solar Analyst tools provided in the ArcMap software can estimate the radiation received at any given point or across an area. To assess the spatial and temporal distribution of solar radiation in the Paraw Mountain, in this study, this tool was used to estimate the direct, diffuse, and global solar radiation and the duration of radiation in this area for different months of 2016. The estimations of radiation duration showed that in this area, May, June, and July experienced the highest and December had the lowest monthly total radiation duration. The results also showed that the south and southwest-facing slopes and the flat areas had the highest radiation durations and the north and northeast-facing slopes had the shortest radiation durations.

The estimations of direct, diffuse, and global solar radiations in the study area showed that July had the highest and December the lowest amounts of total monthly radiation. It was found that the diffuse radiation was the highest in the north and northeast-facing slopes and the lowest in the south and southwest-facing slopes and the flat areas. For both direct and global radiations, the estimates were the lowest in the north and northeast-facing slopes and the highest in the south and southwest-facing slopes and the flat areas. The results also showed that in the Paraw Mountain, the amount of radiation increased with altitude. The total annual solar radiation duration in the study area (2016) was estimated to range from a minimum of 382.674 hours to a maximum of 4310.9 hours. The total global radiation in the area was estimated to be between 1005.556 and 7467.3 MJ/m² per year. The standard amount of solar radiation for PV system installations is $> = 1.15$ MWh/m²/yr or 4140 MJ/ m²/yr [41]; as a result, this site is suitable for solar energy harvesting.

In the performance evaluation of the employed tool, the coefficient of determination (R^2) was calculated as 0.89. This evaluation showed the acceptable accuracy of the model and

that the tool could have accurate solar radiation estimates, which is subsequently used in the site location of solar panels, for areas without radiometric stations and those with high altitudes and complex terrains. This conclusion is consistent with the findings of Sabziparvar et al. (2015), who used the same tool to estimate the total radiation in four provinces of Iran, used statistical tests to compare the results with the measurements, and ultimately reported the good accuracy of this method in estimating total solar radiation. The results were also consistent with the findings of Valizadeh (2014), which showed the acceptable speed and accuracy of this tool in estimating solar radiation. The studies of Hofierka and Suri (2002), Ramachandra (2006), Pons and Ninyerola (2008), and Moren et al. (2018) reached similar conclusions.

5. ACKNOWLEDGEMENT

NOMENCLATURE

S_{Const}	Solar constant (1367 Wm^{-2})
β	The transmissivity of the atmosphere
$m(\theta)$	The relative optical path length
$SunGap_{\theta,\alpha}$	The gap fraction for the sun map sector
$SunDur_{\theta,\alpha}$	The time duration or potential daylength
$AngIn_{\theta,\alpha}$	The angle of incidence between the centroid of the sky sector and the axis normal to the surface
θ	The solar zenith angle
Elev	Altitude of site (m)
G_z	The surface zenith angle
G_a	The surface azimuth angle
R_{glb}	The global normal radiation
P_{dif}	The proportion of global normal radiation flux that is diffused
Dur	The time interval for analysis
$SkyGap_{\theta,\alpha}$	The gap fraction for the sky sector
$Weight_{\theta,\alpha}$	The proportion of diffuse radiation originating in a given sky sector relative to all sectors
R_{glb}	The global normal radiation
R^2	Coefficient of determination
θ_1 and θ_2	The bounding zenith angles of the sky sector
Div_{azi}	The number of azimuthal divisions in the sky map

Appendix

See Figs. A1–A4.

Figure A1. Radiation duration map in the study area in 12 months of 2016

Figure A2. Temporal and spatial distribution of the sum of direct radiation in the study area in 12 months of 2016. The unit of radiation in the maps is (Wh/m^{-2})
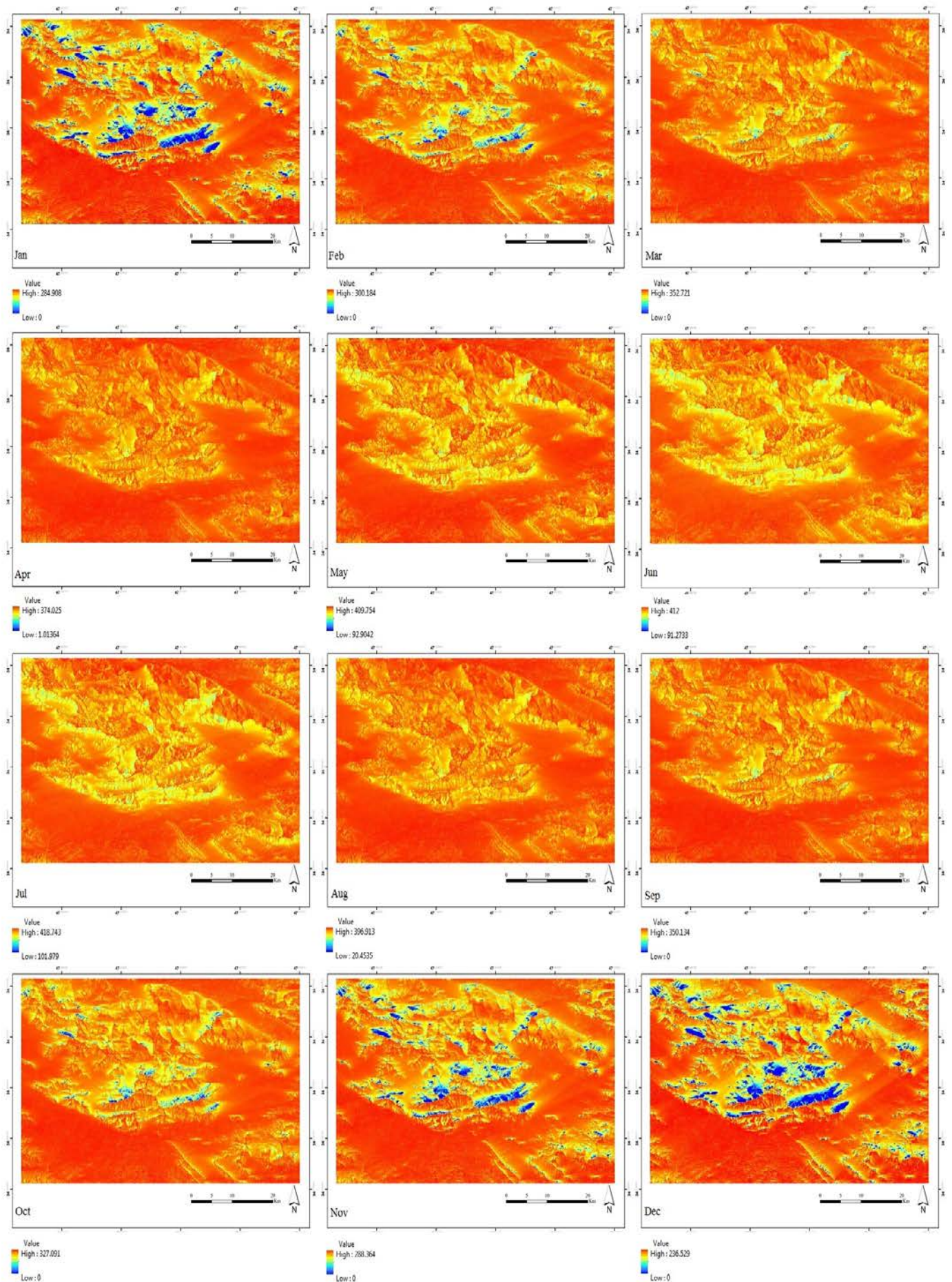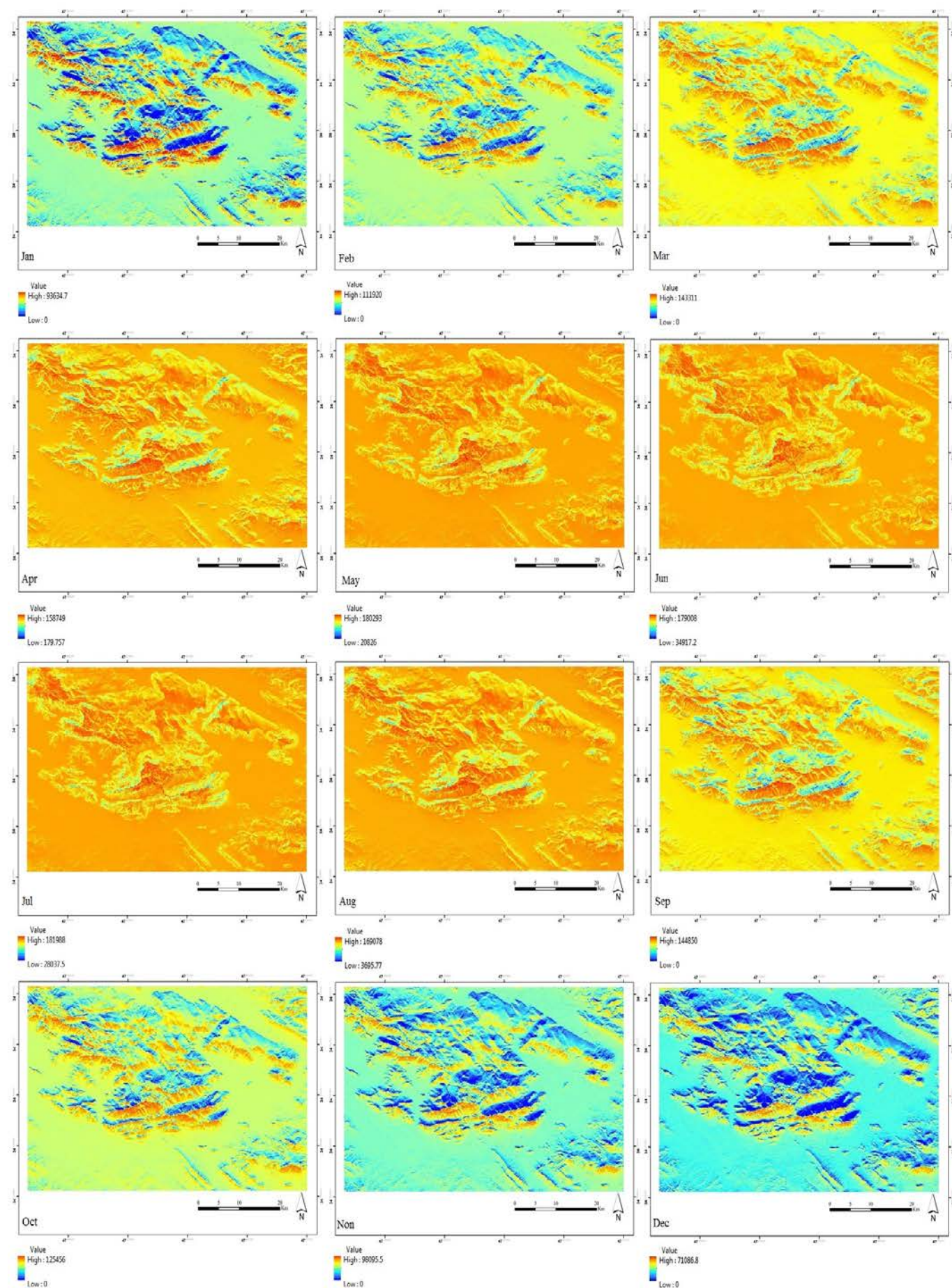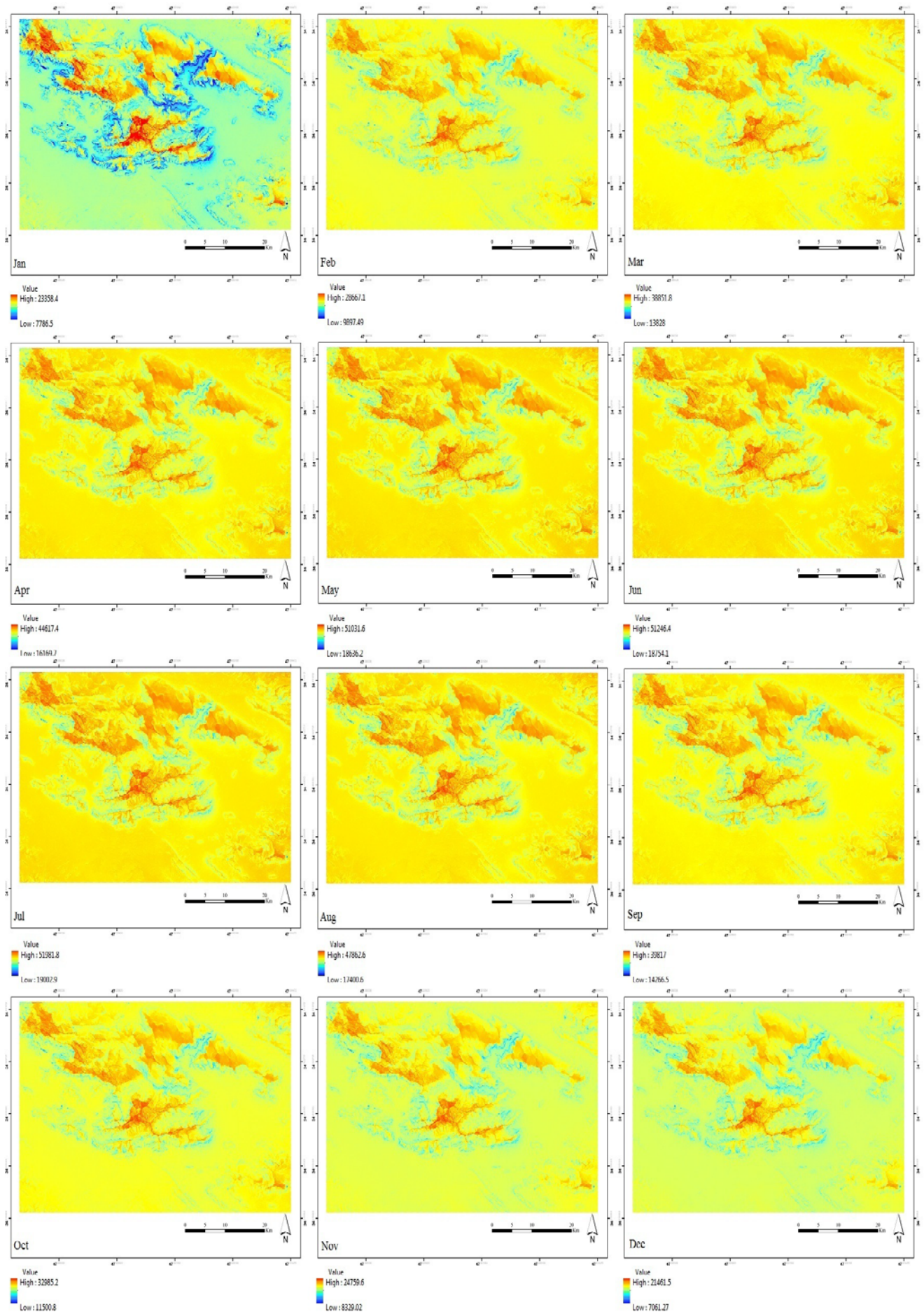
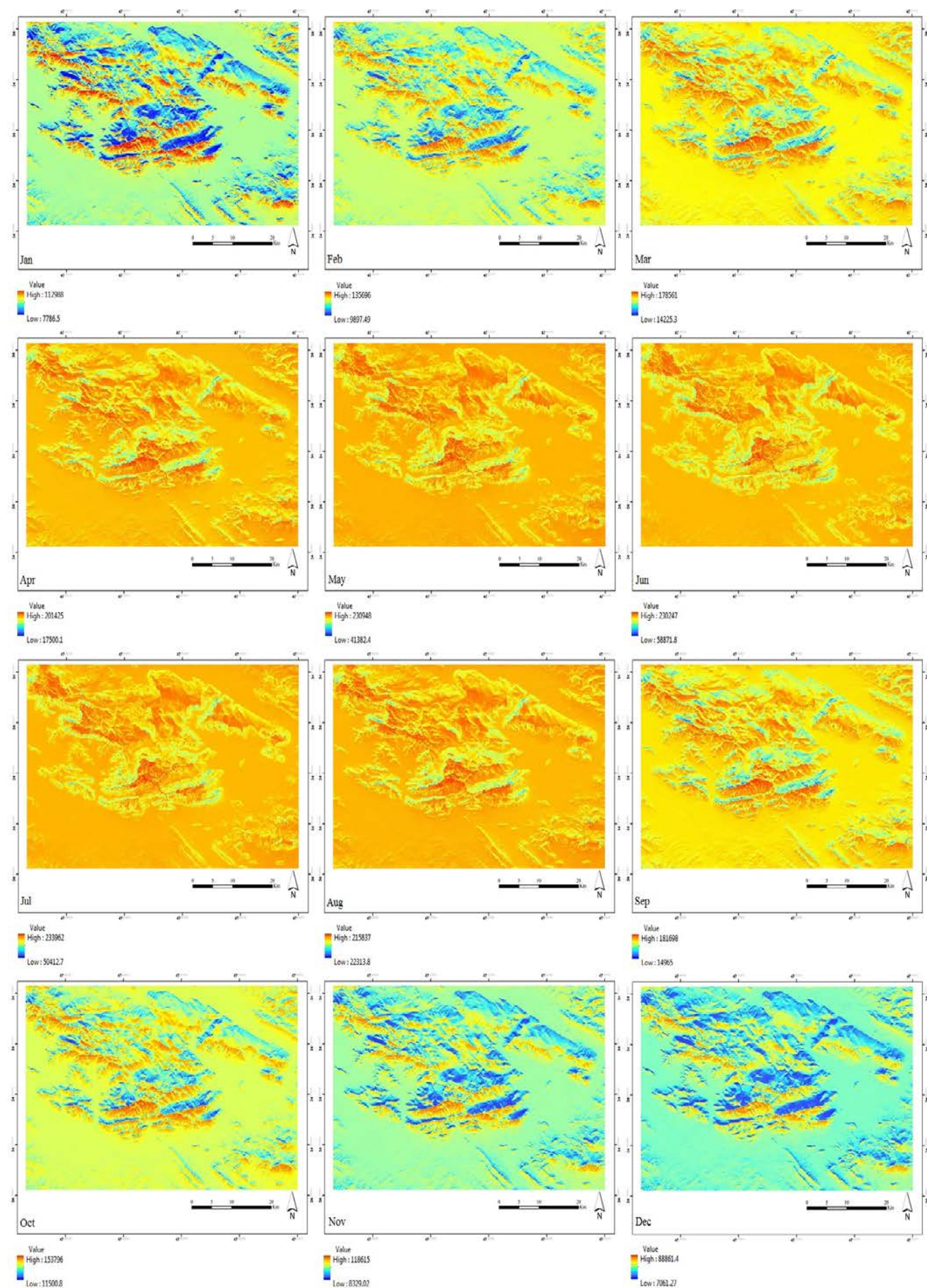**Figure A3.** Temporal and spatial distribution of the sum of diffuse radiation in the study area in 12 months of 2016

Figure A4. Temporal and spatial distribution of the sum of global radiation in the study area in 12 months of 2016

REFERENCES

1. Mostaufiolmamaleki, R., Essentials of astronomy Earth in the universe, Scientific Publication Center of Islamic Azad University Press, (1996). (http://www.lib.ir).

2. Tavousi, T., The climatic application of solar radiation in environmental planning, Sistan and Baluchestan University Press, Zahedan, (2017). (https://climatology.ir/wp-content/uploads/2017/11/Solar-Radiation.pdf).

3. Sabziparvar, A., Khatar, B. and Mohebzadeh, H., "Assessment of GIS ability in zonation of the seasonal and annual distribution of total solar radiation (Case study: Central provinces of Iran)", *Iranian Journal of Geophysics*, Vol. 9, No. 2, (2015), 14-29. (In Farsi). (http://www.ijgeophysics.ir/article_33580.html).

4. Liu, B. and Jordan, R., "Daily insolation on surfaces tilted towards equator", *ASHRAE Journal*, Vol. 10, (United States), (1961). (https://www.osti.gov/biblio/5047843-daily-insolation-surfaces-tilted-towards-equator).

5. Hay, J.E., "Calculation of monthly mean solar radiation for horizontal and inclined surfaces", *Solar Energy*, Vol. 23, No. 4, (1979), 301-307. (https://doi.org/10.1016/0038-092X (79)90123-3).

6. Steven, M.D. and Unsworth, M.H., "The angular distribution and interception of diffuse solar radiation below overcast skies", *Quarterly Journal of the Royal Meteorological Society*, Vol. 106, No. 447, (1980), 57-61. (https://doi.org/10.1002/qj.49710644705).

7. Reindl, D.T., Beckman, W.A. and Duffie, J.A., "Evaluation of hourly tilted surface radiation models", *Solar Energy*, Vol. 45, No. 1, (1990), 9-17. (https://doi.org/10.1016/0038-092X (90)90061-G).

8. Tian, Y.Q., Davies-Colley, R.J., Gong, P. and Thorrold, B.W., "Estimating solar radiation on slopes of arbitrary aspect", *Agricultural and Forest Meteorology*, Vol. 109, No. 1, (2001), 67-74. (https://doi.org/10.1016/S0168-1923 (01)00245-3).

9. Kavyani, M.R. Microclimatology, Tehran: Samt Press, (2012). (https://samta.samt.ac.ir/content/13634/%D9%85%DB%8C%DA%A9%D8%B1%D9%88%DA%A9%D9%84%DB%8C%D9%85%D8%A7%D8%AA%D9%88%D9%84%D9%88%DA%98%DB%8C?lang=en).

10. Valizadeh Kamran, K. "Estimation of potential evapotranspiration with Estefnz method and GIS techniques in Eastern Azerbaijan", *Journal of Geography and Planning*, Vol. 18, No. 49, (2014), 317-334. (In Farsi). (https://geoplanning.tabrizu.ac.ir/article_2217.html).

11. Hofierka, J. and Suri, M., "The solar radiation model for open source GIS: Implementation and applications", *Proceedings of The Open Source GIS-GRASS User's Conference*, Vol. 2002, (2002), 51-70. (https://www.scirp.org/(S(351jmbntvnsjt1aadkposzje))/reference/ReferencesPapers.aspx?ReferenceID=1413518).

12. Dozier, J. and Frew, J., "Rapid calculation of terrain parameters for radiation modeling from digital elevation data", *IEEE Transactions on Geoscience and Remote Sensing*, Vol. 28, No. 5, (1990), 963-969. (https://doi.org/10.1109/36.58986).

13. Ramachandra, T.V., "Solar energy potential assessment using GIS", *Energy Education Science and Technology*, Vol. 18, No. 1/2, (2006), 101. (https://www.researchgate.net/publication/256454051_Solar_energy_potential_assessment_using_GIS).

14. Pons, X. and Ninyerola, M., "Mapping a topographic global solar radiation model implemented in a GIS and refined with ground data", *International Journal of Climatology*, Vol. 28, No. 13, 1821-1834. (https://doi.org/10.1002/joc.1676).

15. Batlles, F.J., Bosch, J.L., Tovar-Pescador, J., Martinez-Durban, M., Ortega, R. and Miralles, I., "Determination of atmospheric parameters to estimate global radiation in areas of complex topography: Generation of global irradiation map", *Energy Conversion and Management*, Vol. 49, No. 2, 336-345. (https://doi.org/10.1016/j.enconman.2007.06.012).

16. Gastli, A. and Charabi, Y., "Solar electricity prospects in Oman using GIS-based solar radiation maps", *Renewable and Sustainable Energy Reviews*, Vol. 14, No. 2, (2010), 790-797. (https://doi.org/10.1016/j.rser.2009.08.018).

17. Wong, M.S., Zhu, R., Liu, Z., Lu, L., Peng, J., Tang, Z. and Chan, W.K., "Estimation of Hong Kong's solar energy potential using GIS and remote sensing technologies", *Renewable Energy*, Vol. 99, (2016), 325-335. (https://doi.org/10.1016/j.renene.2016.07.003).

18. Zhang, Y., Chang, X. and Liang, J., "Comparison of different algorithms for calculating the shading effects of topography on solar irradiance in a mountainous area", *Environmental Earth Sciences*, Vol. 76, No. 7, (2017), 295. (https://doi.org/10.1007/s12665-017-6618-5).

19. Zhang, Y.L., Li, X., Cheng, G.D., Jin, H.J., Yang, D.W., Flerchinger, G.N., Chang, X.L., Wang, X. and Liang, J., "Influences of topographic shadows on the thermal and hydrological processes in a cold region mountainous watershed in northwest China", *Journal of Advances in Modeling Earth Systems*, Vol. 10, No. 7, (2018), 1439-1457. (https://doi.org/10.1029/2017MS001264).

20. Moreno, H.A., Ogden, F.L. and Alvarez, L.V., "Unstructured-mesh terrain analysis and incident solar radiation for continuous hydrologic modeling in mountain watersheds", *Water*, Vol. 10, No. 4, (2018), 398. (https://doi.org/10.3390/w10040398).

21. Choi, Y., Suh, J. and Kim, S.M. "GIS-based solar radiation mapping, site evaluation, and potential assessment: A review", *Applied Sciences*, Vol. 9, No. 9, (2019),1960. (https://doi.org/10.3390/app9091960).

22. Buffat, R., Grassi, S. and Raubal, M., "A scalable method for estimating rooftop solar irradiation potential over large regions", *Applied Energy*, Vol. 216, (2018), 389-401. (https://doi.org/10.1016/j.apenergy.2018.02.008).

23. Hoseinzadeh, S. and Azadi, R., "Simulation and optimization of a solar-assisted heating and cooling system for a house in Northern of Iran", *Journal of Renewable and Sustainable Energy*, Vol. 9, No. 4, (2017), 045101. (https://doi.org/10.1063/1.5000288).

24. Hoseinzadeh, S., Hadi Zakeri, M., Shirkhani, A. and Chamkha, A.J., "Analysis of energy consumption improvements of a zero-energy building in a humid mountainous area", *Journal of Renewable and Sustainable Energy*, Vol. 11, No. 1, (2019), 015103. (https://doi.org/10.1063/1.5046512).

25. Yousef Nezhad, M.E. and Hoseinzadeh, S., "Mathematical modelling and simulation of a solar water heater for an aviculture unit using MATLAB/SIMULINK", *Journal of Renewable and Sustainable Energy*, Vol. 9, No. 6, (2017), 063702. (https://doi.org/10.1063/1.5010828).

26. REN21, Renewables 2016 global status report, (2016). (https://www.ren21.net/wp-content/uploads/2019/05/REN21_GSR2016_FullReport_en_11.pdf).

27. https://www.irimo.ir.

28. https://earthexplorer.usgs.gov/.

29. https://desktop.arcgis.com/.

30. Kavyani, M.R. and Alijani, B., The foundation of climatology, Tehran: Samt Press, (2005). (In Farsi). (https://samta.samt.ac.ir/content/9117/%D9%85%D8%A8%D8%A7%D9%86%DB%8C-%D8%A2%D8%A8-%D9%88%D9%87%D9%88%D8%A7%D8%B4%D9%86%D8%A7%D8%B3%DB%8C).

31. Rich, P.M., Dubayah, R., Hetrick, W.A. and Saving, S.C., "Using viewshed models to calculate intercepted solar radiation: Applications in ecology", *American Society for Photogrammetry and Remote Sensing Technical Papers*, (1994), 524-529. (http://professorpaul.com/publications/rich_et_al_1994_asprs.pdf).

32. Rich, P.M. and Fu, P., "Topoclimatic habitat models", *Proceedings of the Fourth International Conference on Integrating GIS and Environmental Modeling*, (2000). (http://precisionviticulture.com/files/rich_2000_topoclimate_gisem4_96.pdf).

33. Fu, P., "A geometric solar radiation model with applications in landscape ecology", Ph.D. Thesis, Department of Geography, University of Kansas, Lawrence, Kansas, USA, (2000). (https://biosurvey.ku.edu/geometric-solar-radiation-model-applications-landscape-ecology).

34. Fu, P. and Rich, P.M., "The solar analyst 1.0 manual", Helios Environmental Modeling Institute (HEMI), USA, (2000). (http://professorpaul.com/publications/fu_rich_2000_solaranalyst.pdf).

35. Fu, P. and Rich, P.M., "A geometric solar radiation model with applications in agriculture and forestry", *Computers and Electronics in Agriculture*, Vol. 37, (2002), 25-35. (https://doi.org/10.1016/S0168-1699 (02)00115-1).

36. Bakirci, K., "Correlations for estimation of daily global solar radiation with hours of bright sunshine in Turkey", *Energy*, Vol. 34, No. 4, (2009), 485-501. (https://doi.org/10.1016/j.energy.2009.02.005).

37. Besharat, F., Dehghan, A.A. and Faghih, A.R., "Empirical models for estimating global solar radiation: A review and case study", *Renewable*

and Sustainable Energy Reviews, Vol. 21, (2013), 798-821. (https://doi.org/10.1016/j.rser.2012.12.043).

38. Chen, J.L., Li, G.S., Xiao, B.B., Wen, Z.F., Lv, M.Q., Chen, C.D., Jiang, Y., Wang, X.X. and Wu, S.J., "Assessing the transferability of support vector machine model for estimation of global solar radiation from air temperature", *Energy Conversion and Management*, Vol. 89, (2015), 318-329. (https://doi.org/10.1016/j.enconman.2014.10.004).

39. Zolfaghari, H., Earth's climate, Razi University Press, Kermanshah, (2014). (https://lib.razi.ac.ir/).

40. Alijani, B., Iran's climate,Tehran: Payame Noor University Press, (2012). (https://samta.samt.ac.ir/).

41. Li, D., "Using GIS and remote sensing techniques for solar panel installation site selection", Master's Thesis, University of Waterloo, (2013). (http://hdl.handle.net/10012/7960).

Sensorless FCS-MPC-Based Speed Control of a Permanent Magnet Synchronous Motor Fed by 3-Level NPC

Sajad Saberi, Behrooz Rezaie*

Department of Computer and Electrical Enginnering, Babol Noshirvani Univercity of Technology, P. O. Box: 47148-71168, Babol, Mazandaran, Iran.

A B S T R A C T

This paper presents a sensorless speed control algorithm based on Finite Control Set Model Predictive Control (FCS-MPC) for Permanent Magnet Synchronous Motor (PMSM) fed by a 3-level Neutral-Point Clamped (NPC) converter. The proposed scheme uses an anti-windup Proportional-Integral (PI) controller concept to generate the reference electromagnetic torque using the error of speed. Then, FCS-MPC uses this torque reference and other parameters such as a current limitation, neutral point voltage unbalance, and switching frequency to control the converter gate signals. Also, an Adaptive Nonsingular Fast Terminal Sliding Mode Observer (ANFTSMO) was employed to estimate rotor position precisely in positive (clockwise) and negative (counterclockwise) speed to eliminate the encoder. The proposed algorithm has fast dynamics and low steady-state error. Moreover, torque fluctuation and current distortion reduced compared with Space Vector Pulse Width Modulation (SVPWM) based speed control and Direct Predictive Speed Control (DPSC). Simulation results using MATLAB/SIMULINK® demonstrate the performance of the proposed scheme.

1. INTRODUCTION

Wind energy is the fastest growing among all renewable energy systems and it has become possible due to the rapid advances in the size of wind generators as well as the developments in power electronics [1]. Variable-speed Wind Energy Conversion Systems (WECS) can be controlled over a wide range of wind speeds to facilitate their operability at maximum power coefficients, thus allowing them to obtain larger energy capture from the wind [2, 3]; therefore, speed control is the vital factor of Maximum Power Point Tracking (MPPT) of this type of WECSs [4, 5].

The most promising topology for variable WECSs is the direct-driven, multi-pole Permanent Magnet Synchronous Machine (PMSM) [5] which is characterized by more advantages than fixed-speed ones such as higher power density, fast dynamic response, improved efficiency, and reduced mechanical stress [5-7].

Field-Oriented Control (FOC) and Direct Torque Control (DTC) are the most common strategies to control PMSMs [8, 9]. Windup problem and bandwidth limitation (due to existence of modulator) make FOC a non-ideal controller choice [10]. DTC uses switching table to control motor torque directly. Given that output voltage vectors are not always optimal, this method suffers from high torque and stator flux ripples [11, 12].

While the complexity of converters increases, the necessity of applying advanced control strategies that are capable of

considering multivariable systems and handling additional control objectives is undeniable [13]. Multivariable structure, excellent performance in the presence of nonlinearities, and constraints consideration make MPC one of the best choices for drive systems [14, 15]. Finite Control Set Model Predictive Control (FCS-MPC) is one of the MPC methods that takes advantage of the fact that the number of possible switching states is limited; therefore, it is possible to predict the effect of each Voltage Space Vector (VSV) to determine the best VSV for the next sampling time [16].

FCS-MPC has been used to control the current in several converter topologies [16-19]. Because of the inherent sluggish behavior of the mechanical system, the ordinary Proportional Integral (PI) controller does not provide a fast response to reference speed change [19]. To overcome this problem, Direct Predictive Speed Control (DPSC) without cascade structure has been introduced [20-22].

A DPSC strategy directly controls the speed of the motor and achieves high-speed control dynamics [13]. Compared to current dynamic, mechanical dynamic is very slow and this significant difference between time constants leads to torque fluctuation and current distortion. Therefore, the designer needs to consider a longer prediction horizon for DPSC [23]. Longer prediction horizon means more different switching states that increase the computation time so drastically that real-time implementation is not feasible in general [24]. In [13], a DPSC method with a shorter prediction horizon was used to control the speed of a PMSM fed by 3-level NPC inverter. Results in [13] were acceptable, but two-step prediction horizon means $27^2 = 729$ different switching

*Corresponding Author's Email: brezaie@nit.ac.ir (B. Rezaie)
URL: http://www.jree.ir/article_122410.html

states, which is far from 27 switching states for one-step prediction horizon; therefore, this paper proposes a one-step prediction horizon method.

One of the key factors of all speed control schemes of the PMSM is the precise sensing of speed and position using a dedicated external sensor or the exact estimation using a fast and accurate observer. Eliminating encoder used to measure the speed and position of the shaft increases the reliability and applicability of PMSM and leads to schemes with more compact constructions and lower costs [25].

The most common method for the position and speed estimation of PMSM is the back electromotive force (back-EMF) method [26, 27]. Despite the simplicity of this method, it yet shows excellent results in high-speed applications [28, 29]. However, one of the well-known problems of this method is the dependency of back-EMF on the speed of the rotor. When motor works in the low-speed range, since back-EMF is small, accurate estimation of position becomes a challenging task [27-29]. In [23], a startup strategy was designed to provide a better estimation at low speeds. In [31], an active flux estimator was used to ensure a better estimation at lower speeds. However, this method is not able to estimate position in the reverse mode.

In this paper, a full range position and speed estimator using an Adaptive Nonsingular Fast Terminal Sliding Mode Observer (ANFTSMO) [25] was employed to estimate the PMSM rotor angle and speed without an encoder. ANFTSMO can not only solve the chattering problem in the low-speed region, but also track the rotor angle at reverse speeds quickly, accurately, and without chattering [25].

To control the speed of PMSM in the presence of current/torque limitation, in the proposed method, first, we design a reference torque to use in FCS-MPC; then, a cost function using current references, torque reference, torque constraint, and switching constraint is designed. By replacing the speed error term with the electromagnetic term in the cost function, the necessity of using multiple horizons is obviated and the proposed method becomes almost as fast as a predictive speed control scheme with lower torque oscillation, current distortion, and steady-state error.

The main contribution of the paper is as follows:

- Rotor position estimation using ANFTSMO
- Designing a discrete electromagnetic torque reference signal for FCS-MPC
- Proposing a new objective function for FCS-MPC-based speed controller.

It is worth mentioning that the novelty of the paper is in utilizing the designed torque reference as a part of the cost function to minimize the oscillation of speed and torque.

The organization of the paper is as follows. Section 2 gives a description of model including PMSM and inverter and their equations. Section 3 introduces the FCS-MPC algorithm and the proposed method. Section 4 explains cost function terms and considerations. Section 5 introduces and discusses simulation results. Section 6 concludes the paper.

2. SYSTEM DESCRIPTION

Fig. 1 shows a topology including PMSM fed by 3-level NPC. The PMSM and inverter models are described in the following subsections.
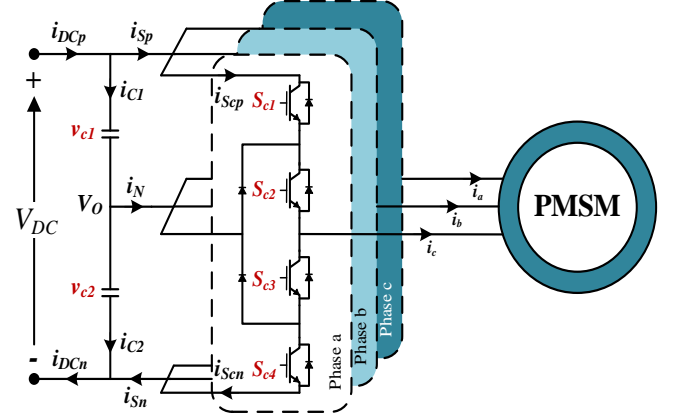

Figure 1. PMSM fed by 3-level NPC topology

2.1. PMSM model

By assuming a Surface-Mounted PMSM (SPMSM) with the same inductance for d and q axes, the dynamic model for the SPMSM in the d-q reference frame can be described as follows [16]:

$$\frac{di_d}{dt} = \frac{1}{L_s}\left(v_d - R_s i_d + \omega_e L_s i_q\right)$$

$$\frac{di_q}{dt} = \frac{1}{L_s}\left(v_q - R_s i_q - \omega_e L_s i_d - \omega_e \psi_{mg}\right)$$

$$T_e = \frac{3}{2}Z_p \psi_{mg} i_q \tag{1}$$

$$\frac{d\omega_e}{dt} = \left(\frac{Z_p}{J_m}\left(T_e - T_L\right) - \frac{B_v}{J_m}\omega_e\right)$$

A discrete model of PMSM is needed to predict the future values of current and torque for FCS-MPC. To decrease the calculation burden, the model can be rewritten in discrete time using a simple discretization method like the Euler method [32].

$$i_d[k+1] = \left(1 - \frac{T_s R_s}{L_s}\right)i_d[k]...$$
$$+ \frac{T_s}{L_s}v_d[k] + T_s\omega_e[k]i_q[k]$$

$$i_q[k+1] = \left(1 - \frac{T_s R_s}{L_s}\right)i_q[k] + \frac{T_s}{L_s}v_q[k]... \tag{2}$$
$$+ T_s\omega_e[k]i_q[k] - \frac{T_s\psi_{mg}}{L_s}\omega_e[k]$$

$$T_e[k+1] = \frac{3}{2}Z_p\psi_{mg}i_q[k+1]$$

2.2. Inverter mode

The power circuit of NPC inverter for one phase is shown in Figure 1. S_{xq} represents the switching state of phase x and switch q with x={a, b, c} and q={1, 2, 3, 4}. Table 1 shows the values of S_{xq} and its equivalent voltages. For three phases of this inverter, 27 switching states are generated [33]. It is worth mentioning that to prevent short circuit, $S_{x3} = 1-S_{x1}$ and $S_{x4} = 1-S_{x2}$.

Table 1. Switching table of one phase of NPC inverter

S_x	S_{x1}	S_{x2}	S_{x3}	S_{x4}	U_x
P = 1	1	1	0	0	$V_{dc}/2$
0	0	1	1	0	0
N = −1	0	0	1	1	$-V_{dc}/2$

To use in (1), one needs to convert it to and using Park and Clarke transformation as follows:

$$v_{dq} = \begin{bmatrix} v_d & v_q \end{bmatrix}^T = MDU_x$$
$$M = \begin{bmatrix} \cos\theta & -\sin\theta \\ \sin\theta & \cos\theta \end{bmatrix}$$
$$D = \frac{2}{3}\begin{bmatrix} 1 & -1/2 & -1/2 \\ 0 & \sqrt{3}/2 & -\sqrt{3}/2 \end{bmatrix} \quad (3)$$

where D is Clarke transformation, M is the Park transformation matrix and θ is the electrical angle of the rotor [8].

Unbalanced neutral point voltage V_o has negative impact on the output voltage and semiconductor switch stress [34]. FCS-MPC has the ability to control V_o by predicting the voltage of the neutral point using 3-phase currents and switching states as follows [34]:

$$\frac{dV_O}{dt} = \frac{dV_{c1}}{dt} - \frac{dV_{c2}}{dt} = \frac{1}{C}\left\{\left(I_{Sp} - I_{Sn}\right)\right\}$$
$$V_O[k+1] = V_O[k] + \frac{T_s}{C}\left(I_{Sp}[k] - I_{Sn}[k]\right) \quad (4)$$

3. FCS-MPC DESCRIPTION

Figure 2 illustrates the operating principle of FCS-MPC [35]. Due to the finite number of switching states S_i, FCS-MPC can predict all possible system states x^p over a sampling period T_s based on system model and measured values. Then, depending on the objectives, a cost function C can be defined to discover the best possible switching.

As an example, considering Figure 2 in the first step, $x_2^p[k+1]$ is closest to the reference x^{ref}; thus, S_2 is selected and applied at t = k. Following the same procedure, S_3 will be selected for the second step and used at t = k + 1.
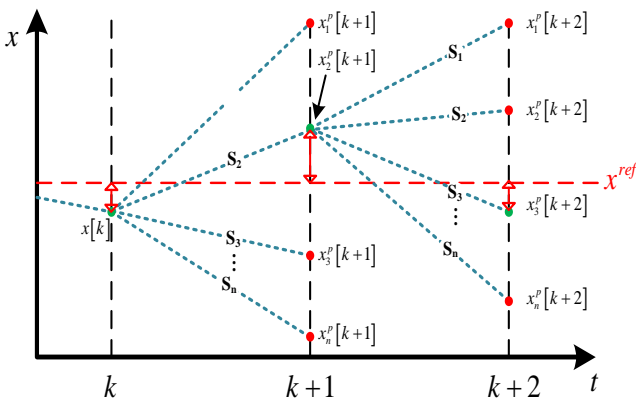
Figure 2. Operating principle of FCS-MPC

4. COST FUNCTION DESIGN

According to the FCS-MPC scheme, cost function has a significant effect on system performance [16]. By properly selecting the cost function, FCS-MPC can control multiple objectives at the same time. However, proper selection of the items and weightings is a challenging task. In this section, items of the cost function are discussed.

4.1. Tracking term

The main objective of the controller is to control the speed of PMSM. First, a reference is designed for electromagnetic torque. The design procedure is based on an anti-windup PI controller concept [36].

$$T_e^{ref}[k+1] = T_e^{ref}[k] + k_1\left(e_\omega[k] - e_\omega[k-1]\right)...$$
$$+ k_2 T_s\left(e_w[k] + \overline{e}[k]\right) \quad (5)$$

where T_e^{ref} is the electromagnetic torque reference to use in FCS-MPC, k_1 and k_2 are coefficients, and e_ω and $\overline{e}$ are as follows:

$$e_\omega[k] = \omega^{ref}[k] - \omega[k]$$
$$\overline{e}[k] = \begin{cases} T_e^{max} - T_e^{ref}[k] & T_e^{ref}[k] > T_e^{max} \\ -T_e^{max} - T_e^{ref}[k] & T_e^{ref}[k] < -T_e^{max} \\ 0 & o.w \end{cases} \quad (6)$$

After reference generation for T_e, its error can be used in the cost function.

$$e_{T_e} = T_e^{ref}[k+1] - T_e[k+1] \quad (7)$$

In surface-mounted PMSM with $L_d = L_q$ [6], the d-axis current does not affect electromagnetic torque and can be controlled independently. Thus, we can consider an error for d-axis current control.

$$e_{i_d} = i_d^{ref}[k+1] - i_d[k+1] \quad (8)$$

It is worth mentioning that $i_d^{ref}[k+1]$ is not accessible and if we use $i_d^{ref}[k]$ instead, it may lead to a delay in the system. Here, extrapolation method is used to build $i_d^{ref}[k+1]$ from current and past values of i_d^{ref} as follows [37]:

$$i_d^{ref}[k+1] = 3i_d^{ref}[k] - 3i_d^{ref}[k-1] + i_d^{ref}[k-2] \quad (9)$$

By combining e_{T_e} and e_{i_d} into one function, tracking term of the cost function will be as (10):

$$C_T = \begin{bmatrix} e_{i_d} & e_{T_e} & e_\omega \end{bmatrix}\begin{bmatrix} \lambda_{i_d} & 0 & 0 \\ 0 & \lambda_{T_e} & 0 \\ 0 & 0 & \lambda_\omega \end{bmatrix}\begin{bmatrix} e_{i_d} \\ e_{T_e} \\ e_\omega \end{bmatrix} \quad (10)$$

where λ_{i_d}, λ_{T_e}, and λ_ω are the weighting factors.

4.2. Zero term

Zero term is a part of the cost function that should be kept at zero. Here, only the neutral point voltage is considered for this term.

$$C_Z = \lambda_{V_o} (V_o)^2 \tag{11}$$

4.3. Constraint term

The constraint term may consist of multiple parts such as current limitation, torque limitation, and switching limitation. We considered the current limitation and switching limitation using (12) and (13).

$$C_{CI} = \begin{cases} \lambda_{I_m} \left(\sqrt{i_d^2 + i_q^2} - I_m \right) & \sqrt{i_d^2 + i_q^2} > I_m \\ 0 & o.w \end{cases} \tag{12}$$

$$C_{CS} = \lambda_S \left(\sum_{x=a,b,c} \left| S_x[k+1] - S_x[k] \right| \right) \tag{13}$$

where λ_{I_m} and λ_S are the weighting factors.

Using C_{CI}, we limit the current to the maximum allowed value and C_{CS} helps have a lower switching frequency by considering switch state as a variable. Thus, if we have two different switching with the same cost, the one with a lower switching change will be chosen.

As an example, if the last switching is S = [1 0 -1] and in next sampling, S_n = [0 0 -1] and S_m = [1 1 -1] have the same cost, the former one will be chosen, because it has just one switching in phase a and switching states in phase b and c will remain unchanged.

By incorporating C_{CI} and C_{CS} into one term, the constraint term is written as follows:

$$C_C = C_{CI} + C_{CS} \tag{14}$$

Finally, by considering the tracking term, the zero term, and the constraint term in one equation, the cost function to be minimized using FCS-MPC becomes

$$C = C_T + C_Z + C_C \tag{15}$$

Remark: A combination of multiple variables in a single cost function is not a straightforward task when they have different natures (in units or values). Finding optimal weighting factors is still an open problem, but there are some methods to find these factors correctly [38, 39]. Designing weighting factors is not in the scope of this paper and in this work, factors are designed using normalization and multiple simulations.

5. SIMULATION AND RESULTS

To demonstrate the performance of the proposed method in this section, the method is compared with two other methods, i.e., a DSPC using FCS-MPC introduced in [20] and an FOC method with a cascade structure using anti-windup PI as speed controller and SVPWM modulator [40]. Moreover, for the latter one, a system without a modulator is considered to

check the ideal case without switching. In these references, similar to our study, one-step prediction horizon has been used to decrease the oscillation.

Figure 3 illustrates the block diagram of the proposed method, and Figure 4 shows the flowchart for more details. Also, the parameters of the PMSM, inverter, and controller are presented in Table 2. Furthermore, the angle of the rotor is estimated using the method in [24] for all three controller schemes.
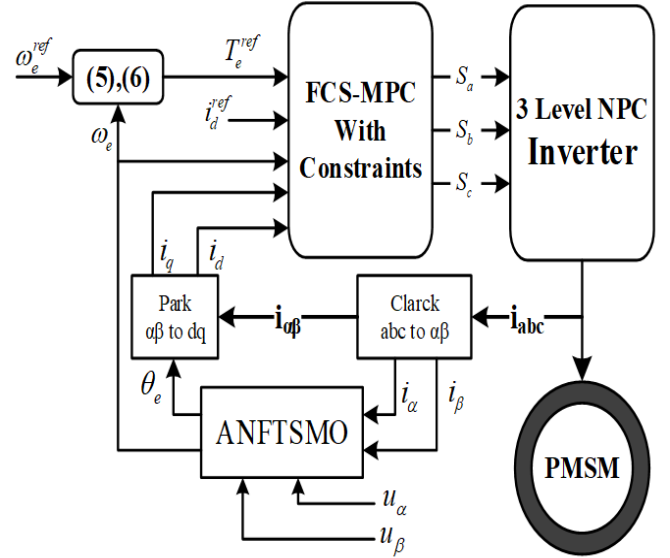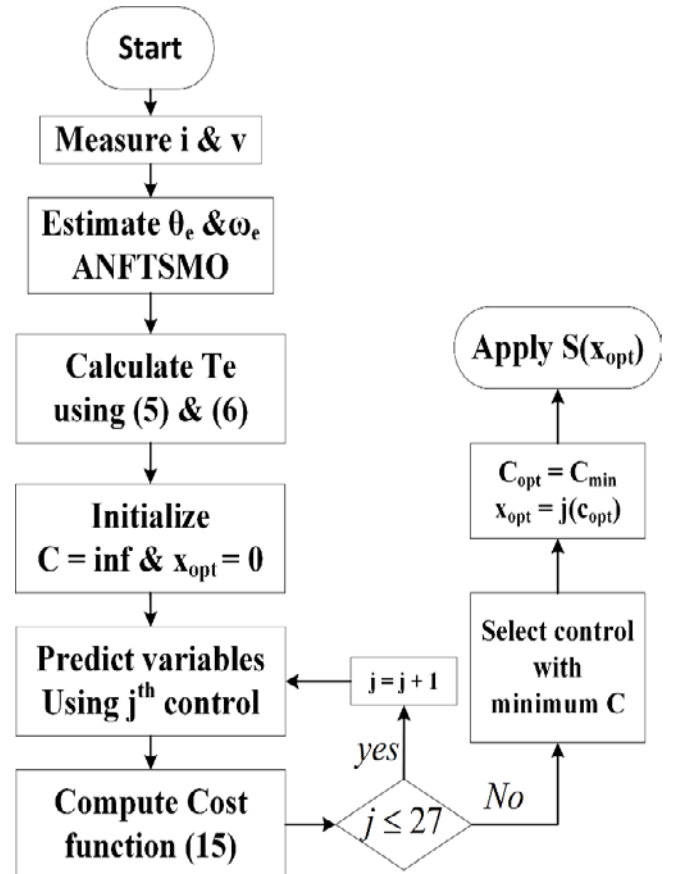

Figure 3. Block diagram of the proposed method

Figure 4. Proposed method flowchart

Table 2. System and controller parameters

Variable	Parameter	Value	Symbol
Sampling time	T_s	10	μs
Stator resistance	R_s	6.8	Ω
Stator inductance	L_s	8	mH
Flux linkage	ψ_{mg}	0.41	web
Pair poles	Z_P	3	
Moment of inertia	J_m	0.0212	kg/m^2
Viscose damping	B_v	0.31	Ns/m
DC voltage	V_{DC}	120	V
Current limitation	I_{max}	6.5	A
Torque limitation	T_{em}	12	Nm
Proportional factor	k_1	30	
Integral factor	k_2	10000	

Figure 5 shows the reference value of speed, reference value of T_e along with actual and estimated values of motor shaft position during simulation. It is clear that the ANFTSMO estimated rotor position accurately not only at low and high speeds but also during speed direction change.
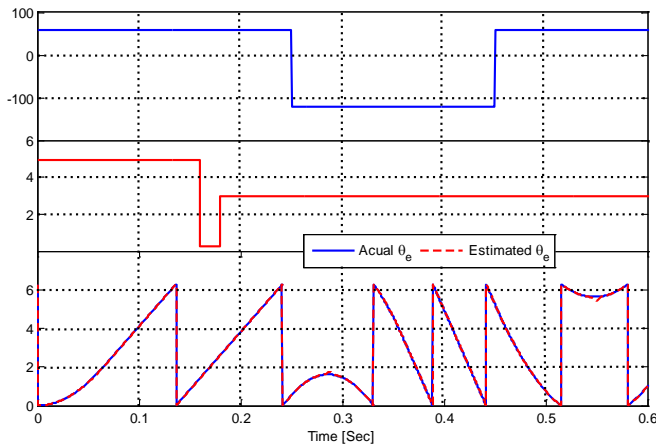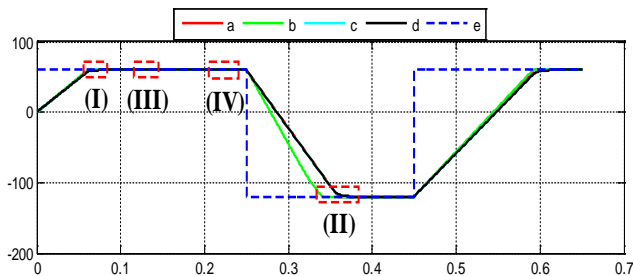

Figure 5. Reference for speed and mechanical torque and the rotor angle

Figure 6 shows speed change during the simulation for four methods as mentioned above and for more details, Figure 7 illustrates zoomed areas of Figure 6 defined with red dotted rectangles.

Figure 6. Speed change during simulation, a) Proposed method, b) DSPC, c) Ideal FOC, d) SVPWM FOC, and e) Reference speed

Section (I) of Figure 7 shows the step change of the reference speed. As can be seen, due to the slow dynamic of speed, compared to current dynamic, the DPSC method has oscillatory behavior with the one-step horizon. Moreover, the FOC method has a lower speed even by considering the ideal case, without switching and modulator. The main reason

behind this lower speed dynamic is the cascade scheme, which forces the designer to have a lower bandwidth in outer loop. Also, by adding the modulator and switching, the FOC has a lower speed than the ideal case. However, the proposed method has a faster dynamic than the FOC method and smaller overshoot and lower oscillation than original DPSC. When the speed error term e_ω reaches near zero, the torque component added to the cost function, with a faster dynamic, will have greater impact on the optimal value for switching selection; thus, the sluggish nature of the cost function is almost obviated and motor speed has very lower oscillation than DPSC.

Section (II) of Figure 1 shows step down of speed and has almost the same behavior as step up change. Section (III) shows speed change during mechanical torque variation, it can be seen that FOC and the proposed method have the same behavior. Finally, Section (IV) shows the steady-state response of the system for the proposed method and FOC. Because of the optimal selection of voltage vectors, the proposed method has very lower steady-state error; however, in return, it suffers from variable switching frequency unlike FOC. To have a quantitative criterion for speed and torque distortion, using the Mean Square Error (MSE) for the speed and torque variables, as described in (16), the results can be shown in Table 3. It can be observed that the proposed method has a lower speed and torque distortion than SVPWM. This advantage is because the designed torque reference is considered as part of the cost function to minimize the oscillation of speed and torque.

$$\text{Speed MSE} = \sum_{j=1}^{N}\left(\omega_e(j) - \omega_e^{ref}\right)^2$$

$$(16)$$

$$\text{Torque MSE} = \sum_{j=1}^{N}\left(T_e(j) - T_e^{ref}\right)^2$$
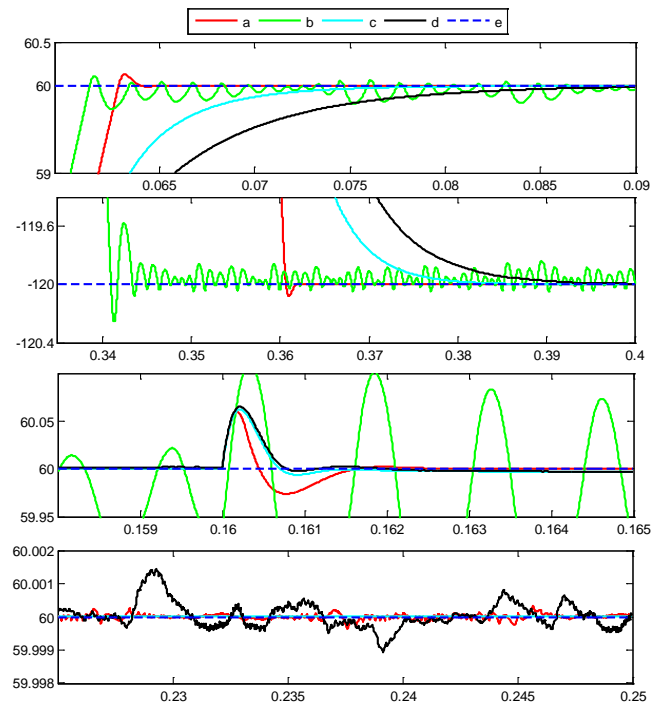

Figure 7. Zoomed area of Figure 3, (I): Motor speed during reference speed step-up variation, (II): Motor speed during reference speed step-down variation. (III): Motor speed during load torque variation, and (IV): Motor speed in a steady state, a) Proposed method, b) DPSC, c) Ideal FOC, d) SVPWM FOC, and e) Reference speed

Table 3. Speed and torque MSE for the proposed method and SVPWM method

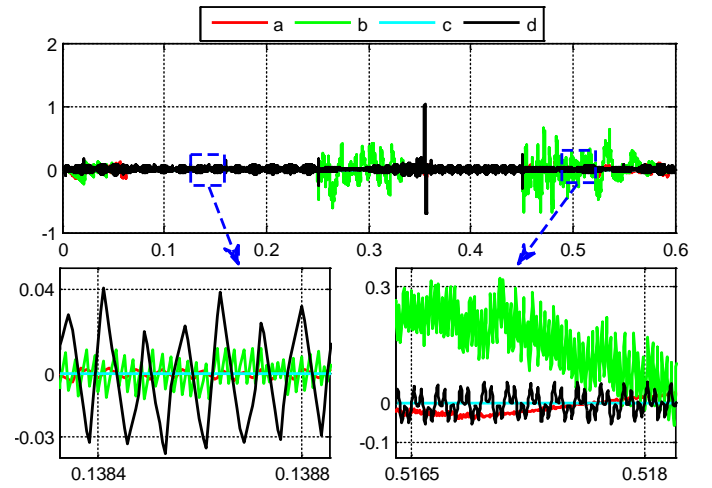|	Proposed method	SVPWM
Speed MSE	$6.85e^{-5}$	$160e^{-5}$
Torque MSE	0.0348	0.176

Figure 8 illustrates variations of electromagnetic torque T_e during simulation and for more details, Figure 9 shows the zoomed area of red rectangles in Figure 8.

From Figure 9, Sections (I) and (II), it can be seen that in step-up and step-down speed changes, because of the nature of the predictive control, the proposed method has no overshoot or under-shoot. Also, in the DPSC, there is a high gain fluctuation in T_e, which can reduce the life expectancy of motor shaft.

Section (III) of Figure 9 illustrates the steady-state performance of T_e for all the methods mentioned above. Despite the DPSC which has high oscillation because of the difference between mechanical and electrical time constants as well as the ideal FOC which experiences no oscillation, the proposed method is subject to much less oscillation than SVPWM FOC.
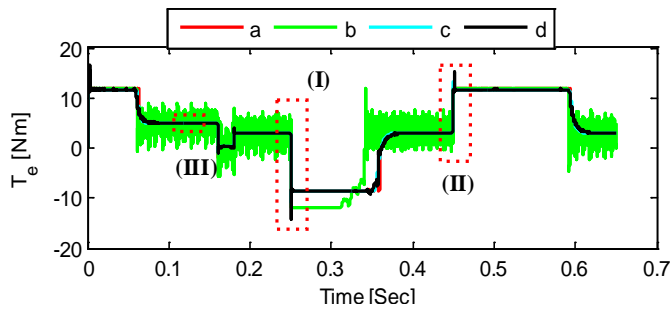
Figure 8. Electromagnetic torque variation during the simulation, a) proposed method, b) DPSC, c) Ideal FOC, and d) SVPWM FOC
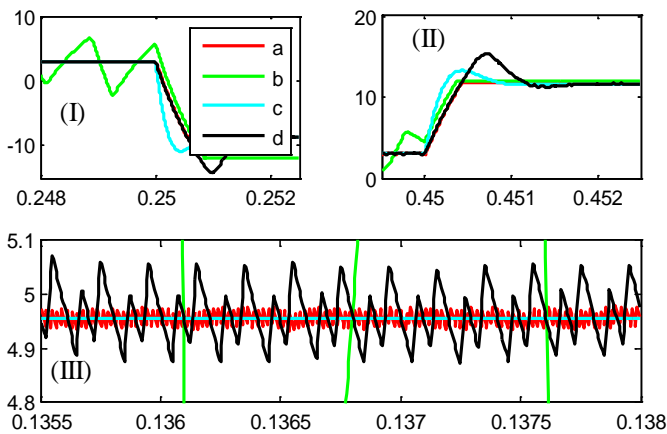
Figure 9. Zoomed area of Figure 5, (I): during step-down reference speed, (II): during step-up reference speed, (III): in steady-state, a) proposed method, b) DPSC, c) Ideal FOC, d) SVPWM FOC

For surface-mounted PMSMs, one of the controller's objectives is to keep d-axis current at zero to satisfy the MTPA criteria [41]. Figure 10 shows i_d during simulation, showing that in the steady-state and transient phases, the proposed method has a better performance than other methods, except ideal FOC without switching components.

Figure 10. d-axis current variation during simulation time and zoomed areas, a) proposed method, b) DPSC, c) Ideal FOC, and d) SVPWM FOC

6. CONCLUSIONS

In this work, an encoder-less FCS-MPC-based speed control algorithm was proposed for a PMSM fed by a 3-level NPC converter. The controller used an anti-windup PI controller concept to generate reference torque using the error of speed; then, FCS-MPC used this torque and other parameters to control converter gates.

Simulation results demonstrated the effectiveness of the method in the transient and steady state phases. The method has not only a fast response during reference variation but also much lower overshoot or undershoot than FOC method. Moreover, compared with the recent methods like DPSC, the proposed method has much less oscillation in a steady state in both speed and torque characteristics. Future research could continue to explore experimental results and compare the results with methods that used multiple prediction horizon.

7. ACKNOWLEDGEMENT

NOMENCLATURE

Symbol	Description
i_d, i_q	Stator current in dq Ref. frame
v_d, v_q	Stator voltage in dq Ref. frame
R_s	Stator resistance
L_s	Stator inductance
ω_e	Electrical rotor speed
θ	Electrical angle of the rotor
T_e	Electromagnetic torque
T_L	Load torque
Z_P	Number of pole pairs
J_m	Inertia coefficient
B_v	Friction coefficient
ψ_{mg}	Flux linkage
T_s	Sampling time
V_{DC}	DC voltage
I_{max}	Current limitation
T_{em}	Torque limitation
Greek letters	
λ_x	Weighting factors and x = {i_d, i_q, T_e, V_o, I_m}
Subscripts	
$.^{ref}$	Reference value
Abbreviation	

WECS	Wind Energy Conversion System
MPPT	Maximum Power Point Tracking
PMSM	Permanent Magnet Synchronous Machine
FOC	Field-Oriented Control
DTC	Direct Torque Control
ANFTSMO	Adaptive Nonsingular Fast Terminal Sliding Mode Observer
MTPA	Maximum Torque Per Ampere
PI	Proportional Integral
MPC	Model Predictive Control
FCS-MPC	Finite Control Set - MPC
DPSC	Direct Predictive Speed Control
SPMSM	Surface-mounted PMSM

REFERENCES

1. Shi, S. and Lo, K.L., "An overview of wind energy development and associated power system reliability evaluation methods", *Proceedings of 48th International Universities' Power Engineering Conference (UPEC)*, Dublin, (2013), 1-6. (https://doi.org/10.1109/UPEC.2013.6714894).

2. Ackennan, T. and Soder, L., "An overview of wind energy status 2002", *Renewable and Sustainable Energy Reviews*, Vol. 6, No. 1-2, (2002), 67-128. (https://doi.org/10.1016/S1364-0321(02)00008-4).

3. Richardson, R.D. and McNerneyG, M., "Wind energy systems", *Proceedings of the IEEE*, Vol. 81, No. 3, (1993), 378-389. (https://doi.org/10.1109/5.241490).

4. Thongam, J.S., Tarbouchi, M., Beguenane, R., Okou, A.F., Merabet, A. and Bouchard, P., "An optimum speed MPPT controller for variable speed PMSG wind energy conversion systems", *Proceedings of IECON 2012-38th Annual Conference on IEEE Industrial Electronics Society*, Montreal, Quebec, (2012), 4293-4297. (https://doi.org/10.1109/IECON.2012.6389199).

5. Dastres, H., Mohammadi, A. and Rezaie, B., "Adaptive robust control design to maximize the harvested power in a wind turbine with input constraint", *Journal of Renewable Energy and Environment*, Vol. 8, No. 4, (2020), 30-43. (https://doi.org/10.30501/JREE.2020.224180.1093).

6. Barradi, Y., Zazi, K., Zazi, M. and Khali, N., "Control of PMSG based variable speed wind energy conversion system connected to the grid with PI and ADRC approach", *International Journal of Power Electronics and Drive Systems*, Vol. 11, No. 2, (2020), 953-968. (https://doi.org/10.11591/ijpeds.v11.i2.pp953-968).

7. Sain, C., Banerjee, A. and Biswas, P.K., "Modelling and comparative dynamic analysis due to demagnetization of a torque controlled permanent magnet synchronous motor drive for energy-efficient electric vehicle", *ISA Transactions*, Vol. 97, (2020), 384-400. (https://doi.org/10.1016/j.isatra.2019.08.008).

8. Holtz, J., "Advanced PWM and predictive control-An overview", *IEEE Transactions on Industrial Electronics*, Vol. 63, No. 6, (2016), 3837-3844. (https://doi.org/10.1109/tie.2015.2504347).

9. Li, Y., Qu, Y., Shi, H. and Meng, X., "An optimal switching table for PMSM DTC system using zero voltage vector", *Proceedings of 20th International Conference on Electrical Machines and Systems (ICEMS)*, Sydney, NSW, (2017), 1-5. (https://doi.org/10.1109/ICEMS.2017.8056409).

10. Linder, A. and Kennel, R., "Model predictive control for electrical drives", *Proceedings of IEEE 36th Power Electronics Specialists Conference*, Recife, (2005), 1793-1799. (https://doi.org/10.1109/PESC.2005.1581874).

11. Casdaei, D., Profumo, F. and Serra, G., "FOC and DTC: Two variable schemes for induction motors torque control", *IEEE Transactions on Power Electronics*, Vol. 17, No. 5, (2002), 779-788. (https://doi.org/10.1109/tpel.2002.802183).

12. Rahman, M.F., Haque, M.E. and Tang, L.X., "Problems associated with the direct torque control of an interior permanent-magnet synchronous motor drive and their remedies", *IEEE Transactions on Power Electronics*, Vol. 51, No. 4, (2004), 799-809. (https://doi.org/10.1109/tie.2004.831728).

13. Kakosimos, P. and Abu-Rub, H., "Predictive speed control with short prediction horizon for permanent magnet synchronous motor drives", *IEEE Transactions on Power Electronics*, Vol. 33, No. 3, (2018), 2740-2750. (https://doi.org/10.1109/TPEL.2017.2697971).

14. Sarailoo, M., Rezaie, B. and Rahmani, Z., "Fuzzy predictive control of three-tank system based on a novel modeling framework of hybrid systems", *Proceedings of the Institution of Mechanical Engineering, Part I: Journal of System and Control Engineering*, Vol. 228, No. 6, (2014), 369-384. (https://doi.org/10.1177/0959651814524948).

15. Jalili, S., Rezaie, B. and Rahmani, Z., "A novel hybrid model predictive control design with application to a quadrotor helicopter", *Optimal Control Applications and Methods*, Vol. 39, No. 4, (2018), 1301-1322. (https://doi.org/10.1002/oca.2411).

16. Rodriguez, J., Kazmierkowski, M.P., Espinoza, J.R., Zanchetta, P., Abu-Rub, H., Young, H.A. and Rojas, C.A., "State of the art of finite control set model predictive control in power electronics", *IEEE Transactions on Industrial Informatics*, Vol. 9, No. 2, (2013), 1003-1016. (https://doi.org/10.1109/TII.2012.2221469).

17. Wang, F., Mei, X., Rodriguez, J. and Kennel, R., "Model predictive control for electrical drive systems-an overview", *CES Transactions on Electrical Machines and Systems*, Vol. 1, No. 3, (2017), 219-230. (https://doi.org/10.23919/TEMS.2017.8086100).

18. Wang, L. and Gan, L., "Integral FCS predictive current control of induction motor drive", *IFAC Proceedings Volumes*, Vol. 47, No. 3, (2014), 11956-11961. (https://doi.org/10.3182/20140824-6-ZA-1003.00753).

19. Chai, S., Wang, L. andRogres, E., "A cascade MPC control structure for a PMSM with speed ripple minimization", *IEEE Transactions on Industrial Electronics*, Vol. 60, No. 8, (2013), 2978–2987. (https://doi.org/10.1109/TIE.2012.2201432).

20. Fuentes, E.J., Silva, C., Quevedo, D.E. and Silva, E.I., "Predictive speed control of a synchronous permanent magnet motor", *Proceedings of 2009 IEEE International Conference on Industrial Technology*, Gippsland, VIC, (2009), 1-6. (https://doi.org/10.1109/ICIT.2009.4939731).

21. Fuentes, E.J., Silva, C.A. and Yuz, J.I., "Predictive speed control of a two-mass system driven by a permanent magnet synchronous motor", *IEEE Transactions on Industrial Electronics*, Vol. 59, No. 7, (2012), 2840-2848. (https://doi.org/10.1109/TIE.2011.2158767).

22. Fuentes, E., Kalise, D., Rodriguez, J. and Kennel, R.M., "Cascade-free predictive speed control for electrical drives", *IEEE Transactions on Industrial Electronics*, Vol. 61, No. 5, (2014), 2176–2184. (https://doi.org/10.1109/TIE.2013.2272280).

23. Preindl, M. and Bolognani, S., "Model predictive direct speed control with finite control set of PMSM drive systems", *IEEE Transactions on Power Electronics*, Vol. 28, No. 2, (2013), 1007-1015. (https://doi.org/10.1109/TPEL.2012.2204277).

24. Bueno, E.J., Hernandez, A., Rodriguez, F.J., Giro, C., Mateos, R. and Cobreces, S., "A DSP- and FPGA-based industrial control with high-speed communication interfaces for grid converters applied to distributed power generation systems", *IEEE Transactions on Industrial Electronics*, Vol. 56, No. 3, (2009), 654-669. (https://doi.org/10.1109/TIE.2008.2007043).

25. Saberi, S. and Rezaie, B., "A full range permanent magnet synchronous motor position and speed estimation using adaptive non-singular fast terminal sliding mode observer", *Majlesi Journal of Energy Management*, Vol. 8, No. 4, (2019), 17-25. (http://journals.iaumajlesi.ac.ir/em/index/index.php/em/article/view/397).

26. Giri, F., AC electric motors control: advanced design techniques and applications, John Wiley and Sons, (2013), 59-76. (https://doi.org/10.1002/9781118574263).

27. Nahid-Mobarakeh, B., Meibody-Tabar, F. and Sargos, F.M., "Back EMF estimation based sensorless control of PMSM: Robustness with respect to measurement errors and inverter irregularities", *Proceedings of Industry Applications Conference, 39th IAS Annual Meeting. Conference Record of the 2004 IEEE*, Vol. 3, (2004), 1858-1865. (https://doi.org/10.1109/IAS.2004.1348723).

28. Hassan, M., Mahgoub, O. and Shafei, A.E., "ANFIS based MRAS speed estimator for sensorless control of PMSM", *Proceedings of 2013 Brazilian Power Electronics Conference, COBEP 2013*, (2013), 828-835. (https://doi.org/10.1109/COBEP.2013.6785211).

29. Xiao, D., Guan, D.Q., Rahman, M.F. and Fletcher, J., "Sliding mode observer combined with fundamental PWM excitation for sensorless control of IPMSM drive", *Proceedings of IECON 2014-40th Annual Conference of the IEEE Industrial Electronics Society, IEEE*, (2014), 895-901. (https://doi.org/10.1109/IECON.2014.7048607).

30. Nagarajan, V., Balaji, M. and Kamaraj, V., "Back-emf-based sensorless field-oriented control of PMSM using neural-network-based controller with a start-up strategy", *Advances in Intelligent Systems and*

Computing, Vol. 325, (2015), 449-457. (https://doi.org/10.1007/978-81-322-2135-7_48).

31. An, L., Franck, D. and Hameyer, K., "Sensorless field oriented control using back-EMF and flux observer for a surface mounted permanent magnet synchronous motor", *International Journal of Applied Electromagnetics and Mechanics*, Vol. 45, No. 1-4, (2014), 845-850. (https://doi.org/10.3233/JAE-141915).

32. Kazantzis, N. and Kravaris, C., "Time-discretization of nonlinear control systems via Taylor methods", *Computers & Chemical Engineering*, Vol. 23, No. 6, (1999), 763-784. (https://doi.org/10.1016/S0098-1354(99)00007-1).

33. Rodriguez, J. and Cortes, P., "Predictive control of a three-phase neutral-point clamped inverter", *Proceedings of Predictive Control of Power Converters and Electrical Drives*, *IEEE*, (2012), 65-79. (https://doi.org/10.1002/9781119941446.ch5).

34. Zhang, Z., Wang, F., Wang, J., Rodríguez J. and Kennel, R., "Nonlinear direct control for three-level NPC back-to-back converter PMSG wind turbine systems: Experimental assessment with FPGA", *IEEE Transactions on Industrial Informatics*, Vol. 13, No. 3, (2017), 1172-1183. (https://doi.org/10.1109/TII.2017.2678500).

35. Kouro, S., Cortes, P., Vargas, R., Ammann, U. and Rodriguez, J., "Model predictive control-A simple and powerful method to control power converters", *IEEE Transactions on Industrial Electronics*, Vol. 56, No. 6, (2009), 1826-1838. (https://doi.org/10.1109/TIE.2008.2008349).

36. Sazawa, M., Yamada, T., Ohishi, K. and Katsura, S., "Anti-windup algorithm with priority to proportional control output of speed PI controller for precision servo system", *Electrical Engineering in Japan (English translation of Denki Gakkai Ronbunshi)*, Vol. 170, No. 3, (2010), 57-64. (https://doi.org/10.1002/eej.20904).

37. Rodriguez, J. and Cortes, P., Predictive control of power converters and electrical drives, John Wiley & Sons, (2012), 177-190. (https://doi.org/10.1002/9781119941446.ch12).

38. Hackl, C.M., Larcher, F., Dötlinger, A. and Kennel, R.M., "Is multiple objective model-predictive control optimal?", *Proceedings of the 2013 IEEE International Symposium on Predictive Control of Electrical Drives and Power Electronics (PRECEDE)*, Munich, Germany, (2013), 1-8. (https://doi.org/10.1109/SLED-PRECEDE.2013.6684475).

39. Cortés, P., Kouro, S., La Rocca, B., Vargas, R., Rodríguez, J., León, J.I., Vazquez, S. and Franquello, L.G., "Guidelines for weighting factors design in model predictive control of power converters and drives", *Proceedings of IEEE International Conference on Industrial Technology*, (2009), 1-7. (https://doi.org/10.1109/ICIT.2009.4939742).

40. Palanisamy, R. and Krishnasamy, V., "SVPWM for 3-phase 3-level neutral point clamped inverter fed induction motor control", *Indonesian Journal of Electrical Engineering and Computer Science*, Vol. 9, No. 6, (2018), 703-710. (https://doi.org/ijeecs.v9.i3.pp703-710).

41. Bolognani, S., Petrella, R., Prearo, A. and Sgarbossa, L., "Automatic tracking of mtpa trajectory in ipm motor drives based on ac current injection", *Proceedings of IEEE Energy Conversion Congress and Exposition*, (2009), 2340-2346. (https://doi.org/10.1109/TIA.2010.2090842).

Comparative Analysis of Thermal Performance of a Solar Water Heating System Based on the Serpentine and Risers-Head Configurations

Selfa Johnson Zwalnan[a*], Nanchen Nimyel Caleb[b], Mahan Morgan Mangai[c], Nantim Yohanna Sanda[a]

[a] Department of Metallurgical Engineering, Plateau State Polytechnic, Barkin-Ladi, Nigeria.
[b] Department of Computer Engineering, Plateau State Polytechnic, Barkin-Ladi, Nigeria.
[c] Department of Mechanical Engineering, University of Jos, Plateau State, P. O. Box: 930261, Jos, Nigeria.

ABSTRACT

The effect of solar collector configurations on the thermal efficiency of an active solar water heater was investigated using TRNSYS in this study. Two versions of a solar heater were formulated on the basis of serpentine and riser-header flat plate configurations. Both models were simulated based on the same parameters and weather conditions. Besides, in accordance with clear sky and cloudy sky conditions, a parametric analysis was performed to determine the impact of varying parameters on the thermal efficiency of the two models. The results showed that the serpentine-based device model provided about 2.62 % more usable thermal energy than the riser-header configuration. In addition, both models demonstrated the same response and sensitivity to changes in the collector area and the volume of the tank. However, on a cloudy day, the efficiency of serpentine showed a significant improvement and sensitivity to flow variance with an efficiency gap of about 30 % to the riser header configuration.

https://doi.org/10.30501/jree.2020.251190.1150

1. INTRODUCTION

Solar Water Heaters (SWHs) are used to convert solar energy into heat for both domestic and industrial purposes [1, 2]. This technology eliminates our decade-old dependency on traditional heat sources and thereby, reduces greenhouse gas emissions by reducing electricity consumption for thermal energy requirements [3]. However, due to its original higher cost and lower thermal performance than the traditional energy system, the use of this technology is not widely adopted. Most customers would want to know their monthly saving if they were to convert to solar-powered systems. One major factor influencing the thermal efficiency of the collector is energy loss over time. Interestingly, heat loss in solar collectors is significantly governed by the nature of flow in the collector tubing [4]. On the other hand, the nature of flow and its distributions is a function of the shape and geometry of the collector fluid passage [5]. Minimizing heat loss in the solar collector increases the rate at which the solar energy occurring in the collector transforms into usable thermal energy [6]. Consequently, considerable studies have been conducted to address this problem.

To evaluate the effect of flow rate on the technology and economy of flat plate solar water heating systems, Plaza et al. [4] suggested that a high flow rate would lead to higher solar fractions than a low flow rate. However, the energy

consumption of a pump outweighs the gains of using a high flow rate. They, therefore, concluded that a careful search for the proper flow rate to increase the solar fraction and reduce the energy consumption is necessary.

Kim et al. [7] analyzed the thermal performance of the flat plate solar collector based on different shapes of the collector tubing. The goal of their study was to investigate the flow distribution of rectangular, triangular and trapezoidal cross-sections of the collector tubing. Their result revealed that fluid flow in the collector tube with a triangular cross-section was more uniform than the rectangular and trapezoidal sections. Also, in another research, [8, 9] found that the modification of the absorber plate of the primary flat plate collector to a V-groove absorber plate resulted in better thermal performance of the solar collector. Again, they also found that the thermal performance would be better enhanced if the v-groove was made smaller. Jahangiri et al. [10] evaluated the feasibility of the application of solar water heater for space heating and supply of sanitary hot water at 60 °C for a household of 4 persons in 10 provinces of Canada. The study employed the T*Sol simulation software. The findings of the study showed that solar water heater held the potential of reducing the energy demand for hot water in the residential household of Canada by an average of 88.7 % across the ten provinces studied. However, the simulated performance revealed that the system was only capable of supplying an average of 19.18 % of spacing heating demand across the ten studied locations. In a similar study using TSOL, Pahlavan et al. [11] showed that the use of solar water heater in 37 stations in Algeria could

*Corresponding Author's Email: selfajohnspn@gmail.com (S.J. Zwalnan)
URL: http://www.jree.ir/article_122814.html

lead to an annual saving rate of 56783kg/yr of CO_2 in these locations.

Another study by [12] studied the effect of collector arrangement on the thermal performance of a flat plate solar collector. In their conclusion, they agreed that poor collector performance was an indication of an inherently flawed sizing and geometric consideration. Touaba et al. [13] proposed the incorporation of lubricating oil as the absorber plate for a solar water heater integrated with storage tank. Similarly, Hussein et al. [14] enhanced, the thermal performance of a flat plate solar collector using a novel combination of covalent functionalized multi-wall carbon mixed by pure water as the working fluid.

A study to investigate the effect of collector configurations on the thermal performance of the photovoltaic solar thermal energy system was conducted in [9]. In this study, the effect of the collector configuration and the orientation of the building were studied. An extensive review of the various studies conducted in the area of enhancing the thermal performance of solar collectors using nanofluid as working fluid in collectors' tubes was conducted in [15, 16]. In their approach, various properties of the fluid were investigated to determine the sensitivity of the system to change in nanofluid properties. The results of this study showed that molecular structure, hybrid nanofluid content, ingredients, particle shape, temperature, PH value, the concentration of particle volume, and stability of nanofluid had a significant impact on the thermal efficiency of the system. A numerical solution to determining the optimal design parameters of a solar flat plate collector designed to supply hot water was developed in [17]. Matlab software was used to model the time-dependent behavior of the flat plate collector. The sensitivity study shows that the temperature of the heated water and the total coefficient of heat loss decreased with an increase in the water flow rate. The study concluded that the system's flow rate was also a significant indicator of the optimum number of solar collector tubes needed to give the maximum collector outlet water temperatur.Analytical solution to the energy balance of a solar flat plate air heater using the climatic data variables of Jeddah was modeled in [18] to study the thermal performance of a collector. In this study, a computer model of the collector was used to investigate the effect of collector dimension on the collector outlet air temperature. The developed model also investigated the effect of selective coating materials on the solar air heater output temperature. The result showed that the solar air collector coated with nickel-tin outperformed the collector coated with galvanized iron-copper oxide or nickel rhodium black or galvanized iron-cobalt oxide and iron coated with nickel. When comparing the modelled outcome with the measured results, an error of 7.7 % between the modeled output and the experimental performance was also observed. The authors, therefore, concluded that the average annual production of the selectively coated nickel-tin absorber was 29.23 % higher than that of the black painted absorber. In one study, Sachit et al. [19] modeled and simulated the performance of a flat plate solar collector designed to have both the serpentine and the riser-header tube pattern. Also, they compared the performance of the proposed PVT collector with the basic serpentine tube design collector. The result of their findings showed a decrease in the cell temperature with a decrease of about 2 % in the thermal efficiency of the proposed configuration than the serpentine tube pattern configuration. However, a less than 0.04 % improvement to the electrical efficiency of the proposed configuration was observed.

Similarly, different studies have been conducted by many researchers to determine the economics of adopting solar water heating systems for both domestic and industrial applications [10, 20, 21]. In general, a common conclusion is that solar water heating systems have long-term economic and environmental benefits when compared to the conventional energy systems [22-24].

Despite the large volume of research conducted to enhance the thermal performance of the flat plate solar collector, little or no study has provided a side by side thermal assessment of the flat plate collector on an annual basis. Therefore, this research employs a simulation-based approach to evaluate the side by side annual performance of the active solar water heater based on the serpentine and header-riser configurations in the typical tropical climate (Nigeria). The goal here is to assess and compare the influence of collector configuration on the annual thermal output of the heating system in the tropical savannah climate. Additionally, the modeled system was then constructed and tested in order to validate system performance, as predicted by the model. The performance of the system was determined experimentally under the weather and solar condition of Jos, Nigeria.

2. MATERIALS AND METHODS

2.1. System description

The system consists of a flat plate solar collector with a total collector area of 1.5 m^2 which is divided into two sections. In the first section, the collector tubing of the fluid passage is designed based on the risers-header pattern, as shown in Figure 1a. The second section, the fluid channel, is designed in a serpentine pattern, as shown in Figure 1b. Both sections of the collector are distinctively connected to a separate water storage tank of volume 0.03 m^3 (30 litres) through the PVC connecting pipes, thereby creating two independent closed-loop systems. The water in each closed loop is circulated employing a direct current pump powered by a 60 watts solar panel. Notably, the two sections of the collector are covered at the top with a single glass through the entire collector. Consequently, the two sections are identical in all design parameters, as depicted in Table 1. Since water circulation in the system is done through solar pump powered by the solar panel, the natural control ensures that the water is circulated when solar energy falling on the PV module is adequate to produce electrical power. This control is cost-effective and straightforward and eliminates significant costs involved in flow control of solar active water heaters. Figure 2 is the assembled configuration of the proposed solar energy system to be modeled and experimentally evaluated.

2.2. Working principle

When solar radiation from the atmosphere falls on the collector, the absorber plate within the collector is considerably heated to a higher temperature. Consequently, the heat absorbed by the absorber plate is transferred to the circulating fluid (usually water in the direct heating method) flowing through the collector tubing (usually made of copper tubes) attached to the absorber plate. The heated water in the collector returns to the top of the storage tank at a higher temperature. The pump again draws water from the bottom of the tank and pumps it back into the collector, and the entire process is repeated until the sun goes down [25].
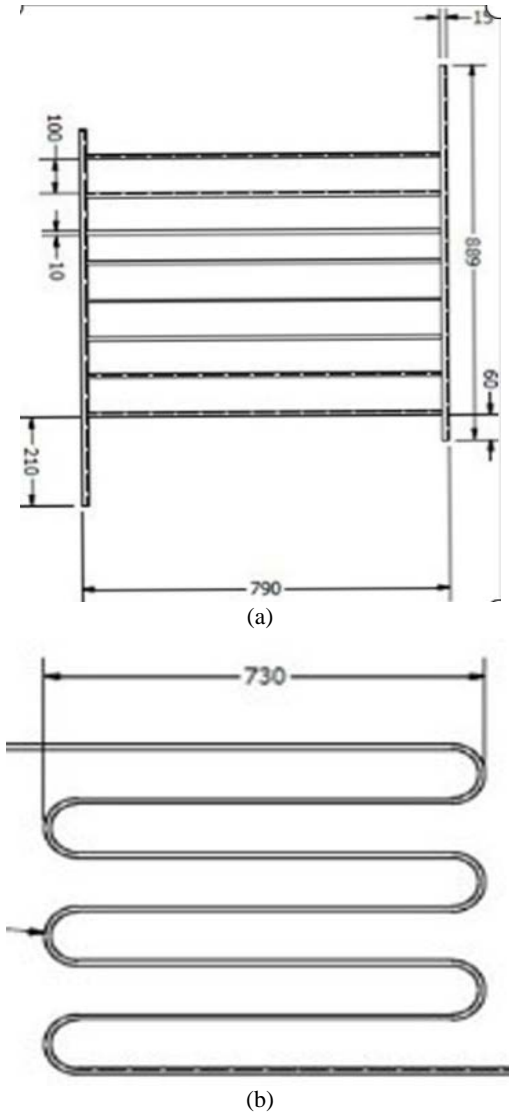
Figure 1. Collector tubing of (a) header-riser section of the collector and (b) serpentine section of the collector
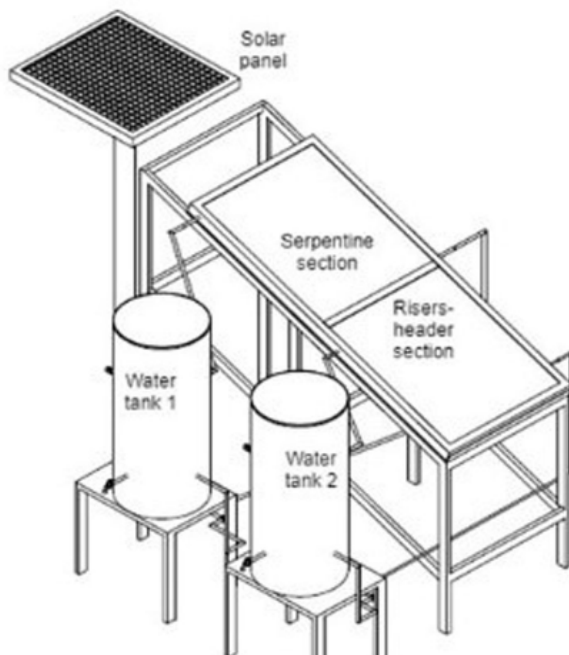

Figure 2. An assembled configuration of the solar water heating system

The process is self-controlled because the pump will continue circulating the water until there is no radiation from the sun. The heated water can be reheated by other forms of conventional heaters when the solar system does not meet up the water temperature requirement.

2.3. The flat-plate energy model

In a steady-state, the Hottel-Whillier-Bliss (HWB) mathematical models and energy balance equations numerically characterize the thermal behavior efficiency of the flat-plate solar collector. At a given moment, the rate of useful energy gain from the solar collector is the positive difference between the energy absorbed by the plate and the energy lost to the atmosphere by the collector, as defined by Eq. (1) [26].

$$\dot{Q_u} = F_R[S - U_L(T_i - T_a)]^+ \tag{1}$$

The plus superscript means that only positive values of the terms are to be used in the square bracket. The absorbed radiation must therefore be greater than the thermal losses, as shown in Figure 3, in order to achieve practical benefits greater than zero.
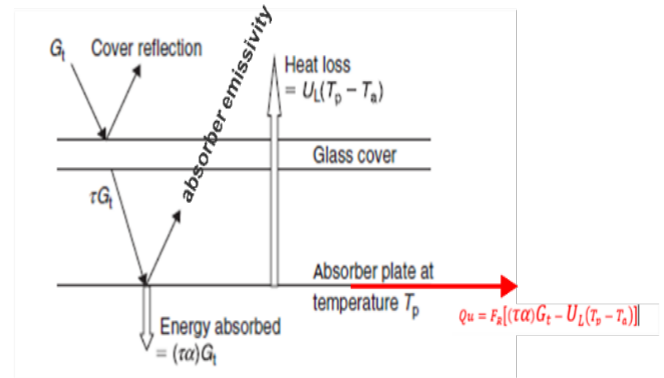

Figure 3. Illustrating the energy balance of a solar collector [27]

In Figure 3, S, U_L, T_i and T_a are the energy absorbed by the absorber plate, the collector overall heat loss coefficient, circulating fluid collector inlet temperature, and the temperature of the surrounding where the collector is placed, respectively. F_R is called the collector heat removal factor. F_R is similar to the heat exchanger effectiveness. For a header-riser flat-plate collector, the collector heat removal factor can be expressed as in Eq.(2) [26]:

$$F_R = \frac{\dot{m}C_p}{A_c U_L}\left[1 - \exp\left(-\frac{A_c U_L F'}{\dot{m}C_p}\right)\right] \tag{2}$$

where F' is the collector efficiency factor expressed as follows:

$$F' = \frac{1/U_L}{W\left[\frac{1}{U_L[D_i+(W-D_i)F]}+\frac{1}{C_b}+\frac{1}{\pi D_i h_{fi}}\right]} \tag{3}$$

F is the standard fin efficiency for straight fins with a rectangular profile, given as:

$$F = \frac{\tanh\left[\frac{m(W-D_i)}{2}\right]}{\frac{m(W-D_i)}{2}} \tag{4}$$

where

$$m = \sqrt{\frac{U_L}{K\delta}} \qquad (5)$$

Moreover, U_L is the overall heat loss coefficient for a flat plate collector and it is composed of the top loss coefficient, the edge loss coefficient, and the back loss coefficient. The relation for collector overall heat loss coefficient, U_L, is expressed as:

$$U_L = U_t + U_e + U_b \qquad (6)$$

Duffie and Beckman [12] made an approximate reference to the top loss coefficient of the collector as:

$$U_{top} = A + B \qquad (7)$$

$$A = \frac{1}{\frac{N_G}{\frac{C}{T_{pm}}\left[\frac{T_{pm}-T_a}{N_G+f}\right]^e + \frac{1}{h_w}}}$$

$$B = \frac{\left[\sigma(T_{pm}^2 + T_a^2)\right]\left[T_a + T_{pm}\right]}{\frac{1}{\varepsilon_p+0.00591N_Gh_w} + \frac{2N_G+f-1+0.133\varepsilon_p}{\varepsilon_g} - N_G}$$

where

$$f = (1 + 0.089h_w - 0.1166h_w\varepsilon_p)(1 + 0.07866N_G) \qquad (8)$$

$$C = 520[1 - 0.000051\beta^2] \qquad (9)$$

$$e = 0.430\left(1 - \frac{100}{T_{pm}}\right) \qquad (10)$$

$$h_w = 2.8 + 3V \qquad (11)$$

The extent of the conduction loss at the back of the collector is such that the radiation is insignificant. Thus, Duffie and Beckman approximated the back loss, as expressed in Equation (12).

$$U_b = \frac{K_{bi}}{x_{bi}} \qquad (12)$$

The edge loss calculated by assuming one-dimensional sideway heat flow around the collector system's perimeter is expressed as:

$$U_e = \frac{K_{ei}}{x_{ei}}\frac{A_e}{A_C} \qquad (13)$$

2.4. Evaluation of collector performance indicators

The efficiency matrix of a collector is the parameter that determines how efficiently the collector transforms the total solar energy it absorbs into either thermal energy or electrical energy. The collector efficiency is defined as the ratio of the useful energy from the collector to the total radiation incident on the collector area. This performance matrix of the collector depends on many factors ranging from collector configuration, collector materials and its operating conditions. Theoretically, the thermal efficiency of the Flat Plate Collector (FPC) is expressed as follows:

$$\eta_{coll} = \frac{Q_u}{H_TA_c} = \frac{F_R[H_T(\tau\alpha)-U_L(T_i-T_a)]^+}{H_T} \qquad (14)$$

Eq. (15) is essential and useful for the realistic assessment of collector efficiency based on the technical data of

manufacturers of commercially obtained solar collectors. However, in this study, the simulated collector efficiency was evaluated through Eq. (14):

$$\eta_{coll} = a_0 - a_1\left(\frac{T_i-T_a}{H_T}\right) - a_2\left(\frac{T_i-T_a}{H_T}\right)^2 \qquad (15)$$

where a_0 is the optical efficiency and a_1 and a_2 represent the first- and second-degree heat loss coefficients obtained by the manufacturer during the indoor testing based on the specific tested flow rate. According to Soteris [27], the value of the optical efficiency a_0 and loss coefficient a_1 of good collectors lies within 0.762 and 0.2125, respectively. Under outdoor testing, it is practical to evaluate the collector efficiency based on Eq. (16) which is the ratio of the quantity of heat received from the fluid exiting the collector and the total amount of solar energy received per unit area of collector in the period usually considered as one hour, where V is the volumetric flow rate of the fluid in the collector and Tout and Tin are the measured outlet and inlet temperatures of the collector.

$$\eta_{coll} = \frac{\rho C_p V(T_{out}-T_{in})}{AH_T} \qquad (16)$$

2.5. System design and simulation

For the design of the systems, a simulation-based approach using TRNSYS software was adopted. In the TRNSYS simulation studio, two models of solar water heating systems have been built (see Figure 4). A serpentine, flat plate collector was used as the heating unit in the first model, while the second version used a riser-header flat solar collector as the heating unit. All other system design parameters and dimensions are the same for both systems, as seen in Table 1. Figure 4 shows the monthly average daily solar and ambient condition of Jos Nigeria (latitude 9.8965° N, Longitude 8.8583° E) under which the modeled systems have been simulated and evaluated. Figure 5 is a schematic of the models of the two systems developed in the TRNSYS simulation studio. The system model was used to simulate and assess the annual performance of the system. From Figure 4, the months of June to August had a lower level of solar radiation. This finding was not unexpected as these months correspond to a period with a high amount of rainfall. Therefore, the sky is mostly covered with heavy cloud.
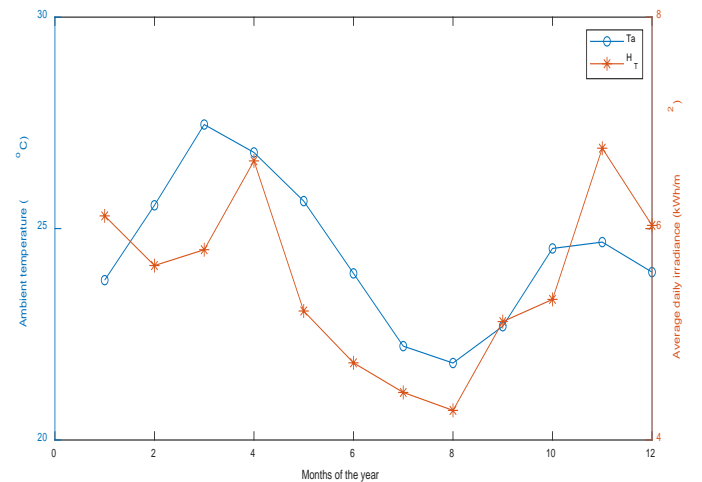

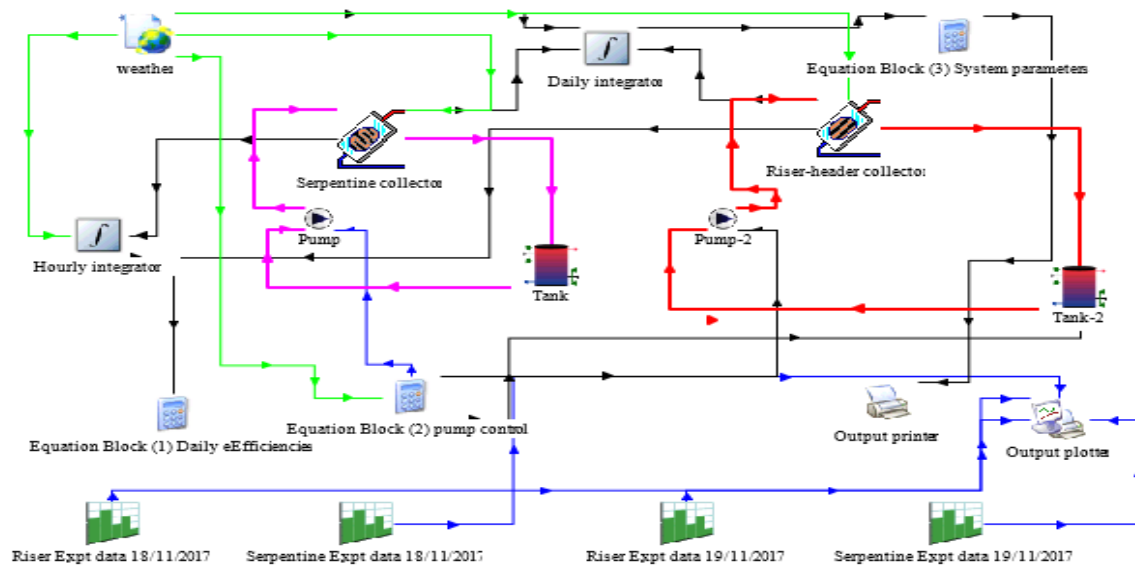**Figure 4.** Monthly average daily solar irradiance and ambient temperature of Jos, Nigeria

Figure 5. TRNSYS model of the solar water heating system based on the riser-header and serpentine collector configurations

The components of the systems model developed are selected from the TRNSYS simulation studio library. Afterwards, each component is assigned parameters as defined in Table 1. Besides, the output of each component that serves as inputs is transmitted through the connectors to other components.

Interestingly, some components usually have inputs for control. With this control input, the designers can decide how and when this component should operate. A summary of the components and their use and function in this modeling is presented in Table 2 below.

Table 1. System parameters and characteristics

No.	Parameters	Serpentine flat plate	Riser flat plate	Unit
1	Collector length	1.0	1.0	m
2	Collector width	0.8	0.8	m
3	Absorber plate thickness	5	5	mm
4	Conductivity of absorber material	243	243	W/m.K
5	Number of serpentine bends/Number of risers	8	8	-
6	Tube spacing	8	8	cm
7	Serpentine/riser length	0.75	0.75	m
8	Inner tube diameter	1.5	1.5	cm
9	Outer tube diameter	2.0	2.0	cm
10	Fluid specific heat	4.190	4.190	kJ/kg.K
11	Absorptance of the absorber plate	0.94	0.94	Fraction
12	Emissivity of the absorber plate	0.15	0.1'5	Fraction
13	Number of identical covers	1	1	-
14	Index of refraction of cover	1.526	1.526	-
15	Collector tilt	17	17	Degrees
16	Pump rated flow	72	72	$Kg/hr.m^2$

Source: Author design parameters

Table 2. Summary of the components used in the simulation

Name in studio	Type No. in library	Function
Weather	Type 15	Serving as a function of processing the weather data of a location from an external weather data file at a given time step and making it accessible to other TRNSYS components.
Serpentine collector	Type 565	This component is a model flat solar plate collector where the tube winds up the collector absorber plate in a serpentine fashion.
Riser-header collector	Type 564	This component is a model flat solar plate collector where the tube connects to the collector absorber plate in a riser-header fashion.
Tank 1&2	Type 534	This subroutine models a fluid-filled, constant volume storage tank.
Riser/serpentine Exptl data	Type 14	Type-14 is entirely general; this component can be used to output a set of numbers that fits an individual purpose. The output is dimensionless.
Equation blocks	Not in the library	This component is a means to write scripts that evaluate the entire system performance or control entire or specific component or to parameterize the model.
plotters and printers	Type 65 and 25	The plotter enables visualization of the system performance, while the printer saves the results into an external file.
Integrator	Type 24	It is a utility component used to process the output of simulation by integration of the output in a specific period.

2.6. Parametric analysis

The TRNedit (a TRNSYS engine that enables parametric studies) was employed to conduct parametric analysis in order to understand the sensitivity of the two solar collector models to changes in conditions and parameters. As a result, the three input parameters, namely the collector flowrate, collector area, and tank capacity, are considered as variables in the TRNSYS model. Consequently, a new input file called the deck file is generated and the TRNedit is now executed to simulate the system based on a range of parameters, as shown in Table 3. The results obtained are discussed in Section 3 in this paper. The parametric study is conducted under two weather conditions in order to understand the importance of the volume and quality of solar radiation in the thermal operation of the system. Therefore, the analysis of the parameters was carried out on the basis of the day with a sunny sky and high radiation and the cloudy day with low solar radiation.

Table 3. Range of parameters for system parametric studies

No.	Collector area (m²)	Volume of tank (m³)	v flow rate (kg/hr)
1	0.7	0.03	50.00
2	0.8	0.04	70.00
3	0.9	0.05	90.00
4	1.0	0.06	110.00
5	1.1	0.07	130.00
6	1.2	0.08	150.00
7	1.3	0.09	170.00
8	1.4	0.10	200.00

Source: Author

2.7. Description of the experimental setup and procedure

To compare the simulated performance of the system with that of the experimental system, the solar heater was constructed (see Figure 6) based on the simulated parameters shown in Table 1. The constructed solar water heating system was installed at the Plateau State Polytechnic Clinic, and the outdoor thermal performance of the systems was experimentally measured. The K-type digital thermocouple with a temperature range of -10 °C to 1200 °C ± and 0.04 % uncertainty was mounted at the collector water inlets and outlets of the two systems to measure the outlet and inlet temperatures of the collectors simultaneously at a time interval of 1 hour starting from 8.00 a.m. to 5.00 p.m. for a day in November.

Within the test period, 0.043 m³ of water was poured into the storage tank before 7.00 a.m. Notably, there is no water drawn from the tank during the experiment to simplify the experimental setup. Furthermore, in each day experiment, the water tank was emptied and charged with fresh water. Moreover, the water circulation pump, which is powered by a solar panel, only runs or circulates water when the solar panel generates enough solar energy. This principle is adopted to circulate the water only when solar energy is available.

2.8. Validation of simulated and predicted performances

The Nash-Sutcliffe Coefficient of Efficiency (NSE) as expressed through Equation (17) [28] was employed to compare the simulated and experimental results so that the simulated model could be validated. The Nash-Sutcliffe Coefficient of Efficiency (NSE) is defined as follows:

$$NSE = 1 - \frac{\sum_{i=1}^{n}(X_{obs,i} - X_{model,i})^2}{\sum_{i=1}^{n}(X_{obs,i} - \overline{X}_{obs})^2} \tag{17}$$

where X_{obs} is the observed value, X_{model} is the modeled value at time/place i., and $\overline{X}_{obs}$ is the mean of the observed values. The value of the NSE ranges from -∞ to 1. The determined NSE value of 1 indicates the exact fit between the model and the experimental values. The closer the NSE value is to 1, the greater the predictive ability of the model used to simulate the actual performance of the system will be.

Figure 6. The developed and installed solar heating experimental setup

3. RESULTS AND DISCUSSION

3.1. Simulated system performance and analysis

The collector inlet temperature significantly affects the collector capacity to convert the absorbed solar energy to useful energy, as seen in Equation (1). Figure 7 shows the simulated variation of inlet temperature from 8.00 a.m to 5.00 p.m for 18th/11/2017 for the modeled collector configurations. According to Figure 7, the temperature behavior of the solar collector slightly differs in terms of the two configurations. The serpentine collector shows greater gain in useful energy evident by the higher inlet temperature than the riser-header collector. This observation is attributed to the collector tubing configuration of the serpentine collector. The spiral patterns of the tubing for the serpentine collector allow the fluid to travel a longer distance in the collector before exiting the collector. Consequently, the heat gain by the fluid is higher for the serpentine than the riser-header collector. According to Figure 6, as the collector inlet temperature increases, the collector efficiency for both the serpentine and the riser header collector decreases. Figure 7 also shows that the collector efficiency of the riser-header collector is slightly lower than that of the serpentine collector. The difference in collector efficiency of the two collectors is not significant, owing to an adequate level of solar radiation on 18/11/2017. However, to ascertain this claim, the parametric analysis of the effect of environmental variables on the collector performance was carried out under two weather scenarios: clear sky and cloudy sky, as presented in the subsequent section.
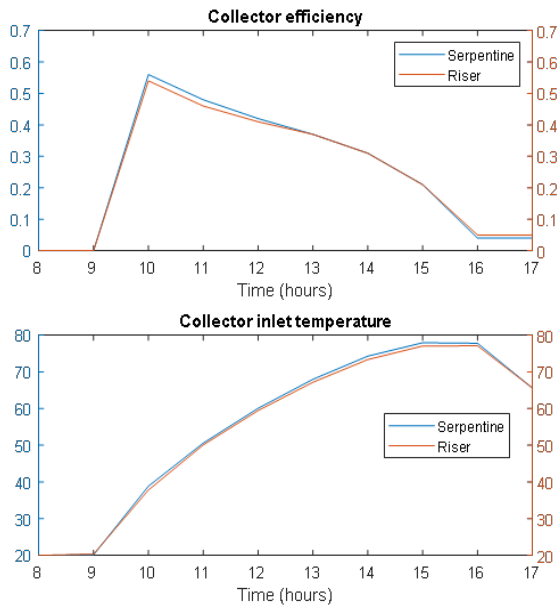
Figure 7. Collector inlet temperature and corresponding efficiency for both serpentine and riser-header collectors

The temperature characteristics of the two configurations, as shown in Figure 6, have not provided significant signs of a big difference between the serpentine and riser-header collector configuration. This assertion supported by the claim of Deng et al. [29] in their findings using Computational Fluid Dynamic (CFD) to calculate the absorber plate temperature of the serpentine and the header-riser configurations of the solar collectors at different collector inlet temperatures. As a result, the analysis of the monthly average daily useful energy of the two collectors is carried out from the simulation result as given in Figure 8. According to this figure, it is clear that the serpentine solar collector has higher useful thermal energy than the header-riser configuration. Concerning the header-riser collector, although Deng et al. [29] showed superior thermal efficiency to the serpentine, the author concluded that the insertion of the flexible silicon tubing in the serpentine tubing was responsible for the reduced efficiency. According to the result of our study and based on the weather condition of the study location (Jos, Nigeria), the annual average useful energy of the serpentine collector was found 2.63 % higher than that of the header-riser collector, as seen in Figure 8. Besides, the monthly analysis of the percentage of the difference in useful energy, as shown in Figure 8b, revealed that the efficacy of the serpentine collector over the riser-header is more significant in months with low solar radiation. This result, therefore, implies that in locations with massive cloud cover, the serpentine collector would strive better than the riser-header collector.

3.2. Collector sensitivity to variance in parameters

For further exploration, the differences in thermal characteristic between the serpentine collector and the riser, header flat plate solar collector, the effect and sensitivity of the two collectors to varying flowrate, tank volume and collector area keeping other condition constants were investigated. Figure 9 shows the response and sensitivity of the two collectors to variance in the collector area while keeping all other parameters constant both for a day with clear sky and a cloudy day. According to Figure 9, for both

collectors, the efficiency of the collector decreases with increase in collector area, while the load and other parameters remain the same. Nonetheless, it is again evident that the serpentine collector shows higher efficiency for both the sunny and cloudy days. Notably, both collectors show the same level of responsiveness to the changes in the collector area as the efficiency line for both collectors exhibits almost the same gradient.
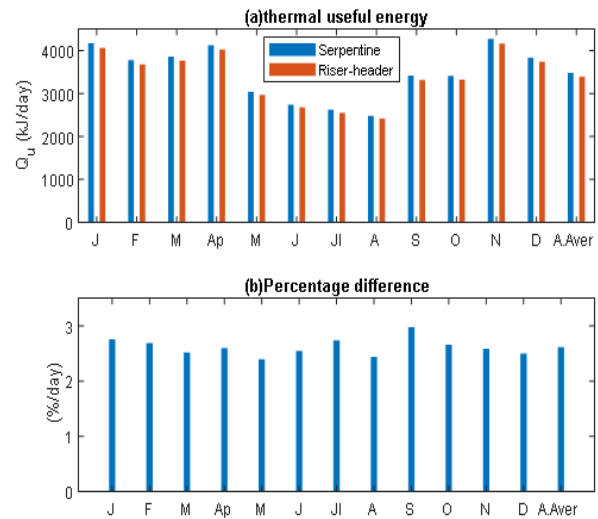

Figure 8. Monthly average daily useful energy and percentage difference in gain of the two collectors
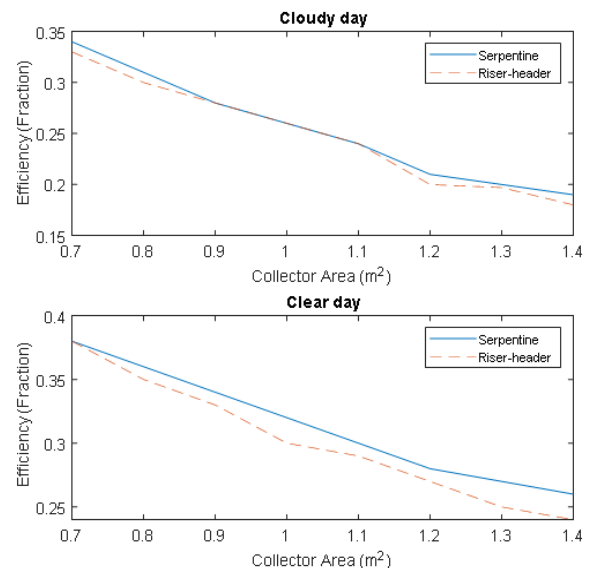

Figure 9. Effect of collector area on the efficiency while keeping other parameters constant

Again, in Figure 10, the graph shows a positive relationship between the collector efficiency and the tank volume. An increase in tank volume is observed to lead to an increase in collector efficiency. However, the serpentine collector still shows higher efficiency than the riser-header collector configuration. Figure 11 shows the variation and sensitivity of the serpentine and the riser-header collector to increase in circulation rate of fluid flow. According to the graph, the riser-header did not show any significant change in the collector efficiency with increasing flow rate for both clear-sky and cloudy sky days.

Interestingly, in Figure 11, the serpentine configuration shows a significant increase in collector efficiency for the flow rate beyond 90 kg/hr on a cloudy day and 170 kg/hr on a clear day. Overall, only the serpentine collector is seen to respond positively to flow rate variations. This observation implies that the serpentine collector configuration response is more sensitive to a change in flow rate, especially with a low level of solar radiation, than the riser-header collector configuration. Therefore, flow rate plays an essential role in increasing the performance of a serpentine collector in a location with a lower solar radiation level than the riser-header configuration.
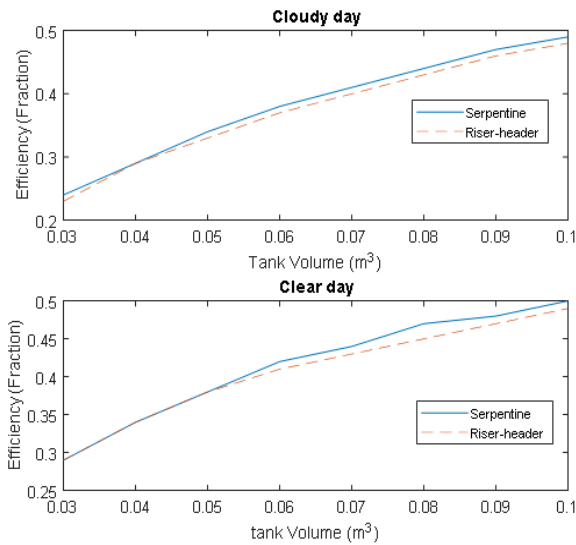

Figure 10. Effect of tank volume on the efficiency while keeping other parameters constant
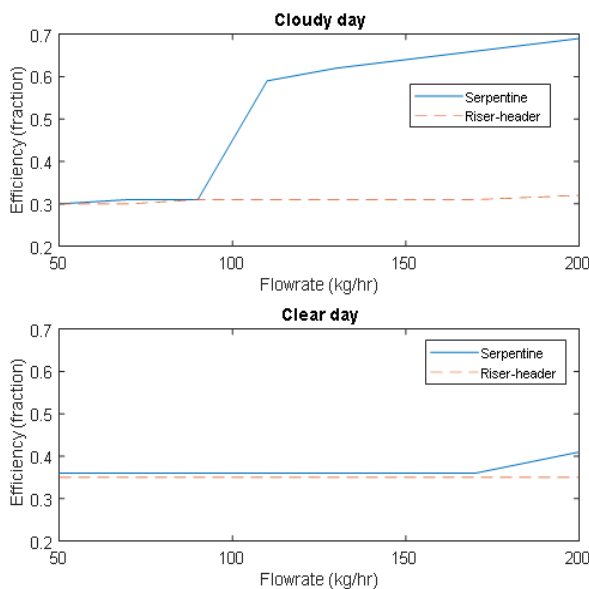

Figure 11. Effect of water flow rate on the efficiency while keeping other parameters constant

3.3. Experimental system performance and model validation

Figure 12 shows the experimental performance of the systems recorded during a test performed on the 18th of November 2017. The thermal behavior of the system shows a very similar trend in the collector inlet temperature as the simulated performance. The collector inlet was considered for comparison because it is the basis upon which the collector efficiency can be evaluated.
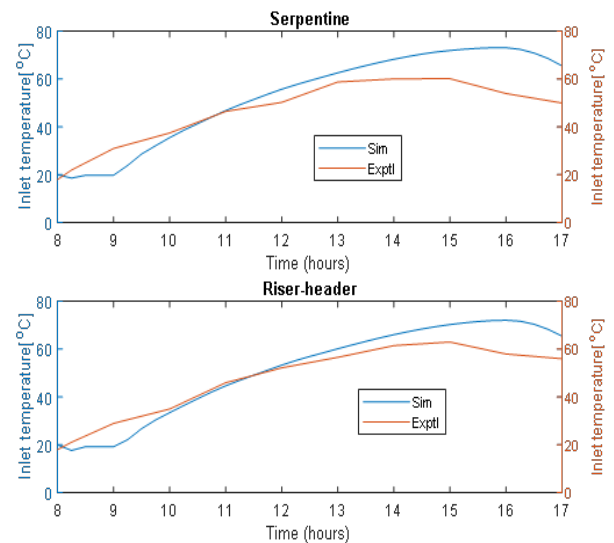

Figure 12. Comparison of the simulated and experimental temperatures of the serpentine and Riser-Header collectors (18th Nov., 2017)

Table 4 shows the calculated NSE between the experimental and simulated performances of the two systems. The experimental performance is in good agreement with the simulated performance with a Nash-Sutcliffe Coefficient of Efficiency (NSE) of 0.82 for both configurations. The Nash-Sutcliffe Coefficient of 0.82 implies that the model predicts the actual performance of the system, with a confidence level of 82 %.

Table 4. NSE between simulated and experimental performances

Collector configuration	NSE
Riser-header	0.82
Serpentine	0.82

4. CONCLUSIONS

The objective of this study is to investigate the effect of solar flat plate configuration on the thermal efficiency of an active solar water heating system. Using TRNSYS software, an active solar water heating system was simulated, and its efficiency was evaluated to achieve this objective. The system was also constructed and tested to validate the predicted performance of the model. The annual thermal output of the serpentine collector from the results obtained was 2.63 % higher than that of the header-riser collector when both collectors operated under the same condition and at a low flow rate of 72 kg/hr. The parametric analysis revealed that both models of the solar heating system demonstrated the same response and sensitivity to variance in the collector area and tank volume. However, the serpentine-based model showed significant improvement and sensitivity to flow variance with an efficiency gap of about 30 % to the riser header configuration on a day with cloudy sky. We, therefore, concluded here that the serpentine model of the solar water heater presented a better choice for locations characterized by highly diffused solar radiation and frequently cloudy sky. The

calculated Nash-Sutcliff coefficient of 0.82 between the modeled inlet temperature of the collector and the measured inlet temperature of the tank on the test day confirmed the validity of the TRNSYS model. The model is, therefore, a fair representation of the complex behavior of the actual system based on the appropriate degree of fit between experimental and simulated results.

5. ACKNOWLEDGEMENT

NOMENCLATURE

F_R	Heat removal factor
$\dot{m}$	Collector fluid mass flow rate (kg/hr.m^2)
C_p	Fluid specific heat (kJ/kg.K)
A_c	Collector area (m^2)
U_L	Overall collector loss coefficient (kJ/m^{2}hr.K)
W	Tube spacing (m)
Cb	Contact resistance (W/m.K)
h_{fi}	Internal fluid heat transfer coefficient (W/m^2.K)
kδ	Plate thermal conductivity and thickness product (kJ/hr.k)
D_i	Internal diameter of the tube (m)
N_G	Number of glass covers
β	Collector tilt (degrees)
$ε_g$	Emittance of glass
$ε_P$	Emittance of plate
Ta	Ambient temperature (K)
T_{pm}	Mean plate temperature (K)
h_w	Wind heat transfer coefficient (W/m^2.K)
x_{bi}	Thickness of back material (m)
K_{ei}	Thermal conductivity of edge insulation materials (kJ/hr.m.k)
A_e	Edge insulation area (m^2)
x_{ei}	Insulation thickness at the edge (m)

REFERENCES

1. Gautam, A., Chamoli, S., Kumar, A. and Singh, S., "A review on technical improvements, economic feasibility and world scenario of solar water heating system", *Renewable and Sustainable Energy Reviews*, Vol. 68, (2017), 541-562. (https://doi.org/10.1016/j.rser.2016.09.104).

2. Luo, X., Ma, X., Xu, Y.F., Feng, Z.K., Du, W.P., Wang, R. and Li, M., Solar water heating system, Handbook of energy systems in green buildings, Wang, R. and Zhai, X. Eds., Springer, Berlin, Heidelberg, (2018), 145-194. (https://doi.org/10.1007/978-3-662-49120-1_32).

3. Romero, R.L., Salmerón, L.J.M., Sánchez, R.J., Rodríguez, E.Á. and Álvarez, D.S., "Analysis of the economic feasibility and reduction of a building's energy consumption and emissions when integrating hybrid solar thermal/PV/micro-CHP systems", *Applied Energy*, Vol. 165, (2016), 828-838. (https://doi.org/10.1016/j.apenergy.2015.12.080).

4. Gomariz, F.P., Lopez, J.M.C. and Munoz, F.D., "An analysis of low flow for solar thermal system for water heating", *Solar Energy*, Vol. 179, (2019), 67-73. (https://doi.org/10.1016/jsolener.2018.12.060).

5. Karami, N. and Rahimi, M., "Heat transfer enhancement in a hybrid microchannel-photovoltaic cell using Boehmite nanofluid", *International Communications in Heat and Mass Transfer*, Vol. 55, (2014), 45-52. (https://www.sciencedirect.com/science/article/pii/S0735193314001134).

6. National Renewable Laboratory (NREL), "High performance flat plate solar thermal collector evaluation", (2015), 1-80. (https://www.nrel.gov/docs/fy16osti/66215.pdf).

7. Kim, S., Choi, E. and Cho, Y.I., "The effect of header shapes on the flow distribution in a manifold for electronic packaging applications", *International Communications in Heat and Mass Transfer*, Vol. 22, No. 3, (1995), 329-341. (https://jglobal.jst.go.jp/en/detail?JGLOBAL_ID=200902148672674963).

8. Zulkifle, I., Alwaeli, A.H.A., Ruslan, M.H., Ibarahim, Z., Othman, M.Y.H. and Sopian, K., "Numerical investigation of V-groove air-collector performance with changing cover in Bangi, Malaysia", *Case Studies in Thermal Engineering*, Vol. 12, (2018), 587-599. (https://doi.org/10.1016/j.csite.2018.07.012).

9. Liu, T., Lin, W., Gao, W., Lou, C., Li, M., Zheng, Q. and Xia, C., "A parametric study on the thermal performance of a solar air collector with a V-groove absorber", *International Journal of Green Energy*, Vol. 4, No. 6, (2007), 601-622. (https://www.tandfonline.com/doi/abs/10.1080/15435070701665370).

10. Jahangiri, M., Alidadi Shamsabadi, A. and Saghaei, H., "Comprehensive evaluation of using solar water heater on a household scale in canada", *Journal of Renewable Energy and Environment (JREE)*, Vol. 5, No. 1, (2018), 35-42. (http://dx.doi.org/10.30501/jree.2018.88491).

11. Pahlavan, S., Jahangiri, M., Alidadi Shamsabadi, A. and Khechekhouche, A., "Feasibility study of solar water heaters in Algeria, A review", *Journal of Solar Energy Research*, Vol. 3, No. 3, (2018), 201-211. (https://jser.ut.ac.ir/article_67424.html).

12. Duffie, J.A. and Beckman, W.A., Solar engineering of thermal processes, Fourth edition, New Jersey, John Wiley & Sons Inc., (2013). (https://www.sku.ac.ir/Datafiles/BookLibrary/45/John).

13. Touaba, O., AitCheikh, S., Slimani, M.E., Bouraiou, A. and Ziane, A., "Investigation and prototyping implementation of a novel solar water collector based on used engine oil as HTF", *Proceedings of 4th International Conference on Electrical Engineering and Control Applications (ICEECA)*, *Bououden, S., Chadli, M., Ziani, S. ZI, editor*, (2019) 779-789. (https://www.scopus.com/record/display.uri?eid=2-s2.0-85092711693).

14. Hussein, O.A, Habib, K., Muhsan, A.S., Saidur, R., Alawi, O.A. and Ibrahim, T.K., "Thermal performance enhancement of a flat plate solar collector using hybrid nanofluid", *Solar Energy*, Vol 204, (2020), 208-222. (https://doi.org/10.1016/j.solener.2020.04.034).

15. Raj, P. and Subudhi, S., "A review of studies using nano fl uids in flat-plate and direct absorption solar collectors", *Renewable and Sustainable Energy Review*, Vol. 84, (2018), 54-74. (https://doi.org/10.1016/j.rser.2017.10.012).

16. Kiliç, F., Menlik, ,T. and Sözen, A,. "Effect of titanium dioxide/water nano fluid use on thermal performance of the flat plate solar collector", *Solar Energy*, Vol. 164, (2018), 101-108. (https://doi.org/10.1016/j.solener.2018.02.002).

17. Hamed, M., Fellah, A., Ben, B.A., "Parametric sensitivity studies on the performance of a flat plate solar collector in transient behavior", *Energy Conversion and Management*, Vol. 78, (2014), 938-947. (http://dx.doi.org/10.1016/j.enconman.2013.09.044).

18. El-Sebaii, A.A. and Al-Snani, H., "Effect of selective coating on thermal performance of flat plate solar air heaters", *Energy*, (2010), 1820-1828. (https://doi.org/10.1016/j.energy.2009.12.037).

19. Sachit, F.A., Rosli, M.A.M., Tamaldin, N., Misha ,S. and Abdullah, A.L., "Modelling, validation and analyzing performance of serpentine-direct PV/T solar collector design", *CFD Letter*, Vol. 11, No. 2, (2019), 50-65. (http://www.akademiabaru.com/doc/CFDLV11_N2_P50_65.pdf).

20. Smyth, M.Ã., Eames, P.C. and Norton, B., "Techno-economic appraisal of an integrated collector/storage solar water heater", *Renewable Energy*, Vol. 29, (2004), 1503-1514. (https://doi.org/10.1016/j.renene.2003.10.009).

21. Lang, T., Ammann, D. and Girod, B., "Profitability in absence of subsidies: A techno-economic analysis of rooftop photovoltaic self-consumption in residential and commercial buildings", *Renewable Energy*, Vol. 87, (2016), 77-87. (https://doi.org/10.1016/j.renene.2015.09.059).

22. Koroneos, C.J. and Nanaki, E.A., "Life cycle environmental impact assessment of a solar water heater", *Journal of Cleaner Production*, Vol. 37, (2012), 154-161. (https://doi.org/10.1016/j.jclepro.2012.07.001).

23. Abdon, A., Zhang, X., Parra, D., Patel, M.K., Bauer, C. and Worlitschek, J., "Techno-economic and environmental assessment of stationary electricity storage technologies for different time scales", *Energy*, Vol. 139, (2017), 1173-1187. (https://doi.org/10.1016/j.energy.2017.07.097).

24. Hussain, S. and Harrison, S.J., "Evaluation of thermal characteristics of a flat plate solar collector with a back mounted air channel", *Applied Thermal Engineering*, Vol. 123, (2017), 940-952. (https://doi.org/10.1016/j.applthermaleng.2017.05.121).

25. Soteris, A.K. and Christos, P., "Modelling of a thermosyphon solar water heating system and simple model", *Renewable Energy*, Vol. 21, (2000), 471-493. (https://doi.org/10.1016/S0960-1481(00)00086-0).

26. Diez, F.J., Navas-Gracia, L.M., Martínez-Rodríguez, A., Correa-Guimaraes, A. and Chico-Santamarta, L., "Modelling of a flat-plate solar collector using artificial neural networks for different working fluid (water) flow rates", *Solar Energy*, Vol. 188, (2019), 1320-1331. (https://doi.org/10.1016/j.solener.2019.07.022).

27. Kalogirou, S.A., Designing and modeling solar energy systems, Solar energy engineering, 2nd edition, Oxford OX5 1GB, UK, Academic Press publications, (2014), 583-689. (https://www.elsevier.com/books/solar-energy-engineering/kalogirou/978-0-12-397270-5).

28. Julien, G. A., Emmanuel, L., Clément, A., Rufin, O. A. and Brice A.S., "Modeling solar energy transfer through roof material in Africa Sub-Saharan Regions", *Renewable Energy*, Vol. 34, (2013), 1-8. (https://doi.org/10.1155/2013/480137).

29. Deng, J., O'Donovan, T.S., Tian, Z., King, J. and Speake, S., "Thermal performance predictions and tests of a novel type of flat plate solar thermal collectors by integrating with a freeze tolerance solution", *Energy Conversion and Management*, Vol. 198, (2019), 111784. (https://doi.org/10.1016/j.enconman.2019.111784).

Research Article

Building Energy Management Using Building Information Modeling: Evaluation of Building Components and Construction Materials

Nima Amani*, Abdul Amir Reza Soroush

Department of Civil Engineering, Chalous Branch, Islamic Azad University, P. O. Box: 46615-397, Chalous, Mazandaran, Iran.

ABSTRACT

Traditionally, building energy model is created in isolation from the architectural building information model and energy analyses have relied on a single analysis tool. The building energy model can be generated more quickly by leveraging existing data from the BIM. The impacts of energy consumption are significant in the building usage phase, which can last several decades. Due to the large share of the final energy consumption in the building sector, accurate analysis of thermal and cooling loads of a building and the efforts to reduce energy losses represent an effective way to reduce energy consumption. Therefore, it is essential to analyze the building energy performance in the design phase, which is when critical decisions are made. This study aims to investigate the impact of the building components and construction materials on building energy efficiency using Building Information Modeling (BIM) technology in a mild climate zone. After reviewing the proposed designs, the main building form was chosen for energy modeling and analysis. Then, building energy consumption analysis was performed based on the basic parameters of the building energy model. Eventually, the most optimal mode was selected by examining different energy consumption forms. This study showed that the building HVAC system always had the largest share of energy consumption. Finally, the results of parametric studies on alternative schemes of energy use intensity optimization showed that 22.59 % savings could be achieved as compared to the base building model in a 30-year time horizon.

1. INTRODUCTION

Buildings are the world's largest energy consumer, according to the United Nations Environment Program [1]. Residential energy consumption has allocated a large percentage of national energy consumption to itself in most countries [2]. Recently, global efforts have been directed at reducing carbon emissions from buildings [3]. Operational energy reduction has been the main focus of the industry because it accounts for a greater proportion of carbon emission throughout the building lifecycle and it is easier to predict than embodied energy [4]. Usually, following the architectural plans and considering construction documents, the building performance analysis should be done [5]. Analyzing the energy performance of a building in its early design stage requires access to specific information such as properties of materials, U-value, and technical systems. Such information is one of the determinants of building energy performance [6]. The geometric information of buildings is usually extracted from architectural drawings. Then, an energy analyst can benefit from this information to define the building's thermal view, which depends on its knowledge, skills, and experience. Therefore, various building energy analysts will generate differing thermal views [5]. BIM is a technology used for

improving productivity and efficiency in the construction industry [7]. A data model created by integrating 3D digital techniques and specific information related to an engineering project is the best description for building information modeling [1]. One of the most significant benefits of BIM lies both in early-stage design and later stages of building energy simulation analysis [8]. Application of BIM in Energy Performance Assessment (EPAs) considerably reduces time and costs [7]. The limitation of energy resources and the significant growth of using them in Iran compared with the worldwide average have doubled the necessity of optimizing energy consumption in this country [9]. According to the information provided in 2016, the share of building fuel consumption is about 41.4 % of the total energy consumption in the country, which is considered the largest energy consumer sector [10]. Due to the high share of energy consumption in this sector, accurate analysis of thermal and cooling loads of a building and the efforts to reduce energy losses represent an effective way of reducing energy consumption. Building Information Modeling enables information sharing and reuses for interoperability between popular software packages in Architecture, Engineering, and Construction industry. BIM-based energy simulation can significantly reduce the costs and time required to create a geometric model [11]. Many different studies have employed BIM technology in the field of building energy management.

*Corresponding Author's Email: nimaamani@iauc.ac.ir (N. Amani)
URL: http://www.jree.ir/article_122911.html

Based on previous studies from the famous database [12-28], it can be concluded that there is a limited body of research on energy efficiency using the simultaneous evaluation of building components and construction materials using Building Information Modeling (BIM) technology. In other words, all related studies were focused on a specific component and there was not any research that had simultaneously investigated the impact of all involved components on energy consumption. This paper carries out energy performance assessment based on BIM technology. The results indicate that the use of BIM technology will lead to design identification, comparison, and reduction of energy consumption in the early stages of design.

2. METHOD

2.1. Methodology

In this study, to examine different design ideas, several conceptual masses were created using Autodesk Revit software with a top-down design approach. The main form of the building for energy modeling and analysis was selected only after reviewing the proposed designs. Then, an exact model of building elements was fabricated. After generating the energy model, the building energy consumption analysis was carried out based on basic parameters. Finally, the most optimal mode was selected by examining different energy consumption forms.

2.2. Case study

The case study is a residential building that is located in a mild climate in Rasht, Iran. The total area of the building is about 101000 m^2 and the project location is in Rasht, Gilan province, Iran (37°18'34.8"N, 49°36'49.0"E). At first, several conceptual masses were created to study different design ideas. The closest form to the real model of the building and items such as the number of units and the area of the building were considered in the construction of conceptual models. Input parameters of the energy model were selected according to the software defaults (as shown in Table 2). Table 1 shows the comparison of different building forms based on the simulation of energy consumption in conceptual masses. After reviewing the proposed designs and creating a real model of the building, an energy analysis was performed. Carrying out the whole building energy analysis is not possible in the cloud due to the software limitation in sending the shade surfaces (max. 10000 surfaces) as well as the number of doors (max. 4096 doors). For this reason, as shown in Figure 1, each block of this residential tower is analyzed separately. Finally, due to increased shade surfaces, the ceiling elements were removed from the building model. The samples of the second-floor plan and penthouse plan are separated by unit type, as shown in Figure 2.

The results of the analysis show that the first form of the building has the lowest energy consumption among others. The cost of energy consumption based on Table 2 parameters is 13.5 USD/m^2/year. Accordingly, the energy use intensity is equal to 110 kWh/m^2/year, as shown in Table 1. In this form, the building orientation is based on the geographical north. Thus, the angle of the building is automatically determined by the software based on the building form and the geographic coordinates of the project. The window-to-wall ratio in all directions is 40 % by default. All windows have shades with a depth of 45.72 cm. Also, the type of windows in the

conceptual model is double-glazed windows without any external coating. The structure of walls in the conceptual model in the form of lightweight walls with typical mild climate insulation and the roof structure is lightweight without insulation. The values of the building infiltration rate, the lighting efficiency, the plug load efficiency, and the operating schedule are adjusted according to the BIM parameter (as shown in Table 2). The building's HVAC system is assumed to have a BIM parameter (Residential 14 SEER/0.9 AFUE Split/Packaged Gas <5.5 ton). This building has no daylighting and occupancy controls system and photovoltaic solar panels. After adjusting the effective parameters for energy consumption, according to Table 3, the energy cost would be 5.71 USD/m^2/year. Accordingly, the energy use intensity would be equal to 75.3 kWh/m^2/year. The building orientation remains unchanged relative to the previous model (base model) and is based on the geographical north. The window's ratio to the northern and southern walls is 40 % by default. These windows have shades as high as 2/3 of the window height. Also, the type of these windows in the conceptual model is triple-glazed windows with low emission. Due to the lack of significant efficiency, the eastern and western windows have been removed from the conceptual model. The structure of walls in the conceptual model is according to Table 2 and the roof structure is lightweight without insulation. The value of the building infiltration rate is 0.17 ACH. The value of the lighting efficiency parameter is assumed to be 3.23 W/m^2. The values of the plug load efficiency and the operating schedule were adjusted according to the BIM parameter. The building's HVAC system is assumed to be a high-efficiency variable air volume system. Also, the building has a daylighting and occupancy control system. Finally, to achieve the highest level of energy efficiency, photovoltaic solar panels were used. To this end, the photovoltaic solar panels were used with a yield of 20.4 % and surface coverage of 90 %. The payback limit of these panels was selected for 30 years. The results of this analysis show that the use of building information modeling technology for adjusting the parameters affecting energy consumption in the conceptual designs can save up to 57.7 % in energy cost. Based on the energy use intensity, this value would be 31.54 %.
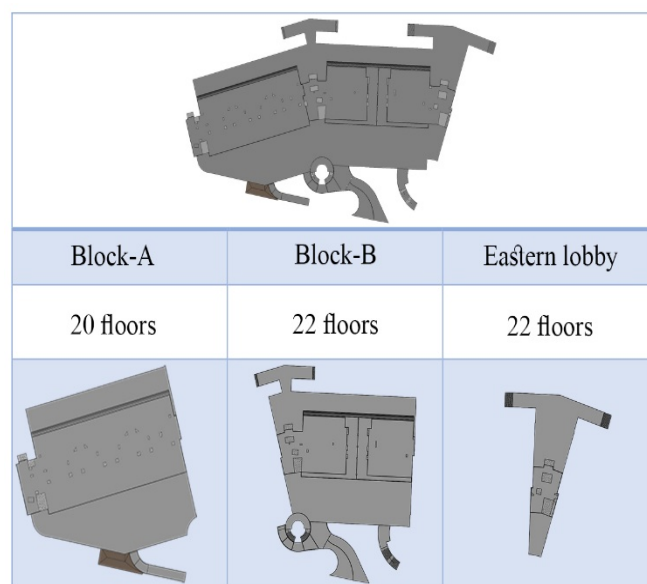

Block-A	Block-B	Eastern lobby
20 floors	22 floors	22 floors

Figure 1. Separation of building blocks for energy analysis

Figure 2. Top left) A sample of the second-floor plan (Block A); Top right) A sample of the penthouse first-floor plan (Block B); Bottom left) A sample of the second-floor plan (Block B); Bottom right) A sample of the penthouse second-floor plan (Block B)

Table 1. Comparison of different building forms in conceptual masses

		Module-1		**Module-2**		**Module-3**	
	Floors	22		43		43	
	Units	548		560		561	
	Height (m)	81.70		159.40		159.40	
Building form		**Energy cost (USD/m²/year)**	**Saving (%)**	**Energy use intensity (kWh/m²/year)**	**Saving (%)**		
Module-1	BIM parameters	13.50	0	110	0		
	Optimized parameters	5.71	57.70	75.30	31.54		
Module-2	BIM parameters	14.10	0	115	0		
	Optimized parameters	7.45	47.16	92.10	19.91		
Module-3	BIM parameters	13.90	0	114	0		
	Optimized parameters	7.24	47.91	88.10	22.72		

Table 2. Basic and optimized parameters based on energy consumption simulation in conceptual masses

Building form	**Module-1**		**Module-2**		**Module-3**	
Energy cost (USD/m²/year)	13.5*	5.71**	14.1*	7.45**	13.9*	7.24**
Effective factor	Input parameter					
Building orientation	BIM°					
WWR (South)	BIM (40 %)°					
Window shades	BIM (0.4572 m)*					
	2/3 Win height**					
Window glass	BIM (Double pane clear-No coating)*					
	Trp LoE**					
WWR (North)	BIM (40 %)°					
Window shades	BIM (0.4572 m)*					
	2/3 Win height**					
Window glass	BIM (Double pane clear-No coating)*					
	Trp LoE**					
WWR (West)	BIM (40 %)*					
	(0 %)**					
Window shades	BIM (0.4572 m)*					
	BIM (No shade)**					
Window glass	BIM (Double pane clear-No coating)*					
	BIM (No window)**					
WWR (East)	BIM (40 %)*					
	(0 %)**					
Window shades	BIM (0.4572 m)*					
	BIM (No shade)**					

Window glass	BIM (Double pane clear-No coating)[*]
	BIM (No window)[**]
Wall construction	BIM (Lightweight construction-Typical mild climate insulation)[*]
	R13+R10 Metal[**]
Roof construction	BIM (Lightweight construction-No insulation)[°]
Infiltration	BIM (None)[*]
	0.17 ACH[**]
Lighting efficiency	BIM (10.76 W/m^2)[*]
	3.23 W/m^2[**]
Daylighting and occupancy controls	None[*]
	Daylighting & occupancy controls[**]
Plug load efficiency	BIM (10.76 W/m^2)[°]
HVAC	BIM[*]
	High Eff. VAV[**]
Operating schedule	BIM (24 Hours)[°]
Panel efficiency (PV)	None[*]
	20.4 %[**]
Payback limit (PV)	None[*]
	30 years[**]
Surface coverage (PV)	0 %[*]
	90 %[**]

[*]Base Model, [**]Optimized, [°]Unchanged

The building energy model requires a group of parameters depending on the analysis tools and specific studies. Table 3 shows the basic parameters of the building energy model as the basis of design. These parameters include HVAC, materials with thermal properties, plug loads, building occupancy, building natural infiltration rate, lighting density and efficiency, natural ventilation, internal heat gains (plug loads and occupancy), thermostat set-point temperatures, and operating schedules. These parameters are specified by the BIM title in the provided data.

Table 3. Basic parameters of the building energy model

Input parameter	Value
HVAC system	Residential 14 SEER/0.9 AFUE Split/Packaged Gaz < 5.5 ton
Area per person	105.82 m^2
Sensible heat gain (per person)	73.27 W
Latent heat gain (per person)	58.61 W
Power load density	10.76 W/m^2
Lighting load density	10.76 W/m^2
Plenum lighting contribution	20 %
Occupancy schedule	24 Hours
Lighting schedule	All day
Power schedule	All day
Outdoor air (per person)	2.36 L/s
Outdoor air (per area)	0.30 L/ (s.m^2)
Unoccupied cooling set point	27.78 °C
Infiltration (ac/h)	None
Fabric *U*-values	
External walls	20 cm concrete block (*U*-value 6.5 W/m^{2}K)
Internal walls	10 cm concrete block (*U*-value 13 W/m^{2}K)
Shear walls	45 cm reinforced concrete (*U*-value 2.3244 W/m^{2}K)
Floor	22.5 cm concrete slab (*U*-value 4.6489 W/m^{2}K)
External doors	Wooden, Single-Flush (*U*-value 2.1944 W/m^{2}K)
Terrace doors	Wood frame with single clear glass (*U*-value 5.6212 W/m^{2}K)
Lobby doors	Metal frame with single clear glass (*U*-value 6.5580 W/m^{2}K)
Elevator doors	Metal (*U*-value 3.7021 W/m^{2}K)
Windows	1/8 in Pilkington single glazing (*U*-value 3.6886 W/m^{2}K)

2.3. Climate data

Climate data are automatically taken from the nearest meteorological station database after the energy model sending as the first element of the environment in which the building is located (Table 4). This information is related to the project location, which is available in the Autodesk Green Building Studio (GBS) software database, and the distance specified in Table 4 is only the storage of data at the desired station. Data on design conditions based on dry-bulb temperature and Mean Coincident Wet Bulb (MCWB) temperature are shown annually in Table 5. Also, Figure 3 shows the average daily minimum and maximum temperature basis on monthly data.
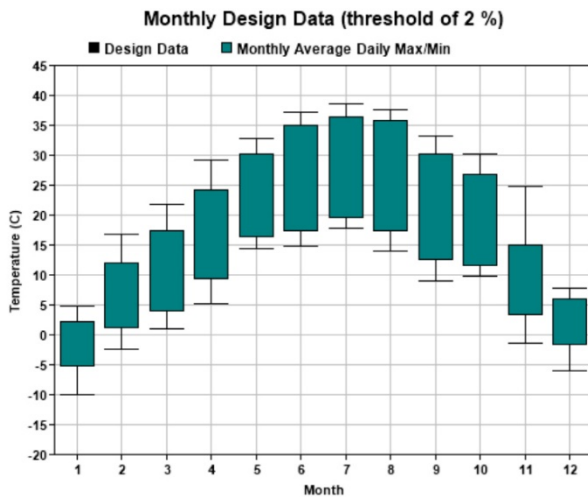
Figure 3. Average of Max. and Min. daily temperatures on a monthly basis [29]

Table 4. Receiving the temperature data from the nearest weather station database by Autodesk Green Building Studio software

Weather station: GBS_06M12_12_002300		Unit: SI	
Distance to project 474.2 mi (763.2 km)			
Latitude=36.4167, Longitude=58.1500			
Cooling degree day		**Heating degree day**	
Threshold	Value	Threshold	Value
18.3 °C	1110	18.3 °C	2047
21.1 °C	657	15.6 °C	1577
23.9 °C	316	12.8 °C	1172
26.7 °C	104	10 °C	807

Table 5. The dry-bulb and Mean Coincident Wet Bulb temperature based on annual data

Annual design conditions			Unit: SI	
Threshold	**Cooling**		**Heating**	
	Dry bulb (°C)	MCWB (°C)	Dry bulb (°C)	MCWB (°C)
0.1 %	39.2	18.1	-10.4	-11.3
0.2 %	38.8	17.9	-9.8	-11.0
0.4 %	38.4	17.9	-9.2	-10.4
0.5 %	38.2	18.0	-8.8	-9.8
1 %	37.3	17.3	-7.6	-8.9
2 %	36.4	16.9	-4.8	-6.5
2.5 %	36.0	16.7	-3.9	-5.7
5 %	34.1	15.8	-1.9	-3.7

2.4. Solar orientation study

This study investigates solar radiation on building surfaces. After setting parameters such as project location, date, time, and time interval, a graphical illustration of solar radiation is given (Figure 4). This study shows that block A (located on the western side of the site) with much sunlight received during a day has a better position than block B.

3. DATA ANALYSIS

After modeling and adjusting the parameters required in Autodesk Revit software (Table 3), an energy model was made using the analysis tab. Then, to send the energy model and receive the data analysis results, an Autodesk account was used. It should be noted that by sending the energy model through the Autodesk Revit software to the Autodesk Insight

software, an energy model will be sent to the Autodesk Green Building Studio software. Also, this software could be used to validate the results of energy analysis.
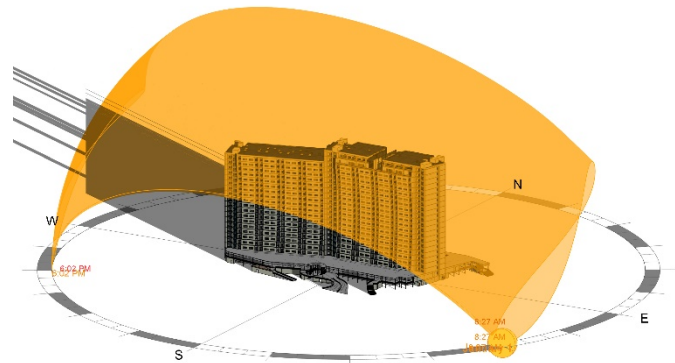
Figure 4. Sunlight radiation on building surfaces

Investigation of the charts of Figure 5 for block A shows that the highest energy cost is in July. According to this analysis, ventilation fans and space cooling have the highest share among all other affecting parameters for energy consumption. Also, the maximum energy use intensity of block A is in January, as shown in Figure 6. The space heat and ventilation fans have had the largest share among other parameters. Accordingly, the highest level of energy consumption based on energy cost is in July and August and energy use intensity is in January and December. The schematic diagrams of energy consumption for block B and the eastern lobby are similar.
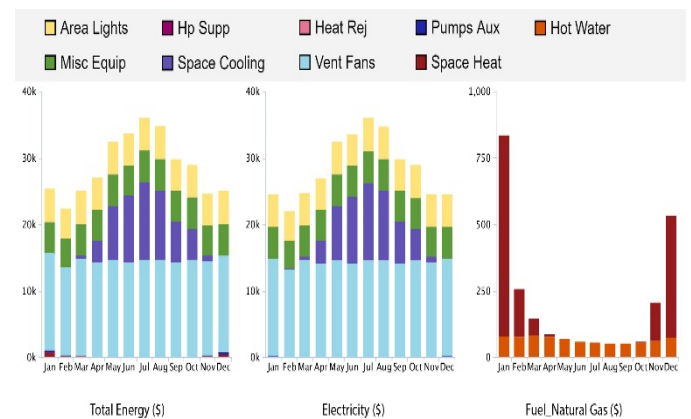
Figure 5. Energy consumption index based on energy cost, Block A
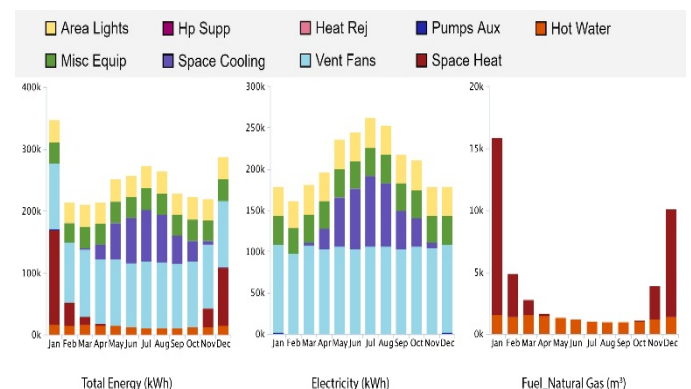
Figure 6. Energy consumption index based on energy use intensity, Block A

4. DISCUSSION

The results of the analysis show that block A has the lowest energy consumption. The cost of energy consumption based on the parameters in Table 7 is 13 USD/m²/year, as shown in Table 6. This value for block B and the eastern lobby is 13 and 14.1, respectively. Accordingly, the energy use intensity for blocks A, B, and the eastern lobby will be equal to 112, 119, and 191 kWh/m²/year, respectively. The building orientation, in this case, is based on the geographical north. Thus, the angle of the building is automatically determined by software based on the building form and the project geographic coordinates. The ratios of the window to the northern, southern, eastern and western walls are 16 %, 20 %, 7 %, and 5 %, respectively. The ratio values for blocks B are: 18 %, 22 %, 9 %, and 7 % and for the eastern lobby 15 %, 25 %, 13 %, and 14 %. The shades of all windows are considered by default. Therefore, the windows installed on the terraces use their overhead ceiling as shade. Other windows installed on the surfaces of external walls lacked a shading system. Also, the type of windows was based on the element defined in Autodesk Revit software (as shown in Table 7). The walls and roof structures are shown in Tables 3 and 7. The values of building infiltration rate, lighting efficiency, plug load efficiency, operating schedule, and building's HVAC system were adjusted according to the BIM parameter (as shown in Table 7). This building has no daylighting and occupancy controls system and photovoltaic solar panels. According to Table 7, after adjusting the effective parameters for energy consumption, the energy cost of block A is determined at 5.4 USD/m²/year. This value for block B and the eastern lobby is 6.47 and 8.03, respectively. Accordingly, the energy use intensity for blocks A, B, and the eastern lobby will be equal to 86.7, 99, and 170 kWh/m²/year, respectively. The building orientation in comparison to the previous base model remains unchanged based on the geographical north.

The window's ratio to the northern and southern walls is unchanged and equal to 16 % and 20 % for block A; 18 % and 22 % for block B; 15 % and 25 % for the eastern lobby, respectively. The northern window shades were considered by default, for all blocks. Also, the southern window shades are selected as high as 2/3 of the window height. As shown in Table 7, the type of northern windows was unchanged for all blocks. The type of southern window is of triple-glazed one with low emission. Due to insignificant efficiency, the eastern and western windows were removed from the building model. The walls and roof structure are shown in Table 7. The value of the building infiltration rate is 0.17 ACH. The value of the lighting efficiency parameter is assumed to be 3.23 W/m². The values of plug load efficiency and operating schedules were adjusted according to the BIM parameter. The building's HVAC system was assumed to be a high-efficiency variable air volume system. Also, the building has a daylighting and occupancy control system. Finally, to achieve the highest level of energy efficiency, photovoltaic solar panels were used. For this purpose, the photovoltaic solar panels were used with a yield of 20.4 % and surface coverage of 90 %. The payback limit of photovoltaic panels in Autodesk Insight software is in 10-year, 20-year, and 30-year periods. Considering the arrangement of other parameters affecting energy consumption and related analysis showed that the time period between 20 and 30 years would not affect the output results. Therefore, the payback limit of these panels was considered for 30 years. The results of this analysis showed that the use of building information modeling technology in the adjustment of effective energy consumption parameters could save up to 58.46 % in energy cost for block A. This value for block B and the eastern lobby is 50.23 % and 43.05 %, respectively. Based on this result, this value based on the energy use intensity for blocks A, B, and the eastern lobby is 22.59 %, 16.81 %, and 11 %, respectively.

Table 6. Investigation and comparison of different energy consumption scenarios in building blocks

Building block		Energy cost (USD/m²/year)	Saving (%)	Energy use intensity (kWh/m²/year)	Saving (%)
A	BIM parameters	13	0	112	0
	Optimized parameters	5.40	58.46	86.70	22.59
B	BIM parameters	13	0	119	0
	Optimized parameters	6.47	50.23	99	16.81
Eastern lobby	BIM parameters	14.10	0	191	0
	Optimized parameters	8.03	43.05	170	11

Table 7. Basic and optimized parameters for building energy consumption

Building block	Block A		Block B		Eastern lobby	
Energy cost (USD/m²/year)	13[*]	5.40[**]	13[*]	6.47[**]	14.1[*]	8.03[**]
Effective factor	Input parameter					
Building orientation	BIM[°]					
WWR (South)	BIM (20 %)[°]		BIM (22 %)[°]		BIM (25 %)[°]	
Window shades	BIM[*]					
	2/3 Win height[**]					
Window glass	BIM (Sgl Clr)[*]					
	Trp LoE[**]					
WWR (North)	BIM (16 %)[°]		BIM (18 %)[°]		BIM (15 %)[°]	
Window shades	BIM[°]					
Window glass	BIM (Sgl Clr)[°]					
WWR (West)	BIM (5 %)[*]	(0 %)[**]	BIM (7 %)[*]	(0 %)[**]	BIM (14 %)[*]	(0 %)[**]

Window shades	BIM[*]					
	BIM (No Shade)[**]					
Window glass	BIM (Sgl Clr)[*]					
	BIM (No Window)[**]					
WWR (East)	BIM (7 %)[*]	(0 %)[**]	BIM (9 %)[*]	(0 %)[**]	BIM (13 %)[*]	(0 %)[**]
Window shades	BIM[*]					
	BIM (No shade)[**]					
Window glass	BIM (Sgl Clr)[*]					
	BIM (No window)[**]					
Wall construction	BIM (Concrete masonry units)[*]					
	R13+R10 Metal[**]					
Roof construction	BIM (Concrete, Cast in situ)[°]					
Infiltration	BIM (None)[*]					
	0.17 ACH[**]					
Lighting efficiency	BIM (10.76 W/m^2)[*]					
	3.23 W/m^{2}[**]					
Daylighting and occupancy controls	None[*]					
	Daylighting & occupancy controls[**]					
Plug load efficiency	BIM (10.76 W/m^2)[°]					
HVAC	BIM[*]					
	High Eff. VAV[**]					
Operating schedule	BIM (24 Hours)[°]					
Panel efficiency (PV)	None[*]					
	20.4 %[**]					
Payback limit (PV)	None[*]					
	30 years[**]					
Surface coverage (PV)	0 %[*]					
	90 %[**]					

[*]Base Model, [**]Optimized, [°]Unchanged

It should be noted that this study was performed to convince the employer of the worth and benefit of BIM technology in optimizing energy consumption in a real project. As mentioned, due to the software limitations in sending the energy model, the building blocks were divided and also the ceiling elements were removed from the building model. Thus, the thermal height on the first and other floors was 4 m and 3.7 m, respectively. This building could have lower energy consumption than the values obtained in this analysis due to the implementation of the ceiling elements during the construction phase and reduced computational height of the spaces as a result. However, the results of this analysis show that block A has the lowest energy consumption. Considering the similar materials and equipment, this is due to the building orientation with the actual north of the region (geographic north). Accordingly, with the implementation of block B along the block A, the lowest energy consumption resulting from the maximum solar radiation during a day can be achieved. Also, this study shows that the results of the conceptual model analysis are more acceptable than the results of the actual building model. It can be useful in the early stages of decision-making for the project.

5. CONCLUSIONS

To investigate different design ideas, several conceptual masses were created in Autodesk Revit software. Next, the main form of the building was chosen only after reviewing the proposed designs in terms of energy cost as well as considerations such as project location, site scope, building height, facilities, and project cost. Then, an exact model of the building elements was created in Autodesk Revit software.

Finally, after generating and analyzing the energy model, the most optimal mode was selected by examining different forms of energy consumption. The results of this analysis showed that the use of building information modeling technology in adjusting the affected energy consumption parameters would save up to 58.46 % in energy cost for block A, compared to the base building model in a 30-year time horizon. This value was 50.23 % for block B and 43.05 % for the eastern lobby. As a result, this value would be 22.59 %, 16.81 %, and 11 % for blocks A, B, and the eastern lobby, respectively, based on the energy use intensity. The results of this study showed that the use of Building Information Modeling (BIM) technology in optimizing the building energy consumption could significantly save energy costs. Also, the results of this study showed that the building HVAC system always had the highest share of energy consumption. Therefore, choosing the right type of HVAC system could achieve the lowest level of energy consumption in the building.

6. ACKNOWLEDGEMENT

NOMENCLATURE

ACH	Air Changes per Hour
AFUE	Annual Fuel Utilization Efficiency
BIM	Building Information Modeling
Clr	Clear

Eff	Efficiency
HVAC	Heating, Ventilation, and Air Conditioning
LoE	Low Emissivity
PV	Photovoltaics
R13+R10	Construction material
SEER	Seasonal Energy Efficiency Ratio
Sgl	Single
Trp	Triple
VAV	Variable Air Volume
WWR	Window-to-Wall Ratio

REFERENCES

1. Guo, S.J. and Wei, T., "Cost-effective energy saving measures based on BIM technology: Case study at National Taiwan University", *Energy and Buildings*, Vol. 127, (2016), 433-441. (https://doi.org/10.1016/j.enbuild.2016.06.015).

2. Swan, L.G. and Ugursal, V.I., "Modeling of end-use energy consumption in the residential sector: A review of modeling techniques", *Renewable and Sustainable Energy Reviews*, Vol. 13, No. 8, (2009), 1819-1835. (https://doi.org/10.1016/j.rser.2008.09.033).

3. Amani, N. and Kiaee, E., "Developing a two-criteria framework to rank thermal insulation materials in nearly zero energy building using multi-objective optimization approach", *Journal of Cleaner Production*, Vol. 276, (2020), 122592. (https://doi.org/10.1016/j.jclepro.2020.122592).

4. Banteli, A. and Stevenson, V.E., "Building information modelling (BIM) as an enabler for whole-building embodied energy and carbon calculation in Early-Stage building design", *WIT Transactions on the Built Environment*, Vol. 169, (2017), 89-100. (https://doi.org/10.2495/BIM170091).

5. Egwunatum, S., Joseph-Akwara, E. and Akaigwe, R., "Optimizing energy consumption in building designs using Building Information Model (BIM)", *Slovak Journal of Civil Engineering*, Vol. 24, No. 3, (2016), 19-28. (https://doi.org/10.1515/sjce-2016-0013).

6. Schlueter, A. and Thesseling, F., "Building information model based energy/exergy performance assessment in early design stages", *Automation in Construction*, Vol. 18, No. 2, (2009), 153-163. (https://doi.org/10.1016/j.autcon.2008.07.003).

7. Choi, J., Shin, J., Kim, M. and Kim, I., "Development of openBIM-based energy analysis software to improve the interoperability of energy performance assessment", *Automation in Construction*, Vol. 72, (2016), 52-64. (https://doi.org/10.1016/j.autcon.2016.07.004).

8. Douglass, C.D., "Instructional modules demonstrating building energy analysis using a building information model", Unpublished master's thesis, University of Illinois, Urbana-Champaign, (2010). (https://www.ideals.illinois.edu/bitstream/handle/2142/18219/Douglass_Christian.pdf?sequence=1).

9. Amani, N., "Building energy conservation in atrium spaces based on ECOTECT simulation software in hot summer and cold winter zone in Iran", *International Journal of Energy Sector Management*, Vol. 12, (2018), 298-313. (https://doi.org/10.1108/IJESM-05-2016-0003).

10. Ministry of Energy, "Energy balance sheet, Office of planning and economics of electricity and energy", (2016), (Accessed Jan. 20, 2019). (in Farsi). (http://pep.moe.gov.ir).

11. Ahn, K.U., Kim, Y.J., Park, C.S., Kim, I. and Lee, K., "BIM interface for full vs. semi-automated building energy simulation", *Energy and Buildings*, Vol. 68, No. PART B, (2014), 671-678. (https://doi.org/10.1016/j.enbuild.2013.08.063).

12. Abanda F.H. and Byers, L., "An investigation of the impact of building orientation on energy consumption in a domestic building using emerging BIM (Building Information Modelling)", *Energy*, Vol. 97, (2016), 517-527. (https://doi.org/10.1016/j.energy.2015.12.135).

13. Ahuja, R., Sawhney, A. and Arif, M., "Driving lean and green project outcomes using BIM: A qualitative comparative analysis", *International Journal of Sustainable Built Environment*, Vol. 6, No. 1, (2017), 69-80. (https://doi.org/10.1016/j.ijsbe.2016.10.006).

14. Wong, K. and Fan, Q., "Building information modelling (BIM) for sustainable building design", *Facilities*, Vol. 31, No. 3, (2013), 138-157. (https://doi.org/10.1108/02632771311299412).

15. Chen, K., Xu, G., Xue, F., Zhong, R.Y., Liu, D. and Lu, W., "A physical internet-enabled Building Information Modelling system for prefabricated construction", *International Journal of Computer Integrated Manufacturing*, Vol. 31, No. 4-5, (2018), 349-361. (https://doi.org/10.1080/0951192X.2017.1379095).

16. Beazley, S., Heffernan, E. and McCarthy, T.J., "Enhancing energy efficiency in residential buildings through the use of BIM: The case for embedding parameters during design", *Energy Procedia*, Vol. 121, (2017), 57-64. (https://doi.org/10.1016/j.egypro.2017.07.479).

17. Bonenberg, W. and Wei, X., "Green BIM in sustainable infrastructure", *Procedia Manufacturing*, Vol. 3, (2015), 1654-1659. (https://doi.org/10.1016/j.promfg.2015.07.483).

18. Cepurnaite, J., Ustinovicius, L. and Vaisnoras, M., "Modernization with BIM technology through scanning building information", *Procedia Engineering*, Vol. 208, (2017), 8-13. (https://doi.org/10.1016/j.proeng.2017.11.014).

19. Gourlis, G. and Kovacic, I., "Building Information Modelling for analysis of energy efficient industrial buildings–A case study", *Renewable and Sustainable Energy Reviews*, Vol. 68, No. 2, (2017), 953-963. (https://doi.org/10.1016/j.rser.2016.02.009).

20. Gao, H., Koch, C. and Wu, Y., "Building information modelling based building energy modelling: A review", *Applied Energy*, Vol. 238, (2019), 320-343. (https://doi.org/10.1016/j.apenergy.2019.01.032).

21. Marzouk, M. and Abdelaty, A., "BIM-based framework for managing performance of subway stations", *Automation in Construction*, Vol. 41, (2014), 70-77. (https://doi.org/10.1016/j.autcon.2014.02.004).

22. Rezaei, F., Bulle, C. and Lesage, P., "Integrating building information modeling and life cycle assessment in the early and detailed building design stages", *Building and Environment*, Vol. 153, (2019), 158-167. (https://doi.org/10.1016/j.buildenv.2019.01.034).

23. Zhang, C., Nizam, R.S. and Tian, L., "BIM-based investigation of total energy consumption in delivering building products", *Advanced Engineering Informatics*, Vol. 38, (2018), 370-380. (https://doi.org/10.1016/j.aei.2018.08.009).

24. Amani, N., "Energy simulation and management of the main building component materials using comparative analysis in a mild climate zone", *Journal of Renewable Energy and Environment (JREE)*, Vol. 7, No. 3, (2020), 29-46. (https://doi.org/10.30501/jree.2020.227079.1101).

25. Sadeghifam, A.N., Meynagh, M.M., Tabatabaee, S., Mahdiyar, A., Memari, A. and Ismail, S., "Assessment of the building components in the energy efficient design of tropical residential buildings: An application of BIM and statistical Taguchi method", *Energy*, Vol. 188, (2019), 116080. (https://doi.org/10.1016/j.energy.2019.116080).

26. Venkatraj, V., Dixit, M., Yan., W. and Lavy, S., "Evaluating the impact of operating energy reduction measures on embodied energy", *Energy and Buildings*, Vol. 226, (2020), 110340. (https://doi.org/10.1016/j.enbuild.2020.110340).

27. Ding, Z., Liu, S., Luo, L. and Liao, L., "A building information modeling-based carbon emission measurement system for prefabricated residential buildings during the materialization phase", *Journal of Cleaner Production*, Vol. 264, (2020), 121728. (https://doi.org/10.1016/j.jclepro.2020.121728).

28. Singh, P. and Sadhu, A., "Multicomponent energy assessment of buildings using building information modeling", *Sustainable Cities and Society*, Vol. 49, (2019), 101603. (https://doi.org/10.1016/j.scs.2019.101603).

29. I.R. Iran of Meteorological Organization, (2019). (www.irimo.ir/index.php?newlang=eng/).

The Effect of Proton-Exchange Membrane Fuel Cell Configuration Changing from Straight to Cylindrical State on Performance and Mass Transport: Numerical Procedure

Tuhid Pashaee Golmarz[a], Sajad Rezazadeh[a*], Maryam Yaldagard[b], Narmin Bagherzadeh[a]

[a] Department of Renewable Energies, School of Mechanical Engineering, Urmia University of Technology, P. O. Box: 57166-17165, Urmia, West Azerbaijan, Iran.
[b] Department of Engineering, School of Chemical Engineering, Urmia University, P. O. Box: 57561-51818, Urmia, West Azerbaijan, Iran.

ABSTRACT

In the present work, a Proton-Exchange Membrane Fuel Cell (PEMFC) as a three-dimensional and single phase was studied. Computational fluid dynamics and finite volume technique were employed to discretize and solve a single set of flow fields and electricity governing equations. The obtained numerical results were validated with valid data in the literature and good agreement was observed between them. The main purpose of this paper is to investigate the effect of deformation of the geometric structure of a conventional cubic fuel cell into a cylindrical one. For this purpose, some important parameters indicating the operation of the fuel cell such as oxygen distribution, water, hydrogen, proton conductivity of the membrane, electric current density, and temperature distribution for two voltage differences between the anode and cathode and the proposed models were studied in detail. Numerical results showed that in the difference of voltages studied, the proposed new model had better performance than the conventional model and had a higher current density, in which at V = 0.4 [V], about a 10.35 % increase in the amount of electric current density was observed and the average increment in generated power was about 8 %, which could be a considerable value in a stack of cells. Finally, the discussion of critical parameters for both models was presented in more detail. The core idea of the results is that the Oxygen and Hydrogen utilization, water creation, and heat generation are greater in the new model.

1. INTRODUCTION

Fuel cells are some kinds of gadgets that transform the synthetic energy of vaporous or fluid reactants into electrical energy. The reactants are precluded from chemically reacting by isolating them with an electrolyte. This layer is in connection with permeable electrode parts. Additionally, the electrolyte layer interferes with the electrochemical reactions occuring at the anodes by directing a particular particle during the activity of the power device. As a standard power module, a proton or oxide particle current is passed through the electrolyte and parts of the heterogeneous anode and cathode structures. This sort works with hydrogen and oxygen as responding gases [1]. Various specialists have zeroed in on various parts of the power device. Bernardi and Verbrugge [2, 3] examined a one-dimensional model giving worthy outcomes about the electrochemical responses and transport marvels in energy units. Fuller and Newman [4] investigated a straightforward model of the film anode. They studied the fixation arrangement hypothesis for the film and warm impacts. Nguyen and White [5] spoke to a two-dimensional model. They chipped away at electro-assimilation drag power

just as warmth moved from the strong stage to the gas stage through the stream channels for water transport marvels. Dutta et al. examined a three-dimensional type of PEMFC [6]. Berning et al. built up a consistent state, three-dimensional, non-isothermal model to foresee PEM energy component responses [7]. Yang et al. [8] expanded the exhibition of a PEM energy unit. Such high force densities are achieved through better usage of Pt crystallites in the response layer. This improved presentation can be accomplished by making a flimsy impetus layer on the film surface. The power in the front surface impetuses is too basic to limit the coagulation of Pt particles when the energy units are exposed to long haul activity. Some other authors tested variable numerical methods to check the capability of these types of procedures like Akbari et al. [9] and Carral et al. [10]. They utilized the Lattice–Boltzmann strategy to show the water bead dynamic conduct and a limited component procedure to reproduce the PEMFC stack routinely. Ahmadi et al. [11] mathematically and tentatively examined a PEM energy component. Their outcomes demonstrated that the capability of cells improved by expanding the working weight. They likewise explored the GDL mathematical setup impact on PEM energy component execution. The outcomes demonstrated an observable increment in current thickness at comparative cell voltages in

*Corresponding Author's Email: sor.mems@gmail.com (S. Rezazadeh)
URL: http://www.jree.ir/article_126342.html

comparison with the base model. Rezazadeh et al. [12] proposed a three-dimensional and single-stage CFD model of a PEMFC with two gas circulation stream channels and Layer Cathode Gathering (MEA). They examined the working weight impact in their paper. Also, the impact of mathematical arrangement of Gas Dissemination Layers (GDLs) on cell execution indicated that the watched model, with unmistakable GDLs, developed the cell execution and the customary model. While examination and advancement in the field of energy units have been followed, these frameworks and their applications are still amazingly perplexing and costly and are not appropriate for business use. Significant points of ongoing advancements are focused on the cost decrease and enormous volume assembling of the impetus layers, films, and bipolar plates. An explanatory arrangement is dependent on the bother strategy to fathom the progression and force conditions overseeing the stream in gas channels of a PEMFC having roundabout and curved cross-areas, as explored by Ahmadi et al. [20]. Moreover, Pashaee et al. [21] conducted a numerical investigation of bent shape channel impact on execution and circulation of species in a Proton-Trade Layer Power module.

According to the performed researches, the main focus is on the conventional form of the fuel cell (straight model) and it has been recognized that the configuration changing of the whole PEM to cylindrical state is a suitable idea for the study. Therefore, in the present work, a 3D numerical study of novel-cylindrical-cell shape effect on execution and species dispersion in a PEM fuel cell was investigated in more detail. Some important parameters such as species mass fractions, cell temperature, cathode overpotential, and electrical current density were illustrated and contrasted with the simple model outcomes. In doing so, a user can choose the best model for any certain applications. A list of nomenclature for better understanding the terms of the governing equations can be found in [18].

2. MATHEMATICAL MODEL

Figures 1 and 2 show a schematic of a solitary cell of a PEMFC (base model). It includes two permeable terminals, a polymer electrolyte film, a two-impetus layer, and two-gas distributor plates. The MEM layer is inserted between the gas channels. The present non-isothermal model includes some assumptions. The following simplifications have been applied to the governing equation defining:

- All gases are thought to be an ideal gas combination.
- The GDLs and impetus layers are homogeneously permeable.
- The stream is incompressible and laminar due to low-pressure slopes and speeds.
- The volume of fluid stage water in the space is irrelevant; thus, the stream field is a solitary phase.

3. GOVERNING EQUATIONS

In this numerical reenactment, a solitary area model formulation was applied to administering conditions. These overseeing conditions comprise mass preservation, momentum, species, and charge equations, which can be written as follows:
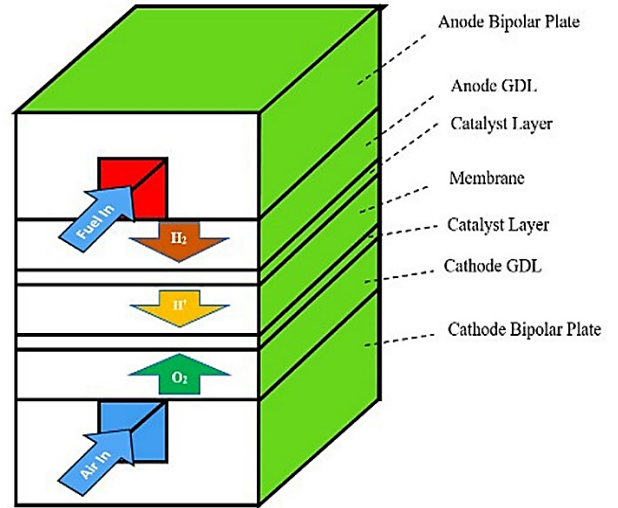
Figure 1. Simplified shape of a PEM fuel cell (base model)
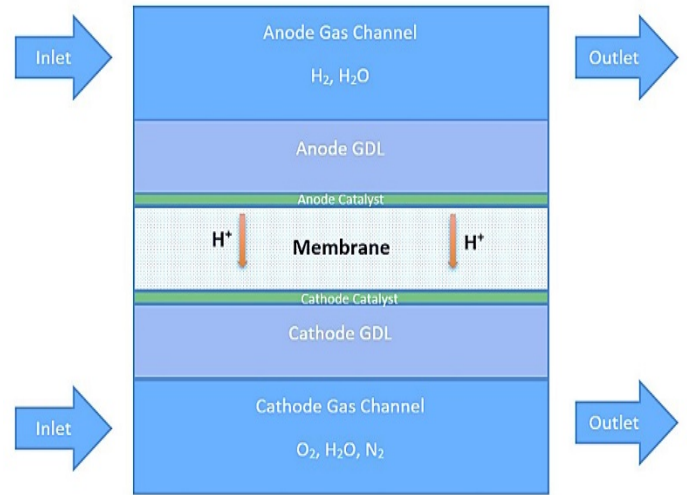
Figure 2. PEMFC in lateral view

$$(\nabla \cdot \rho u) = 0 \tag{1}$$

$$\frac{1}{(\varepsilon^{eff})^2} \nabla \cdot (\rho u u) = -\nabla P + \nabla \cdot (\mu \nabla u) + S_u \tag{2}$$

$$\frac{1}{(\varepsilon^{eff})^2} \nabla \cdot (\rho u u) = -\nabla P + \nabla \cdot (\mu \nabla u) + S_u \tag{3}$$

$$\nabla \cdot (u C_k) = \nabla \cdot (D_k^{eff} \nabla C_k) + S_k \tag{4}$$

$$\nabla \cdot (K_e^{eff} \nabla \Phi_e) + S_\Phi = 0 \tag{5}$$

In Equation (1), the mixture density is denoted by ρ. ε is the efficient porosity entrant porous inductor, and the viscosity of the gas mixture in the momentum equation is denoted by μ as in Eq. (2). Su is the source of momentum equation term and is used to describe Darcy's drag for flow through porous gas diffusion layers and catalyst layers. More information about the governing equations and source terms is available in references [13-25].

4. BOUNDARY CONDITION

The mentioned governing equations are solved by using the boundary condition, which is shown in Table 1. Figure 3 shows the solution procedure. Accordingly, an initial voltage is introduced first. Then, all equations are solved. Finally, if the convergence criterion is met, the process ends and the current density is calculated.

Table 1. The boundary condition of the fuel cell

Boundary condition	The location
$u = u_{in}, T = T_{in}, v = 0, C_{H2} = C_{H2,in}^{a}, \ C_{H2O} = C_{H2O}^{a}$	Anode channel inlet
$u = u_{in}, T = T_{in}, v = 0, C_{O2} = C_{O2,in}^{c}, \ C_{N2} = C_{N2}^{c}$	Cathode channel inlet
$\dfrac{\partial u}{\partial x} = \dfrac{\partial v}{\partial x} = \dfrac{\partial w}{\partial z} = 0, \qquad \dfrac{\partial T}{\partial x} = 0$	Anode and cathode channel exit
$\dfrac{\partial u}{\partial y_{h_1^-}} = \varepsilon_{eff,GDL} \dfrac{\partial u}{\partial y_{h_1^+}}, \dfrac{\partial v}{\partial y_{h_1^-}} = \varepsilon_{eff,GDL} \dfrac{\partial v}{\partial y_{h_1^+}}, \dfrac{\partial w}{\partial y_{h_1^-}} = \varepsilon_{eff,GDL} \dfrac{\partial w}{\partial y_{h_1^+}}$	Gas channel and GDL interface
$\varepsilon_{eff,GDL} \dfrac{\partial u}{\partial y_{h_2^-}} = \varepsilon_{eff,CL} \dfrac{\partial u}{\partial y_{h_2^+}}, \varepsilon_{eff,GDL} \dfrac{\partial u}{\partial y_{h_2^-}} = \varepsilon_{eff,CL} \dfrac{\partial u}{\partial y_{h_2^+}}, \varepsilon_{eff,GDL} \dfrac{\partial u}{\partial y_{h_2^-}} = \varepsilon_{eff,CL} \dfrac{\partial u}{\partial y_{h_2^+}}$	GDL and catalyst layer interface
$u = v = w = Ci = 0$	Catalyst layer and membrane interface
$u = v = w = Ci = 0, T_{surface} = 353K$	Top wall of channel
$u = w = 0, T_{surface} = T_{wall}$	Bottom wall of channel
$\phi_{sol} = 0, \dfrac{\partial \phi_{mem}}{\partial y} = 0$	Anode bipolar
$\phi_{sol} = V_{cell}, \dfrac{\partial \phi_{mem}}{\partial y} = 0$	Cathode bipolar
$\dfrac{\partial \phi_{mem}}{\partial x} = 0, \dfrac{\partial \phi_{mem}}{\partial z} = 0, \dfrac{\partial \phi_{sol}}{\partial x} = 0, \dfrac{\partial \phi_{sol}}{\partial z} = 0$	External surfaces
$u = u_{in}, T = T_{in}, v = 0, C_{H2} = C_{H2,in}^{a}, \ C_{H2O} = C_{H2O}^{a}$	Anode channel inlet
$u = u_{in}, T = T_{in}, v = 0, C_{O2} = C_{O2,in}^{c}, \ C_{N2} = C_{N2}^{c}$	Cathode channel inlet
$\dfrac{\partial u}{\partial x} = \dfrac{\partial v}{\partial x} = \dfrac{\partial w}{\partial z} = 0, \qquad \dfrac{\partial T}{\partial x} = 0$	Anode and cathode channel exit
$\dfrac{\partial u}{\partial y_{h_1^-}} = \varepsilon_{eff,GDL} \dfrac{\partial u}{\partial y_{h_1^+}}, \dfrac{\partial v}{\partial y_{h_1^-}} = \varepsilon_{eff,GDL} \dfrac{\partial v}{\partial y_{h_1^+}}, \dfrac{\partial w}{\partial y_{h_1^-}} = \varepsilon_{eff,GDL} \dfrac{\partial w}{\partial y_{h_1^+}}$	Gas channel and GDL interface
$\varepsilon_{eff,GDL} \dfrac{\partial u}{\partial y_{h_2^-}} = \varepsilon_{eff,CL} \dfrac{\partial u}{\partial y_{h_2^+}}, \varepsilon_{eff,GDL} \dfrac{\partial u}{\partial y_{h_2^-}} = \varepsilon_{eff,CL} \dfrac{\partial u}{\partial y_{h_2^+}}, \varepsilon_{eff,GDL} \dfrac{\partial u}{\partial y_{h_2^-}} = \varepsilon_{eff,CL} \dfrac{\partial u}{\partial y_{h_2^+}}$	GDL and catalyst layer interface
$u = v = w = Ci = 0$	Catalyst layer and membrane interface
$u = v = w = Ci = 0, T_{surface} = 353K$	Top wall of channel
$u = w = 0, T_{surface} = T_{wall}$	Bottom wall of channel
$\phi_{sol} = 0, \dfrac{\partial \phi_{mem}}{\partial y} = 0$	Anode bipolar
$\phi_{sol} = V_{cell}, \dfrac{\partial \phi_{mem}}{\partial y} = 0$	Cathode bipolar
$\dfrac{\partial \phi_{mem}}{\partial x} = 0, \dfrac{\partial \phi_{mem}}{\partial z} = 0, \dfrac{\partial \phi_{sol}}{\partial x} = 0, \dfrac{\partial \phi_{sol}}{\partial z} = 0$	External surfaces

Figure 3. Solution procedure

5. MODEL VALIDATION

To verify the model, numerical results of the base case were compared with the experimental data presented by Ticianelli et al. [13], as shown in Fig. 3a, and there was good agreement between them. Energy unit working conditions and geometric boundaries are given in Table 2. A completely humidified entrance condition is utilized for anode and cathode. The exchange current at anode and cathode can be portrayed by Tafel conditions [11].

Table 2. Geometrical parameters and operating conditions [13]

Parameter	Units	Value
Gas channel length	m	0.05
Gas channel width	m	0.001
Cell width	m	0.002
Gas diffusion layer thickness	m	0.00026
Catalyst layer thickness	m	0.0000129
Membrane thickness	m	0.00023
Cell temperature	K	353.15
Anode pressure	atm	3
Cathode pressure	atm	5

In this model, the organized meshes are utilized and in impetus layers where the electrochemical reactions occur, the lattices are smaller. In addition, a grid freedom test was executed and then, the ideal number of meshes was selected (Figure 4b-c). According to the results, 240000 and 480000 cells have approximately the same output; therefore, for short computation time and fast convergence, 240000 cells were chosen as the best and useful ones.

Figures 5 to 8 show O_2, H_2O, current density, and temperature distributions through the cell width for four cross-sections on the interface between cathode catalyst and membrane layer of 10, 20, 30, and 40 mm in the Z direction for the basic model. Figure 5 shows O_2 mass fractions for two voltages 0.4 and 0.6. It is shown that both trends for graphs are similar, but the value of 0.6 V is slightly more than 0.4 V. A declined process in the mass fraction from z=10 mm to z=40 mm demonstrates an increase in O_2 consumption. This increment causes greater water production for which Figure 6 serves as a clear verification. The current density distribution is presented in Figure 7. It is found that current density is higher at points below the side edges of channels. A temperature graph is observed in Figure 8. It is shown that high temperatures occur in the middle position of the cross line, since, based on Figure 6, the lowest H_2O mass fraction is at that point.
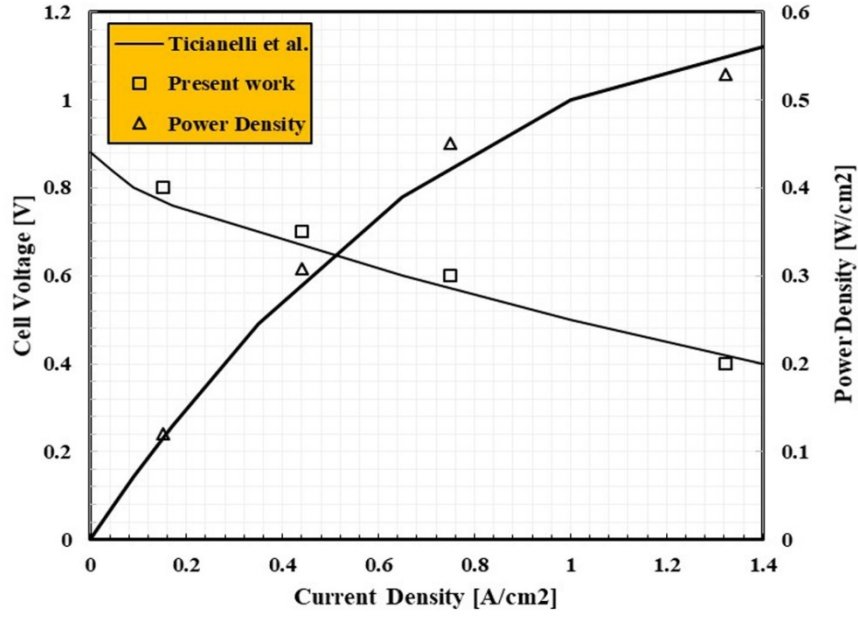
(a)
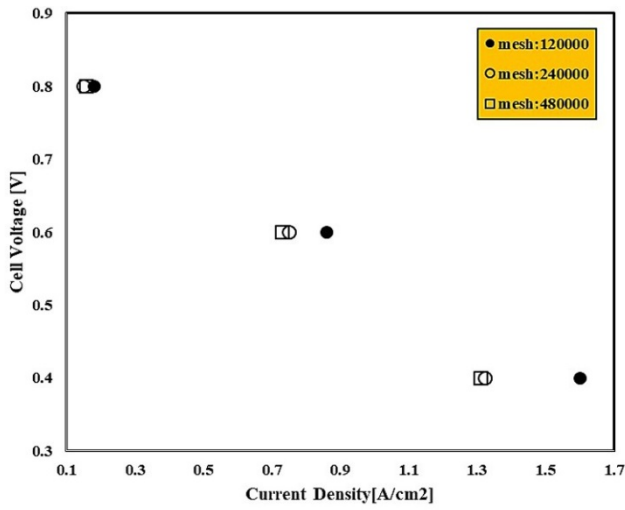
(b)
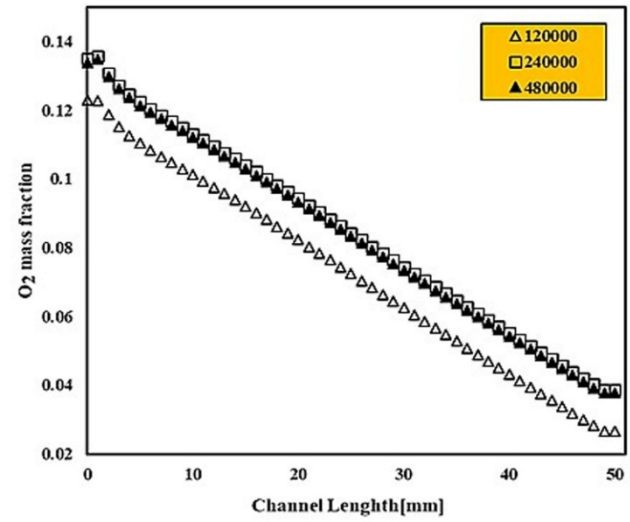
(c)

Figure 4. a) Comparison of experimental data; b) and c) grid independency
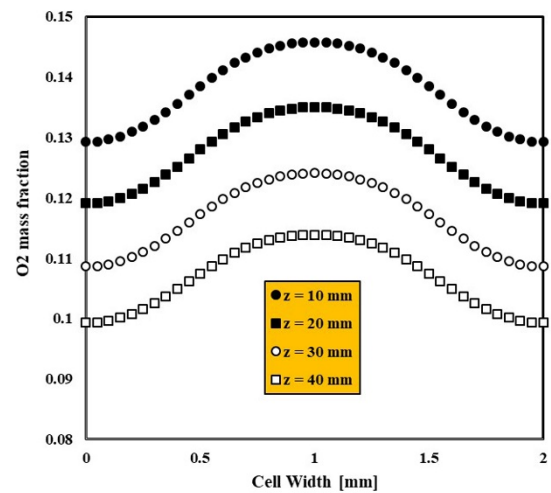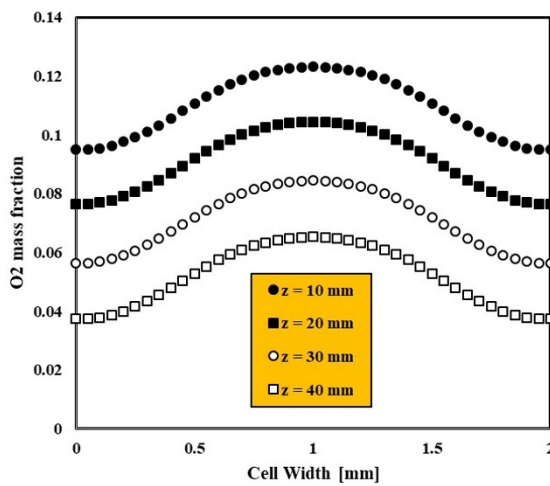
Figure 5. O_2 distribution in the width of the cell for four sections at V=0.4 [V] (Left) and V=0.6 [V] (Right)
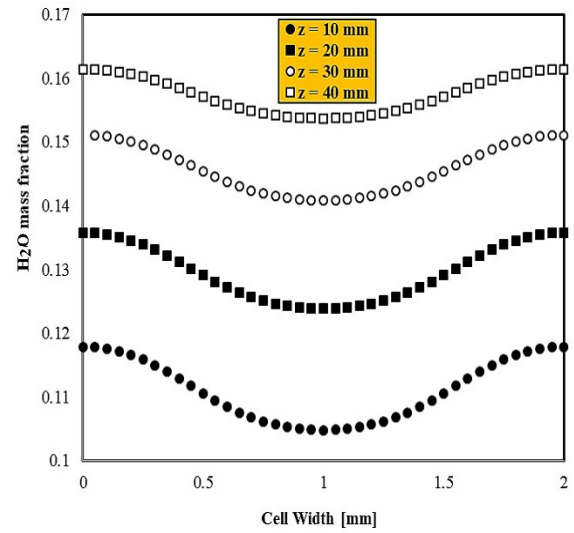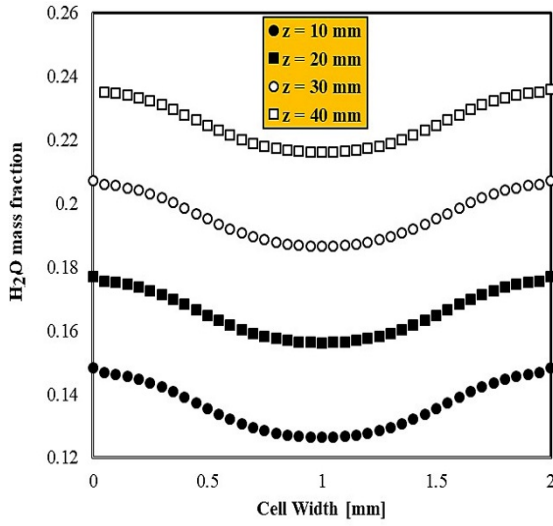
Figure 6. H_2O distribution in the width of the cell for four sections at V=0.4 [V] (Left) and V=0.6 [V] (Right)
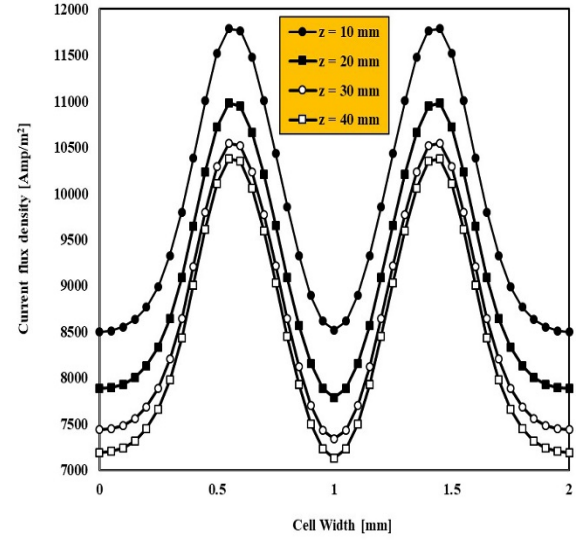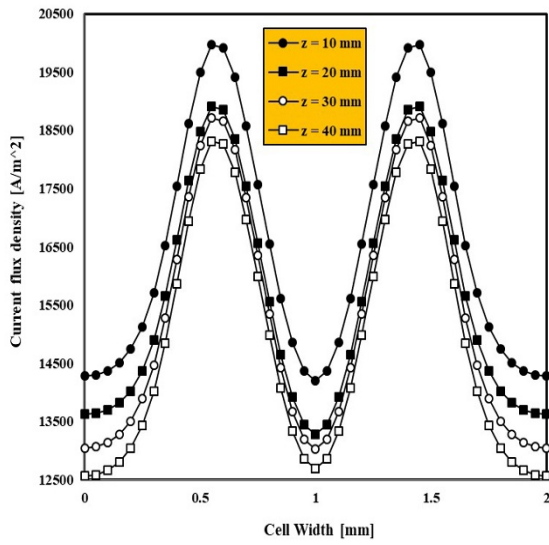
Figure 7. Current density distribution in the width of the cell for four sections at V=0.4 [V] (Left) and V=0.6 [V] (Right)
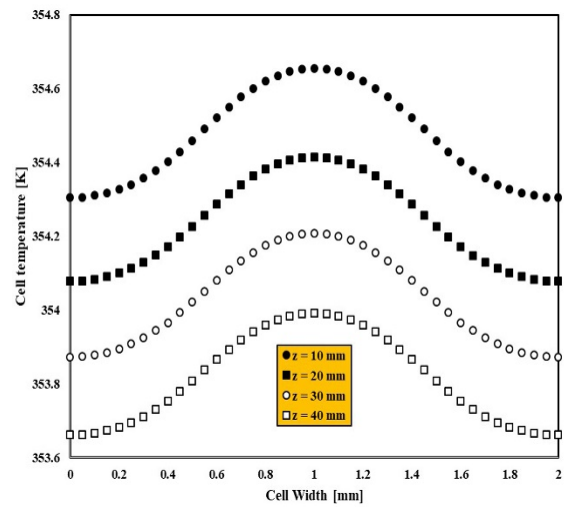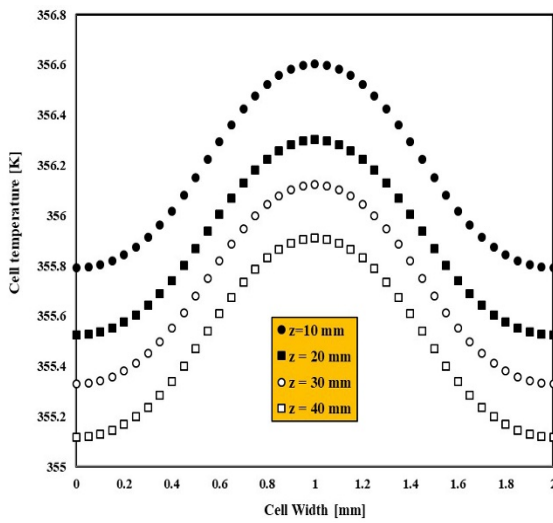
Figure 8. Temperature distribution in the width of the cell for four sections at V=0.4 [V] (Left) and V=0.6 [V] (Right)

5.1. Novel structure of gas channel

In this work, as the new model, a cylindrical fuel cell was simulated. Figure 9b shows a view of this geometry. Figure 10 shows the geometrical characteristic of the novel model. Key parameters such as O_2 and H_2O mass fraction, vathode over potential, temperature, and protonic conductivity were calculated and compared with those in the base model.
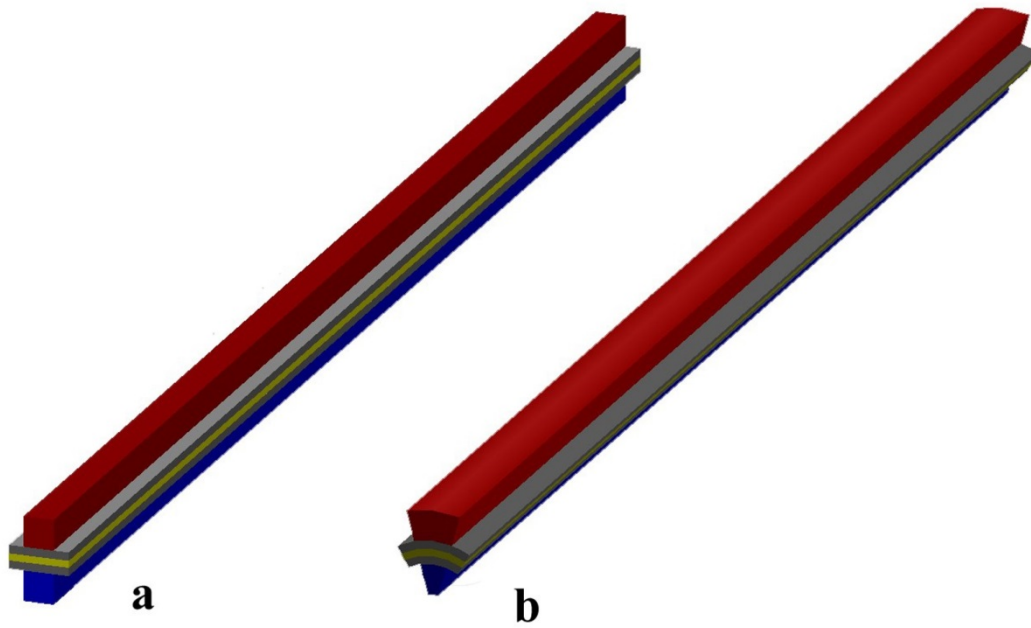
Figure 9. a) base model, b) Cylindrical shape
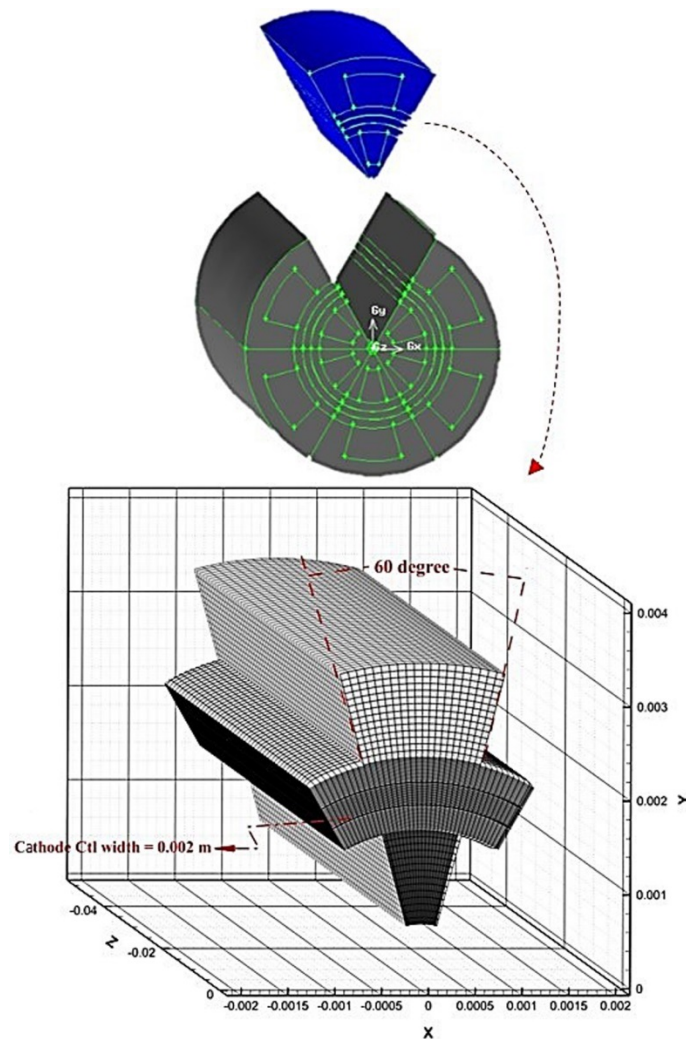
Figure 10. Geometric characteristics of the new model

6. RESULTS AND DISCUSSION

Figures 11 and 12 compare the current density with FC Power for both models, respectively. The cylindrical model operates outperforms the base model. In Table 3, the geometrical conditions of the base and proposed models are presented. Since the cross-section area of the cathode gas channel in the

proposed model is less than that in the base one, according to the continuity equation, the velocity of the incoming gas flow will be higher. In doing so, diffusion of oxygen to the electrochemical reaction area is enhanced. Consequently, the new model outperforms the base model. Figures 13 to 16 show the distribution graph and contour of H_2O mass fraction for both models. Water production in the novel model is greater than that in the base model. Figures 17 to 20 are about O_2 mass fraction. It is observed that O_2 consumption increases through the channel from the entrance to the exit point in the base model and it increases to a greater degree in the middle points of the channel.
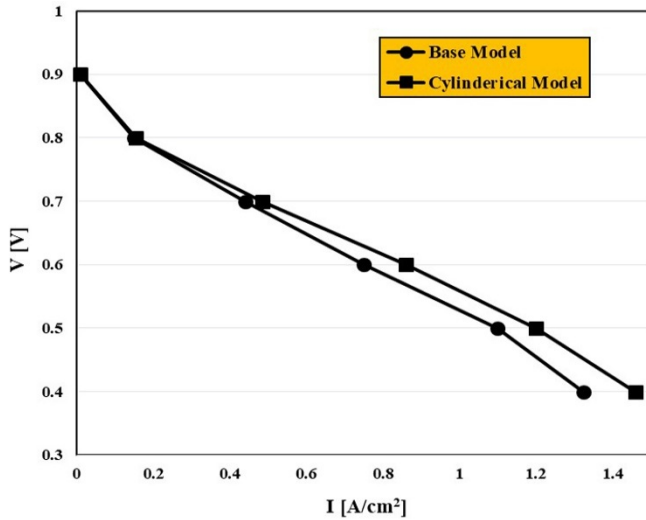
Figure 11. Current density for both models
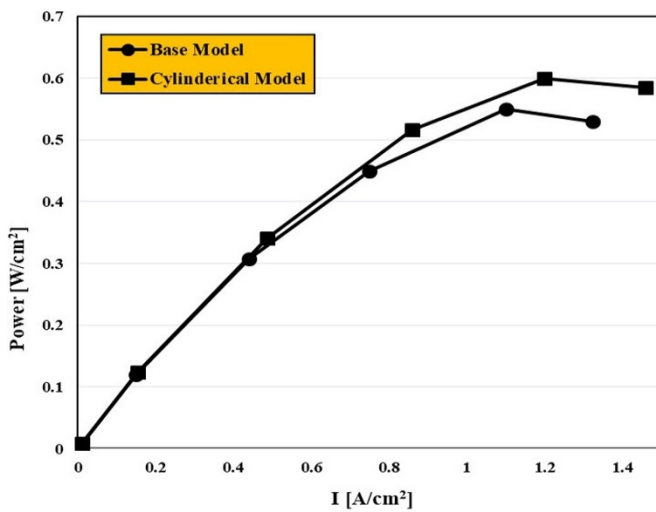
Figure 12. Fuel cell power for both models

Table 3. Geometrical condition of the novel model

	Units	Base model	Proposed model
Cathode gas channel area	m^2	10^{-6}	5.95×10^{-7}
Anode gas channel area	m^2	10^{-6}	2.12×10^{-6}
Reaction area	m^2	10^{-4}	10^{-4}
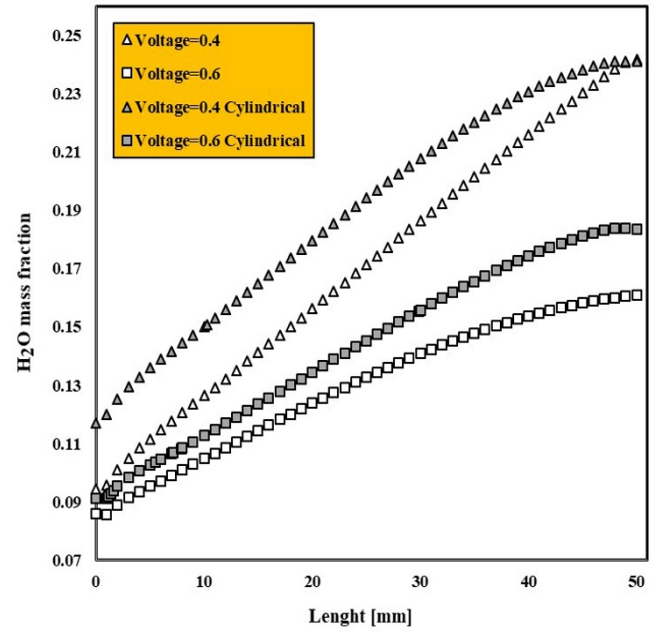
Figure 13. H_2O mass fraction through cathode catalyst layer for both models
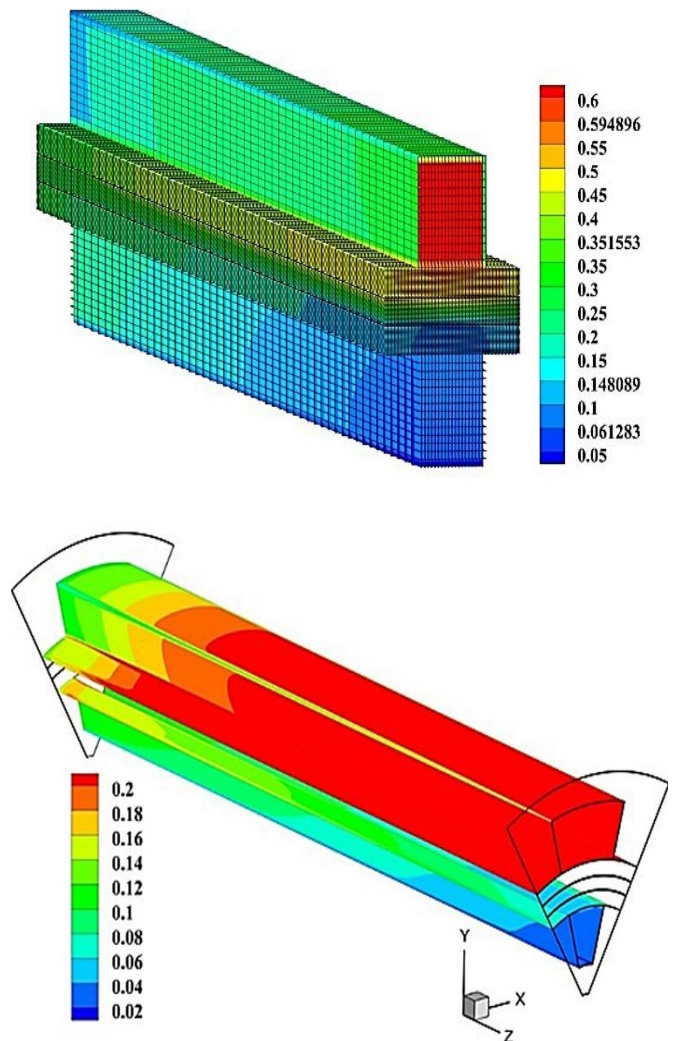
Figure 14. 3D H_2O contour for V=0.4 [V]: The base model (top) and the proposed model (bottom)

Base model. V = 0.4 [V]

Base model. V= 0.6 [V]

Cylindrical model. V = 0.4 [V]

Cylindrical model. V= 0.6 [V]
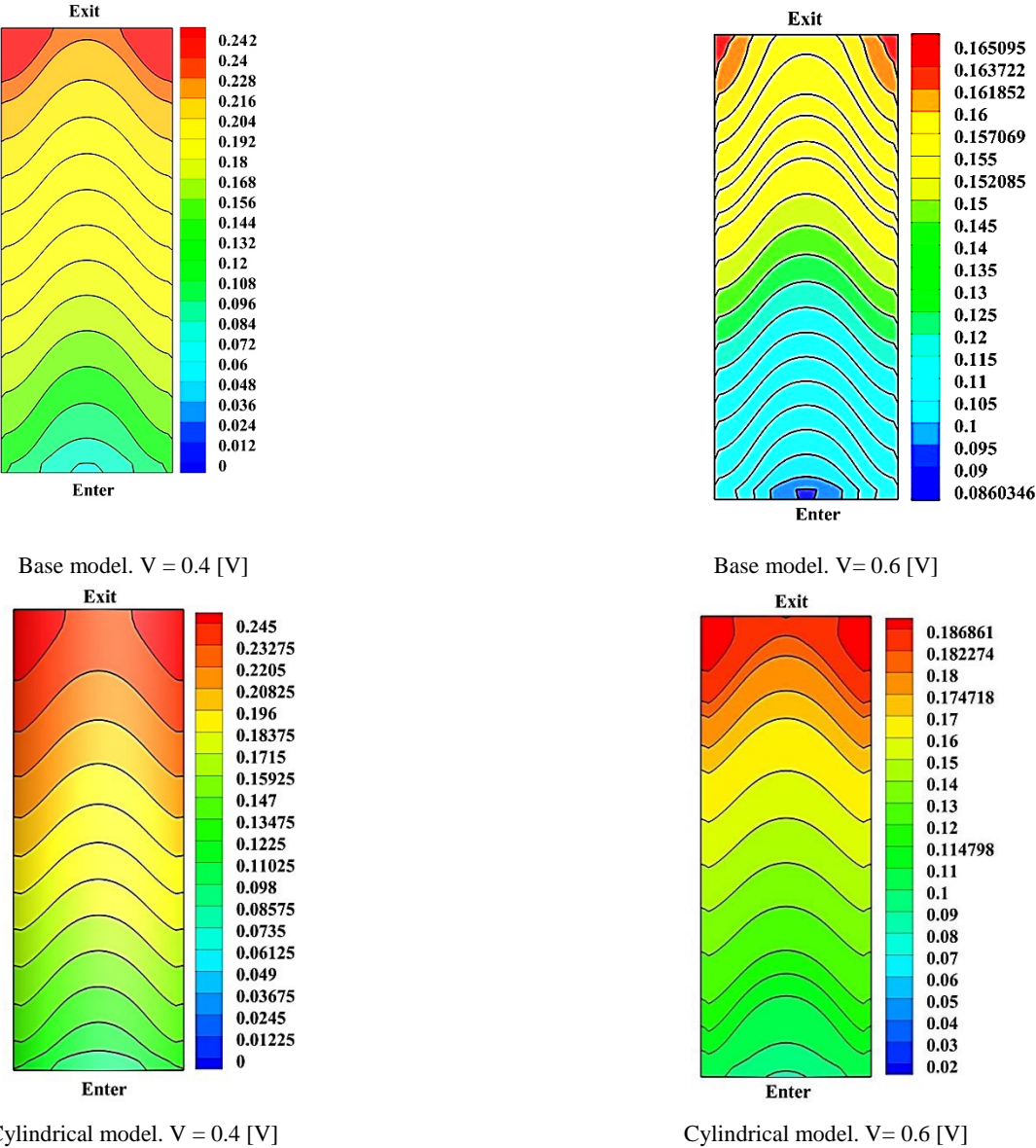
Figure 15. H_2O mass fraction contours through the cathode catalyst layer for both models

Cylindrical model. V= 0.4 [V]

Cylindrical model. V= 0.6 [V]
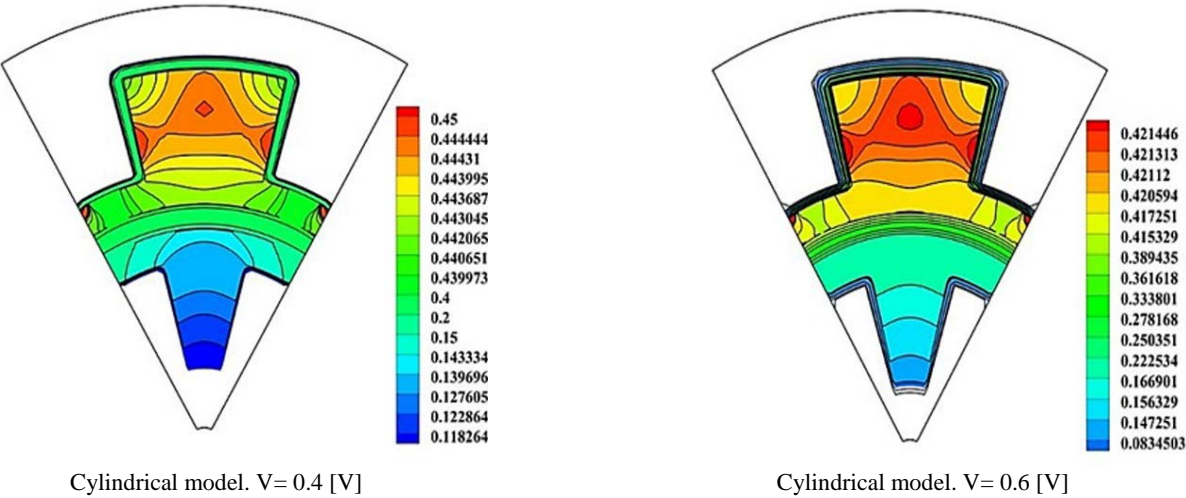
Figure 16. H_2O mass fraction contours for the cylindrical models at z = 25 mm
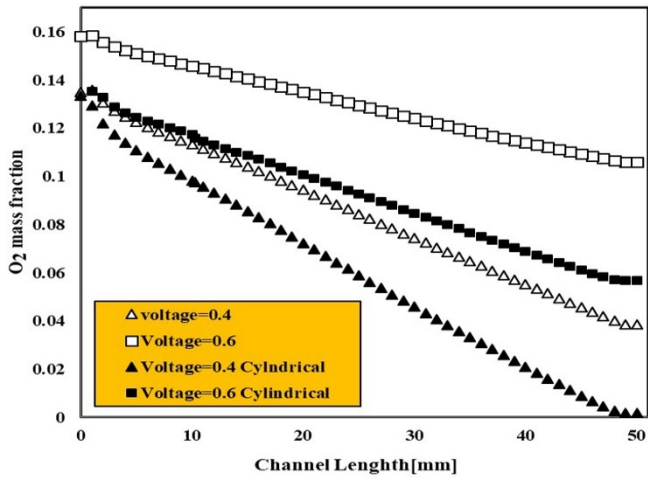
Figure 17. O_2 mass fraction through the cathode catalyst layer for both models

Figure 20 shows the contour of O_2 mass fraction for both voltages in a cross-section at z = 25 mm. It is observed that O_2 consumption mostly occurs near the membrane layer. In the same procedure, Figure 16 shows the H_2O mass fraction through the cell width.

Figure 21 is a temperature contour for four cross-sections in the cylindrical model in the case of both voltages. Additionally, a contour is shown at z = 25 mm. As mentioned before, the lower the water mass fraction, the higher the temperature, which is in the middle of the cell as shown in the contours. In addition, Figure 22 is a line graph for temperature through the cell length. According to this figure, the temperature at low voltage is greater than that at high voltage and its value is higher in the new cylindrical model.

Base model. V= 0.4 [V]

Base model. V= 0.6 [V]

Cylindrical model. V= 0.4 [V]

Cylindrical model. V= 0.6 [V]
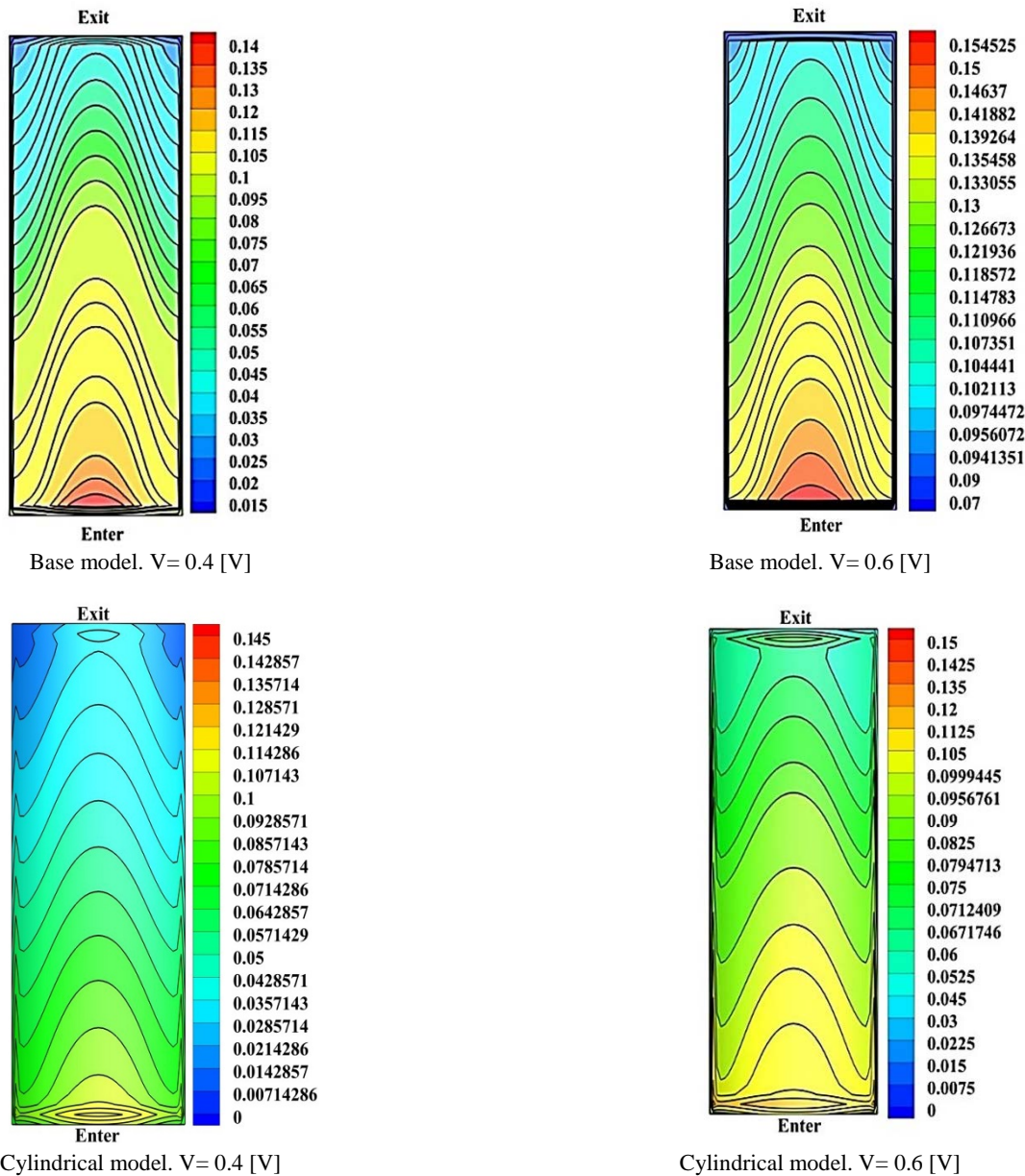
Figure 18. O_2 mass fraction contours through the cathode catalyst layer for both models
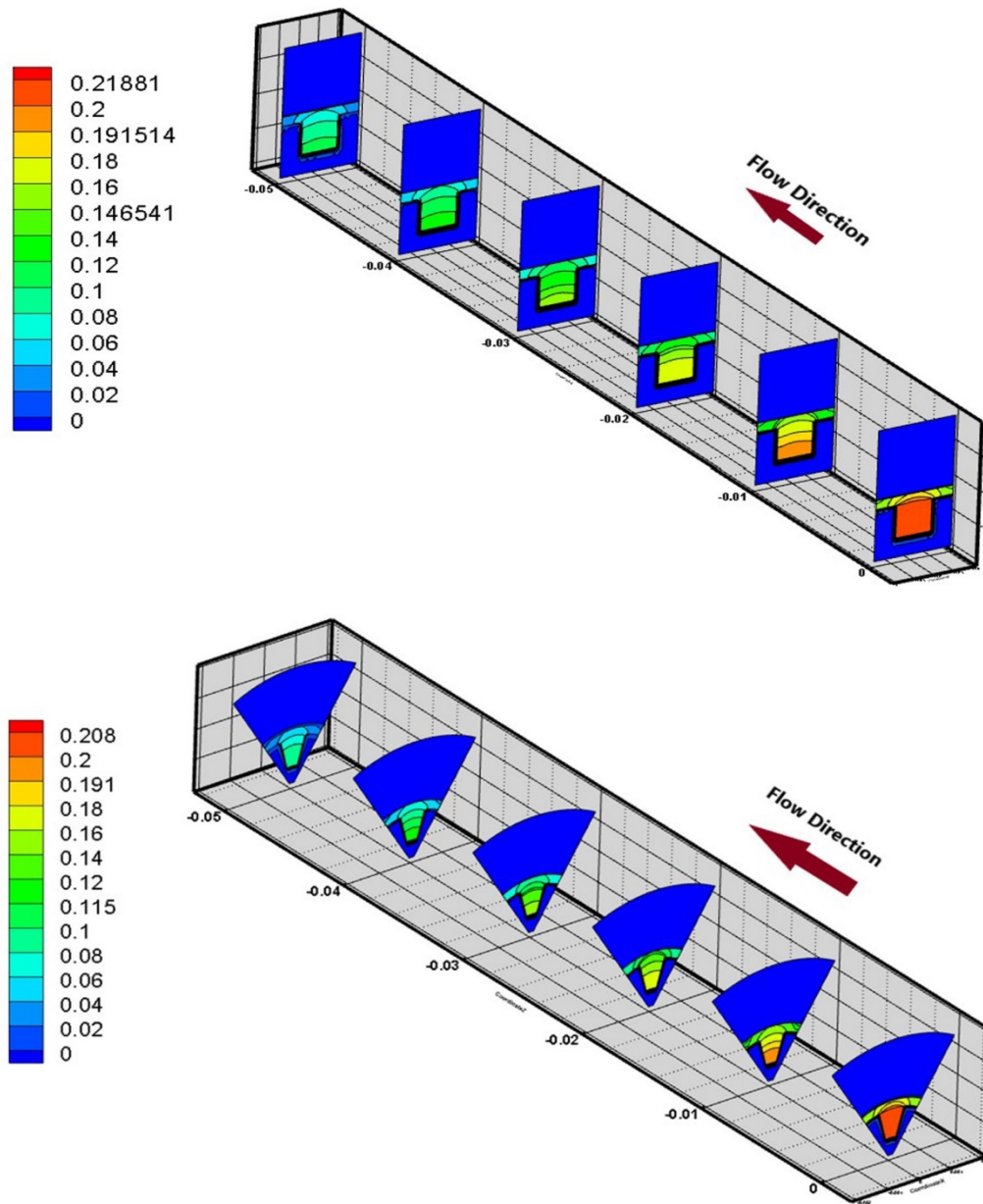
Figure 19. 3D O_2 contour for both model for V=0.4 [V]

Cylindrical model. V= 0.4 [V]   Cylindrical model. V= 0.6 [V]
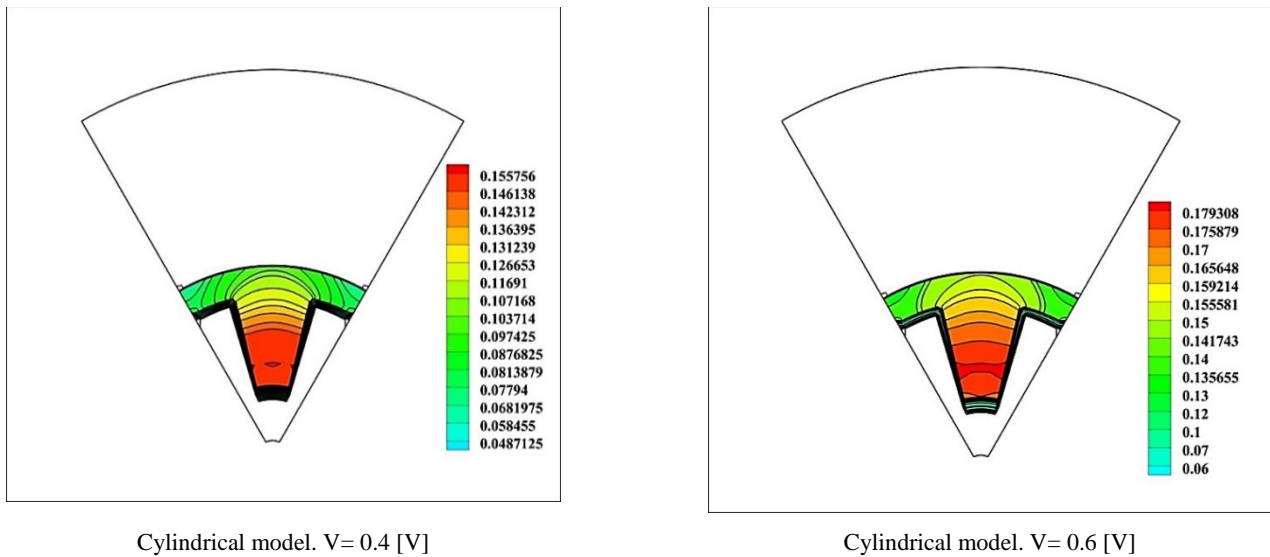
Figure 20. O_2 mass fraction contours for cylindrical models at z = 25 mm
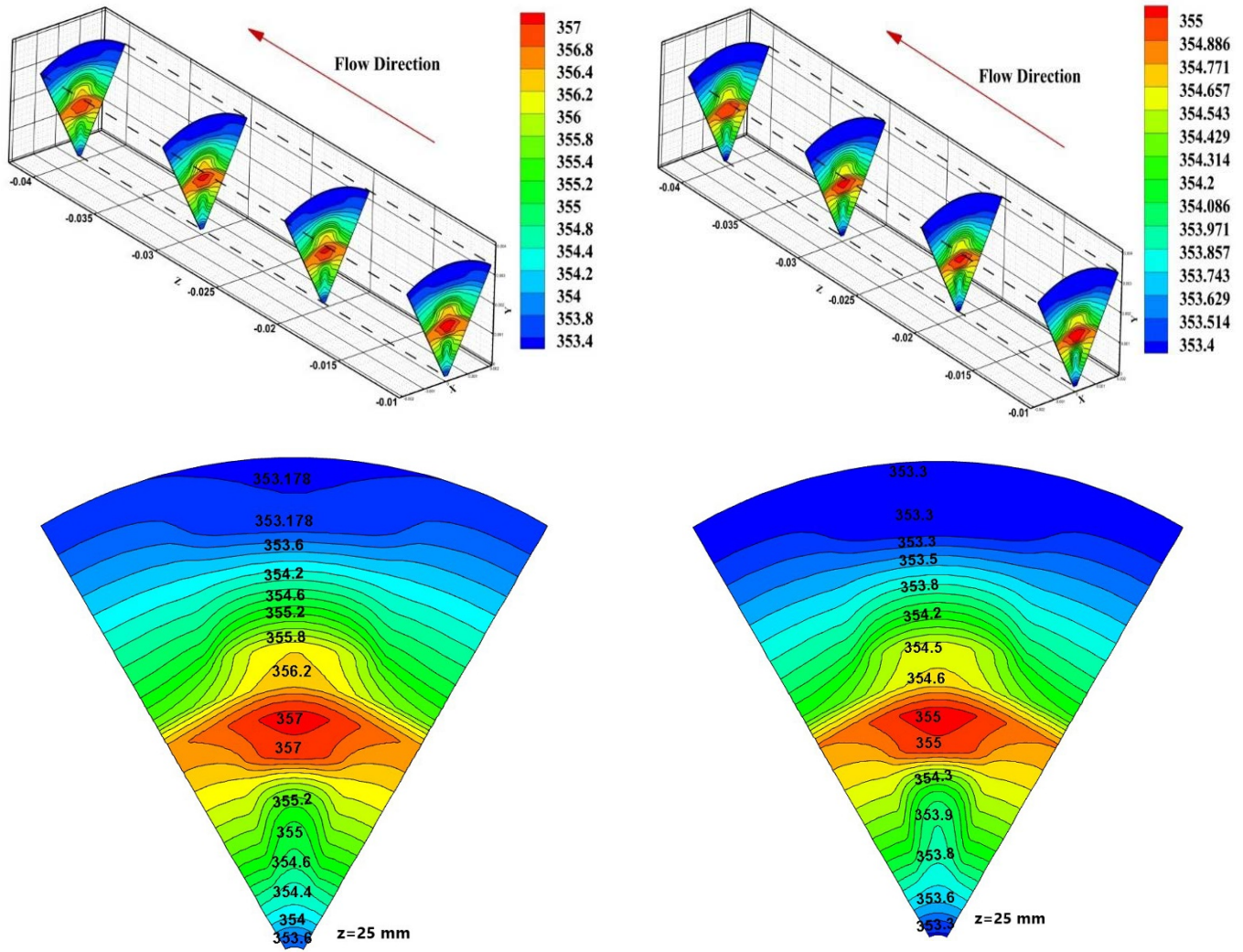
Figure 21. Temperature contours for cylindrical models at V= 0.4 [V] (Left) and V= 0.6 [V] (Right)
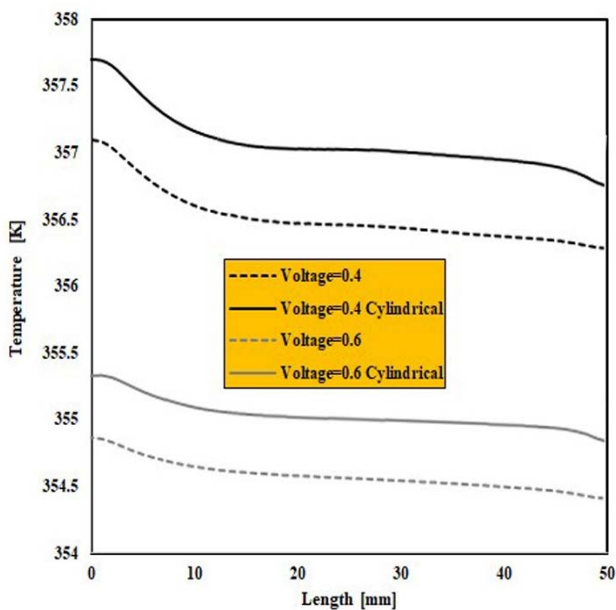
Figure 22. Cell temperature through the cathode catalyst layer for both models
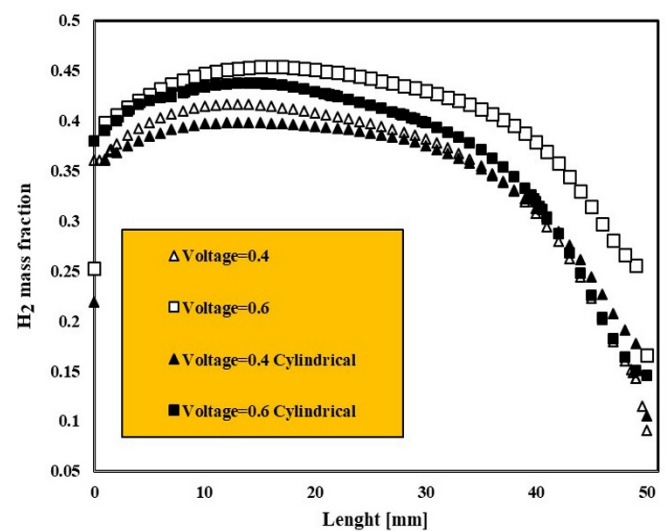
Figure 23. Anode H_2 mass fraction for both models

Figure 23 shows H_2 mass fractions for the anode zone. This figure certifies previous tips.

Cathode Protonic Conductivity (CPC) is an important parameter of water distribution, as shown in Figure 24. Cathode Over Potential (COP) parameter considerably corresponds to the amount of O_2. The less oxygen there is, the greater COP factor will be, as shown in Figure 25.
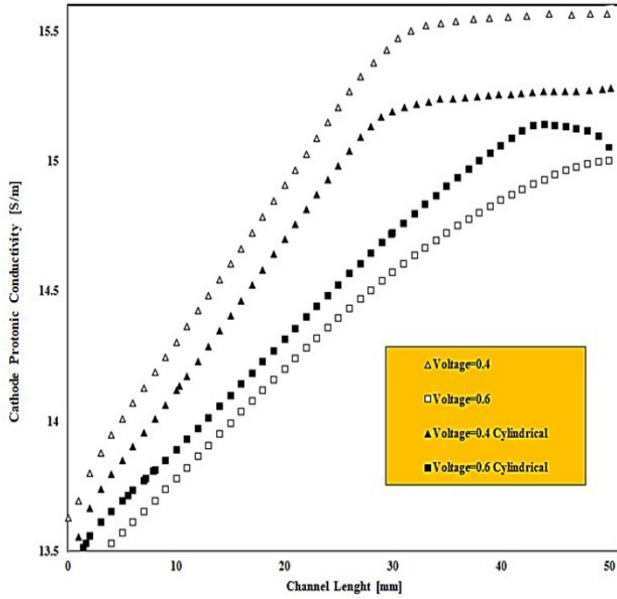
Figure 24. CPC parameter for both models
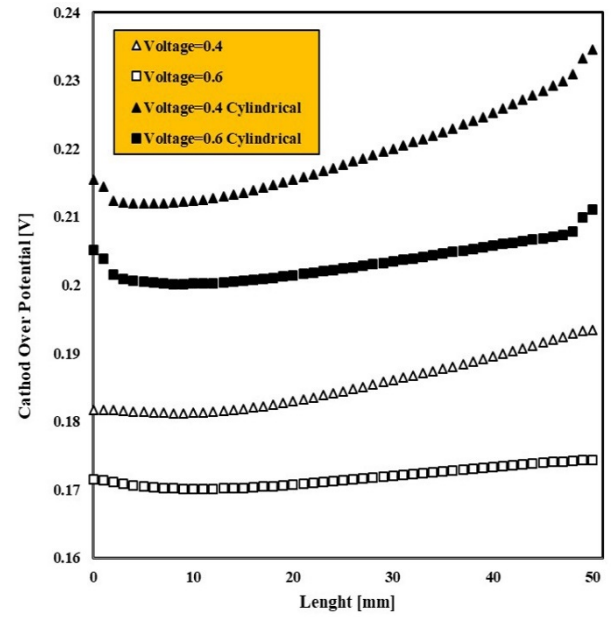
Figure 25. COP parameter for both models

As shown in Figure 25, it is found that the COP factor at low voltage is quite significant and the cylindrical configuration has a higher value for COP. Figures 26 and 27 show the current density distribution graph through the cell length and

contours related to this parameter for both models. It is found that the novel model is endowed with higher efficiency, meaning that this model has greater current density and significant performance.
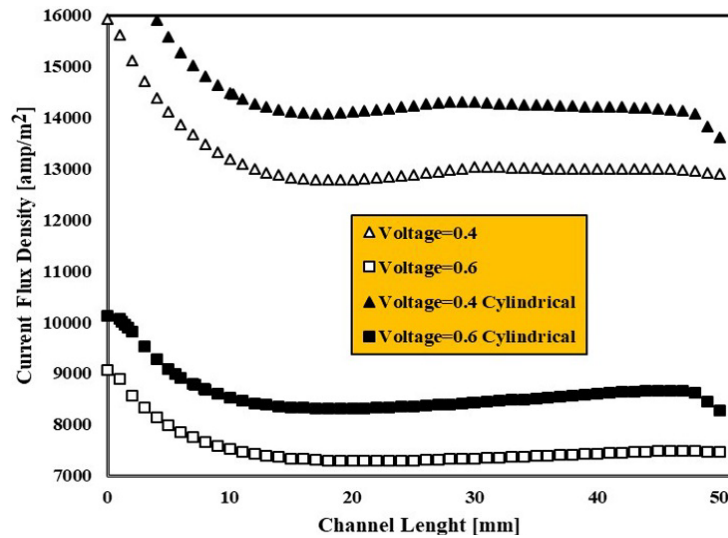
Figure 26. Current density for both models

Base model. V= 0.4 [V]

Base model. V= 0.6 [V]
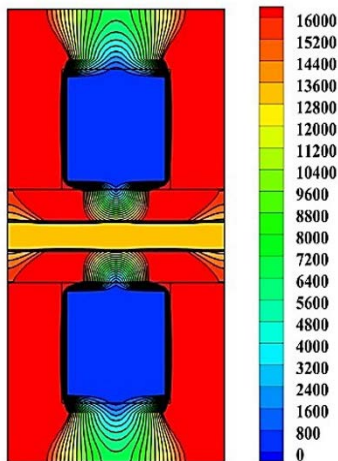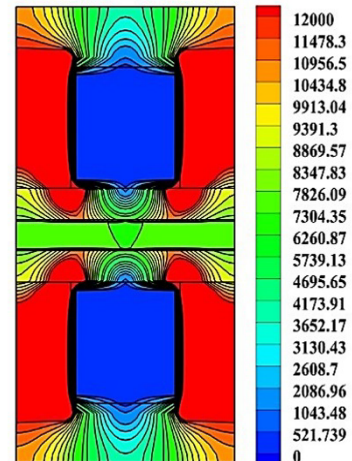
Cylindrical model. V= 0.4 [V]   Cylindrical model. V= 0.6 [V]
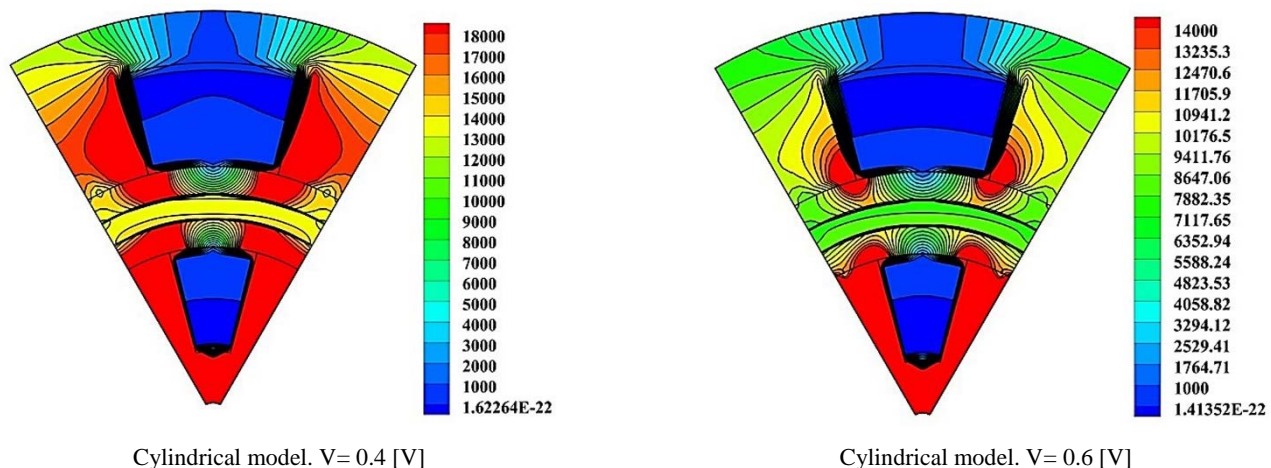
Figure 27. Current density contours for both models

7. CONCLUSIONS

In the present work, a base model and the novel geometry of PEM fuel cells were numerically simulated. Finite Volume Method (FVM) was used for discretizing the governing equations. Validation of obtained numerical results was done and good agreement was concluded. The results showed that the new proposed model extracted higher electrical current density (10.35 %) than the base model at V=0.4 [V], and the average increment in generated power was about 8 %, which could be a considerable value in a stack of cells. Moreover, the oxygen and hydrogen consumption and consequently, water production and heat generation were quite high under the new model. In addition, it can be mentioned that the COP factor at low voltage was significantly high and the cylindrical configuration had a higher value for COP.

8. FUTURE RECOMMENDATION

As a future recommendation, some points can be represented as follows:

- Changing the cathode and anode zones and studying the corresponding effect on cell performance.
- Considering the same channel cross-section for both configurations instead of the same reaction area and comparing the results with each other.
- Utilizing ethane, methane, and propane as fuels for cell and investigating the effect of C presence in reactions.

9. ACKNOWLEDGEMENT

REFERENCES

1. Fuel cells, Editor: Kreuer, K.-D., Springer, New York, (2013). (https://doi.org/10.1007/978-1-4614-5785-5).

2. Bernardi, D.M. and Verbrugge, M.W., "Mathematical model of a gas discussion electrode bonded to a polymer electrolyte", *American Institute of Chemical Engineers Journal*, Vol. 37, No. 8, (1991), 1151-1163. (https://doi.org/10.1002/aic.690370805).

3. Bernardi, D.M. and Verbrugge, M.W., "A mathematical model of the solid-polymer-electrolyte fuel cell", *Journal of Electrochemical Society*, Vol. 139, No. 9, (1992), 2477-2491. (https://doi.org/10.1149/1.2221251).

4. Fuller, T.F. and Newman, J., "Water and thermal management in solid-polymer-electrolyte fuel cells", *Journal of Electrochemical Society*,

5. Nguyen, T.V. and White, R.E., "Water and heat management model for proton-exchange-membrane fuel cells", *Journal of the Electrochemical Society*, Vol. 140, (1993), 2178-2186. (https://doi.org/10.1149/1.2220792).

6. Dutta, S., Shimpalee, S. and Van Zee, J.W., "Three-dimensional numerical simulation of straight channel PEM fuel cells", *Journal of Applied Electrochemistry*, Vol. 30, (2000), 135-146. (https://doi.org/10.1023/a:1003964201327).

7. Berning, T. and Djilali, N., "Three-dimensional computational analysis of transport phenomena in a PEM fuel cell: A parametric study", *Journal of Power Source*, Vol. 124, (2003), 440-452. (https://doi.org/10.1016/s0378-7753(03)00816-4).

8. Yang, T., Park, G., Pugazhendhi, P., Lee, W. and Kim, C.S., "Performance improvement of electrode for polymer electrolyte membrane fuel cell", *Korean Journal of Chemical Engineering*, Vol. 19, No. 3, (2002), 417-420. (https://doi.org/10.1007/bf02697149).

9. Molaeimanesh, G.R. and Akbari, M.H., "Water droplet dynamic behavior during removal from a proton exchange membrane fuel cell gas diffusion layer by Lattice-Boltzmann method", *Korean Journal of Chemical Engineering*, Vol. 31, No. 4, (2014), 598-610. (https://doi.org/10.1007/s11814-013-0282-6).

10. Carral, C. and Mélé, P., "A numerical analysis of PEMFC stack assembly through a 3DFinite element model", *International Journal of Hydrogen Energy*, Vol. 39, No. 9, (2014), 4516-4530. (https://doi.org/10.1016/j.ijhydene.2014.01.036).

11. Ahmadi, N., Dadvand, A., Rezazadeh, S. and Mirzaee, I., "Analysis of the operating pressure and GDL geometrical configuration effect on PEM fuel cell performance", *Journal of the Brazilian Society of Mechanical Sciences and Engineering*, Vol. 38, (2016), 2311-2325. (https://doi.org/10.1007/s40430-016-0548-0).

12. Rezazadeh, S. and Ahmadi, N., "Numerical investigation of gas channel shape effect on proton exchange membrane fuel cell performance", *Journal of the Brazilian Society of Mechanical Sciences and Engineering*, Vol. 37, (2017), 789-802. (https://doi.org/10.1007/s40430-014-0209-0).

13. Ticianelli, E.A., Derouin, C.R., Redondo, A. and Srinivasan, S., "Methods to advance technology of proton exchange membrane fuel cell", *Journal of The Electrochemical Society*, Vol. 135, No. 9, (1988), 2209-2214. (https://doi.org/10.1149/1.2096240).

14. Ahmadi, N., Pourmahmoud, N., Mirzaee, I. and Rezazadeh, S., "Three-dimensional computational fluid dynamic study of the effect of the different channel and shoulder geometries on cell performance", *Australian Journal of Basic and Applied Sciences*, Vol. 5, No. 12, (2011), 541-556. (http://www.ajbasweb.com/old/ajbas/2011/December-2011/541-556.pdf).

15. Ahmadi, N., Rezazadeh, S., Mirzaee, I., and Pourmahmoud, N., "Three-dimensional computational fluid dynamic analysis of the conventional PEM fuel cell and investigation of prominent gas diffusion layers effect", *Journal of Mechanical Science and Technology*, Vol. 26, No. 8, (2012), 2247-2257. (https://doi.org/10.1007/s12206-012-0606-1).

16. Lin, W., Husar, A., Zhou, T. and Liu, H., "A parametric study of PEM fuel cell performances", *International Journal of Hydrogen Energy*,

Vol. 28, No. 11, (2003), 1263-1272. (https://doi.org/10.1016/s0360-3199(02)00284-7).

17. Ahmadi, N., Rezazadeh, S. and Mirzaee, I., "Study the effect of various operating parameters of proton exchange membrane", *Periodica Polytechnica. Chemical Engineering*, Vol. 59, No. 3, (2015), 221-235. (https://doi.org/10.3311/ppch.7577).

18. Ahmadi, N., Rezazadeh, S., Dadvand, A. and Mirzaee, I., "Numerical investigation of the effect of gas diffusion layer with semicircular prominences on polymer exchange membrane fuel cell performance and species distribution", *Journal of Renewable Energy and Environment (JREE)*, Vol. 2, No. 2, (2015), 36-46. (https://doi.org/10.30501/JREE.2015.70069).

19. Ahmadi, N., Rezazadeh, S., Dadvand, A. and Mirzaee, I., "Modelling of gas transport in proton exchange membrane fuel cells", *Institution of Civil Engineers*, Vol. 170, No. 4, (2017), 163-179. (https://doi.org/10.1680/jener.15.00015).

20. Ahmadi, N., Dadvand, A., Rezazadeh, S. and Mirzaee, I., "Modeling of polymer electrolyte membrane fuel cell with circular and elliptical cross-section gas channels: A novel procedure", *International Journal of Energy Research*, Wiley, (2018). (https://doi.org/10.1002/er.4069).

21. Pashaee Golmarz, T., Rezazadeh, S. and Bagherzadeh, N., "Numerical study of curved-shape channel effect on performance and distribution of species in a proton-exchange membrane fuel cell: Novel structure", *Journal of Renewable Energy and Environment (JREE)*, Vol. 5, No. 2, (2018), 10-21. (https://doi.org/10.30501/JREE.2018.88506).

22. Zunyan, H., Liangfei, X., Jianqiu, L., Qing, W., Yangbin, Sh., Xiaojing, Ch., Wei, D. and Minggao, O., "Mechanistic insight into the accelerated decay of fuel cells from catalyst-layer structural failure", *Energy Conversion, and Management*, Vol. 227, (2021), 113568. (https://doi.org/10.1016/j.enconman.2020.113568).

23. Olabi, A., Wilberforce, T. and Abdelkareem, M., "Fuel cell application in the automotive industry and future perspective", *Energy*, Vol. 214, (2021), 118955. (https://doi.org/10.1016/j.energy.2020.118955).

24. Xun, Zh., Yuan, Zh., Ding-Ding, Y., Rong, Ch., Tong, Zh. and Qiang, L., "Discrete-holes film fueling anode heads for high performance air-breathing microfluidic fuel cell", *Journal of Power Sources*, Vol. 482, (2021), 228966. (https://doi.org/10.1016/j.jpowsour.2020.228966).

25. Chen, K., Laghrouche, S. and Djerdir, A., "Performance analysis of PEM fuel cell in the mobile application under real traffic and environmental conditions", *Energy Conversion and Management*, Vol. 227, (2021), 113602. (https://doi.org/10.1016/j.enconman.2020.113602).

A Factorial Study of the Effect of Rhamnolipid and Stirring on the Electricity Production, Desalination, and Wastewater Treatment Efficiencies of a Five-Chamber Microbial Desalination Cell

Abubakari Zarouk Imoro[a*], Moses Mensah[b], Richard Buamah[c]

[a] Department of Environment, Water and Waste Engineering, University for Development Studies, P. O. Box: 1882, Nyankpala, Ghana.
[b] School of Graduate Studies, Regional Maritime University, P. O. Box: GP 1115, Accra, Ghana
[c] Department of Civil Engineering, Kwame Nkrumah University of Science and Technology, P. M. B. Kumasi, Ghana.

ABSTRACT

This study was conducted to improve the voltage production, desalination, and COD removal efficiencies of a five-chamber Microbial Desalination Cell (MDC). To do this, rhamnolipid was added to anolytes only and catholytes stirred to determine the effects of these factors on the MDC activity. This was followed by a factorial study to investigate the effects of the interactions of rhamnolipid and stirring on the voltage production, desalination, and COD removal efficiencies of the MDC. Increasing the concentration of rhamnolipid to 240 mg/L improved the peak voltage produced from 164.50 ± 0.11 to 623.70 ± 1.32 mV. Also, the desalination efficiency increased from 20.16 ± 1.97 % when no rhamnolipid was added to 24.89 ± 0.50 % at a rhamnolipid concentration of 240 mg/L, and COD removal efficiency increased from 48.74 ± 8.06 % to 64.17 ± 5.00 % at a rhamnolipid concentration of 400 mg/L. In the stirring experiments, increasing the number of stirring events increased peak voltage from 164.50 ± 0.11 to 567.27 ± 18.06 mV. Similarly, desalination and COD removal efficiencies increased from 20.16 ± 1.97 % and 48.74 ± 8.06 % to 24.26 ± 0.97 % and 50.23 ± 1.60 %, respectively, when the number of stirring events was more than twice a day. In the factorial study, voltage production, desalination, and COD removal efficiencies were 647.07 mV, 25.50 %, and 68.15 %, respectively. However, the effect of the interaction between rhamnolipid and stirring was found to be insignificant ($p > 0.05$). Thus, the addition of only rhamnolipid or the stirring of catholytes only can improve the performance of the five-chamber MDC.

1. INTRODUCTION

The improvement of the electricity generation capacity, desalination, and wastewater treatment efficiencies of the Microbial Desalination Cell (MDC) is necessary for its scale-up [1, 2]. To this end, several interventions including those investigated by Zhang et al. [3] and Morel et al. [4] have been made, in which ion-exchange resins were employed to improve the desalination efficiency of MDCs. Other researchers have considered modifying the conventional three-chamber MDC design to improve the performance and flexibility of the technology [5-7].

Many attempts have been made to use relatively inexpensive catholytes [8, 9] and anolytes [10, 11] to make the technology affordable for scale-up. These attempts encapsulate the use of wastewaters as anolytes [9, 10] and tap water as catholytes [8, 9]. Also, other researchers have used biocathodes [9, 12, 13] as a relatively cheaper and more environmentally friendly option. However, affordability should not compromise electricity generation, desalination, and wastewater treatment

efficiencies of MDCs and MFCs. Thus, Wen et al. [14] recommended adding rhamnolipid to anolytes as a measure to increase the electricity generation capacity of MFCs. Biosurfactants including rhamnolipid are microbial products that can reduce surface tension and facilitate microbial mineralization of substrates [15]. Besides, rhamnolipid can reduce the resistance of bacteria cell membranes to electron transfer outside cells, thus supporting electricity generation in BES [14].

In another study, Rismani-Yazdi et al. [16] reported that the stirring/aeration of catholytes of MFCs was a good strategy for reducing mass transport losses in the cathode chamber of this class of bioelectrochemical system. The reduction of mass transport losses is necessary for increasing the quantity of electricity produced by BES. Also, it has been reported that stirring (turbulence in water) increases the concentration of oxygen in water [17] and this is necessary to ensure the efficient operation of MDCs that rely on oxygen as a terminal electron acceptor [9].

Given the possibilities of rhamnolipid and stirring to increase the voltage production, desalination, and COD removal efficiencies of MDCs, we investigated the effect of rhamnolipid and stirring on these parameters associated with a

*Corresponding Author's Email: zaroukimoro@yahoo.com (A.Z. Imoro)
  URL: http://www.jree.ir/article_126862.html

five-chamber microbial desalination cell. Also, the effect of the interaction between rhamnolipid and stirring on the electricity generation, desalination, and COD removal efficiencies of the MDC was investigated using a 2^2 factorial design. Factorial designs create protocols that allow for several factors to vary at different levels to produce measurable effects in responses [18]. The presence or absence of significant interaction effects is realized when factors are combined and examined together [18]. Hence, the factorial design was used in this study.

2. MATERIALS AND METHOD

2.1. MDC construction

The MDC studied in this research was carved from polyoxymethylene cylinders and supported with cylindrical gaskets (Figure 1). Its compartments were held together with stainless steel bolts and nuts. Anode and cathode had empty bed volumes of 230 cm^3 each, while the desalination chamber had a volume of 77 cm^3. The anode chamber was separated from the desalination chamber by anion exchange membrane (AEM, Membrane International, New Jersey, USA) and the Cathode, Cation Exchange Membrane (CEM, Membrane International, New Jersey, USA). The cathode chamber roof of the MDC had a 4 cm × 6 cm portion cut opened to make room for the aeration and stirring of the water catholyte. Two additional chambers (neutralization chambers), i.e., one adjacent to the anode chamber (N_A) and the other adjacent to the cathode chamber (N_C), were added to create a five-chamber MDC. The neutralization chambers had internal volumes of 150 cm^3 each. The neutralization chamber adjacent to the end of the anode was separated by a CEM, while that to the end of the cathode was separated by an AEM. The anode was a carbon fiber-fill material (0.984" brush part, 400,000 tips per square inch, Mill-Rose, Ohio, USA) and the cathode, a cloth gas diffusion electrode (fuel cell store, New York, USA). The objective of the neutralization chambers is to hold water that will dilute the concentrations of H$^+$ and OH$^-$ built-up in anolytes and catholytes over the course of experiments. This was the pH control measure employed in this study. In an earlier study, a two-chamber tubular MDC was used for pH control [19].
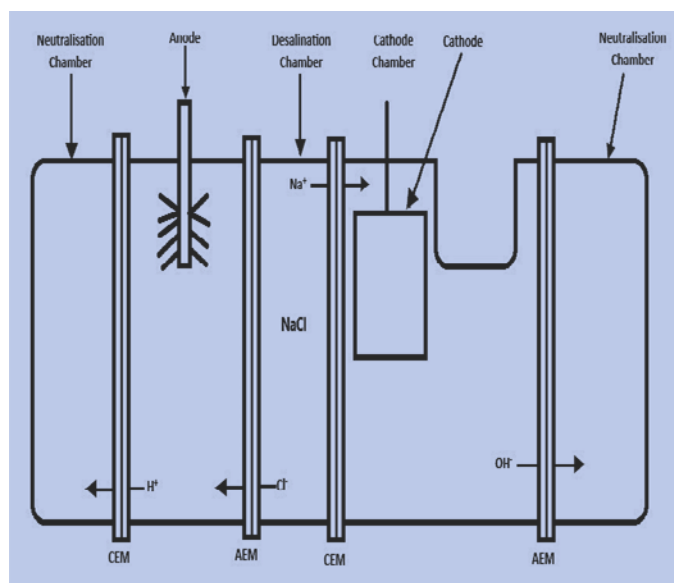

Figure 1. Schematic of the five-chamber microbial desalination cell (FCMDC)

2.2. Medium

The anolyte of the five-chamber MDC contained 3 g/L sodium acetate in 200 ml wastewater (filtrate of cow dung and rumen contents mixed in distilled water) supplemented with 20 ml of mineral solution (5 g/l NH$_4$Cl and 2.5/l NaCl). The initial COD concentration of the simulated wastewater was 645.00 ± 2.30 mg/L with a pH of 7.08 ± 0.02 and electrical conductivity of $2.37 \times 10^{-3} \pm 0.03$ mS/cm. A 220 ml tap water with a pH of 7.11 ± 0.09 and electrical conductivity of 1.01 ± 0.02 mS/cm was used as catholyte. Tap water was used as catholyte because it is a more environmentally friendly option. The neutralization chambers contained 100 ml of each of distilled water (pH, 7.04), while the desalination chamber contained 75 ml of 35 g/l NaCl solution. Rhamnolipid used was 90 % pure (AGAE Technologies LLC, Oregon, USA) and dissolved in distilled water at concentrations of 80, 160, 240, 320, and 400 mg/L.

2.3. Experimentation, analysis, and calculations

The anolyte of the MDC was inoculated with pre-acclimated bacteria, as described by Cao et a. [20]. Experiments were carried out in two stages. Stage 1 determined the concentrations of rhamnolipid and stirring speeds that would produce the best voltages, desalination, and wastewater treatment results. Stage 2 involved conducting a factorial study in which the selected rhamnolipid concentrations and stirring speeds (factors) were randomized at different levels to obtain the best combination of these factors which would yield the best outcomes. The concentrations of rhamnolipids studied were 80, 160, 240, 320, and 400 mg/l. This range of concentrations was chosen based on the work of Wen et al. [14]. The stirring regimes studied were Regime 1 (10 seconds of stirring, once a day), Regime 2 (10 seconds of stirring, 12-hour interval, twice a day), Regime 3 (10 seconds of stirring, 8-hour interval, three times a day), Regime 4 (10 seconds of stirring, 6-hour interval, four times a day), and Regime 5 (10 seconds of stirring, 4-hour interval, six times a day). These stirring regimes with a speed of 60 rpm were selected in terms of cathode chamber volume and effect of stirring on water flux from the cathode chamber into adjacent chambers. In the control experiment, neither rhamnolipid nor stirring was applied. For the factorial study, rhamnolipid varied at concentrations of 240 and 160 mg/l that represented high (1) and low (-1) levels of the factor (rhamnolipid), respectively. Stirring regimes varied were Regime 3 and Regime 1 representing high (1) and low (-1) levels, respectively. These factor levels (240 and 160 mg/l, and Regime 3 and Regime 1) were selected because they facilitated the highest and moderate electricity generation rates, desalination, and COD removal performances of the MDC. Regime 3 was particularly chosen because it not only produced large outputs of the measured parameters but also required a comparatively fewer stirring events. The factorial study was designed using DOE in Minitab16. The voltages were measured every five minutes across a 1000 Ω external resistor with a digital multimeter (Keithley 2700, Ohio, USA). A voltage drop below 45 mV indicated the end of the desalination cycle. Cyberscan Waterproof pH/conductivity/TDS/°C/°F PC 300 series multi-parameter (Eutech instruments-Thermo scientific, Massachusetts, USA) was used for measuring conductivity and pH changes. The dissolved oxygen levels were monitored using Hach HQ30d Flexi DO/Temp-meter (Loveland,

Colorado, USA) and COD levels measured using the reactor digestion method. Desalination and removal percentage of

COD was calculated through Equations 1 and 2.

$$\% \text{ Desalination} = \frac{\text{Initial saltwater conductivity} - \text{final saltwater conductivity}}{\text{Initial salt conductivity}} \times 100 \%$$ (1)

$$\% \text{ COD removed} = \frac{\text{Initial COD} - \text{Final COD}}{\text{Initial COD}} \times 100 \%$$ (2)

3. RESULTS AND DISCUSSION

3.1. Effect of rhamnolipid on voltage production

The average peak voltage produced by the MDC in the control experiment was 164.50 ± 0.11 mV (Figure 2). Upon the addition of rhamnolipid to anolytes, the peak voltage production increased from 164.5 ± 0.11 to 623.70 ± 1.32 mV at a rhamnolipid concentration of 240 mg/L (Figure 2). Thereafter, voltage production declined as the concentration of the rhamnolipid increased (Figure 2). The initial increments in voltage productions were associated with the ability of rhamnolipid to make substrate bioavailable to exoelectrogens so that it can be used in electricity production. This is possible through the ability of rhamnolipid to reduce surface tension and increase micelle formation which facilitate biodegradation of substrates [15, 21]. Also, the addition of rhamnolipid increased the electrical conductivity of the anolyte, thereby enhancing electricity production. For instance, the mere addition of rhamnolipid at a concentration of 240 mg/L increased the electrical conductivity of anolyte from $2.37 \times 10^{-3} \pm 0.03$ to 5.33 ± 0.17 mS/cm. Increment in the electrical conductivity of anolytes through rhamnolipid addition was also reported by Wen et al. [14]. On the other hand, a decrease in voltage production after a rhamnolipid concentration of 240 mg/L was attributed to the possibility that the higher concentrations (>240 mg/L) of the rhamnolipid inhibited the metabolic activities of exoelectrogens. According to Nickzad and Deziel [22], bacteria are intolerant of high concentrations of rhamnolipid. *Staphylococcus aureus*, for instance, is very intolerant of rhamnolipids, even at lower concentrations [23].
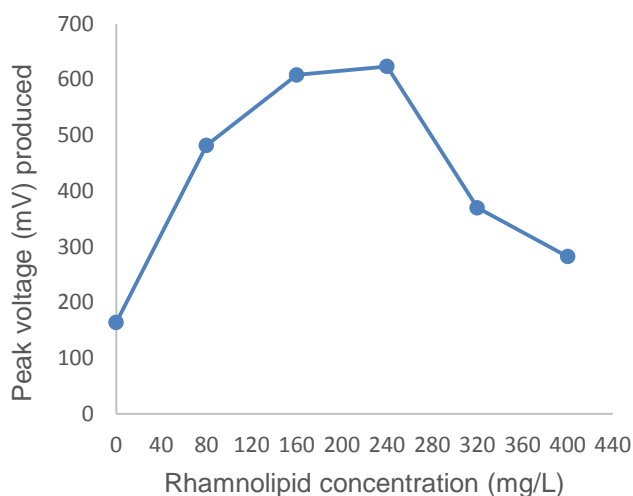
24.89 ± 0.50 % at a rhamnolipid concentration of 240 mg/L. The percentage of salt removal was in the order of voltage production. That is, increasing the concentration of rhamnolipid increased the desalination percentage up to a rhamnolipid concentration of 240 mg/L and thereafter, decreased to 21.83 ± 3.06 % at a rhamnolipid concentration of 400 mg/L (Figure 3). Since desalination in the MDC technology relies on electricity production in principle [24], a similarity in trend observed between voltage production and percentage desalination was a reflection of this fact.

It was also observed that the concentration gradient in the less concentrated water in the neutralization chambers, anolyte, and catholyte facilitated water osmosis into the desalination chamber, thereby diluting the concentrated saltwater in the desalination chamber. The result was an increase in the volume of water in the desalination chamber to ~ 77 cm^3. Ping et al. [8] and Mehanna et al. [25] also reported dilution as a contributing factor in desalination in their studies. In the study of Mehanna et al. [25], for example, the concentration gradient (dilution effect) could contribute to conductivity reduction by as high as 43 ± 6 % in a 20 g/L salt solution.
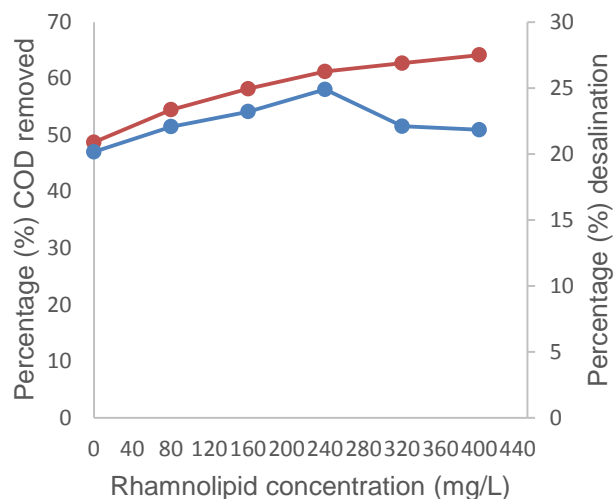
Figure 3. Desalination and COD removal efficiencies under rhamnolipid addition. [Zero (0) on the horizontal axis represents control experiment, the blue line represents percentage desalination and the red line represents percentage COD removed]

3.3. Effect of rhamnolipid on COD removal

A COD removal efficiency of 48.74 ± 8.06 % was produced from the control experiment and this was improved when rhamnolipid was added to anolytes (Figure 3). At a rhamnolipid concentration of 80 mg/L, the COD removal efficiency of the MDC was 54.48 ± 3.43 %. Further addition of rhamnolipid resulted in a COD removal efficiency of 64.17 ± 5.00 at 400 mg/L (Figure 3). The positive effect of rhamnolipid on COD reduction was probably due to its ability to make substrates bioavailability to microbes. Whang et al.

Figure 2. Peak voltages produced under rhamnolipid addition. [Zero (0) on the horizontal axis represents control experiment]

3.2. Effect of rhamnolipid on desalination

The addition of rhamnolipid improved the desalination performance of the MDC under study. Percentage desalination increased from 20.16 ± 1.97 % in the control experiment to

[21] articulated this by reporting that rhamnolipids lower surface tension and thereby, increase the bioavailability of substrates to microbes for biodegradation. The higher COD removal at a rhamnolipid concentration of 400 mg/L was attributed to the degradation of substrates by other bacteria that coexisted with exoelectrogens in the anode chamber. This was possibly the case because beyond 240 mg/L rhamnolipid concentration, the voltage production declined (Figure 2), implying that exoelectrogens were negatively affected by higher concentrations of rhamnolipd.

3.4. Effect of stirring on voltage production

The control experiment recorded the least voltage (164.50 ± 0.11 mV) produced, while the experiments operating with the stirring regimes 3, 4, and 5 produced the highest peak voltage of ~ 567.27 ± 18.06 mV, on average (Figure 4). The higher peak voltage production of the higher stirring regimes (3, 4, and 5) was attributed to their support of higher oxygen concentration in the water catholyte (Table 1). Oxygen is required for reduction reactions in the cathode chamber. In an earlier work, Kokabien and Gude [26] also observed that voltage production was high when the oxygen concentration of catholyte was high. This positive relationship between electricity production and oxygen concentration was also reported by Rismani-Yazdi et al. [16] and Oh et al. [27]. These earlier works concluded that power productions were proportional to dissolved oxygen concentrations in bioelectrochemical systems. The production of similar voltage outputs (Figure 4) among the stirring regimes 3, 4, and 5 was attributed to their provision of similar oxygen concentrations (Table 1) in the water catholyte.
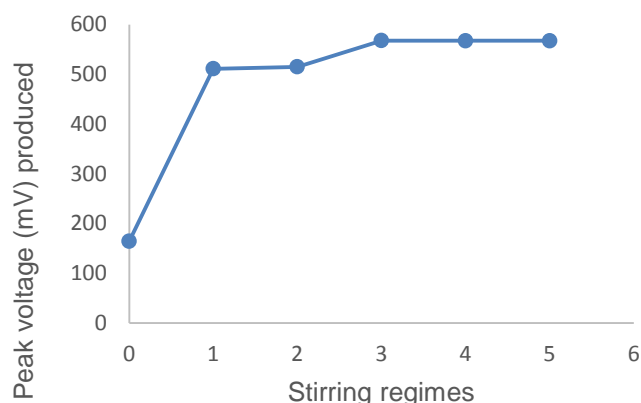

Figure 4. Effect of stirring regimes on peak voltage production. [Zero (0) on the horizontal axis represents control experiment]

Table 1. Dissolved oxygen (DO) concentrations of catholyte

Stirring regime	DO (mg/L)	Temperature (ºC)
1	7.60 ± 10	28 ± 1.10
2	7.70 ± 1.51	28 ± 1.19
3	8.70 ± 20	28 ± 2.12
4	8.70 ± 1.11	28 ± 0.07
5	8.64 ± 0.60	28 ± 0.42

3.5. The effect of stirring on desalination

The highest percentage of desalination (~24.26 ± 0.97 %) was achieved when either of Stirring Regimes 3, 4, or 5 was

applied and the least produced in the control experiment (Figure 5). Percentage of desalination increased in the same order as voltage production. This observation was attributed to the fact that desalination in MDCs principally relies on voltage production and this creates a positive correlation between voltage production and desalination. Voltage production causes the separation and movement of Cl⁻ and Na⁺ ions out of the desalination chamber into the anode and cathode chambers, respectively, thereby causing desalination in the middle chamber [20].
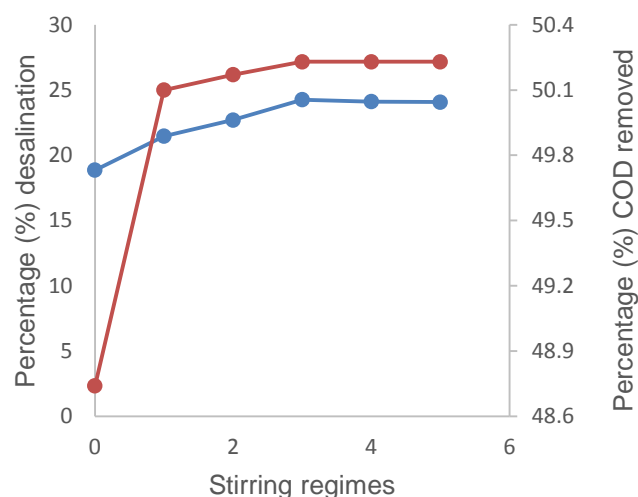

Figure 5. Effect of stirring regimes on desalination and COD removal efficiencies. [Zero (0) on the horizontal axis represents control experiment, the blue line represents percentage desalination and the red line represents percentage COD removed]

3.6. Effect of stirring on COD removal

The percentage of COD removal from anolytes increased from 48.74 ± 8.06 % in the control experiment to ~ 50.03 % ± 1.60 in the experiments operating with the stirring regimes 3, 4, and 5 (Figure 5). This was a rather marginal increase. It was also observed that the effect of stirring on COD removal assumed a similar trend as the effect of stirring on voltage production (Figure 4). This similarity in trend was probably because of the relationship between voltage production and COD removal. As exoelectrogens biodegrade substrates (COD removal), electrons are released and then, transferred to the cathode through the anode for voltage production [28]. Thus, when exoelectrogens find the use of the anode more favorable for energy gain, more substrates are biodegraded for voltage production and consequently, much more COD is removed. Also voltage production increases when the cathode chamber conditions are favorable (adequate supply of oxygen) and since stirring increases the concentration of dissolved oxygen in the catholyte, it thus supports COD removal through voltage production.

3.7. Effect of factor interaction (rhamnolipid and stirring) on voltage production, desalination, and COD removal

3.7.1. Effect of factor interaction (rhamnolipid and stirring) on peak voltage production

The highest peak voltage produced in the factorial study was 647.07 mV (Table 2). This was achieved with a rhamnolipid concentration of 240 mg/l and the stirring regime 3. This

voltage (647.07 mV) was higher than the highest voltage obtained (567.77 mV; Figure 4) when only stirring was the factor being investigated and the 623.70 mV (Figure 2) obtained when rhamnolipid was the only factor studied in the preliminary experiments.

The higher voltage production performance in the factorial experiment was possibly due to the simultaneous improvement in both anolyte and catholyte conditions. The addition of rhamnolipid accelerates electron transfer out of bacteria cells [14] while stirring of catholyte provides adequate dissolved oxygen concentration in the cathode chamber (Table 1). Under adequate oxygen concentrations, mass transport losses (voltage loss) can be reduced in oxygen-depended cathodes, thereby improving voltage production [16].

An ANOVA output (Appendix A) showed that although the interaction of stirring and rhamnolipid improved voltage production, such interaction effect was not significant ($p = 0.337$). However, the main effects of stirring and rhamnolipid individually were significant ($F = 33.40$, $p = 0.000$) on voltages produced (Appendix A). The significance of the main effects of rhamnolipid and stirring was attributed to the ability of rhamnolipid to reduce internal resistance [14] and stirring (water turbulence) to increase oxygen concentration in water [17].

The insignificant effect of the factor interaction on voltage production was attributed to the possibility that the factor combinations at all levels (whether high, low, or both) produced near-optimal voltages attainable with the MDC. Thus, operating the MDC with any factor combination would not lead to marked changes in peak voltages as observed (Table 2).

The factorial analysis yielded the model equation:

Voltage = 639.732 + 4.185 (Rhamnolipid concentration) + 1.997 (Stirring regime)   (3)

R^2 for the model was 89.45 %.

3.7.2. Effect of factor interaction (rhamnolipid and stirring) on desalination

The highest percentage of desalination recorded in the factorial study was 25.50 %. This was produced when both rhamnolipid concentration and stirring were high (Table 2). This desalination percentage was higher than the highest desalination efficiency (24.89 %) achieved when rhamnolipid was the only factor studied (Figure 3) and 24.26 % achieved (Figure 5) when stirring was the only factor studied in the preceding experiment. The improved desalination performance of the MDC under considerable stirring regime and a high rhamnolipid concentration was attributed to the improved voltage production (Table 2) under these conditions (240 mg/l rhamnolipid and regime 3). In MDCs, desalination results from electricity production and thus improved voltage productions leads to improved percentage desalination and, in turn, promoted the desalination percentage [24].

The factorial analysis also revealed that the interactive effect of rhamnolipid and stirring did not produce a significant ($p = 0.073$, Appendix B) effect on desalination percentage. This was evident in the marginal difference (~ 1%) between the desalination percentage in the preceding experiments and that recorded in the factorial study. This insignificant effect of factor interaction on desalination was traceable to the insignificant effect of the factor combinations of rhamnolipid and stirring on voltage production. An effect on voltage production directly affects desalination because of the dependence of desalination on voltage production.

However, the ANOVA from the factorial study showed that the main effects of rhamnolipid and stirring individually were significant ($p = 0.000$, Appendix B).

The model produced from the factorial analysis for percentage desalination had a high R^2 value of 90.49 % and was defined by:

% Desalination = 24.3917 + 0.6250 (Rhamnolipid concentration) + 0.3583 (Stirring regime)   (4)

Table 2. Performances of the FCMDC in the factorial study

Standard order	Run order	Rhamnolipid concentration (Coded units)	Stirring regime (Coded units)	Responses		
				% Desalination	Peak voltage (mV)	% COD
7	1	-1	1	24.00	640.50	65.47
4	2	1	1	25.50	645.71	68.15
6	3	1	-1	24.50	642.53	67.43
11	4	-1	1	24.30	638.00	65.92
9	5	-1	-1	23.50	630.92	65.00
5	6	-1	-1	23.20	633.09	64.88
8	7	1	1	25.10	643.22	67.91
3	8	-1	1	24.60	635.87	66.24
12	9	1	1	25.00	647.07	67.6
10	10	1	-1	24.80	640.97	67.89
1	11	-1	-1	23.00	634.90	65.32
2	12	1	-1	25.20	644.00	67.31
Where; -1 represents rhamnolipid concentration at 160 mg/L (Low) and 1 represents 240 mg/L (High)						
-1 represents stirring regime 1 (Low) and 1 represents stirring regime 3 (High)						

3.7.3. Effect of rhamnolipid and stirring on COD reduction

With the factor combination of high rhamnolipid concentration (240 mg/L) and high stirring regime (stirring regime 3), a high percentage of COD reduction of 68.15 % was achieved. This was higher than the 61.26 % produced when only rhamnolipid (240 mg/L) was the factor investigated (Figure 3) and the 50.23 % achieved when stirring was the factor investigated (Figure 5) in the preliminary experiments. An analysis of variance (Appendix C) showed that the interaction between rhamnolipid and stirring had no significant (p = 0.221) effect on COD reduction. This possibly resulted from the fact that COD reduction was primarily affected by anode chamber conditions, where COD removal took place. Thus, an improvement in the cathode chamber conditions might not ensure an improved efficiency in COD removal.

The predictive model derived from the factorial study for % COD removal was:

% COD = 66.5933 + 1.1217 (Rhamnolipid concentration) + 0.02883 (Stirring regime)   (5)

R^2 value of the model was 95.63 %

4. CONCLUSIONS

The addition of rhamnolipid to the anolyte and the stirring of the catholyte of the MDC studied improved the MDC's voltage production, desalination, and COD removal efficiencies. An appropriate increase in the concentration of the rhamnolipid and an increase in the number of stirring events increased the voltage production, desalination, and COD removal efficiencies of the MDCs. The positive effect of rhamnolipid on the MDC peaked at a concentration of 240 mg/L for voltage production and desalination, whereas for COD removal, it peaked at the rhamnolipid concentration of 400 mg/L. In the experiment involving stirring, the positive effect of stirring peaked at regime 3 (three stirring events a day). It was also found that the main effects of the rhamnolipid and stirring were significant in the factorial study. However, their interaction effects were insignificant on the voltage production, desalination, and COD removal of the MDC.

5. ACKNOWLEDGEMENT

NOMENCLATURE

MDC	Microbial Desalination Cell
MFC	Microbial Fuel Cell
FCMDC	Five Chamber Microbial Desalination Cell
BES	Bioelectrochemical System
COD	Chemical Oxygen Demand
DO	Dissolve Oxygen

APPENDICES

APPENDIX A. Analysis of variance for voltages (coded units)

Source	DF	Seq. SS	Adj. SS	Adj. MS	F	P
Main effects	2	258.011	258.011	129.005	33.40	0.000
2-Way interactions	1	4.037	4.037	4.037	1.05	0.337
Residual error	8	30.899	30.899	3.862		
Total	11	292.947				

Appendix B. Analysis of variance for desalination (coded units)

Source	DF	Seq. SS	Adj. SS	Adj. MS	F	P
Main effects	2	6.2283	6.2283	3.11417	35.93	0.000
2-Way interactions	1	0.3675	0.3675	0.36750	4.24	0.073
Residual error	8	0.6933	0.6933	0.08667		
Total	11	7.2892				

Appendix C. Analysis of variance for COD (coded units)

Source	DF	Seq. SS	Adj. SS	Adj. MS	F	P
Main effects	2	16.0953	16.0953	8.04763	86.74	0.000
2-Way interactions	1	0.1633	0.1633	0.16333	1.76	0.221
Residual error	8	0.7423	0.7423	0.09278		
Total	11	17.0009				

REFERENCES

1. Alhimali, H., Jafary, T., Al-Mamun, A., Baawain, M.S. and Vakili-Nezhaad, G.R., "New insights into the application of microbial desalination cells for desalination and bioelectricity generation", *Biofuel Research Journal*, Vol. 24, (2019), 1090-1099. (https://dx.doi.org/10.18331/BRJ2019.6.4.5).

2. Santoro, C., Abad, F.B., Serov, A., Kodali, M., Howe, K.J., Soavi, F. and Atanassov, P., "Supercapacitive microbial desalination cells: New class of power generating devices for reduction of salinity content", *Applied Energy*, Vol. 208, (2017), 25-36. (https://dx.doi.org/10.1016/j.apenergy.2017.10.056).

3. Zhang, F., Chen, M., Zhang, Y. and Zeng, R.J., "Microbial desalination cells with ion exchange resin packed to enhance desalination at low salt concentration", *Journal of Membrane Science,* Vol. 417, No. 417-418, (2012), 28-33. (https://doi.org/10.1016/j.memsci.2012.06.009).

4. Morel, A., Zuo, K., Xia, X., Wei, J., Lou, X., Liang, P. and Huang, X., "Microbial desalination cells packed with ion-exchange resin to enhance water desalination rate", *Bioresource Technology*, Vol. 118, (2012), 243-248. (https://doi.org/10.1039/c002307h).

5.   Chen, X., Xia, X., Liang, P., Cao, X., Sun, H. and Huang, X., "Stacked microbial desalination cells to enhance water desalination efficiency", *Environmental Science Technology*, Vol. 45, No. 6, (2011), 2465-2470. (https://doi.org/10.1021/es103406m).

6.   Ping, Q. and He, Z., "Improving the flexibility of microbial desalination cells through spatially decoupling anode and cathode", *Bioresource Technology*, Vol. 144, (2013), 304-310. (https://doi.org/10.1016/j.biortech.2013.06.117).

7.   Daud, S.M., Daud, W.R.W., Bakar, M.H.A., Kim, B.H., Somalu, M.R., Andanstuti M., Jahim J.J.M.D. and Muhammed A.S.A., "Low-cost novel clay earthenware as separator in microbial electrochemical technology for power output improvement", *Bioprocess Biosystems Engineering*, Vol. 43, (2020), 1369-1379. (https://doi.org/10.1007/s00449-020-02331-7).

8.   Ping, Q., Cohen, B., Dosoretz, C. and He, Z., "Long-term investigation of fouling of cation and anion exchange membranes in microbial desalination cells", *Desalination*, Vol. 325, (2013), 48-55. (https://doi.org/10.1016/j.desal.2013.06.025).

9.   Abubakari, Z.I., Mensah, M., Buamah, R. and Abaidoo, R.C., "Assessment of the electricity generation, desalination and wastewater treatment capacity of a plant microbial desalination cell (PMDC)", *International Journal of Energy and Water Resource*, Vol. 3, (2019), 213-218. (https://doi.org/10.1007/s42108-019-00030-y).

10. Luo, H., Xu, P. and Ren, Z., "Long-term performance and characterization of microbial desalination cells in treating domestic wastewater", *Bioresource Technology*, Vol. 120, (2012), 187-193. (https://doi.org/10.1016/j.biortech.2012.06.054).

11. Li, Y., Styczynski, J., Huang, Y., Xu, Z., McCutcheon, J. and Li, B., "Energy-positive wastewater treatment and desalination in an integrated microbial desalination cell (MDC)-microbial electrolysis cell (MEC)", *Journal of Power Sources*, Vol 356, (2017), 529-538. (https://doi.org/10.1016/j.jpowsour.2017.01.069).

12. Wang Jian, H., Ewusi-Mensah, D. and Jingyu H., "Using *C. vulgaris* assisted microbial desalination cell as a green technology in landfill leacheate pre-treatment: A factorperformance relation study", *Journal of Water Reuse and Desalination*, Vol. 10, No. 1, (2020), 1-16. (https://doi.org/10.2166/wrd.2019.073).

13. Khazraee Zamanpour, M., Kariminia, H.R. and Vossoghi, M., "Electricity generation, desalination and microalgae cultivation in a biocathode-microbial desalination cell", *Journal of Environmental Chemical Engineering*, Vol. 5, No. 1, (2016). (http://dx.doi.org/10.1016/j.jece.2016.12.045).

14. Wen, Q., Kong, F., Ren, Y., Cao, D., Wang, G. and Zheng, H., "Improved performance of microbial fuel cell through addition of rhamnolipid", *Electrochemical Communication*, Vol. 12, (2010), 1710-1713. (https://doi.org/10.1016/j.elecom.2010.10.003).

15. Pacwa-Płociniczak, M., Płaza, G.A., Piotrowska-Seget, Z. and Swaranjit, S. C., "Environmental applications of biosurfactants: Recent advances", *International Journal of Molecular Sciences*, Vol. 12, No. 1, (2011), 633-665. (https://doi.org/10.3390/ijms12010633).

16. Rismani-Yazdi, H., Carver, S.M., Christy, A.D. and Tuovinen, O.H., "Cathodic limitations in microbial fuel cells: An overview", *Journal of Power Sources*, Vol. 180, (2008), 683-694. (https://doi.org/10.1016/j.jpowsour.2008.02074).

17. Atapaththu, K.S.D., Asaeda, T., Yamamuro, M. and Kamiya, H., "Effects of water turbulence on plant, sediment and water quality in reed (*Phragmites Australis*) community", *Bratislava*, Vol. 36, No. 1, (2017), 1-9. (https://doi.org/10.1515/eko-2017-0001).

18. London, K, and Wright, D.B., Factorial design, Encyclopedia of survey research methods, Thousand Oaks, Sage Publications Inc., USA, (2011). (http://dx.doi.org/10.4135/9781412963947).

19. Jafary, T., Al-Mamun, A., Alhimali, H., Baawain, M.S., Rahman, S., Tarpeh, W.A., Dhar, B.R. and Kim, B.H., "Novel two-chamber tubular microbial desalination cell for bioelectricity production, wastewater treatment and desalination with focus on self-generated pH control", *Desalination*, Vol. 481, (2020), 114358. (https://doi.org/10.1016/j.desal.2020.114358).

20. Cao, X., Huang, X., Liang, P., Xiao, K., Zhuo, Y., Zhang, X. and Logan, B.E., "A new method for water desalination using microbial desalination cells", *Environmental Science Technology*, Vol. 43, (2009), 7148-7152. (https://doi.org/10.102/es901950j).

21. Whang, L.M., Liu, P.W.G., Ma, C.C. and Cheng, S.S., "Application of rhamnolipid and surfactin for enhanced diesel biodegradation–Effects of pH and ammonium addition", *Journal of Hazardous Materials*, Vol. 164, (2009), 1045-1050. (https://doi.org.10.1016/j.jhazmat.2008.09.006).

22. Nickzad, A. and Deziel, E., "The involvement of rhamnolipids in microbial cell adhesion and biofilm development–An approach for control?", *Letters in Applied Microbiology*, Vol.58, (2014), 447-453. (https://doi.org/10.1111/lam.12211).

23. Silva, S.S., Carvalho, J.W.P., Aires, C.P. and Nitschke, M., "Disruption of *Staphylococcus aureus* biofilms using rhamnolipid biosurfactants", *Journal of Dairy Science*, Vol. 100, No. 10, (2017), 7873. (http//doi.org/10.3168/jds.2017-13012).

24. Yang, E., Mi-Jin, C., Kyoung-Yeol, K., Kyu-Jung, C. and In, S.K., "Effect of initial salt concentrations on cell performance and distribution of internal resistance in microbial desalination cells", *Environmental Technology*, Vol. 36, No. 7, (2014), 852-860. (https://doi.org/10.1080/09593330.2014.964333).

25. Mehanna, M., Saito, T., Yan, J., Hickner, M., Cao, X., Huang, X. and Logan, B.E., "Using microbial desalination cells to reduce water salinity prior to reverse osmosis", *Energy and Environmental Science*, Vol. 3, (2010), 1114-1120. (https://doi.org/10.1039/c002307h).

26. Kokabian, B. and Gude, V.G., "Sustainable photosynthetic biocathode in microbial desalination cells", *Chemical Engineering Journal*, Vol. 262, (2015), 958-965. (https://doi.org/10.1016/j.cej.2014.10.048).

27. Oh, S., Min, B. and Logan, B. E., "Cathode Performance as a factor in electricity generation in microbial fuel cells", *Environmental Science Technology*, Vol. 38, No. 18, (2004), 4900-4904. (https://doi.org/10.1021/es049422p CCC: $27.50).

28. Guang, L., Ato Koomson, D., Jingyu, H., Ewusi-Mensah, D. and Miwomunyuie, N., "Performance of exoelectrogenic bacteria used in microbial desalination cell technology", *International Journal of Environmental Research and Public Health*, Vol. 17, (2020), 1121. (https://doi.org/10.3390/ijerph17031121).

Study of Long-Term Stability of Perovskite Solar Cells: Highly Stable Carbon-Based Versus Unstable Gold-Based PSCs

Mohammad Reza Shekari[a], Seyed Mohammad Sadeghzadeh[a], Mahdi Golriz[b*]

[a] *Department of Electrical Engineering, Shahed University, P. O. Box: 18155-159, Tehran, Tehran, Iran.*
[b] *Space Transportation Research Institute, Iranian Space Research Center, P. O. Box 13445-754, Tehran, Tehran, Iran.*

A B S T R A C T

In recent decade, Perovskite Solar Cells (PSCs) have received considerable attention compared to other photovoltaic technologies. Despite the improvement of Power Conversion Efficiency (PCE) of PSCs, the chemical instability problem is still a matter of challenge. In this study, we have fabricated two kinds of PSCs based on gold and carbon electrodes with the optimal PCE of about 15 % and 10.2 %, respectively. We prepared a novel carbon electrode using carbon black nanopowder and natural graphite flaky powder for Hole Transport Material (HTM) free carbon-based PSC (C-PSC). Current density-voltage characteristics over time were measured to compare the stability of devices. Scanning Electron Microscope (SEM) and Energy-dispersive X-ray Spectroscopy (EDS) analyses were carried out to study applied materials, layer, and surface structures of the cells. The crystal structure of perovskite and its association with the stability of PSCs were analyzed using an obtained X-ray diffraction (XRD) pattern. As a result, the constructed HTM-free C-PSC demonstrated high stability against air, retaining up to 90 % of its optimal efficiency after 2000 h in the dark under ambient conditions (relative humidity of (50 ± 5); average room temperature of 25 °C) in comparison to constructed gold-based PSCs (Gold-PSC) which are not stable at times. The experimental results show that novel low-cost and low-temperature carbon electrode could represent a wider prospect of reaching better stability for PSCs in the future.

1. INTRODUCTION

The general chemical formula for perovskite compounds is ABX_3, where A, B are two cations of very different sizes and X is an anion that bonds to both. For example, $CH_3NH_3PbI_3$ has very high light absorption capacity and offers proper electronic properties, which is a suitable candidate for Perovskite Solar Cells (PSCs). The structure has a band gap of 1.5 eV, which is proper for light absorption purposes [1]. The combination of the organic material + lead + halogen has attracted the attention of many researchers because of its special characteristics such as high absorption coefficient, the ability to adjust the band gap, high movement of the charges, and the distribution of electrons in nanostructured solar cells. The most common type of PSCs includes the FTO/compact TiO_2/mesoporous TiO_2/$CH_3NH_3PbI_3$/Hole Transporter Material (HTM)/back contact, as the back connection could be made by Au, Ag, carbon, etc. [2-8].

Study on PSCs was initiated by investigation of the Dye-Synthesized Solar Cells (DSSCs) in 2009 by A. Kojima et al., as the obtained efficiency of 3.8 % attracted the attention of the researchers and led to the extended studies in this field [9]. Higher efficiencies could be also obtained by substitution of

the liquid electrolytes with the p-type solid spiro-MeOTAD [10-12]. Mixed halide perovskites including $CH_3NH_3PbI_{3-x}Cl_x$ and $CH_3NH_3PbI_{3-x}Br_x$ were also studied by the researchers and they resulted in the higher efficiency of PSCs because of greater electron-hole diffusion lengths in contrast to triiodide ($CH_3NH_3PbI_3$) perovskite absorber [13-15]. PSCs combined with other solar cell technologies such as tandem method could also achieve higher efficiency [16-17].

Although perovskite is promising, it has many disadvantages that limit its applications. The corrosion issues in contact with perovskite and silver, which results in the formation of silver halide, the high price of Au electrodes, and the need for the vacuum evaporation techniques, are some of the factors that limit the application of PSCs [18-20]. Also, the fabricating technology of this generation of cells still requires expensive metals such as Au and Ag as the electrodes, which are coated in vacuum conditions under thermal evaporation. Obviously, the high cost of these metals on a large scale and the need for enormous energy in the evaporation process in vacuum conditions will disrupt inexpensive techniques. Therefore, we would look for an appropriate alternative. The low-cost carbon would be an ideal material as a proper alternative to Au because of their similar performance. Graphite, carbon black, coal powder, carbon cloth, spongy carbon, and Carbon Nano-Tube (CNT) are well-known carbon materials that have been used as carbon electrodes in

fabricating PSCs so far [21-24]. Accessibility, chemical stability, environmental friendliness, and controllable porosity are all advantageous features of carbon materials [25]. Low cost, high efficiency, and proper stability are the challenges of the researchers for development of the organic/inorganic PSCs [26]. Z. Li et al. laminated films of CNT network on $CH_3NH_3PbI_3$ substrate as a hole-collector using the vapor deposition chemical method. In the absence of an organic HTM and metal contact, they made a solar cell with an efficiency rate of up to 6.87 %. Meanwhile, preparation of the CNT electrode requires temperatures higher than 1150 °C [27]. The components including organic materials, lead, and halogens are unstable at high temperatures or in contact with some other solvents; hence, it is essential to apply a low-temperature method for the preparation of these materials [28]. Since perovskite is unstable at high temperatures or in contact with some solutions, preparation of the carbon layer will be challenging. The low-temperature electrode layer deposition on the perovskite could be used to select and optimize the material and structure of this type of cell without destroying its structure [29]. In 1996, for the first time, Gratzel and Kay reported a proper construction method of DSSCs in a continuous non-vacuum process by simple printing techniques using a carbon electrode and with an efficiency rate of 6.7 % [30]. In another report prepared by H. Zhou et al., the constructed cells represented optimal efficiency at about 9 % as their stability in the darkness was 2000 h. The possibility of constructing a carbon layer on a perovskite layer at lower temperatures (without damaging it) was also studied, thus facilitating the construction steps and increasing the possibility of stability [31]. As a result of the instability of the perovskite at temperatures higher than 150 °C, the carbon electrode could be deposited at low temperatures using doctor blade coating method [32]. Due to the bipolar characteristic of $CH_3NH_3PbI_3$, this material could act as a light absorber and hole transporter at the same time. Also, electron and hole are effectively injected into the n-type conductors and carbon electrode, respectively [33]. For the first time, L. Etgar et al. reported the preparation of HTM-free PSCs with an efficiency rate of 5 %, which proved that perovskite acted simultaneously as a light absorber and a HTM. The removal of HTM increases the stability and reduces costs as the manufacturing process becomes easier and the optimal efficiency for HTM-free cells reaches up to 10.85 % [34]. The conductivity and mechanical performance of the carbon layer play an important role in collecting the hole. Besides, in the case of using carbon derivatives in the carbon electrode layer and achieving an optimum thickness of carbon electrode, the series resistance of the cell with carbon electrode will decrease, which leads to an increase in efficiency [31, 35]. In 2013, Z. Ku et al. presented a report on the construction of a carbon electrode, which plays the role of a hole-conductor. They used carbon derivatives such as spheroidal and flaky graphite via a screen printing method. The results indicated that the solar cell with a carbon black/spheroidal graphite electrode was more stable and presented the efficiency of 6.64 %, which represented a better performance than the flaky graphite spheroidal-based device and made it comparable to a gold material version. Besides, filling up the pores of TiO_2 layers was done more efficiently by the spheroidal graphite than the flaky graphite. They also achieved proper stability in environmental conditions over 840 h [36]. They deposited the perovskite film using the dip-coating method and through diffusion into the carbon layer

and ZrO_2 insulating layer. Then, they provided the conditions for drying the cell in a dark environment. They used the screen printing method for the other layers, including the carbon electrode layer, ZrO_2 and TiO_2 layers [37-38]. In this type of Carbon-based Perovskite Solar Cells (C-PSCs), since the thickness of the carbon layer affects the electrical conductivity, the researchers also tried to improve the Power Conversion Efficiency (PCE) of the cell by changing the thickness of the electrode layer [39]. Black carbon and graphite or a mixture of them (carbon paste) can be used a carbon electrode in the solar cells using film deposition methods such as the screen printing and doctor-blade coating. For example, in 2012, L. Zhang et al. studied the effect of particle size of graphite used in the carbon electrode on the efficiency of solar cells as well as the effect of electrode thickness and the PCE in optimum condition, which reached 11.65 % [40]. H. Wang et al. also studied the effect of carbon black and the dosage and percentage of carbon black and graphite in the electrode. They reached the highest efficiency (7.08 %) at 20 % of carbon black ratio, because carbon black would greatly influence the uniform formation of perovskite film. The efficiency remains relatively unchanged after 900 h, which indicates its proper stability [35].

The stability of PSCs is effectively related to the destruction of perovskite crystals over time. In general, given that perovskite is sensitive to moisture, the process of destruction is completed besides oxygen and light in the form of the following equations, where Eqs. 1 and 2 occur due to the moisture and Eq. 3 is caused by oxygen. Eq. 4 is accelerated under the effect of sunlight; therefore, all three factors increase the destruction trend besides each other. Changing the color of PSCs from black to light yellow over time represents the decomposition of perovskite crystals [41-45].

$$CH_3NH_3PbI_3 \text{ (s)} \leftrightarrow PbI_2 \text{ (s)} + CH_3NH_3I \text{ (aq)} \tag{1}$$

$$CH_3NH_3I \text{ (aq)} \leftrightarrow CH_3NH_2 \text{ (aq)} + HI \text{ (aq)} \tag{2}$$

$$4HI \text{ (aq)} + O_2 \text{ (g)} \leftrightarrow 2I_2 \text{ (s)} + 2H_2O \text{ (l)} \tag{3}$$

$$2HI \text{ (aq)} \leftrightarrow H_2 \text{ (g)} + I_2 \text{ (s)} \tag{4}$$
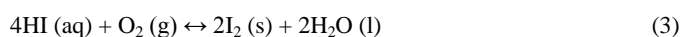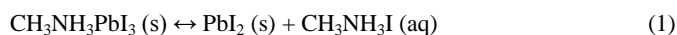
In 2019, X. Wu et al. improved the moisture stability and efficiency of the C-PSCs by inserting an inorganic Copper (I) thiocyanate (CuSCN) as an HTM between perovskite and carbon electrode to suppress the electron recombination process and using highly conductive CNT networks to form a robust interface of CuSCN/CNT and reached a PCE value up to 17.58 % [46]. Also, Q. Chu et al. developed an efficient low temperature, solution-processed Poly(3-hexylthiophene-2,5-diyl) P3HT/graphene Hole Transport Layer (HTL) for improving the hole transport and reported a record efficiency rate of 18.1 % for C-PSCs, which showed outstanding stability towards moisture, oxygen, and light [47]. Recently, S. Wang et al. reported that Cs^+ doping in methylammonium lead iodide perovskite $(Cs_xMA_{1-x}PbI_3)$ led to the manufacturing of remarkably stable HTM-free C-PSC which maintained up to 90 % of its initial PCE under a high-humidity condition after 1000 h [48]. In terms of water polarity, destruction of perovskite crystals occurs even in a low-moisture environment and the deconstruction time is delayed; if not protected against moisture, they will rapidly decompose and the PCE of cell extremely decrease. Low-cost carbon electrode due to its hydrophobic nature prevents the diffusion of moisture into the structure of the cell and plays an

HTM role, which is cheaper than Au and spiro-MeOTAD. Carbon is almost purely based on aromatic and non-polar sheets such that the interaction of extremely polar molecules such as water is very weak and leads to hydrophobia of the carbon electrode surface and high contract angle with water drops [36, 49-50]. The contact angle of water on the carbon surface is 113°, which reflects its hydrophobicity. Also, the contact angle of water on the silver and gold surface is less than 90°, which shows that their hydrophilic surface is semi-wetted by water. Higher contact angles do not allow water to be distributed or absorbed on the surface; thus, it takes a drop shape and slides [31].

Apart from the thermal stability of perovskite, the thermal stability of the HTM matters and basically, inorganic protective and blocking layers are stable. In 2014, S.N. Habisreutinger et al. considered the resistance against water diffusion and thermal stability factors, attenuated thermal destruction, and improved the thermal stability by substitution of the organic HTM with the Single-Walled carbon Nano-Tubes (SWNTs), embedded in a polymer isolator, as the efficiency was improved by 15.3 % [51]. In 2016, A. Baranwal et al. fabricated a three-layer printable HTM-free PSC with a mesoporous carbon back contact and demonstrated the thermal stability over 1500 h at 100 °C using a side-sealing UV-curable encapsulation method [52]. Moreover, using $Cs_xFA_{1-x}PbBr_xI_{3-x}$ and $Cs_xNa_{1-x}PbI_3$ light absorber perovskites was reported by researchers to enhance the thermal stability of the HTM-free C-PSCs [53-54].

In this research, two types of PSCs based on the gold electrode (Gold-PSC with HTM) and carbon electrode (HTM-free C-PSC) were constructed. The objective of this work is to demonstrate the effect of carbon electrode on the stability of HTM-free C-PSC in comparison to the Gold-PSC with HTM as well as the variation of efficiency versus time in order to propose some solutions for improving stability. We applied a novel carbon paste containing carbon black nanopowder (Average Nanoparticle Size: 30 nm) and natural graphite flaky powder (approximately 3 µm) at a weight ratio of 2:3 and also obtained a thickness of 20 µm for carbon electrode using the doctor-blade coating method, which makes this study distinguishable from the other researches in terms of carbon electrodes.

2. EXPERIMENTAL

2.1. Meterials

In this work, the following materials were used: Titanium isopropoxide or TTIP ($Ti[OCH(CH_3)_2]_4$) with 97 % purity, density of 0.967 g/cm^3 (20 °C) from Sigma-Aldrich (Tetraisopropyl orthotitanate); Hydrochloric acid (HCl) with 37 % purity, density of 1.19 g/cm^3 (20 °C) from Merck; Ethanol (C_2H_5OH) with 99.9 % purity, density of 0.79 g/cm^3 (20 °C) from Merck (Ethyl alcohol); Lead (II) iodide (PbI_2) with 99.99 % purity, density of 6.16 g/cm^3 (25 °C) from Sigma-Aldrich (Plumbous iodide); Dimethylformamide or DMF ($HCON(CH_3)_2$) with 99.8 % purity, density of 0.94 g/cm^3 (20 °C) from Merck; Methylammonium iodide (CH_3NH_3I) with 99.9 % purity from Sigma-Aldrich; Isopropanol ($CH_3CH(OH)CH_3$) with 99.5 % purity, density of 0.786 g/cm^3 (20 °C) from Merck; Chlorobenzene (C_6H_5Cl) with 99 % purity, density of 1.105-1.107 g/cm^3 (d 20 °C/4 °C) from Sigma-Aldrich (Phenyl chloride); Spiro-OMeTAD ($N^2,N^2,N^2{}',N^2{}',N^7,N^7,N^7{}',N^7{}'$-octakis(4-

methoxyphenyl)-9,9′-spirobi[9H-fluorene]-2,2′,7,7′-tetramine) with 99 % (HPLC) purity from Sigma-Aldrich; Bis(trifluoromethylsulfonyl)amine lithium salt (LiTFSl, $CF_3SO_2NLiSO_2CF_3$) with 99 % purity, density of 1.33 g/cm^3 from Sigma-Aldrich (Lithium bistrifluoromethanesulfonimidate); Acetonitrile (CH_3CN) with 99.8 % purity, density of 0.786 g/cm^3 from Sigma-Aldrich (Ethyl nitrile); 4-Tert-butylpyridine or TBP ($C_9H_{13}N$) with 98 % purity, density of 0.923 g/cm^3 (25 °C) from Sigma-Aldrich; Carbon black nanopowder (Average Nanoparticle Size: 30 nm) with 99 % purity from MTI Corporation; Natural graphite flaky powder (approximately 3 µm) with 99.9 % purity from US-Nano; Ethyl cellulose from Sigma-Aldrich; Terpineol ($C_{10}H_{18}O$) from Sigma-Aldrich; Zirconium oxide nanopowder (ZrO_2, APS: 20 nm) with 99.95 % purity, density of 5.89 g/cm^3 from US-Nano; Zinc powder (Zn) with 99.995 % purity from Sigma-Aldrich; Titanium tetrachloride or TTC ($TiCl_4$) with 99.9 % purity from Sigma-Aldrich; Transparent TiO_2 paste (20-25 nm particle size) from Sharif Solar; Fluorine doped tin oxide-coated glass slide (FTO glass) from Sigma-Aldrich; and acetone (CH_3COCH_3) with 99.8 % purity, density of 0.79 g/cm^3 (20 °C) from Merck (Dimethyl ketone).

2.2. Preparation procedures and deposition methods

Figures 1a and 1b represent two cross-sectional areas of a Gold-PSC with HTM and a HTM-free C-PSC, respectively. The main difference between the structures below is the use of an HTM (spiro-MeOTAD) in the Gold-PSC. The sequence of layers of the constructed cells is as follows:

a. Gold-PSC with HTM: FTO / Blocking Layer (compact TiO_2) / Mesoporous TiO_2 / Perovskite ($CH_3NH_3PbI_3$) / HTM (spiro-MeOTAD) / Au Electrode

b. HTM-free C-PSC: FTO / Blocking Layer (compact TiO_2) / Mesoporous TiO_2 / Perovskite ($CH_3NH_3PbI_3$) / Carbon Electrode
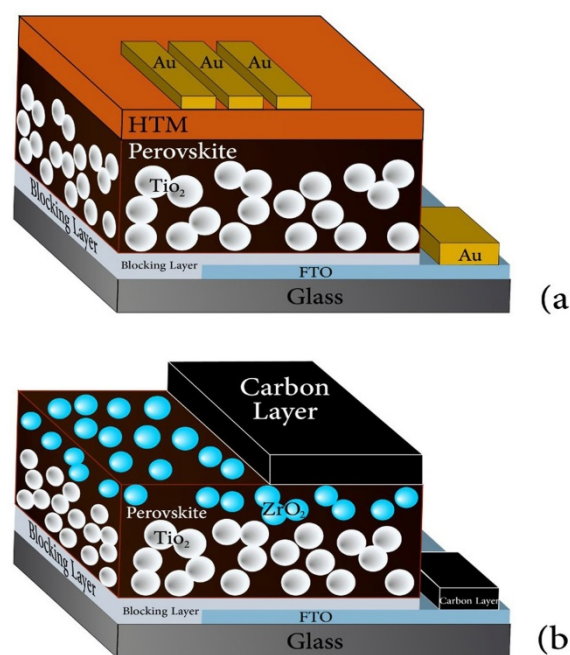

Figure 1. Cross-sectional structures of (a) the Gold-PSC with HTM and (b) the HTM-free C-PSC

First, we etched one side of the FTO glasses (each square part including 4 cells (1.4 cm × 1.4 cm)) by using HCl (2 M) and Zinc powder to prevent short circuits from occurring. Then, the etched glasses were washed in an ultrasonic bath. In this report, we have fabricated 6 PSCs including 5 Gold-PSCs with HTM and one HTM-free C-PSC. In order to prepare the mentioned structures, four types of solutions (block solution, lead iodide (PbI_2) solution, CH_3NH_3I solution, and spiro-MeOTAD solution) and one type of carbon ink were made and the thin films were deposited step by step. For the preparation of the block solution, we used TTIP, ethanol and, HCl. Also, the final block solution was filtered using a syringe filter (pore size: 220 nm). A proper dosage of the block solution was then poured on the FTO glass all at once and film deposition was blocked using a spin coater device starting at 2000 rpm for 30 s as the thickness of the layer reached about 40 nm. Afterward, one part of the cells parallel to the etched sides was cleaned by ethanol. In order to use the electrical connections, this part of the cells should be cleaned at the end of each film deposition process except perovskite film deposition. After heating the piece in the oven at 500 °C for 1 h, 4 cells were disconnected and the layers underwent treatment in the $TiCl_4$ solution for 30 min at 70 °C. For mesoporous TiO_2 film deposition, the TiO_2 paste diluted by ethanol at a weight ratio of 1:3.5 was deposited by spin coating method at 5000 rpm for 30 s. After that, the part of the cells which had been cleaned by ethanol in the previous film deposition was cleaned by ethanol again. Then, it was placed in the oven at 500 °C for half an hour. Once the temperature reached 70 °C, layers were removed and put on the hot plate; note that during the deposition of perovskite layers, the temperature should be fixed at 70 °C. Lead iodide solution including PbI_2 and DMF stirred at 70 °C for 12 h. It was then filtered using a syringe filter (pore size: 450 nm). We know that this solution should be kept at 70 °C during the film deposition process and if the temperature is lowered at this step, it becomes semi-crystalline immediately.

Perovskite film deposition was conducted by spin coating method using the PbI_2 solution at a speed of 6500 rpm for the duration of 5 s. The cells were then put in the oven at 70 °C for 30 min. After cooling down, the cells were placed inside the pre-prepared CH_3NH_3I solution at a concentration of about 10 mg/ml in isopropanol and the film deposition was conducted using dip-coating method. This way, each cell was placed inside the solution one by one for the duration of 20 s. Then, the cells were removed from the mentioned solution and placed inside the isopropanol solution. Finally, the devices were dried using the spin coater at a speed of 4000 rpm for 10 s and re-dried in the oven at 70 °C for 30 min.

For HTM film deposition of 5 Gold-PSCs, we prepared 2 solutions including spiro-MeOTAD in chlorobenzene and LiTFSI in Acetonitrile, respectively. After adding some TBP to the first solution, some of the second solution was also added to the obtained solution. Then, the last obtained spiro-MeOTAD solution was put under stirring at 60 °C for half an hour. Moreover, it was finally filtered using a syringe filter (pore size: 220 nm). Spiro-MeOTAD film deposition was conducted by spin coating method at 4000 rpm for the duration of 30 s. At this step, the cleaned part of the cells was gently cleaned again using the acetone solution. After passing 12 h from the deposition of spiro-MeOTAD, Au electrode film deposition for the 5 Gold-PSCs was conducted using the vacuum evaporation method.

For electrode film deposition of the HTM-free C-PSC after the perovskite film deposition, prepared carbon ink was deposited by a doctor-blade method, in which a sticker (with 30 μm thickness size) was also applied for reaching a thickness of 20 μm.

2.3. Preparation of carbon ink

For the preparation of the carbon paste, 2 g of carbon black nanopowder mixed with 3 g of natural graphite flaky powder and 0.5 g of ethyl cellulose was added to 25 g of Terpineol. Initially, to evaporate the solvents that exist in carbon paste, it was put in the oven for 12 h at 120 °C to prevent any possible reaction of perovskite with the solutions existing in carbon paste; this is because Terpineol material used in the carbon paste could destroy the perovskite immediately. In order to prepare carbon ink, 5 g of pre-dried carbon paste was mixed with 4 g of ZrO_2 nanopowder and 15 ml of chlorobenzene, which was then milled for 2 h to be completely homogenized.

2.4. Measurement and analysis devices

2.4.1. Current density-voltage (J-V) characterization

We used an IV-curve tracer from IRASOL to obtain current density-voltage (J-V) curves where solar simulator from IRASOL and power meter were used. We provided the following parameters for the cells using these devices: short-circuit current density (J_{SC}), open-circuit voltage (V_{OC}), the voltage at which the maximum power occurs (V_{max}), the current density at which the maximum power occurs (J_{max}), maximum power (P_{max}), efficiency of solar cell (PCE or η %), Fill Factor (FF) or the ratio of maximum obtainable power to the product of the open-circuit voltage and short-circuit current, and series resistance due to electrodes' connection (R_S). Eq. 5 and Eq. 6 show separately calculations of PCE and FF [16].

$$PCE\ (\eta\ \%) = \frac{J_{max} \cdot V_{max}}{P_{in}} * 100 = \frac{J_{sc} \cdot V_{oc} \cdot FF}{P_{in}} * 100 \qquad (5)$$

$$FF = \frac{J_{max} \cdot V_{max}}{J_{sc} \cdot V_{oc}} \qquad (6)$$

The manufactured cells have been tested under standard experimental conditions (T=25 °C and under AM1.5 conditions; intensity of incident light (P_{in})=100 mW.cm^{-2}). Both during the test and at the time of keeping the cells in a dark condition for stability analysis, the relative humidity in the laboratory is (50 ± 5) %.

2.4.2. SEM and EDS characterization

Samples were coated with Au and their morphologies were studied using Scanning Electron Microscope (SEM) images. Moreover, Energy-dispersive X-ray Spectroscopy (EDS) analyses were obtained using a Field-Emission Scanning Electron Microscope (FE-SEM) from TESCAN (MIRA3).

2.4.3. X-ray diffraction (XRD)

X-Ray Diffraction (XRD) pattern was obtained using an X-ray diffractometer from GNR (Explorer). Films were scanned in the reflection mode using an incident X-ray of Cu Kα (40 KV and 30 mA) with a wavelength of 1.54 A° at a step size of 0.01° and a scan rate of 1°/min from 2θ = 5° to 100°.

3. RESULTS AND DISCUSSION

Figures 2a and 2b indicate the 5 Gold-PSCs (No. 1-5) and the HTM-free C-PSC (No. 6) constructed in this research, respectively. During the construction of the cells, we have studied different thicknesses and layer surfaces in various film depositing conditions to obtain the optimum layer in terms of thickness, quality, and uniformity. The blocking layer was the first layer studied for construction which is necessary for preventing recombination of electrons and the generated holes due to radiation and it also controls electron loss in contrast to the FTO and the perovskite layer. If this layer is very thinner (less than 25 nm), it cannot quickly release photoelectrons, which leads to a decrease in J_{SC} and, thus, a reduction in PCE. Moreover, if this layer is highly thick (more than 80 nm), it leads to increased resistance in the path of photoelectrons. Thus, the photovoltaic performance of the cells extremely depends on the thickness of this layer [55-56].
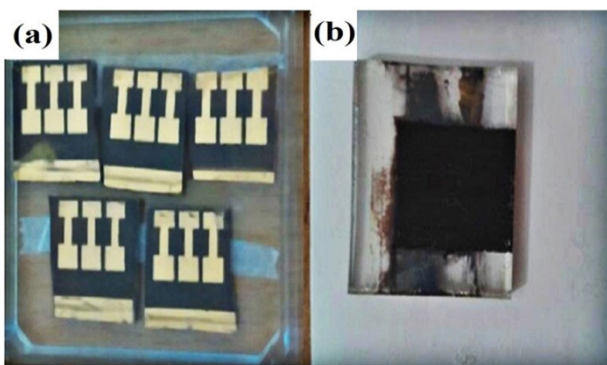
Figure 2. Constructed cells including (a) the 5 Gold-PSCs (No. 1-5) and (b) the HTM-free C-PSC (No. 6)

According to the studies of other researchers, we know that the optimal photovoltaic parameter occurs when the thickness of block layer is between 40 and 80 nm [57]. We achieved a thickness in this range using experimental experiences as follows. First, we tested 2.5 ml and 2 ml of block solution for 2 FTO glasses and the thickness of the prepared blocking layer for each FTO glass was obtained as about 140 nm and 100 nm, respectively. Therefore, these cases were not proper for construction purposes. SEM images of the surface and the thickness of the blocking layer for each case are observed in Figures 3 a-d. Then, blocking layer deposition was taken using 1 ml of the block solution for a new case as the thickness of the layer reached a little more than 40 nm. Figures 4a and 4b indicate the surface and the cross-section images of the blocking layer in this condition, where the thickness seems adequate for PCE goals.

The mesoporousTiO2 layer or the second film deposited in this research is effective in formation of the perovskite structure. In this report, the thickness of this layer was obtained about 250 nm, which is proper for the construction of the PSCs. This layer could also be deposited using alternative materials like Al_2O_3. M. Lee et al. reported using Al_2O_3 instead of mesoporous TiO_2 and obtained similar efficiency in 2012 [58]. The surface and the cross-section SEM images of the mesoporous TiO_2 layer are separately shown in Figures 4c and 4d. The TiO_2 films (mesoporous TiO_2 layer + blocking layer) range is specified in Figure 4d, where the total thickness is about 300 nm. TiO_2 mesoporous film thickness could be changed by variation in TiO_2 paste concentration by adding ethanol. Depletion region for the PSCs is a region some part of which is inside the mesoporous TiO_2 layer and another part is inside the perovskite layer and consists of n and p areas. If we consider the thickness of mesoporous TiO_2 film less than 250 nm, in so far as perovskite penetrates inside mesoporous TiO_2 layer, the thickness of the depletion region severely decreases, which leads to severe efficiency reduction [59-60]. The thickness of the mesoporous TiO_2 layer affects the thickness of the perovskite layer because perovskite diffuses into this structure and perovskite crystals will form there. Some parts of perovskite also are formed on this layer and a total thickness of 300 nm is obtained. The thickness of the perovskite layer on mesoporous TiO_2 layer is about 350 nm. According to the morphology of the TiO_2 films (Figs. 4a and 4c), it is illustrated that TiO_2 nanoparticles size is smaller in mesoprous film than block film. Therefore, the specific surface area of the mesoprous film is higher than that of blocking film.
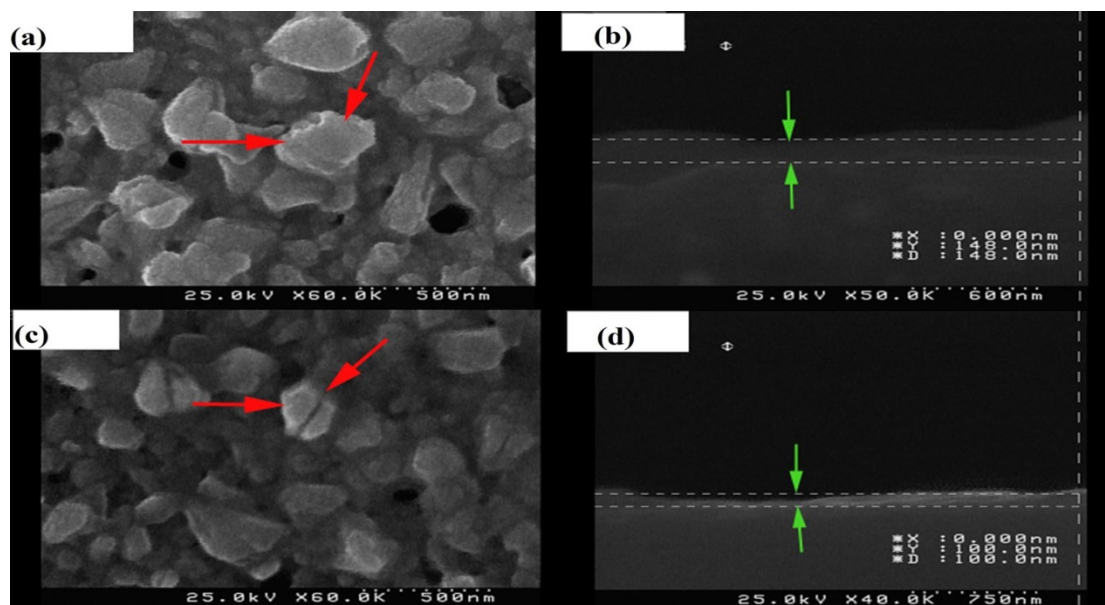

Figure 3. (a) The surface and (b) the cross-section SEM images of the blocking layer for deposition of 2.5 ml of the block solution, (c) the surface, and (d) the cross-section SEM images of the blocking layer for deposition of 2 ml of the block solution
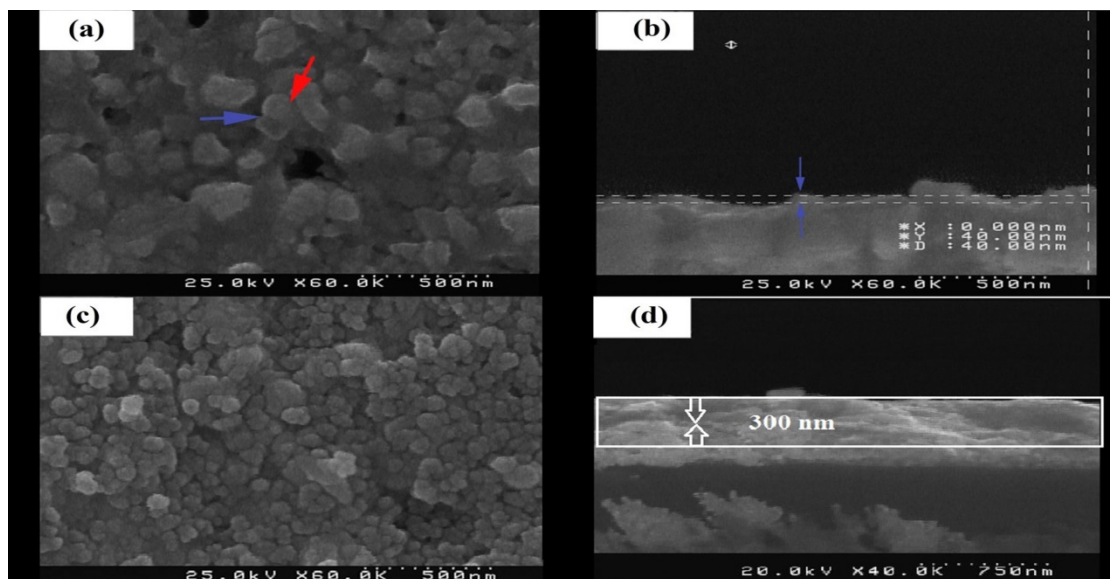
Figure 4. (a) The surface and (b) the cross-section SEM images of the blocking layer for deposition of 1 ml of the block solution; (c) the surface and (d) the cross-section SEM images of the mesoporous TiO₂ layer

In order to better understand the PSCs structure, one of the Gold-PSCs (cell No. 4) was tested through cross-section and surface analyses using an FE-SEM, and the results of EDS analysis are presented below. This cell was also broken for a cross-sectional image and its cross-section was covered with gold using Desk Sputter Coater. Figure 5a is an image of cell No. 4 broken from the cross-section. The variation in cell color results from decomposition of perovskite and its conversion to PbI₂ crystals. The cell surface on a scale of 2 mm is seen with specified areas of A and B in Figure 5b, in which area B is located on the Au electrode and area A is placed on the other surface of the cell. Besides, the area A where area C is specified and the area B are separately shown in Figures 5c and 5d on a scale of 5 µm. The results of EDS analysis for areas C and B could be seen in Figures 5e and 5f, respectively. Regarding the penetration depth defined for the FE-SEM during EDS analysis, the existing elements from the top layer to the down layer are specified in both analyses and the difference between two analyses is the gold in area B.
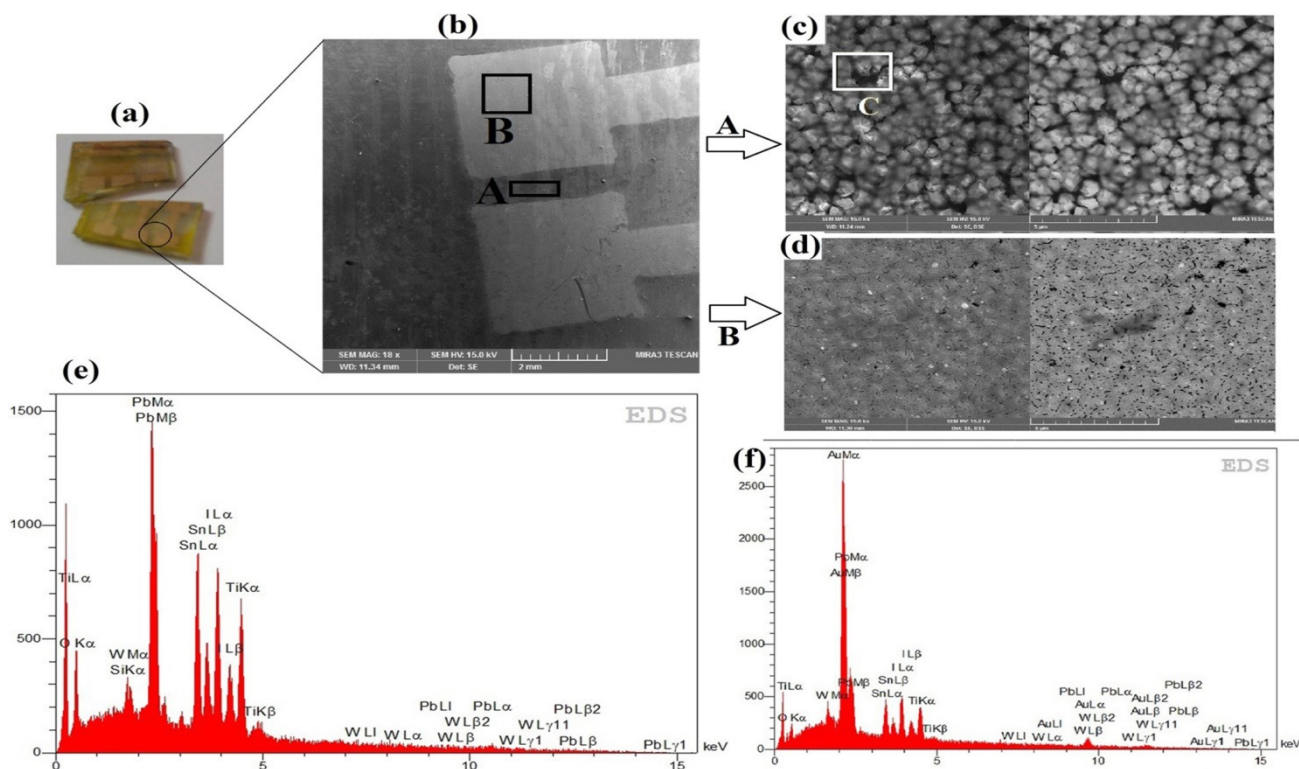
Figure 5. Images of (a) the broken cell No. 4 and (b) its surface on a scale of 2 mm; Top-view SEM images of the areas (c) A and (d) B on a scale of 5 µm; EDS analyses of the areas (e) C and (f) B

In Figure 6a, a cross-sectional image of cell No. 4 on a scale of 1 µm is seen where type of each layer and its thickness are specified and PbI₂ crystals could be seen in the place of perovskite. EDS analysis related to area D specified in the cross-sectional image is shown in Figure 6b. W, Al, and Sn are elements of FTO glass that are specified by the apparatus

(FE-SEM/EDS system) and the rests are the elements related to cell construction.

Five Gold-PSCs (No. 1-5) were tested three times after construction immediately and their photovoltaic parameters are shown in Table 1.
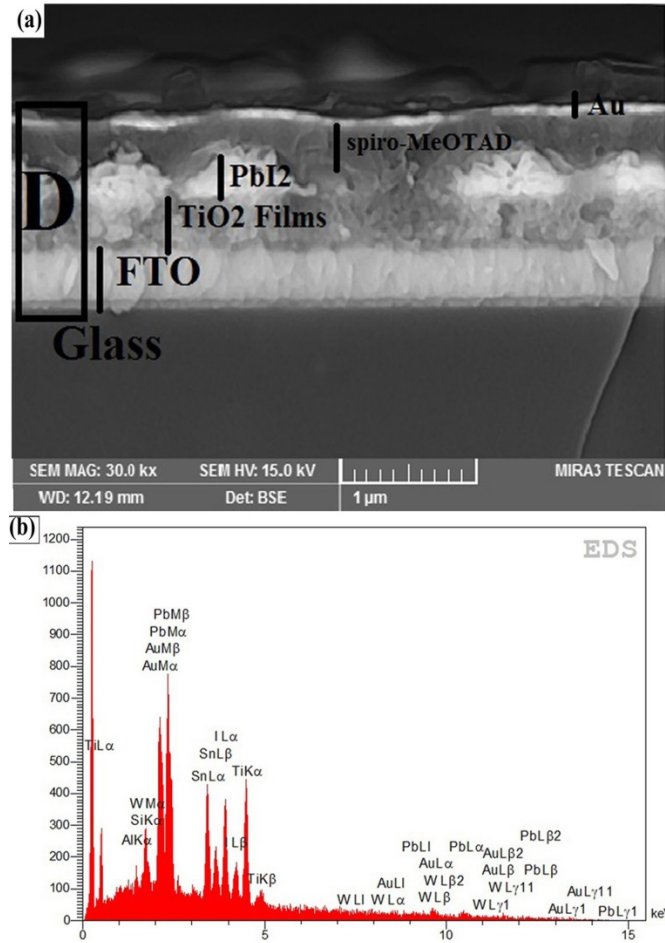
Table 1. Photovoltaic parameters of the 5 Gold-PSCs (No. 1-5) after construction

Cell number	V_{SC} (V)	J_{SC} (mA/cm^{-2})	FF	PCE (%)
1	0.96	20.4	0.69	13.51
	1.02	21.68	0.62	13.74
	0.98	21.88	0.59	12.58
2	1.08	23.25	0.54	13.6
	1.04	21.93	0.49	11.31
	1.13	23	0.55	14.32
3	1.03	24.12	0.57	14.25
	1.05	**24.2**	**0.59**	**14.95**
	1.04	24.52	0.58	14.88
4	0.99	20.42	0.67	13.56
	1.02	20.58	0.66	14.01
	1.01	19.74	0.67	13.42
5	1.15	18.1	0.68	14.31
	1.15	19.48	0.65	14.59
	1.12	17.68	0.6	11.95
Average	1.05	21.4	0.61	13.66
Standard deviation	± 0.06	± 2.16	± 0.06	± 1.03

Figure 6. (a) The cross-sectional SEM image of the cell No. 4 and (b) EDS analysis of the area D

The average PCE for these cellswas 13.66 % and cell No. 3 enjoyed optimal efficiency which was about 15 % at V_{OC} of 1.05 V, J_{SC} of 24.2 mA.cm^{-2}, and FF of about 0.59. The photovoltaic parameters of the HTM-free C-PSC (cell No. 6) were also measured after construction including V_{OC} = 0.89 (V), J_{SC} = 17.88 (mA.cm^{-2}), FF = 0.53, and PCE = 8.56 %. Figures 7a and 7b show the current density-voltage (J-V) graphs of the optimum Gold-PSC (cell No. 3) and cell No. 6 after construction under both illumination and dark conditions.

Figure 8 indicates an SEM image of the cross-sectional area of cell No. 6, in which the 20 µm thickness of the carbon layer is obvious. Cell No. 6 could be compared with similar research by H. Zhou et al. in which a 20.6 µm thickness average of carbon electrode led to optimal efficiency for HTM-free C-PSC [31]; however, they only used commercial conductive carbon paste for preparing carbon ink and achieved an average PCE of about 7 %.
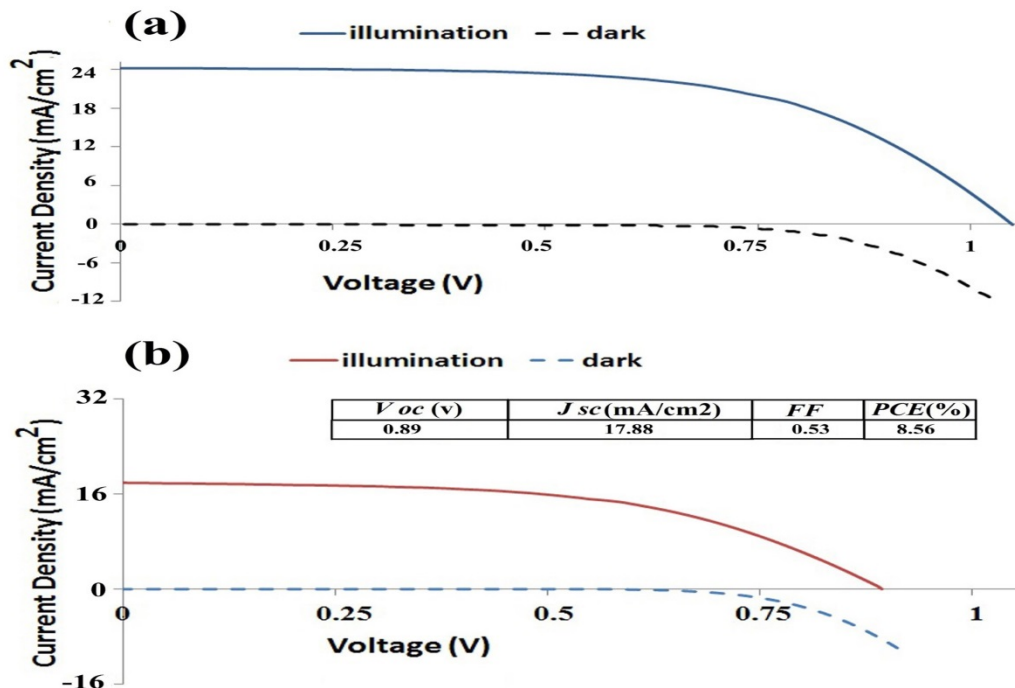
Figure 7. J-V graphs of (a) cell No. 3 and (b) cell No. 6 after construction under both illumination and dark conditions
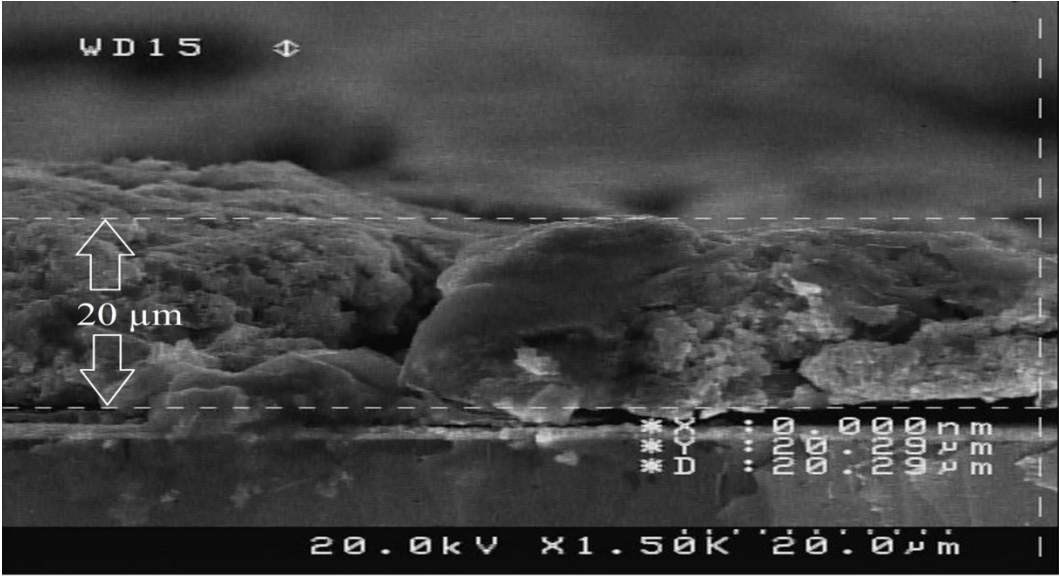
Figure 8. The cross-sectional SEM image of cell No. 6

The series resistance of solar cells could be calculated from their data and J-V graphs. R_S values of cell No. 3 and cell No. 6 under illumination conditions are calculated:

$$R_{s\,cell\,No.3} = 79\ \Omega,\ R_{s\,cell\,No.6} = 105\ \Omega$$

The higher series resistance for cell No. 6 is one reason for its lower efficiency since high series resistance leads to a decrease in J_{SC} and thus, a reduction in efficiency.

Table 2 shows the properties of cells No. 6 and No. 3 kept in a dark condition after construction at time intervals. The table itself indicates that the cell with carbon electrode experiences lower variations of the photovoltaic parameters than the cell with Au electrode; therefore, cell No. 6 is more stable. Furthermore, the parameters of cell No. 6 increased during 48 h after construction, which reflects the positive effect of the carbon layer on the performance of PSC. The PCE of cell

No. 6 experienced a maximum value of 10.2 % after 48 h. Table 2 indicates that the photovoltaic parameters of cell No. 6 were slightly reduced after 2000 h. On the contrary, parameters of cell No. 3 including J_{SC}, V_{OC}, and FF were reduced when compared to the initial data. According to Eq. 5, by reducing the photovoltaic parameters, the efficiency also decreased. Since the reduction of PCE over time is significant, cell No. 3 has not adequate stability.

After deposition of carbon ink (pre-dried carbon paste + ZrO_2 nanopowder + chlorobenzene) on the perovskite layer, the newly deposited carbon electrode starts to penetrate into the perovskite film until to be completely dried;thus, we could obtain better electrical conductivity and optimum efficiency after 48 h. The positive effect of carbon electrode implies reaching better conductivity after 2 days and it is an advantage that is not observed for gold electrode.

Table 2. Variation of the parameters of cell No. 3 and cell No. 6 over the time

Cell No. 3				Cell No. 6			
PCE (%)	V_{OC} (V)	J_{SC} (mA/cm^{-2})	FF	PCE (%)	V_{OC} (V)	J_{SC} (mA/cm^{-2})	FF
14.95	**1.05**	**24.2**	**0.59**	8.56	0.89	17.88	0.53
12.33	1.01	20.56	0.58	9.52	0.91	18.1	0.57
10	0.98	20.31	0.49	**10.2**	**0.94**	**18.4**	**0.59**
6.1	0.97	19.56	0.31	9.69	0.93	18.36	0.56
5.01	0.91	17.47	0.31	9.66	0.93	18.34	0.56
3.22	0.88	14.78	0.24	9.36	0.92	18.3	0.55
2.43	0.66	9.48	0.38	9.24	0.92	18.26	0.55
1.14	0.58	7.68	0.25	9.2	0.9	18.01	0.56

Cell No. 6 with carbon electrode deposited by a doctor-blade method including 40 % of carbon black nanopowder (30 nm) and 60 % of natural flaky graphite powder (3 µm) showed a proper PCE in comparison to the same devices for other researchers who applied various mixtures of carbon black and graphite in terms of percentage and particle size as the carbon electrode with different thicknesses for fabricating HTM-free C-PSCs [32, 35, 36, 40, 61-65]. Z. Liu et al. [32], H. Wang et al. [35], Z. Ku et al. [36], G. Yue et al. [61], Z. Liu et al. [62], X. Chang et al. [63], and J. Li et al. [64] manufactured various HTM-free C-PSCs with optimized PCEs of 6.88 %, 7.08 %, 6.64 %, 7.29 %, 6.21 %, 5 %, and 10.4 %, respectively. H. Wang et al. [35] obtained their optimum C-PSC using drop-coated perovskite and a printed

carbon electrode with a thickness of 5 µm made of 20 % of carbon black and 80 % of flaky graphite powder. Z. Liu et al. [32] prepared the optimum carbon film mixed with graphite flakes (10 µm), nano-graphite powder (40 nm) and carbon black powder (40 nm) at a weight ratio of 1:2:1, which was printed with a thickness of 65 µm; in another research [62], they improved the initial PCE of their carbon/graphite-based device from 6.21 % to 8.61 % by packaging with polydimethylsiloxane (PDMS). The HTM-free C-PSC made by G. Yue et al. [61] indicated that the mass fraction of 25 % carbon black particles on the surface and interspace of graphite flakes could improve the charge transfer by creating the most suitable contact sites with the perovskite layer and thus, could increase PCE of the device up to 7.29 %.

Figure 9 represents the variation of PCE and FF overtime for cell No. 3 and cell No. 6. J-V graphs of cell No. 6 at different time intervals are seen in Figure 10a, reflecting high stability as well. In addition, graphs of the variation of J_{SC} and V_{OC} are also shown at the inset. Cell No. 6 achieved a PCE value of 9.2 % which maintained 90 % of its optimal performance after 2000 h. J-V graphs of cell No. 3, which is not stable, show significant variations in Figure 10b and PCE is considerably reduced from 15 % to 1.14 % after 2000 h. Therefore, the above results represent that cell No. 6 is more stable and low-cost than the Gold-PSCs in this research and is comparable with some other newly constructed HTM-free C-PSCs during the last two years in terms of stability [24, 44, 48, 54, 66-70]. For example, the optimized device made by X. Wu et al. [46] retained over 80 % of its initial performance under a relative humidity of (80 ± 10) % after 1000 h of continuous illumination of one sun condition or the low-cost coal-based device manufactured by F. Meng et al. [24] maintained over 80 % of its initial PCE and achieved a PCE value of 8.60 % after 120 h in an ambient atmosphere at room temperature (humidity 30 %). Other recent HTM-free C-PSCs fabricated by J. Liu et al. [67], B. Zong et al. [68], and X. Zhang et al. [69] retained 85 % (after 55 days under dark conditions (23 °C and 30 % humidity)), 96 % (after 576 h in an atmosphere with humidity of about 45 %), and 95 % (after 20 days in air (relative humidity of 25 %-35 %)) of their initial efficiency, respectively.
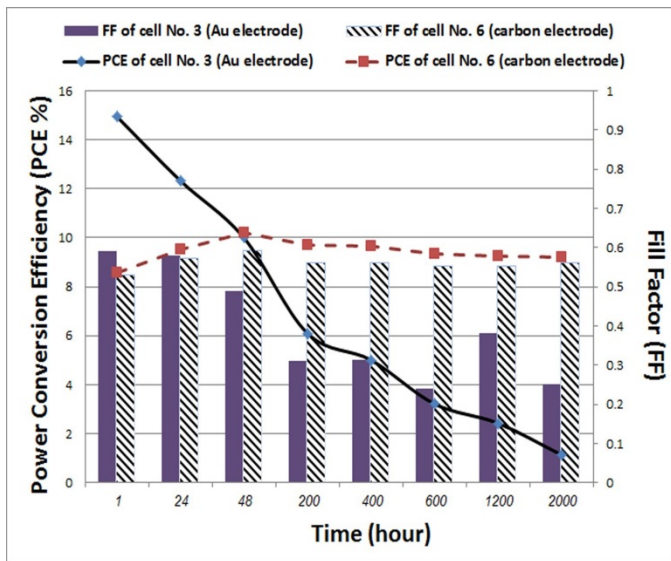
Figure 9. Variation of PCE and FF versus time for cell No. 3 and cell No. 6

In order to better understand the concept of stability and the sensitivity of the stability of PSCs, cell No. 5 was taken out of keeping place after 3000 h. This point should be mentioned that the keeping place of the cells is in a dark place under relative humidity of (50 ± 5) % at the average temperature of 25 °C which is suitable condition for controlling the stability of cells. Then, the decision was made on performing XRD analysis for cell No. 5. The original XRD pattern for cell No. 5 is seen in Figure 11a. Furthermore, Figure 11b shows an XRD pattern (Log-Scale for vertical axis) in which peaks are labeled by name and Miller indices (hkl). Here, for the XRD pattern, there are 27 peaks out of which 15 cases are related to TiO_2 and PbI_2. All peaks related to TiO_2, PbI_2, and Au are specified in the graph and it is obvious that SnO_2 and SiO_2 peaks are related to FTO glass.
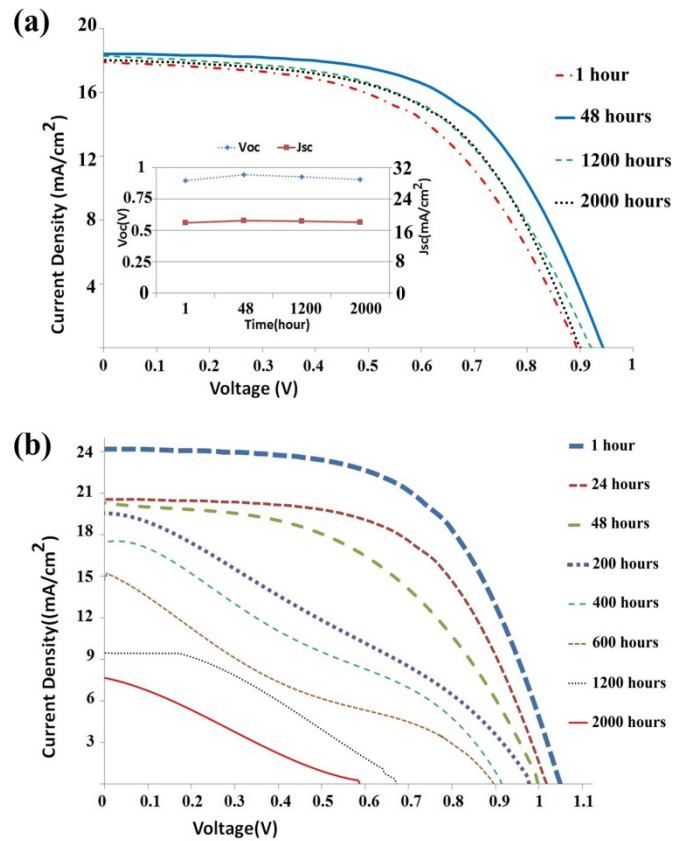

Figure 10. J-V graphs of (a) cell No. 6 and (b) cell No. 3 over time
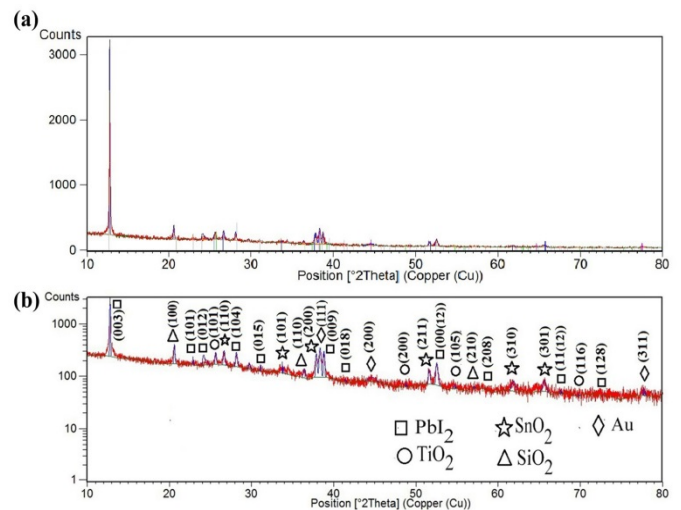

Figure 11. (a) Original XRD pattern for cell No. 5 and (b) with Log-Scale for vertical axis on which peaks are labeled by name and Miller indices (hkl)

Values of 2θ related to the peaks of each layer are presented in Table 3a in which the peaks specified with * are the highest peaks for each layer. Table 3b shows values of 2θ, θ, COS(θ), β or FWHM (°), β or FWHM (radian) related to the highest peaks for TiO_2 (JCPDS card no. 21-1272. The reason for the presence of mixed phase of TiO_2 is that we used amorphous TTIP for the preparation of the block solution and PbI_2 (JCPDS card no. 07-0235) is specified. FWHM is the integral breadth of a reflection (in radians 2θ) located at 2θ; this quantity is also sometimes denoted by Δ (2θ).

Here, by using XRD pattern (X'Pert HighScore Plus software) and by interpretation of Debye-Scherrer method, average crystallite size for TiO_2 and PbI_2 is calculated. As is

known, the average crystallite size is calculated by Debye-Scherrer equation in the form of Eq. 7 [71-75], where D is the average crystallite size in Ångström (Å), λ is the X-ray wavelength in Ångström (Å), β or FWHM is the peak width of the diffraction peak profile at half maximum height resulting from small crystallite size in radians and K is a constant related to crystallite shape, normally taken as 0.9. The value of β on 2θ axis of diffraction profile must be in radian. This can be attributed to the fact that "crystallite size" is not synonymous with "particle size", while X-Ray diffraction is sensitive to the crystallite size inside the particles. Since anode material of X-ray diffractometer is copper (Cu), λ value is 1.54 (Å). (λ = 1.54 (Å) = 0.154 nm).

$$D = \frac{K.\lambda}{\beta.COS(\theta)} \qquad (7)$$

$$D_{TiO_2} = \frac{0.9*1.54\ (Å)}{0.97511*0.00247} = 576\ (Å) = 58\ nm$$

$$D_{PbI_2} = \frac{0.9*1.54\ (Å)}{0.99379*0.00075} = 1859\ (Å) = 186\ nm$$

According to the Debye-Scherrer equation, the average crystallite size for TiO_2 and PbI_2 crystals is about 58 nm and 186 nm, respectively. As observed, the results exhibited that perovskite crystals of cell No. 5 were completely decomposed and were replaced by PbI_2 crystals with the average crystallite size of 186 nm after 3000 h, which demonstrated unstable properties of the Gold-PSCs.

Table 3. Values of (a) 2θ related to the peaks of each layer and (b) 2θ, θ, COS(θ), β or FWHM (°) , β or FWHM (radian) related to the highest peaks of TiO_2 and PbI_2

(a)	2θ (°) related to the peaks					
PbI_2	**12.7690***	22.8672	24.1230	28.1308	31.0825	38.7830
	41.4030	52.5087	58.5630	67.5930	72.8330	
TiO_2	**25.6203***	48.7630	54.6830	69.7930		
SnO_2	26.6404	33.7440	**37.8630***	51.5712	61.8423	65.6005
SiO_2	**20.5946***	36.3864	57.0430			
Au	**38.3079***	44.6031	77.6930			
(b)	2θ (°)	θ (°)	COS (θ)	FWHM (°)	FWHM (radian)	
PbI_2	12.7690	6.3845	0.99379	0.04309	**0.00075**	
TiO_2	25.6203	12.8101	0.97511	0.14191	**0.00247**	

4. CONCLUSIONS

In summary, we have successfully manufactured two types of PSCs including five Gold-PSCs based on Au electrode and one HTM-free C-PSC based on carbon electrode. The five Gold-PSCs showed an average initial PCE of 13.66 % and the optimum Gold-PSC achieved high PCE of about 15 %, whereas the HTM-free C-PSC exhibited an initial PCE value of 8.56 %, which is less than that of Gold-PSCs because of its higher series resistance (R_S), leading to a decrease in J_{SC} and the reduction of PCE. For fabricating the HTM-free C-PSC, a kind of carbon paste consisting of carbon black nanopowder (30 nm) and natural flaky graphite powder (3 µm) was developed at a weight ratio of 2:3 and it was applied to deposition of carbon electrode by a doctor-blade method with a thickness of 20 µm. The PCE value of the HTM-free C-PSC experienced a moderate rise up to 10.2 % within 48 h followed by a gradual drop to 9.2 % after 2000 h which demonstrated outstanding stability over the period in the dark under ambient conditions (relative humidity of (50 ± 5) %, average room temperature of 25 °C) because of retaining up to 90 % of its optimal PCE. In the same period, the PCE value of the optimized Gold-PSC declined dramatically to 1.14 %, which proved unstable behavior over time toward air and moisture. This study indicated complete destruction of perovskite crystals and conversion to PbI_2 crystals using XRD analysis. More importantly, the constructed HTM-free C-PSC was comparable with other newly constructed devices in terms of stability. The present work paves the way for developing low-cost and highly-stable PSCs in the future and is also helpful to improve the efficiency of C-PSCs further.

5. ACKNOWLEDGEMENT

REFERENCES

1. Almora, O., Vaillant-Roca, L. and Garcia-Belmonte, G., "Perovskite solar cells: A brief introduction and some remarks", *Revista Cubana de Fisica*, Vol. 34, No. 1, (2017), 58-68. (http://revistacubanadefisica.org/index.php/rcf/article/view/RCF_34-1_58).

2. Chouk, R., Haouanoh, D., Aguir, C., Bergaoui, M., Toubane, M., Bensouici, F., Tala-Ighil, R., Erto, A. and Khalfaoui, M., "Dye sensitized TiO_2 and ZnO charge transport layers for efficient planar perovskite solar cells: Experimental and DFT insights", *Journal of Electronic Materials*, Vol. 49, No. 2, (2020), 1396-1403. (https://doi.org/10.1007/s11664-019-07839-7).

3. Wei, H. and Huang, J., "Halide lead perovskites for ionizing radiation detection", *Nature Communications*, Vol. 10, No. 1066, (2019). (https://doi.org/10.1038/s41467-019-08981-w).

4. Kang, A.K., Zandi, M.H. and Gorji, N.E., "Fabrication and degradation analysis of perovskite solar cells with graphene reduced oxide as hole transporting layer", *Journal of Electronic Materials*, Vol. 49, (2020), 2289-2295. (https://doi.org/10.1007/s11664-019-07893-1).

5. Maleki, E, Ranjbar, M. and Kahani, S.A., "The effect of antisolvent dropping delay time on the morphology and structure of the perovskite layer in the hole transport material free perovskite solar cells", *Progress in Color, Colorants and Coatings*, Vol. 14, No. 1, (2021), 47-54. (https://dx.doi.org/10.30509/pccc.2021.81671).

6. Sarvari, R., Agbolaghi, S. and Massoumi, B., "Engineered organic halide perovskite solar cells by incorporation of surface‐manipulated graphenic nanosheets", *Journal of Materials Science: Materials in Electronics*, Vol. 30, No. 10, (2019), 9281-9288. (https://doi.org/10.1007/s10854-019-01258-4).

7.   Sarvari, R., Agbolaghi. S. and Massoumi, B., "Role of graphene ordered modifiers in regulating the organic halide perovskite devices", *Optical Materials*, Vol. 92, (2019), 81-86. (https://doi.org/10.1016/j.optmat.2019.04.014).

8.   Agbolaghi, S., "Efficacy beyond 17 % via engineering the length and quality of grafts in organic halide perovskite/CNT photovoltaics", *New Journal of Chemistry*, Vol. 26, No. 43, (2019), 10567-10574. (https://doi.org/10.1039/C9NJ02074H).

9.   Kojima, A., Teshima, K., Shirai, Y. and Miyasaka, T., "Organometal halide perovskites as visible-light sensitizers for photovoltaic cells", *Journal of the American Chemical Society*, Vol. 131, No. 17, (2009), 6050-6051. (https://doi.org/10.1021/ja809598r).

10. Corpus-Mendoza, A.N., Cruz-Silva, B.S., Ramirez-Zúñiga, G., Moreno-Romero, P. M., Liu, F. and Hu, H., "Use of magnetic fields for surface modification of PbI$_2$ layers to increase the performance of hybrid perovskite solar cells", *Journal of Electronic Materials*, Vol. 49, (2020), 3106-3113. (https://doi.org/10.1007/s11664-020-08009-w).

11. Ankireddy, K., Lavery, B.W. and Druffel, T., "Atmospheric processing of perovskite solar cells using intense pulsed light sintering", *Journal of Electronic Materials*, Vol. 47, (2018), 1285-1292. (https://doi.org/10.1007/s11664-017-5893-y).

12. Heo, J.H., Im, S.H., Noh, J.H., Mandal, T.N., Lim, C.S., Chang, J.A., Lee, Y.H., Kim, H.J., Sarkar, A., Nazeeruddin, Md.K., Grätzel, M. and Seok, S.-Il, "Efficient inorganic–organic hybrid heterojunction solar cells containing perovskite compound and polymeric hole conductors", *Nature Photonics*, Vol. 7, No. 6, (2013), 486-491. (https://doi.org/10.1038/nphoton.2013.80).

13. Thakur, N., Mehra, R. and Devi, C., "Efficient design of perovskite solar cell using parametric grading of mixed halide perovskite and copper iodide", *Journal of Electronic Materials*", Vol. 47, (2018), 6935-6942. (https://doi.org/10.1007/s11664-018-6620-z).

14. limi, B., Mollar, M., Marí, B. and Chtourou, R., "Thin film of perovskite (mixed-cation of lead bromide FA$_{1-x}$MA$_x$PbBr) obtained by one-step method", *Journal of Electronic Materials*", Vol. 48, (2019), 8014-8023. (https://doi.org/10.1007/s11664-019-07638-0).

15. Phan Vu, T., Nguyen, M.T., Nguyen, T.T., Vu, T.D., Nguyen, D.L., An, N.M., Nguyen, M.H., Sai, C.D., Bui, V.D., Hoang, C.H., Truong, T.T., Lai, N.D. and Tran, T.N., "Three-photon absorption induced photoluminescence in organo-lead mixed halide perovskites", *Journal of Electronic Materials*", Vol. 46, (2017), 3622-3626. (https://doi.org/10.1007/s11664-017-5407-y).

16. Hadadian, M., Smått, J.H. and Correa-Baena, J.P., "The role of carbon-based materials in enhancing the stability of perovskite solar cells", *Energy & Environmental Science*, Vol. 13, No. 5, (2020), 1377-1407. (https://doi.org/10.1039/C9EE04030G).

17. Hosseinnezhad, M., "Enhanced performance of dye-sensitized solar cells using perovskite/DSSCs tandem design", *Journal of Electronic Materials*, Vol. 48, (2019), 5403-5408. (https://doi.org/10.1007/s11664-019-07272-w).

18. Leijtens, T., Eperon, G.E., Pathak, S., Abate, A., Lee, M.M. and Snaith, H.J., "Overcoming ultraviolet light instability of sensitized TiO$_2$ with meso-superstructured organometal tri-halide perovskite solar cells", *Nature Communications*, Vol. 4, No. 1, (2013), 1-8. (https://doi.org/10.1038/ncomms3885).

19. Domanski, K., Correa-Baena, J.P., Mine, N., Nazeeruddin, Md.K., Abate, A., Saliba, M., Tress, W., Hagfelft, A. and Grätzel, M., "Not all that glitters is gold: Metal-migration-induced degradation in perovskite solar cells", *ACS Nano*, Vol. 10, No. 6, (2016), 6306-6314. (https://doi.org/10.1021/acsnano.6b02613).

20. Lee, J., Singh, S., Kim, S. and Baik, S., "Graphene interfacial diffusion barrier between CuSCN and Au layers for stable perovskite solar cells", *Carbon*, Vol. 157, (2020), 731-740. (https://doi.org/10.1016/j.carbon.2019.10.101).

21. Cao, K., Zuo, Z., Cui, J., Shen, Y., Moehl, T., Zakeeruddin, S.M., Grätzel, M. and Wang, M., "Efficient screen printed perovskite solar cells based on mesoscopic TiO$_2$/Al$_2$O$_3$/NiO/carbon architecture", *Nano Energy*, Vol. 17, (2015), 171-179. (https://doi.org/10.1016/j.nanoen.2015.08.009).

22. Zhang, N., Guo, Y., Yin, X., He, M. and Zou, X., "Spongy carbon film deposited on a separated substrate as counter electrode for perovskite-based solar cell", *Materials Letters*, Vol. 182, (2016), 248-252. (https://doi.org/10.1016/j.matlet.2016.07.004).

23. Aitola, K., Domanski, K., Correa-Baena, J.P., Sveinbjörnsson, K., Saliba, M., Abate, A., Grätzel, M., Kauppinen, E., Johansson, M.J.,

Tress, W., Boschloo, G. and Hagfeldt, A., "High temperature-stable perovskite solar cell based on low-cost carbon nanotube hole contact", *Advanced Materials*, Vol. 29, No. 17, (2017), 1606398. (https://doi.org/10.1002/adma.201606398).

24. Meng, F., Gao, L., Yan, Y., Cao, J., Wang, N., Wang, T. and Ma, T., "Ultra-low-cost coal-based carbon electrodes with seamless interfacial contact for effective sandwich-structured perovskite solar cells", *Carbon*, Vol. 145, (2019), 290-296. (https://doi.org/10.1016/j.carbon.2019.01.047).

25. Fagiolari, L. and Bella, F., "Carbon-based materials for stable, cheaper and large-scale processable perovskite solar cells, *Energy & Environmental Science*, Vol. 12, No. 12, (2019), 3437-3472. (https://doi.org/10.1039/C9EE02115A).

26. Yang, Y., Xiao, J., Wei, H., Zhu, L., Li, D., Luo, Y., Wu, H. and Meng, Q., "An all-carbon counter electrode for highly efficient hole-conductor-free organo-metal perovskite solar cells", *RSC Advances*, Vol. 4, No. 95, (2014), 52825-52830. (https://doi.org/10.1039/C4RA09519G).

27. Li, Z., Kulkarni, S.A., Boix, P.P., Shi, E., Cao, A., Fu, K., Wong, L.H., Xiong, Q., Zhang, J., Batabya, S.K., Mhaisalkar, S.G. and Mathews, N., "Laminated carbon nanotube networks for metal electrode-free efficient perovskite solar cells", *ACS Nano*, Vol. 8, No. 7, (2014), 6797-6804. (https://doi.org/10.1021/nn501096h).

28. Wang, S., Jiang, P., Shen, W., Mei, A., Xiong, S., Jiang, X., Rong, Y., Tang, Y., Hu, Y. and Han, H., "A low-temperature carbon electrode with good perovskite compatibility and high flexibility in carbon based perovskite solar cells", *Chemical Communications*, Vol. 55, No. 19, (2019), 2765-2768. (https://doi.org/10.1039/C8CC09905G).

29. Zhou, H., Shi, Y., Wang, K., Dong, Q., Bai, X., Xing, Y.,Du, Y. and Ma, T., "Low-temperature processed and carbon-based ZnO/CH$_3$NH$_3$PbI$_3$/C planar heterojunction perovskite solar cells", *The Journal of Physical Chemistry C*, Vol. 119, No. 9, (2015), 4600-4605. (https://doi.org/10.1021/jp512101d).

30. Kay, A. and Grätzel, M., "Low cost photovoltaic modules based on dye sensitized nanocrystalline titanium dioxide and carbon powder", *Solar Energy Materials and Solar Cells*, Vol. 44, No. 1, (1996), 99-117. (https://doi.org/10.1016/0927-0248(96)00063-3).

31. Zhou, H., Shi, Y., Dong, Q., Zhang, H., Xing, Y., Wang, K., Du, Y. and Ma, T., "Hole-conductor-free, metal-electrode-free TiO$_2$/CH$_3$NH$_3$PbI$_3$ heterojunction solar cells based on a low-temperature carbon electrode", *The Journal of Physical Chemistry Letters*, Vol. 5, No. 18, (2014), 3241-3246. (https://doi.org/10.1021/jz5017069).

32. Liu, Z., Shi, T., Tang, Z., Sun, B. and Liao, G., "Using a low-temperature carbon electrode for preparing hole-conductor-free perovskite heterojunction solar cells under high relative humidity", *Nanoscale*, Vol. 8, No. 13, (2016), 7017-7023. (https://doi.org/10.1039/C5NR07091K).

33. Fu, H., "Review of lead-free halide perovskites as light-absorbers for photovoltaic applications: from materials to solar cells", *Solar Energy Materials and Solar Cells*, Vol. 193, (2019), 107-132. (https://doi.org/10.1016/j.solmat.2018.12.038).

34. Etgar, L., Gao, P., Xue, Z., Peng, Q., Chandiran, A.K., Liu, B., Nazeeruddin, Md.K. and Grätzel, M., "Mesoscopic CH$_3$NH$_3$PbI$_3$/TiO$_2$ heterojunction solar cells", *Journal of the American Chemical Society*, Vol. 134, No. 42, (2012), 17396-17399. (https://doi.org/10.1021/ja307789s).

35. Wang, H., Hu, X. and Chen, H., "The effect of carbon black in carbon counter electrode for CH$_3$NH$_3$PbI$_3$/TiO$_2$ heterojunction solar cells", *RSC Advances*, Vol. 5, No. 38, (2015), 30192-30196. (https://doi.org/10.1039/C5RA02325D).

36. Ku, Z., Rong, Y., Xu, M., Liu, T. and Han, H., "Full printable processed mesoscopic CH$_3$NH$_3$PbI$_3$/TiO$_2$ heterojunction solar cells with carbon counter electrode", *Scientific Reports*, Vol. 3, No. 3132, (2013). (https://doi.org/10.1038/srep03132).

37. Xu, M., Rong, Y., Ku, Z., Mei, A., Liu, T., Zhang, L., Li, X. and Han, H., "Highly ordered mesoporous carbon for mesoscopic CH$_3$NH$_3$PbI$_3$/TiO$_2$ heterojunction solar cell", *Journal of Materials Chemistry A*, Vol. 2, No. 23, (2014), 8607-8611. (https://doi.org/10.1039/C4TA00379A).

38. Rong, Y., Ku, Z., Mei, A., Liu, T., Xu, M., Ko, S., Li, X. and Han, H., "Hole-conductor-free mesoscopic TiO$_2$/CH$_3$NH$_3$PbI$_3$ heterojunction solar cells based on anatase nanosheets and carbon counter electrodes", *The Journal of Physical Chemistry Letters*, Vol. 5, No. 12, (2014), 2160-2164. (https://doi.org/10.1021/jz500833z).

39. Xu, M., Liu, G., Li, X., Wang, H., Rong, Y., Ku, Z., Hu, M., Yang, Y., Liu, L., Liu, T. and Chen, J., "Efficient monolithic solid-state dye-sensitized solar cell with a low-cost mesoscopic carbon based screen printable counter electrode", *Organic Electronics*, Vol. 14, No. 2, (2013), 628-634. (https://doi.org/10.1016/j.orgel.2012.12.015).

40. Zhang, L., Liu, T., Liu, L., Hu, M., Yang, Y., Mei, A. and Han, H., "The effect of carbon counter electrodes on fully printable mesoscopic perovskite solar cells", *Journal of Materials Chemistry A*, Vol. 3, No. 17, (2015), 9165-9170. (https://doi.org/10.1039/C4TA04647A).

41. Fu, Q., Tang, X., Huang, B., Hu, T., Tan, L., Chen, L. and Chen, Y., "Recent progress on the long-term stability of perovskite solar cells", *Advanced Science*, Vol. 5, No. 5, (2018), 1700387. (https://doi.org/10.1002/advs.201700387).

42. Khenkin, M.V., Katz, E.A., Abate, A., Bardizza, G., Berry, J.J., Brabec, C. and Cheacharoen, R., "Consensus statement for stability assessment and reporting for perovskite photovoltaics based on ISOS procedures", *Nature Energy*, Vol. 5, No. 1, (2020), 35-49. (https://doi.org/10.1038/s41560-019-0529-5).

43. Wang, Y., Wu, T., Barbaud, J., Kong, W., Cui, D., Chen, H., Yang, X. and Han, L., "Stabilizing heterostructures of soft perovskite semiconductors", *Science*, Vol. 365, No. 6454, (2019), 687-691. (https://doi.org/10.1126/science.aax8018).

44. Wang, R., Mujahid, M., Duan, Y., Wang, Z.K., Xue, J. and Yang, Y., "A review of perovskites solar cell stability", *Advanced Functional Materials*, Vol. 29, No. 47, (2019), 1808843. (https://doi.org/10.1002/adfm.201808843).

45. Hong, Q.M., Xu, R.P., Jin, T.Y., Tang, J.X. and Li, Y.Q., "Unraveling the light-induced degradation mechanism of CH₃NH₃PbI₃ perovskite films", *Organic Electronics*, Vol. 67, (2019), 19-25. (https://doi.org/10.1002/solr.201900394).

46. Wu, X., Xie, L., Lin, K., Lu, J., Wang, K., Feng, W., Fan, B. and Wei, Z., "Efficient and stable carbon-based perovskite solar cells enabled by the inorganic interface of CuSCN and carbon nanotubes", *Journal of Materials Chemistry A*, Vol. 7, No. 19, (2019), 12236-12243. (https://doi.org/10.1039/C9TA02014D).

47. Chu, Q.Q., Ding, B., Peng, J., Shen, H., Li, X., Liu, Y. and Catchpole, K.R., "Highly stable carbon-based perovskite solar cell with a record efficiency of over 18 % via hole transport engineering", *Journal of Materials Science & Technology*, Vol. 35, No. 6, (2019), 987-993.(https://doi.org/10.1016/j.jmst.2018.12.025).

48. Wang, S., Liu, H., Bala, H., Zong, B., Huang, L., Guo, Z.A. and Zhang, Z., "A highly stable hole-conductor-free Cs$_x$MA$_{1-x}$PbI₃ perovskite solar cell based on carbon counter electrode", *Electrochimica Acta*, Vol. 335, (2020), 135686. (https://doi.org/10.1016/j.electacta.2020.135686).

49. Chen, H. and Yang, S., "Stabilizing and scaling up carbon-based perovskite solar cells", *Journal of Materials Research*, Vol. 32, No. 16, (2017), 3011-3020. (https://doi.org/10.1557/jmr.2017.294).

50. Yu, Z., Chen, B., Liu, P., Wang, C., Bu, C., Cheng, N. and Zhao, X., "Stable organic–inorganic perovskite solar cells without hole-conductor layer achieved via cell structure design and contact engineering", *Advanced Functional Materials*, Vol. 26, No. 27, (2016), 4866-4873. (https://doi.org/10.1002/adfm.201504564).

51. Habisreutinger, S.N., Leijtens, T., Eperon, G.E., Stranks, S.D., Nicholas, R.J. and Snaith, H.J., "Carbon nanotube/polymer composites as a highly stable hole collection layer in perovskite solar cells", *Nano Letters*, Vol. 14, No. 10, (2014), 5561-5568. (https://doi.org/10.1021/nl501982b).

52. Baranwal, A.K., Kanaya, S., Peiris, T.N., Mizuta, G., Nishina, T., Kanda, H. and Ito, S.,"100 °C thermal stability of printable perovskite solar cells using porous carbon counter electrodes", *ChemSusChem*, Vol. 9, No. 18, (2016), 2604-2608. (https://doi.org/10.1002/cssc.201600933).

53. Wang, P., Chai, N., Wang, C., Hua, J., Huang, F., Peng, Y. and Cheng, Y.B., "Enhancing the thermal stability of the carbon-based perovskite solar cells by using a Cs$_x$FA$_{1-x}$PbBr$_x$I$_{3-x}$ light absorber", *RSC Advances*, Vol. 9, No. 21, (2019), 11877-11881. (https://doi.org/10.1039/C9RA00043G).

54. Xiang, S., Li, W., Wei, Y., Liu, J., Liu, H., Zhu, L. and Chen, H., "Natrium doping pushes the efficiency of carbon-based CsPbI₃ perovskite solar cells to 10.7 %", *iScience*, Vol. 15, (2019), 156-164. (https://doi.org/10.1016/j.isci.2019.04.025).

55. Liu, H., Bala, H., Zhang, B., Zong, B., Huang, L., Fu, W. and Zhan, Z., "Thickness-dependent photovoltaic performance of TiO₂ blocking layer for perovskite solar cells", *Journal of Alloys and Compounds*, Vol. 736, (2018), 87-92. (https://doi.org/10.1016/j.jallcom.2017.11.081).

56. Gouda, L., Rietwyk, K.J., Hu, J., Kama, A., Ginsburg, A., Priel, M. and Zaban, A., "High-resolution study of TiO₂ contact layer thickness on the performance of over 800 perovskite solar cells", *ACS Energy Letters*, Vol. 2, No. 10, (2017), 2356-2361. (https://doi.org/10.1021/acsenergylett.7b00718).

57. Sung, Y.M., "Deposition of TiO₂ blocking layers of photovoltaic cell using RF magnetron sputtering technology", *Energy Procedia*, Vol. 34, (2013), 582-588. (https://doi.org/10.1016/j.egypro.2013.06.788).

58. Lee, M.M., Teuscher, J., Miyasaka, T., Murakami, T.N. and Snaith, H.J., "Efficient hybrid solar cells based on meso-superstructured organometal halide perovskites", *Science*, Vol. 338, No. 6107, (2012), 643-647. (https://doi.org/10.1126/science.1228604).

59. Aharon, S., Gamliel, S., El Cohen, B. and Etgar, L., "Depletion region effect of highly efficient hole conductor free CH₃NH₃PbI₃ perovskite solar cells", *Physical Chemistry Chemical Physics*, Vol. 16, No. 22, (2014), 10512-10518. (https://doi.org/10.1039/C4CP00460D).

60. Laban, W.A. and Etgar, L., "Depleted hole conductor-free lead halide iodide heterojunction solar cells", *Energy & Environmental Science*, Vol. 6, No. 11, (2013), 3249-3253. (https://doi.org/10.1039/C3EE42282H).

61. Yue, G., Chen, D., Wang, P., Zhang, J., Hu, Z. and Zhu, Y., "Low-temperature prepared carbon electrodes for hole-conductor-free mesoscopic perovskite solar cells", *Electrochimica Acta*, Vol. 218, (2016), 84-90. (https://doi.org/10.1016/j.electacta.2016.09.112).

62. Liu, Z., Sun, B., Shi, T., Tang, Z. and Liao, G., "Enhanced photovoltaic performance and stability of carbon counter electrode based perovskite solar cells encapsulated by PDMS", *Journal of Materials Chemistry A*, Vol. 4, No. 27, (2016), 10700-10709. (https://doi.org/10.1039/C6TA02851A).

63. Chang, X., Li, W., Zhu, L., Liu, H., Geng, H., Xiang, S. and Chen, H., "Carbon-based CsPbBr₃ perovskite solar cells: All-ambient processes and high thermal stability", *ACS Applied Materials & Interfaces*, Vol. 8, No. 49, (2016), 33649-33655. (https://doi.org/10.1021/acsami.6b11393).

64. Li, J., Yao, J.X., Liao, X.Y., Yu, R.L., Xia, H.R., Sun, W.T. and Peng, L.M., "A contact study in hole conductor free perovskite solar cells with low temperature processed carbon electrodes", *RSC Advances*, Vol. 7, No. 34, (2017), 20732-20737. (https://doi.org/10.1039/C7RA00066A).

65. Meng, F., Liu, A., Gao, L., Cao, J., Yan, Y., Wang, N. and Ma, T., "Current progress in interfacial engineering of carbon-based perovskite solar cells", *Journal of Materials Chemistry A*, Vol. 7, No. 15, (2019), 8690-8699. (https://doi.org/10.1039/C9TA01364D).

66. Xiao, Y., Wang, C., Kondamareddy, K.K., Liu, P., Qi, F., Zhang, H. and Zhao, X.Z., "Enhancing the performance of hole-conductor free carbon-based perovskite solar cells through rutile-phase passivation of anatase TiO₂ scaffold", *Journal of Power Sources*, Vol. 422, (2019), 138-144. (https://doi.org/10.1016/j.jpowsour.2019.03.039).

67. Liu, J., Zhou, Q., Thein, N.K., Tian, L., Jia, D., Johansson, E.M. and Zhang, X., "In situ growth of perovskite stacking layers for high-efficiency carbon-based hole conductor free perovskite solar cells", *Journal of Materials Chemistry A*, Vol. 7, No. 22, (2019), 13777-13786. (https://doi.org/10.1039/C9TA02772F).

68. Zong, B., Fu, W., Guo, Z.A., Wang, S., Huang, L., Zhang, B. and Zhang, Z., "Highly stable hole-conductor-free perovskite solar cells based upon ammonium chloride and a carbon electrode", *Journal of Colloid and Interface Science*, Vol. 540, (2019), 315-321. (https://doi.org/10.1016/j.jcis.2019.01.035).

69. Zhang, X., Zhou, Y., Li, Y., Sun, J., Lu, X., Gao, X. and Liu, J.M., "Efficient and carbon-based hole transport layer-free CsPbI₂Br planar perovskite solar cells using PMMA modification", *Journal of Materials Chemistry C*, Vol. 7, No. 13, (2019), 3852-3861. (https://doi.org/10.1039/C9TC00374F).

70. Li, W., Huang, Y., Liu, Y., Tekell, M.C. and Fan, D.E., "Three dimensional nanosuperstructures made of two-dimensional materials by design: Synthesis, properties, and applications", *Nano Today*, Vol. 29, (2019), 100799. (https://doi.org/10.1016/j.nantod.2019.100799).

71. Hammouda, S.B., Salazar, C., Zhao, F., Ramasamy, D.L., Laklova, E., Iftekhar, S. and Sillanpää, M., "Efficient heterogeneous electro-Fenton incineration of a contaminant of emergent concern-cotinine-in aqueous medium using the magnetic double perovskite oxide Sr₂FeCuO₆ as a highly stable catalyst: Degradation kinetics and oxidation products", *Applied Catalysis B: Environmental*, Vol. 240, (2019), 201-214. (https://doi.org/10.1016/j.apcatb.2018.09.002).

72. Hu, Y., Schlipf, J., Wussler, M., Petrus, M.L., Jaegermann, W., Bein, T. and Docampo, P., "Hybrid perovskite/perovskite heterojunction solar cells", *ACS Nano*, Vol. 10, No. 6, (2016), 5999-6007. (https://doi.org/10.1021/acsnano.6b01535).

73. Yu, H., Liu, X., Xia, Y., Dong, Q., Zhang, K., Wang, Z. and Li, Y., "Room-temperature mixed-solvent-vapor annealing for high performance perovskite solar cells", *Journal of Materials Chemistry A*, Vol. 4, No. 1, (2016), 321-326. (https://doi.org/10.1039/C5TA08565A).

74. Siddique, M.N., Ahmed, A. and Tripathi, P., "Electric transport and enhanced dielectric permittivity in pure and Al doped NiO nanostructures", *Journal of Alloys and Compounds*, Vol. 735, (2018), 516-529. (https://doi.org/10.1016/j.jallcom.2017.11.114).

75. Beegum, K.B., Paulose, M., Peter, V.J., Raphael, R., Sreeja, V.G. and Anila, E.I., "Study on the effect of synthesis temperature on the structural and surface morphological and optical properties of methyl ammonium lead iodide nanoparticles by sol-gel method", *IOP Conference Series: Materials Science and Engineering*, Vol. 149, *International Conference on Advances in Materials and Manufacturing Applications (IConAMMA-2016)*, Bangalore, India, (2016), p. 012078. (https://doi.org/10.1088/1757-899X/149/1/012078).

Evaluation a Hybrid Passive Cooling System for a Building Using Experimental and Commercial Software (Design Builder)

Mahnoosh Eghtedari[a], Abbas Mahravan[b*]

[a] Department of Architecture, Kermanshah Branch, Islamic Azad University, Kermanshah, Kermanshah, Iran.
[b] Department of Architecture, Razi University, Kermanshah, Kermanshah, Iran.

ABSTRACT

Increasing fossil fuel consumption in the building, especially in the air-conditioning sector, has increased environmental pollution and global warming. In this research, a zero-energy passive system was designed to ventilate the building and provide comfortable conditions for people in the summer. A hybrid passive system was designed for indoor cooling to minimize fossil energy use. This research was done experimentally- and analytically and by simulation. An experimental study comprising a test chamber and simulation using Builder Design software was carried out to evaluate the cooling and ventilation potential of a hybrid passive system functioning. In the experimental section, air temperature, humidity, and airflow for the outdoor environment and the output of the evaporative cooling channel were measured. These measurements were tested in August from 9:00 AM to 3:00 PM for six consecutive days. The obtained experimental data were given to Design Builder software as an input parameter, and then, the comfort conditions inside the chamber, the dimensions, and location of the air inlet valve into the chamber were examined. The findings showed that the proposed system could reduce the air temperature by an average of 10 $^{\circ}$C and increase the air humidity by 33 %. The findings showed that the air inside the chamber was comfortable during the hottest hours of the day. Raising the valve location, increasing the area, and increasing the volumetric flow rate of the air increased the percentage of dissatisfaction. The findings showed that in addition to wind speed and air temperature, the geometrical shape of the air inlet opening contributes to indoor air comfort conditions.

https://doi.org/10.30501/jree.2021.239940.1131

1. INTRODUCTION

Buildings consume about 40 % of global energy consumption [1-4]. All building services such as Heating, Ventilation, and Air Conditioning (HVAC) systems consume more than 60 % energy in Buildings [5], which is mainly supplied by fossil fuels [6]. Using a passive cooling system can be an alternative method to keep the house cold or reduce the air conditioner load [7]. In ancient architecture, passive techniques were used to achieve summer comfort without the need for mechanical cooling systems. Today, because of the need for an effective method to make efficient energy and biocompatible architecture, the use of natural ventilation methods in buildings has become more significant. One of the methods to create comfortable conditions in the interior is to make use of evaporative cooling in the cooling systems. Evaporative cooling is widely used as a passive cooling method in the built environment. In the system, the movement of air on a wet surface causes water evaporation through the air energy absorption, thereby reducing the temperature and increasing the amount of vapor contained in the air [8]. Evaporative cooling is one of the oldest air-conditioning techniques in dry air climates [9]. Windcatchers were used in Egypt several thousand years ago, and today, a number of them can be found in the Middle East. Some of these windcatchers have porous jars at their depths, while others use a fountain or running water [10]. To produce evaporative cooling, wet surfaces, or water spray can be used inside the windcatcher. Thus, to achieve an excellent indoor condition is a problem in the hot and dry climates. Natural cooling was used in traditional architecture. Windcatchers [11] produced evaporative cooling using a wet surface or water spray in the tower. Some researchers have proposed new evaporative cooling systems [12-15]. In an experimental study in Yazd, two windcatchers with a new design were examined and their cooling rate was compared with a traditional windcatcher [13]. One of the windcatchers was equipped with wet curtains that were suspended inside the duct and the other with wetting surfaces. The cooling performance of the two new systems was compared with that of the conventional system. The experimental results showed that the efficiency of both new units with evaporative cooling systems was better than that of the conventional unit. Further, the experimental results showed that the traditional type reduced the air temperature by 4 $^{\circ}$C, while the windcatchers with wet surfaces and wet curtains reduced an air temperature to 11 $^{\circ}$C and 14 $^{\circ}$C,

*Corresponding Author's Email: a.mahravan@razi.ac.ir (A. Mahravan)
 URL: http://www.jree.ir/article_127543.html

respectively, both of which reduced the air temperature more than the traditional type did.

Another researcher evaluated the performance of an evaporative cooling windcatcher with clay conduits installed within the tower. This study developed a mathematical model and analyzed the condition of air passing through the evaporative cooling column in different external conditions. The results showed that a tower of 4 m height and 0.57 m × 0.57 m cross-section produced airflow of 0.3 m^3⁄s and reduced the internal temperature by 1 t [12].

A method for increasing the airflow rate inside a building is installing a solar chimney within a design [16-21]. One study, investigated the effect of aspect ratio and slope angle of a solar chimney on its thermal performance [18]. The results showed that the highest airflow velocity was created in the solar chimney with a slope angle of 45º. This increase in airflow is 45 % higher than a vertical chimney with similar conditions. Research showed that the optimal amount of solar chimney slope to maximize the speed of airflow was dependent on the latitude of the location and varied from 40º to 60º. Using a solar chimney alone makes the room temperature 4 $^{\circ}$C to 5 $^{\circ}$C lower than that without this passive system. This amount is insufficient to reduce the temperature in the hottest hours when maximum temperature is 40 $^{\circ}$C and does not provide indoor comfort conditions [21].

To increase building ventilation, the impact of a solar chimney coupled with a windcatcher was evaluated [22]. The results showed that solar chimney increased the speed of air conditioning. When the wind velocity is 1 m/s, the windcatcher alone can produce a mass flow rate of 0.75 kg/s, while with the aid of a solar chimney; , it can generate an airflow rate of 1.4 kg/s at 700 w/m^3 of solar radiation [22].

In the reviewed literature, studies have investigated the cooling performance of solar chimneys or windcatchers separately. In this research, by combining two solar chimney systems and evaporative cooling (using clay cylinders in windcatcher), an attempt was made to improve the cooling efficiency of passive systems. Therefore, the purpose of this study is to create thermal comfort conditions in the interior space without the use of energy in the summer and with the help of a new combined cooling system.

2. EXPERIMENTAL

This paper first describes the specifications of a hybrid passive cooling system that includes dimensions and size, construction site, and test time. Then, the comfort conditions inside the chamber are examined according to the geometry and position of the air inlet valve.

2.1. Functional hybrid passive cooling system design

The Hybrid Passive Cooling System (HPCS) consisted consists of two distinctive systems: the Solar Chimney (SC) and Evaporative Cooling Cavity (ECC). The ECC system was connected to the northern facade of the room (Figure 1a), and the SC system was installed in the southern facade of the room (Figure 1b). Air enters through windcatcher openings and passed passes through the clay cylinders. In this section, the air is cooled and diverted downward. The SC system creates a sufficient temperature difference between the interior and exterior by maximizing the solar energy gain and performed air ventilation in the SC and ECC systems (Figure 2).

(a)

(b)

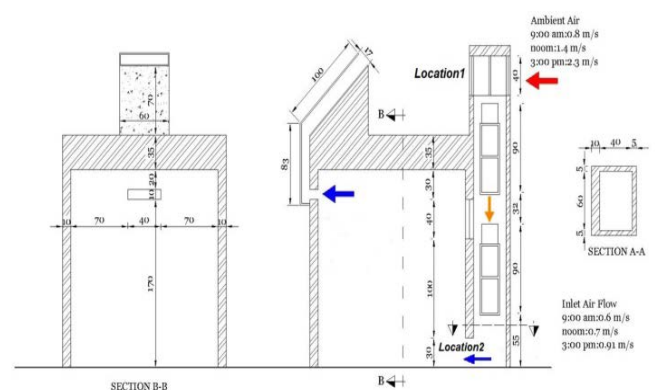**Figure 1.** a) The ECC system is installed in the northern façade, b) The SC system installed in the southern façade

Figure 2. Cross-section of the HPCS system

2.2. Time and place of testing

The proposed hybrid system was built on the campus of Azad University, Kermanshah branch, and was tested in 2018 from August 5 to 10. According to the 10-year statistics of Kermanshah Meteorological Station, which is shown in Figure 3, August is the warmest month of the year therefore, the tests were performed at 9:00 AM, noon, and 3:00 PM. Kermanshah city has a latitude of 34°19'N. The air temperature values of Kermanshah city in August are presented in Table 1.
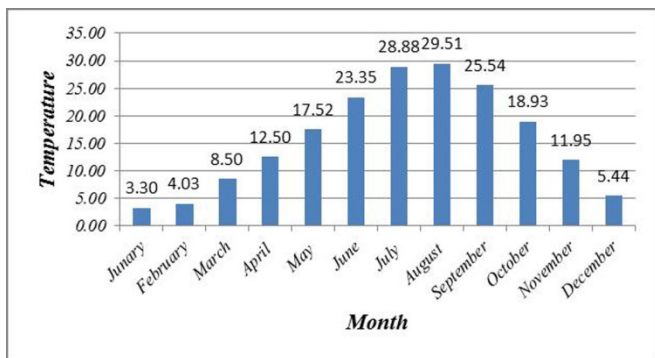

Figure 3. The average temperature of 10 years in Kermanshah city [23]

Table 1. Climate conditions of Kermanshah city (www.kermanshahmet.ir)

Average temperature (°C)	Average humidity (%)	Average wind flow (m/s)	Average solar radiation intensity (wh/(sq.m))
29	21	2	623

2.3. Dimensions and size of the HPCS

- A room with 2 m × 2 m × 2.35 m (L×W×H) dimensions with 10 cm-thick walls and 35 cm-thick ceiling without air filtration.

- An SC with 1m height, 60 cm width, 17 cm air gap, and 45 °C tilt angel. The front side of the SC consisted of a 15 mm-thick glass glazing and the rear part included a 1 m-high absorber wall made of a black-painted aluminum sheet.
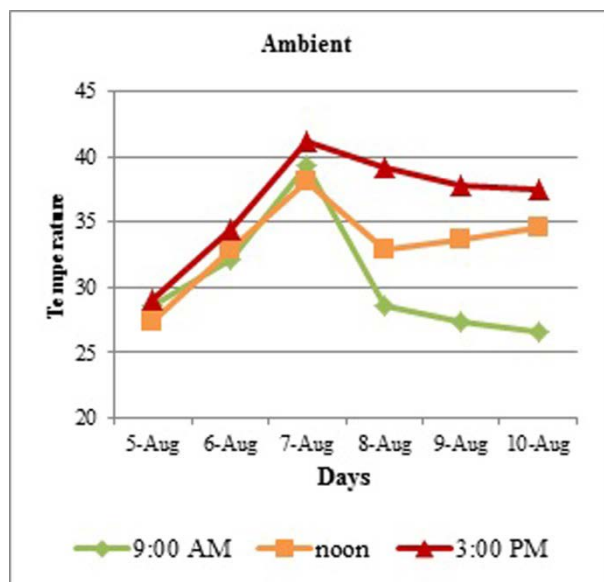
- A 40 cm × 10 cm air outlet of SC placed 20 cm below the ceiling.

- The ECC system with a length of 3.25 m and a 0.6 × 0.4 m cross-section. Each air inlet opening of the wind tower is 40 cm × 40 cm and the air exit opening is 30 cm × 30 cm.

- Four clay cylinders, each with diameter of 20 cm, and height of 90 cm.

2.4. The experimental measurement

To evaluate the comfort conditions, temperature, humidity, and wind speed parameters for outlet air of the tower into the chamber and outside environment were measured experimentally (Figure 2). The measuring instruments in this study are Data logger KH 50 and Flow anemometer AVM-07. The location of the Thermo-hygrometer data logger and anemometer is located in the air inlet valve from outside to inside the windcatcher (Location 1 in Figure 2) and the air outlet valve from the windcatcher to the room (Location 2 in Figure 2).

3. RESULTS AND DISCUSSION

3.1. Temperature, humidity, and wind speed in the HPCS

To assess the weather conditions inside the chamber from August 5 to 10, wind speed, air temperature, and humidity of ambient air and outlet air of the tower into the chamber; were measured. Figures 4 and 5 display the temperatures of ambient air and outlet air of the tower into the chamber, respectively, for six consecutive days at 9:00 AM, noon, and 3:00 PM. According to Figures 4 and 5, the largest difference between the outlet air of the tower into the room and the outside environment is 16.3 °C, which occurred on 7th August at 3:00 PM. According to the data, this system reduced the air temperature by an average of 10 °C and the air temperature of the outlet air of the tower to the chamber was in comfort at all hours. Figures 6 and 7 show that the lowest velocity of the air leaving the tower is on 10th August at 9:00 AM. This value is 0.33 m/s when the ambient airspeed is 0.5 m/s. The highest velocity of the air leaving the tower is at 3:00 PM on August 8th. This value is 1.1 m/s when the ambient airspeed is 1.8 m/s.
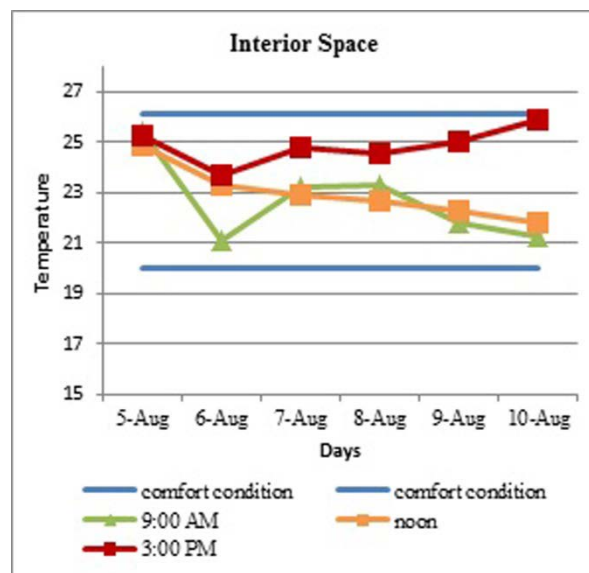

Figure 4. The ambient air temperature of ECC

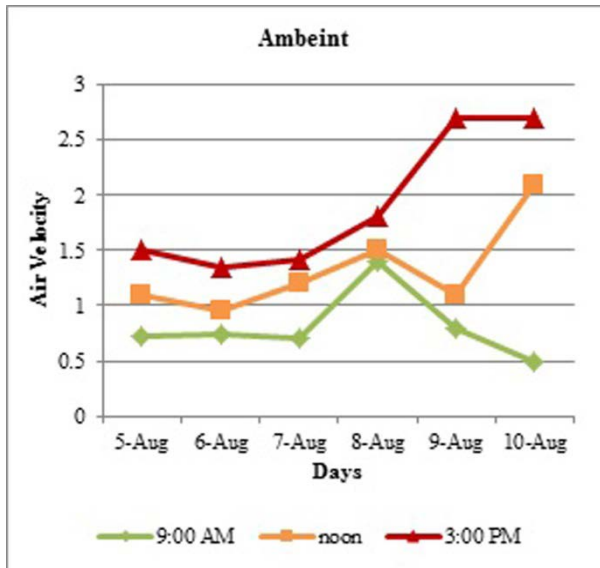**Figure 5.** Interior air temperature of the ECC

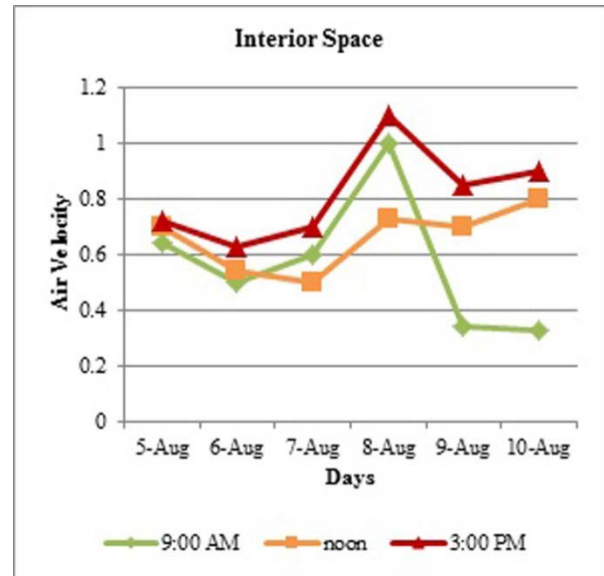**Figure 6.** Ambient air velocity of the ECC

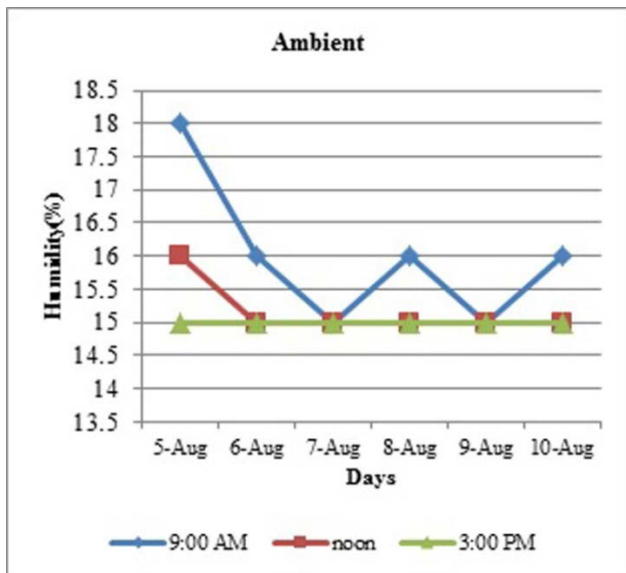**Figure 7.** Interior air velocity of the ECC

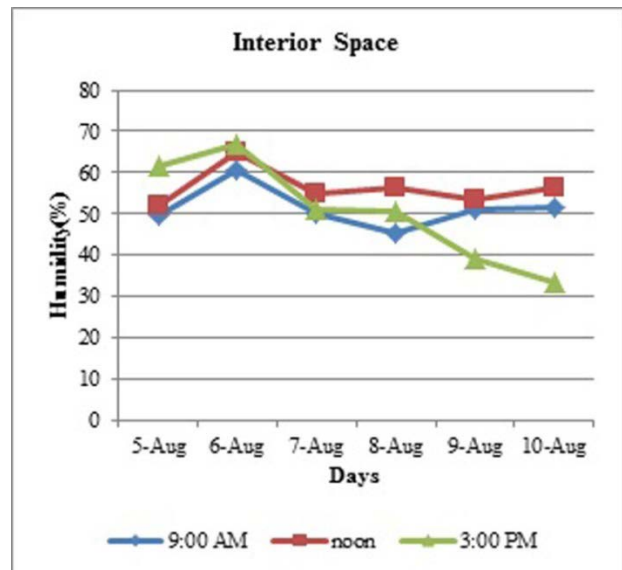
Figure 8. Ambient humidity of the ECC

Figure 9. Interior humidity of the ECC

Based on the collected data, the highest and lowest RH values of the air leaving tower were 60.7 % and 32.6 %, respectively, at 9:00 AM when the RH value of the ambient air was 16 % and 15 %. The highest and lowest RH values of the air leaving tower were 65.1 % and 30.7 %, respectively, at Noon when the RH of ambient air was 15 %. At 3:00 PM, the highest and lowest RH values of the air leaving tower were 66.8 % and 31.3 %, respectively, when RH of ambient air was 15 %. On 24 August, the relative humidity of the room was the lowest in at all hours when the HTD system was not connected. The highest and lowest increases in the amount of RH of air using the ECC system were 50.1 % and 17.22 %, respectively, in which the highest RH was achieved at noon and the lowest RH was at 3 PM (Figures 8 and 9). Then, based on the result, the ECC system can increase RH of air by 33 % on average.

3.2. Investigating the comfort conditions inside the chamber using PMV and PPD methods

Investigating the comfort conditions inside the chamber using PMV and PPD methods, Finger's index is used to check the comfort conditions inside the chamber [24]. The average heat

sensation of a large number of people for an environmental condition is called PMV, which is between cold (-3) and hot (+3) [25]. Air temperature, average radiant temperature, relative humidity, airspeed, metabolic rate, and clothing insulation are used in Fanger's equations [24]. The input variables to the Builder Design software to check the comfort conditions inside the chamber are the ambient air temperature, outlet air temperature of the tower into the chamber, outlet air velocity of the tower into the chamber (Table 2). Also, in this research, the person's posture is assumed to be sitting and the relative rate of clothing is considered to be 0.5 [25].

Table 2. Software input parameters

The ambient air temperature (°C)	Outlet air velocity of the tower (m/s)	The outlet air temperature of the tower (°C)	Time
28.5	0.64	25.42	9:00 AM
32.1	0.7	24.86	Noon
37.53	0.8	26.66	3:00 PM

The simulation was performed in two stages. First, the air comfort conditions inside the chamber were checked at 9:00 AM, noon, and 3:00 PM, when the outlet air temperature of the tower into the chamber is maximum (Table 3).

Table 3. Check the speed, temperature, PPD, and airflow distribution pattern inside the chamber

The ambient air temperature (^{o}C)	Outlet air velocity of the tower (m/s)	The outlet air temperature of the tower (^{o}C)	Time
0.62	0.11	0.2	Average wind speed (m/s)
27.6	25.9	25.73	Average air temperature (^{o}C)
26	13	18	Average percentage of dissatisfaction (PPD)
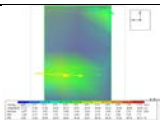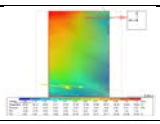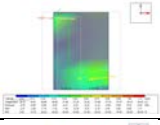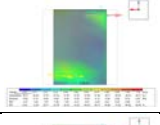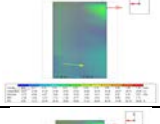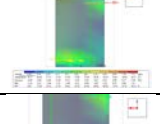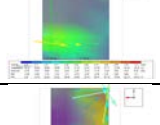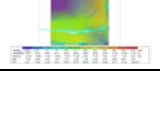
Then, the best position of the air inlet valve in terms of height and geometry to reach the highest level of comfort at 3:00 PM was determined using the software. According to Table 3, the average air velocity and the rate of dissatisfaction with indoor air conditions at noon are 0.11 m/s and 13 %, respectively, which are lower than 9:00 AM and 3:00 PM, however, the average air temperature at 9:00 AM (25.73 ^{o}C) is the minimum.

In this study, Fanger's model was used to investigate the comfort conditions inside the chamber.

Using experimental data, the maximum temperature of the outlet air temperature of the tower into the chamber at 9:00 AM, noon, and 3:00 PM was given to Design Builder software as input parameters. Therefore, the HPCS system can provide indoor air comfort conditions in the hottest hours of the year. After determining that the chamber would be comfortable in the hottest hours using the hybrid system, in the second stage of simulation by changing the location, geometric deformation of the valve, and increasing the volumetric flow rate of the incoming air, the maximum rate of dissatisfaction of residents inside the room was checked. At this stage, the simulations took place at 3:00 PM when the weather conditions inside the chamber had the highest rate of dissatisfaction. In the pictures given in Table 4, blue indicates the lowest percentage of dissatisfaction, green the average, and red the highest percentage of dissatisfaction. First, the location of the air inlet duct valve was considered 30 cm higher. Although relocating the valve increased the inlet air velocity into the chamber, the rate of dissatisfaction increased. Then, the simulations were first performed by maintaining the valve area and the geometric deformation of the valve channel. The maximum increase in air velocity and the largest decrease in temperature occurred in the 45 × 20 valve, however, the lowest rate of dissatisfaction was in the 18 × 50 valve (Table 4).

Table 4. Check the air velocity, temperature, PPD, and distribution pattern of airflow inside the chamber by changing the height of the valve, geometric shape, dimensions, and volumetric flow rate of the air inlet duct

	The maximum percentage of dissatisfaction (PPD)	Maximum air temperature (^{o}C)	The maximum air velocity (m/s)	
	45	28.5	0.52	Change the height of the valve from 10 cm to 40 cm
	40	28.26	0.93	30 × 30
	43.8	27.24	0.53	20 × 45
	42.9	27.62	0.53	45 × 20
	35.88	27.63	0.43	18 × 50
	43.29	27.68	0.5	50 × 18
	43.86	27.23	0.52	50 × 50
	74	27.08	3.99	Increasing the volume flow rate of the valve with dimensions of 50 × 50

Although increasing the valve area accelerated the wind speed, this change increased the percentage of dissatisfaction. At this stage, the volume flow rate of incoming airflow was increased to reduce the percentage of dissatisfaction in the 50 × 50 valve. This disturbed the airflow inside the chamber, which increased the percentage of dissatisfaction. According to the Table 5, the lowest air temperature was obtained by 50 × 50 valve, the highest air velocity in the chamber was obtained by increasing the volumetric airflow in 50 × 50 valve, and the lowest dissatisfaction rate was obtained by 18 × 50 valve.

Table 5. Optimal air valve based on the lowest percentage of dissatisfaction

The lowest percentage of dissatisfaction	The highest percentage of dissatisfaction	Maximum air velocity (m/s)	The lowest temperature (°C)	Valve dimensions (cm)
18 × 50	50 × 50	50 × 50 (Increase volumetric flow rate)	50 × 50	
45 × 20	20 × 45	30 × 30	20 × 45	
Optimum condition: 18 × 50 valve				

4. DISCUSSION

In a new modular windcatcher design, Khani et al. showed that this system could reduce air temperature by a maximum of 13 °C. Badran also demonstrated in the design of the evaporative channel using mathematical equations that the air temperature decreased to 11 °C, while in the windcatcher designed in this study, the maximum decrease in the air temperature was 16 °C. In Badran's design, with a windcatcher height of 4 m and an ambient air velocity of 4 m/s, the air velocity of the valve to the room was 0.8 m/s. Still, in the system designed in this study, using a solar chimney, the air velocity of the tower to the chamber reached 1.26 m/s with a wind speed of 3.25 m/s. Indoor air was in the comfortable condition in the hottest hour (3:00 PM) by the HPCS system. The percentage of dissatisfaction increased upon an increase in the inlet air velocity into the chamber. Although the air velocity in the valve 18 × 50 was lower than in the 45 × 20 (the temperature is the same in both valves), the percentage of dissatisfaction was also lower in this valve.

5. CONCLUSIONS

This study aims to propose a new design hybrid passive system to create comfortable conditions inside the building for summer time. To evaluate the cooling performance of this system, the temperature and air velocity of the outside air and outlet air of the tower into the chamber were measured experimentally; then, the comfort conditions inside the chamber were examined using Design Builder software. To optimize the HPCS and reduce the percentage of dissatisfaction, the position and dimensions of the outlet of the tower into the chamber were inspected. In this study, the ECC system can increase the RH of air by an average of 33 %. Also, the increase in the area of the valve, despite the decrease in air temperature, increased the rate of dissatisfaction. Still, with the geometric deformation of the air inlet valve, the percentage of dissatisfaction decreased and provided thermal comfort conditions for the indoor air chamber. The obtained data showed that in addition to wind speed and air temperature, the geometric shape of the valve could be an effective factor in creating air comfort conditions inside the chamber.

6. FUTURE STUDY

the performance of a solar chimney integrated with a windcatcher in multi-story buildings to investigate the distribution of airflow and its cooling efficiency in existing buildings needs to be studied.

7. ACKNOWLEDGEMENT

NOMENCLATURE

PMV	Predicted Mean Vote
PPD	Predicted Percentage Dissatisfied
RH	Relative Humidity

REFERENCES

1. Santamouris, M. and Kolokotsa, D., "Passive cooling dissipation techniques for buildings and other structures: The state of the art", *Energy and Buildings*, Vol. 57, No. 2, (2013), 74-94. (https://doi.org/10.1016/j.enbuild.2012.11.002).

2. Hossein Ghadiri, M., Lukman, N., Ibrahim, N. and Mohamed, M.F., "Computational analysis of wind-driven natural ventilation in a two sided rectangular wind catcher", *International Journal of Ventilation*, Vol. 12, No. 1, (2013), 51-62. (https://doi.org/10.1080/14733315.2013.11684002).

3. Moosavi, L., Mahyuddin, N., Ghafar, N.A. and Ismail, M.A., "Thermal performance of atria: An overview of natural ventilation effective designs", *Renewable and Sustainable Energy Reviews*, Vol. 34, No. 6, (2014), 654-670. (https://doi.org/10.1016/j.rser.2014.02.035).

4. Chenari, B., Carrilho, J.D. and Silva, M.G., "Towards sustainable, energy efficient and healthy ventilation strategies in buildings: A review", *Renewable and Sustainable Energy Reviews*, Vol. 59, No. 7, (2016), 1426-1447. (https://doi.org/10.1016/j.rser.2016.01.074).

5. Manzano-Agugliaro, F., Montoya, F.G., Sabio-Ortega, A. and García-Cruz, A., "Review of bioclimatic architecture strategies for achieving thermal comfort", *Renewable and Sustainable Energy Reviews*, Vol. 49, No. 9, (2015), 736-755. (https://doi.org/10.1016/j.rser.2015.04.095).

6. Hanif, M., Mahlia, T.M.I., Zare, A., Saksahdan, T.J. and Metselaar, H.S.C., "Potential energy savings by radiative cooling system for a building in tropical climate", *Renewable and Sustainable Energy Reviews*, Vol. 32, No. 4, (2014), 642-650. (https://doi.org/10.1016/j.rser.2014.01.053).

7. Daghigh, R., "Assessing the thermal comfort and ventilation in Malaysia and the surrounding regions", *Renewable and Sustainable Energy Reviews*, Vol. 48, No. 8, (2015), 681-691. (https://doi.org/10.1016/j.rser.2015.04.017).

8. Alaidroos, A. and Krarti, M., "Numerical modeling of ventilated wall cavities with spray evaporative cooling systems", *Energy and Buildings*, Vol. 130, No. 15, (2016), 350-365. (https://doi.org/10.1016/j.enbuild.2016.08.046).

9. Kalantar, V., "Numerical simulation of cooling performance of wind tower (Baud-Geer) in hot and arid region", *Renewable Energy*, Vol. 34, No. 1, (2009), 246-254. (https://doi.org/10.1016/j.renene.2008.03.007).

10. Lechner, N., Sustainable design methods for architects, John Wiley & Sons, New York, (2001). (www.wiley.com/go/permissions).

11. Jafarian, S.M., Haseli, P. and Taheri, M., "Performance analysis of a passive cooling system using underground channel (Naghb)", *Energy and Buildings*, Vol. 42, No. 5, (2015), 559-562. (https://doi.org/10.1016/j.enbuild.2009.10.025).

12. Badran, A.A., "Performance of cool towers under various climates in Jordan", *Energy and Buildings*, Vol. 35, No. 10, (2003), 1031-1035. (https://doi.org/10.1016/S0378-7788(03)00067-7).

13. Bahadori, M.N., Mazidi, M. and Dehghani, A.R., "Experimental investigation of new designs of wind towers", *Renewable Energy*, Vol 33, No. 10, (2008), 2273-2281. (https://doi.org/10.1016/j.renene.2007.12.018).

14. Chiesa, G. and Grosso, M., "Direct evaporative passive cooling of building: A comparison amid simplified simulation models based on experimental data", *Building and Environment*, Vol. 94, No. 1, (2015), 263-272. (https://doi.org/10.1016/j.buildenv.2015.08.014).

15. Bouchahm, Y., Bourbia, F. and Belhamri, A., "Performance analysis and improvement of the use of wind tower in hot dry climate", *Renewable Energy*, Vol. 36, No, 3, (2011), 898-906. (https://doi.org/10.1016/j.renene.2010.08.030).

16. Duffie, J.A. and Beckman, W.A., Solar engineering of thermal processes, John Wiley & Sons, United States, (1991). (https://doi.org/10.1002/9781118671603).

17. Afonso, C. and Oliveira, A., "Solar chimneys: Simulation and experiment", *Energy and Buildings*, Vol. 32, No. 1, (2000), 71-79. (https://doi.org/10.1016/S0378-7788(99)00038-9).

18. Chen, Z.D., Bandopadhayaya, P., Halldorssonb, J., Byrjalsenb, C., Heiselbergb, P. and Lic, Y., "An experimental investigation of a solar chimney model with uniform wall heat flux", *Building and Environment*, Vol. 38, No. 7, (2003), 893-906. (https://doi.org/10.1016/S0360-1323(03)00057-X).

19. Mathur, J., Bansal, N.K., Mathur, S., Jain, N. and Anupma, "Experimental investigations on solar chimney for room ventilation", *Solar Energy*, Vol. 80, No. 8, (2006), 927-935. (https://doi.org/10.1016/j.solener.2005.08.008).

20. Miyazaki, T., Akisawa, A. and Kashiwagi, T., "The effects of solar chimneys on thermal load mitigation of office buildings under the Japanese climate", *Renewable Energy*, Vol. 31, No. 7, (2006), 987-1010. (https://doi.org/10.1016/j.renene.2005.05.003).

21. Punyasompun, S., Hirunlabh, J., Khedari, J. and Zeghmati, B., "Investigation on the application of solar chimney for multi-story buildings", *Renewable Energy*, Vol. 34, No. 12, (2009), 2545–2561. (https://doi.org/10.1016/j.renene.2009.03.032).

22. Bansal, N.K., Mathur, R. and Bhandari, M.S., "A study of solar chimney assisted wind tower system for natural ventilation in buildings", *Building and Environment*, Vol. 29, No. 4, (1994), 495-500. (https://doi.org/10.1016/0360-1323(94)90008-6).

23. Kermanshah Meteorological Department, Statistics and information of Kermanshah province, (2018). (http://www.kermanshahmet.ir/met/amar).

24. Fanger, P., "Thermal comfort: analysis and applications in environmental engineering", McGraw-Hill, New York, (1991). (https://doi.org/10.1177/146642407209200337).

25. ASHRAE Standard 55, Thermal environmental conditions for human occupancy, ASHRAE, New York, (2017). (http://www.ashrae.org/template/TechnologyLinkLanding/category/1631).

Research Article

Spatial Study for Determining the Optimum Scenario for Generating Solar Electricity by Predicting the Land-Use Changes: Case of Alborz Province, Iran

Ali Khatibi, Mohammad Hossein Jahangir*, Fatemeh Razi Astaraei

Department of Renewable Energies and Environment, School of New Sciences and Technologies, University of Tehran, P. O. Box: 14399-57131, Tehran, Tehran, Iran.

P A P E R   I N F O

A B S T R A C T

Land-use change is one of the most important spatial phenomena that can affect the usage of energy technologies. In this study, land-use change in barren and residential areas in Alborz province in Iran was modeled using the cellular automata combined with the Markov Chain from 2001 to 2031. Due to adaptability to the environmental considerations, all protected areas were removed from the study area. Then, an economical and performance-based optimization model was developed; then, by using the status of the two land-use classes in 2031, an optimum scenario was identified for generating solar electricity. Based on the results, the optimum scenario involves installing distributed photovoltaic modules in 18.37 % of residential areas and setting up concentrated solar systems in 0.74 % of barren areas, simultaneously. Economic investigation of the optimum scenario showed that although there were some environmental and political benefits for using the solar electricity such as reduction of air pollutants and more energy safety, the optimum scenario will be costly and non-economical without the government's financial supports.

1. INTRODUCTION

Today, accessibility to energy resources is one of the basic requirements for sustainable development. On the other hand, developing the usage of green energy resources has significant impacts on reducing CO_x emission. Renewable energy takes into account some environmental considerations in addition to the ability to supply energy and, therefore, it is known as the best alternative to fossil fuels [1]. Renewable energy is provided by different resources and it is possible to choose the appropriate resource in accordance with the regional, political, environmental, economic, and technological conditions for the target area.

Solar energy is one of the most common forms of renewable energy that can be used in both electrical and thermal systems. Solar power is an autochthonous energy resource, so it can be used to reduce the grid electricity dependency and improve regional developments. The basis for using the solar energy is the absorption and energy conversion of the photons received from the solar illumination into another form of energy. Generally, solar energy is directly converted into electricity by photovoltaic effect. Generally, photovoltaic systems can be utilized in two major types including concentrated solar farms or distributed photovoltaic panels. Concentrated solar farms are usually installed in the desert and barren areas with the sufficient irradiation, whereas distributed photovoltaic panels

are mostly installed on building's roofs [2]. Therefore, the effective use of solar energy systems needs precise identification of the received solar illumination and it is necessary to investigate the relevant factors such as the accessible region area.

Land-use is changing rapidly on many parts of the Earth due to urbanization. Generally, urbanization can affect all kinds of energy demands. Sometimes, these changes end up with increasing non-productive land-uses in the urban areas such as residential and barren areas. This transition might result potentially in decreasing food farms and bio-resources, but they can be used as suitable places for energy production. Cities as the common type of land-use changes are responsible for three-quarters of global energy consumption and an important part of greenhouse gas emissions subsequently. There are many direct and indirect approaches to evaluating the land-use changes and finding a model to predict such variations is a useful approach for the policy-makers to analyze accessible regions as an infrastructure factor in using renewable energy systems [3].

Based on the findings of many studies, simulation with the cellular automata method was determined as an appropriate approach to assessing land-use changes. Cellular automata can be combined with the Geographic Information System (GIS) and allows modeling the environmental changes. Generally, cellular automata can analyze spatiotemporal data by considering local considerations. In this way, a cell in cellular automata shows a region of the real world. In this model, all the cells have discrete states and each cell is surrounded by its

---

*Corresponding Author's Email: mh.jahangir@ut.ac.ir (M.H. Jahangir)
URL: http://www.jree.ir/article_127961.html

adjacent neighborhood cells. Therefore, the new status of each cell is determined by its previous state and the status of its neighborhood cells by considering the user-defined transition rules [4]. Transition rules in cellular automata can be defined in many different ways. One common approach is to use Markov chain to define them. In the real world, all parameters and rules are not clearly known for modeling; therefore, the rules will be defined according to the objectives and unimportant ones will be ignored. After running the initial cellular automata model, by comprising the observed and simulated data, the used parameters and rules are evaluated and change in required cases; thus, the accuracy of the model will be enhanced [5].

Huang et al. (1995) [6] used some different MCDM (Multi Criteria Decision Making) approaches such as ELECTRE (Elimination Et Choix Traduisant la REalite), TOPSIS (Technique for Order Preference by Similarity to Ideal Solution), and AHP (Analytic Hierarchy Process) to identify the best structure of the renewable energy systems. Their results showed that using the MCDM approaches could achieve optimum states. Mavromatakis et al. (2010) [7] assessed various MCDM approaches to selecting the most appropriate photovoltaic system by considering the environmental and economic conditions simultaneously. They mentioned that considering both economic and environmental factors would lead to identifying a sustainable solution in a long run. Janke (2010) [8] combined GIS and MCDM to determine the best land-use for establishing solar and wind farms. They showed that their approach was computable and also could consider different complex states. Wiginton at al. (2010) [9] assessed the ability of GIS and image processing to determine the available area to establish distributed photovoltaic systems on rooftop of buildings in Canada. Charabi and Gastli (2011) [10] studied the effect of land suitability on establishing large solar farms in Oman by using combination of GIS and MCDM approaches. They expressed that considering the accessible region areas was a key infrastructure factor in reaching higher performance of the solar farms. Sanchez-Lozano et al. (2013) [11] studied the ability of combination of GIS and some MCDM approaches including AHP and TOPSIS to identify the appropriate regions for site selection of a photovoltaic power plant. Amaducci et al. (2018) [12] investigated the impacts of land-use classes and their changes on the photovoltaic power plans, and vice versa. Their findings showed that the performance of the photovoltaic power plans could seriously change due to the type of land-use. Santoli et al. (2019) [13] employed GIS to predict accessibility to the renewable energy resources and electric energy consumptions on municipality scales. They mentioned that although land-use change affects the accessibility to the renewable energy resources, it also affects energy demand simultaneously.

As mentioned before, many distributed and concentrated photovoltaic systems have been established all over the world over the last years. One important question is which approaches (distributed or concentrated) would lead to greater performance for a specific region by considering the environmental concerns and economic benefits simultaneously. In this study, an attempt is made to model the land-use changes to maximize using the solar energy as an important resource of energy as a way to achieve sustainable development. Thus, a GIS-based model was prepared to identify the changes of two land-use classes including

residential and barren areas. After model validation, the status of the considered classes was predicted in the future. Finally, some common different distributed and concentrated photovoltaic systems were considered and the optimum solution was identified by combining the results of the land-use changes and an integrated economic and environmental MCDM. The results of this study suggest an optimum strategy for achieving more renewable energy performance in the study area.

2. METHOD

2.1. Methodology

In this section, study area is introduced and the reason for selecting this area is described. After that, a GIS-based cellular automata model is developed and the used approach to improving its accuracy is discussed alongside the sensitivity analysis of the model. In the last part, an optimization model is introduced for predicting the production of photovoltaic electricity in the study area by considering the concentrated and distributed photovoltaic systems.

2.2. Study area

Alborz province is a crowded province of Iran and is in the 35 km of northwest of Tehran (Figure 1). The Alborz province consists of Karaj, Savojbolagh, Taleqan, Eshtehard, Fardis, and Nazarabad Counties and Karaj is the capital of the province. This province is situated at the foothills of the Alborz Mountains and it is Iran's smallest province in the area. According to the National Census, in 2016, the population of the Alborz province was 2.712 million and 90 % of its population live in urban areas. The population density in Alborz province is between 0 (people per square kilometer) for non-residential areas and 620 (people per square kilometer) in the Karaj city as the most populated area [14]. Alborz province has experienced a high growth rate in population, especially in urban areas in the last decade. Therefore, it is predicted that its population and energy demand will be faced with higher amounts in the future. Iran has about 300 clear sunny days in a year and its average solar radiation is about 2200 kWh per square meter. Studies show that about 9 million MWh of energy can be obtained in a day considering only 1 % of the total area with 10 % system efficiency for solar energy harness [15]. Although studies show that Alborz province does not have the highest potential in accessing solar energy in Iran [16], energy experts recommend using the local power plants to reduce energy loss in the transmission process [17]. Clearly, the main reason for selecting this study area was because of its growing needs of the energy.

2.3. GIS-based cellular modelling of land-use changes

2.3.1. Data preparation

First, satellite images of the study area were collected from the Landsat 7 for 2001 and 2016. Based on technical considerations, it needs maximum irradiation to set up enhanced solar farms as concentrated photovoltaic systems, and it can be accessed in higher amounts on barren areas which have no plants and shadows. The barren area is like deserts and ruins of buildings and so on [19]. On the other hand, the best choice for distributed systems is building's

roofs and blank in-urban spaces which were considered as residential areas. Thus, two land-use classes were selected and extracted from the obtained satellite images. The extraction of land-use classes was done by using the method of similarity of phenomena based on their spectral signatures. it is noteworthy to say that controlling and geo-referencing the used maps should be done before any GIS-based studies. Therefore, the obtained maps were controlled to ensure that all maps had the same coordinate system, projection unit, and cell size. The considered properties of all maps in this study are shown in Table 1 and the observed land-use maps of Alborz province in 2001 are given in Figure 2.

Table 1. The considered map properties in the research

Properties	Values
File type	tiff
Cell size	30×30 m
Projection system	WGS84–UTM39N

To make a geographical model, it was needed to use some other ancillary maps. These maps were used as independent variables and the land-use change was considered as the dependent variable. Generally, all independent variables were divided into two categories including static and dynamic ones. Based on the similar studies, eight variables were employed including six static maps and two dynamic maps. The dynamic maps were distance from the residential area and distance from the barren area, and the statues of these variables changed during the time. Static maps were elevation, slope, aspect (the direction of hillsides), river, road, and water bodies and they were prepared from the database of the Iranian National Cartographic Center [20] and the National Atlas of Iranian Deserts [21]. All used independent variables are shown in Figure 3. It is noteworthy to say that the dynamic maps were generated by the model at each time step of the study.
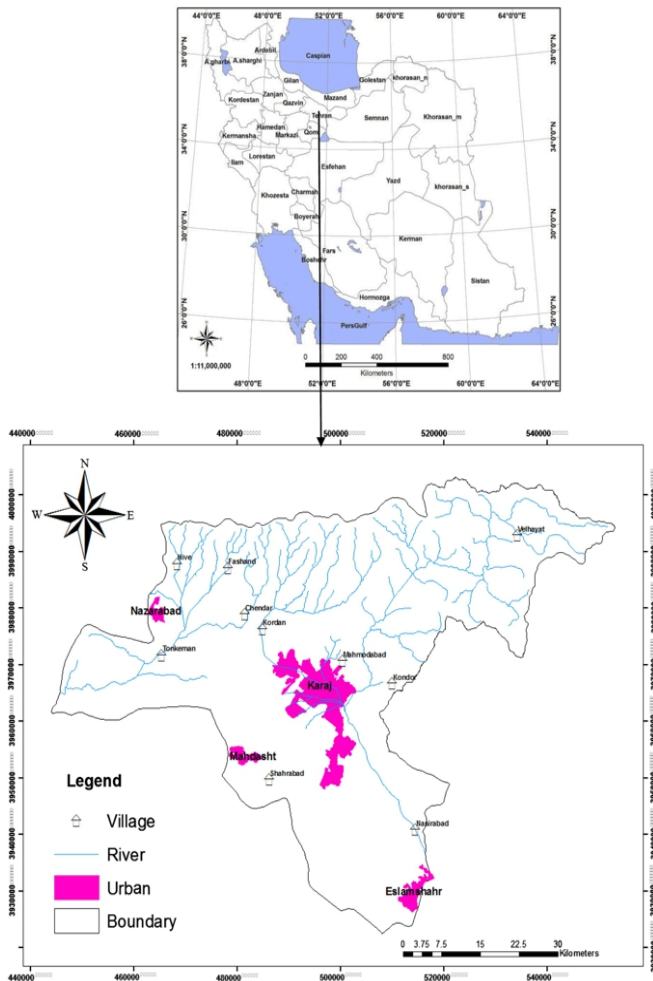
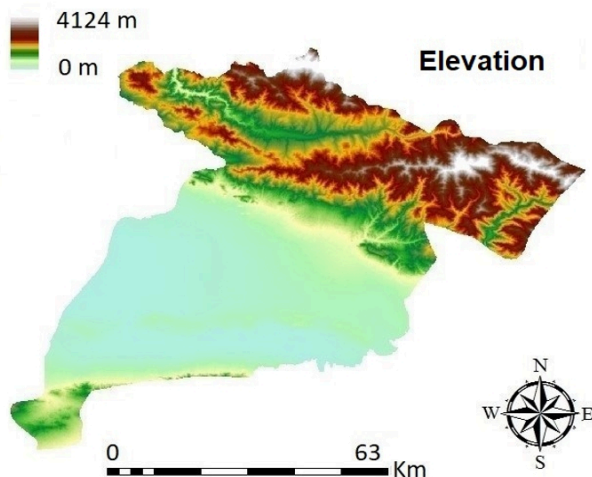**Figure 1.** The location of Alborz province in Iran [18]
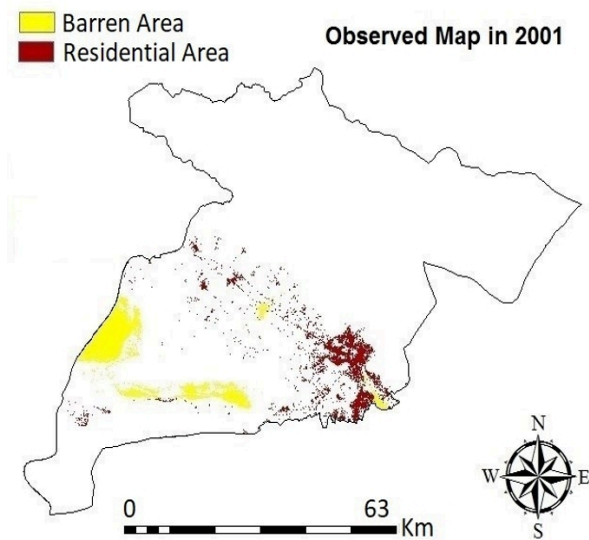
Figure 2. The observed land-use map of Alborz province given from processing satellite images in 2001
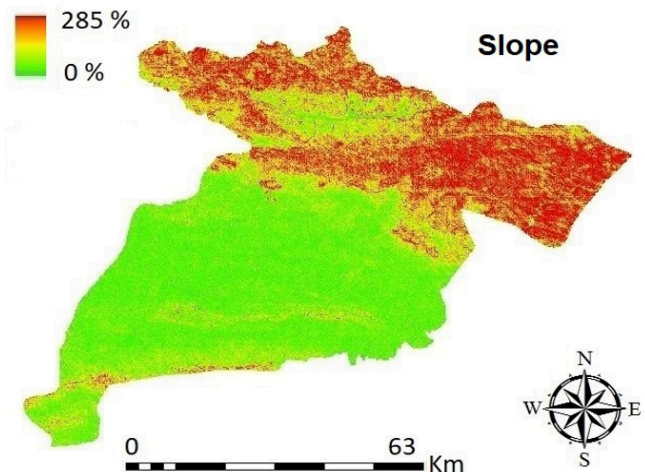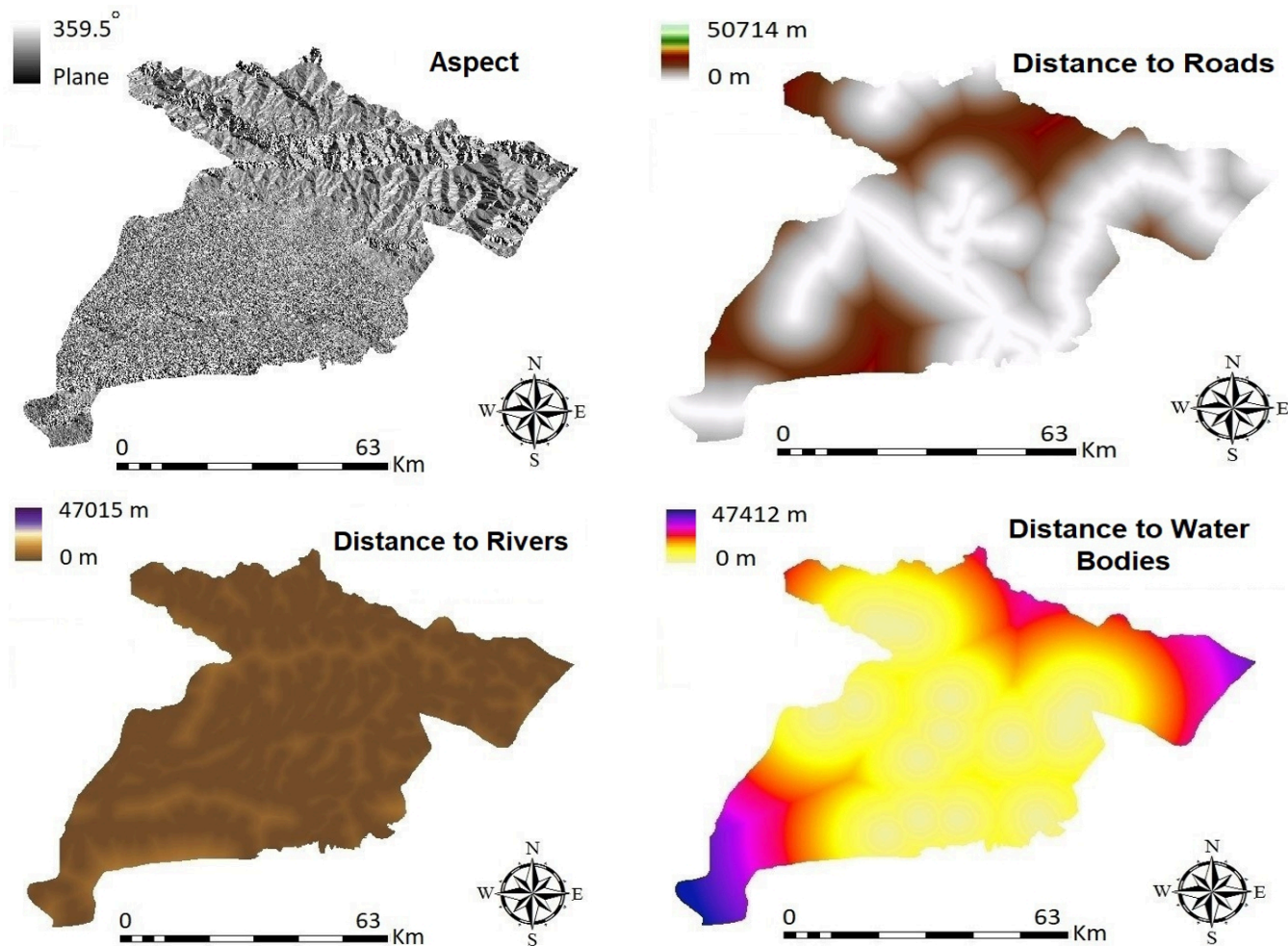
Figure 3. The used maps as independent variables

2.3.2. The model structure

After collecting the required data, the observed maps in 2001 and 2016 were compared by the Markov Chain. Thus, a matrix of coefficients was obtained that indicated the probability of changing one land-use class into another, called transition coefficients. Then, this matrix was divided into intervals per each transition and a new matrix called Weight of Evidence was generated that indicated the weights for each ancillary variable by considering the probability of transition in any regions. After that, ineffective and correlated variables were identified and removed from the model. In the next step, a cellular automata model was run on the observed land-use map in 2011 by considering the matrix of coefficients and all ancillary maps were used as the rules. Therefore, the new status of land-use classes in 2016 was simulated and stored as

a land-use map. At this level, the simulated and observed land-use maps in 2016 were compared using reciprocal fuzzy similarity analysis and minimum similarity [22] between them was determined. If the accuracy of the simulated map was less than 90 %, then by modifying ancillary variables and their weights, the model would be calibrated again and a new simulation was performed. Therefore, the model validation and the sensitivity analysis of the model were done during the modeling process. Simply, identifying the inappropriate dependent variables and eliminating them from the model show the sensitivity of the proposed model to its variables and repeating the simulation process until reaching the appropriate accuracy indicates the model validation. In Figure 4, there is a diagram of the described model. Also, all used variables in the proposed model are shown in Table 2.
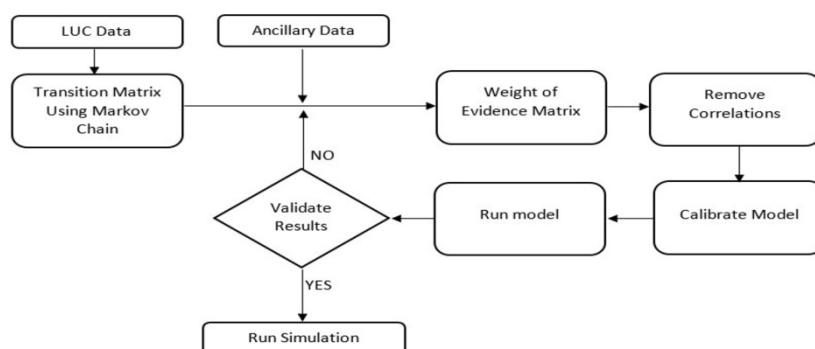

Figure 4. The diagram of the implemented GIS-based model using cellular automata and Markov chain

Table 2. All used variables in the proposed model

Variable	Type	Category
Land-use change	Independent	Dynamic
Distance from the residential area	Independent	Dynamic
Distance from the barren area	Independent	Dynamic
Elevation	Independent	Static
Slope	Independent	Static
Aspect	Independent	Static
River	Independent	Static
Road	Independent	Static
Water bodies	Independent	Static
Initial land-use	Independent	Static

After obtaining the final calibrated model, the simulation was performed to predict the future status of land-use changes. At this level, the model was run by using the observed land-use map in 2016 as the initial data. Because the model was trained by using the data of a period of 15 years, its accuracy cannot be guaranteed for periods over 15 years. Thus, the simulation process will go on for a 15-year period from 2016 to 2031. The final result of this level is a new land-use map that predicts the status of the two studied land-use classes in 2031.

Of note, some other land-use classes such as rangeland, jungle, agricultural farm and water bodies that were eliminated from this study due to environmental considerations. These land-use classes have significant ecological impacts on the ecosystem. For example, these regions might contain the concerned and endangered species or need to be protected because of some geological hazards such as soil erosion. Yousefi et al. (2018) [23] and Esnandeh and Kaboli (2019) [24] in separated studies investigated the conserved areas in Alborz province by considering biological and geological factors. Based on their results, some areas were determined to be considered as ecological conserved areas. In this study, all those regions were removed from the study area to avoid incompatibility of the results with environmental considerations.

For running the proposed model, DINAMICA EGO 4 was used. It is an appropriate tool to perform temporal-spatial simulations by utilizing many pre-defined modules and algorithms [25]. Extracting the land-use maps from the satellite images was done by using ENVI 5, and all pre- and post-processes on the maps were performed by ArcMap 10.3 [26].

2.4. Cost and performance optimization

After simulating the status of land-use map in 2031, a question arises, Which type of photovoltaic systems (concentrated or distributed) can provide much potential for electricity generation in the study area? In this study, it was considered that maximum 30 % of each land-use could be used to set up photovoltaic systems. This value was selected on the basis of consultation with experts and specialists in the relevant fields using DELPHI method. In DELPHI method, some experts were chosen and their opinions about a unique concept were gathered. Then, the obtained answers were analyzed and the modified concept was sent to the experts

again. This process was iterated until the viewpoints of the experts would reach the point of convergence. In this study, 22 experts were selected to do DELPHI method. The multi-crystalline photovoltaic systems are common and have the high efficiency and it seems they will play the most important role in the future solar power systems [27]. In this study, it was assumed that all distributed and concentrated photovoltaic systems would use multi-crystalline technologies. This assumption was considered because the results were independent of the used technology, and then it is possible to make a comparison between the results. Thus, two types of common multi-crystalline photovoltaic systems were considered. The cost and power of each system are given in Table 3.

Table 3. The cost and power for the concentrated and distributed photovoltaic systems considered in this study [28]

Type of system	Technology	Size (m^2)	Power (Wh)	Cost ($)
Distributed photovoltaic module	Multi-crystalline	1.6335	250	187.5
Concentrated photovoltaic system	Multi-crystalline	4047	250×10^4	500000

Although any form of technology can affect the environment, as it was said before, all protected regions were removed from the study area in this research; therefore, there was no direct conflict between the proposed technologies and the ecosystem. In this way, two target parameters including the cost of system and the performance of electricity generation were considered to analyze the introduced photovoltaic systems. In this study, higher performance means higher potential power of the photovoltaic system per a specified area.

In the following, an MCDM model was created by using WSM approach. In this method, several target functions are combined and a normalized weighted sum model is generated as a unique target function [29]. There are many different ways to choose the value of weights. In this study, these values were determined using the DELPHI method and the asked question from experts was whether minimizing the cost of system is more important than the performance of electricity generation, or vice versa. Then, all answers were gathered and the proportion of each choice to the total was determined as the weights. The used MCDM model for this study is represented as Equation 1.

Objectives:
$$\text{Max } (250 \times x_1 + 250 \times 10^4 \times x_2)$$
$$\text{Min } (187.5 \times x_1 + 500000 \times x_2)$$

Constraints:
$$1.6335 \times x_1 \leq 0.3 \times \alpha_1$$
$$4047 \times x_2 \leq 0.3 \times \alpha_2$$
$$x_1, x_2 \geq 0$$

$$(1)$$

where x_1 is the number of distributed photovoltaic modules and x_2 is the number of concentrated photovoltaic systems. The first objective is to maximize the generated power and the second objective is to minimize the cost of the system. α_1 and

α_2 are the area of the accessible residential and barren areas, respectively. The presented numbers in the model are the cost, size, and the power of the studied systems obtained from Table 3. The value of 0.3 indicates the maximum proportion of accessible areas of the proposed land-use classes. By considering the WSM method, the MCDM model is modified as Equation 2.

Objectives:

$$\text{Max } \varphi \times (250 \times x_1 + 250 \times 10^4 \times x_2)$$
$$- \omega \times (187.5 \times x_1 + 500000 \times x_2)$$

Constraints:

$$1.6335 \times x_1 \leq 0.3 \times \alpha_1$$
$$4047 \times x_2 \leq 0.3 \times \alpha_2$$
$$x_1, x_2 \geq 0$$

$$(2)$$

where φ and ω are the weights of the first and second objectives, respectively. Also, it should be noted that $\varphi + \omega = 1$ due to normalizing the model. Finally, the modified model was solved by using LINGO 17.0, which is easy linear optimization software [30].

The x_1 and x_2 are the decision variables of the optimization model. Simply, solving the model shows its sensitivity to these variables. Also, α_1 and α_2 are the outputs of the GIS-based land-use changes model and their sensitivity was discussed in the previous section. On the other hand, all used variables in the optimization model, except the weights, had the same unit and indicated the area. This means the model is strongly dependent on the accessible area. The magnitude of this dependency is impacted by the values of the weights. Investigations showed changes in the weights led to different optimum scenarios. However, in this study, the values of the weights were determined by DELPHI method and they did not change the optimization model. The optimization model was intrinsically validated because the used photovoltaic systems were considered as separate modules. Simply put, each proposed photovoltaic system had specific cost, size, and power. Therefore, the cost, size, and power of the two systems are specified simply and there is no interaction between different systems.

3. RESULTS AND DISCUSSION

3.1. Results

At the first level of simulation, a transition matrix between two land-use maps from 2001 to 2016 was calculated by using the Markov Chain and the result is shown in Table 4. The value of each cell is equivalent to the probability of the corresponding transition. The cells with a value of zero are shown with dashes. It means that the transition did not occur at a specific time interval.

Table 4. The Markov chain transition matrix between land-use maps of 2001 and 2016

	Barren area	**Residential area**
Barren area	-	0.006988
Residential area	0.000061	-

Then, the ancillary maps as the independent variables were added to model and using the anticipated transition matrix, the matrix of coefficients was calculated. The DINAMICA EGO software was employed to assess the significance of each variable per transitions by using the combination of Uncertainty Information Joint method and Regression method. Therefore, the variables that did not affect the results were removed and the final matrix of coefficients was recalculated.

After that, the model was run from 2001 for a fifteen-year period to simulate the land-use status in 2016 (Figure 5). Then, the validation between the simulated and observed maps in 2016 was executed by the reciprocal fuzzy similarity method. In this study, the size of the compared regions was modified from 1 to 33 cells. The compared regions are called moving window and the model accuracy is proved on a spatial scale.
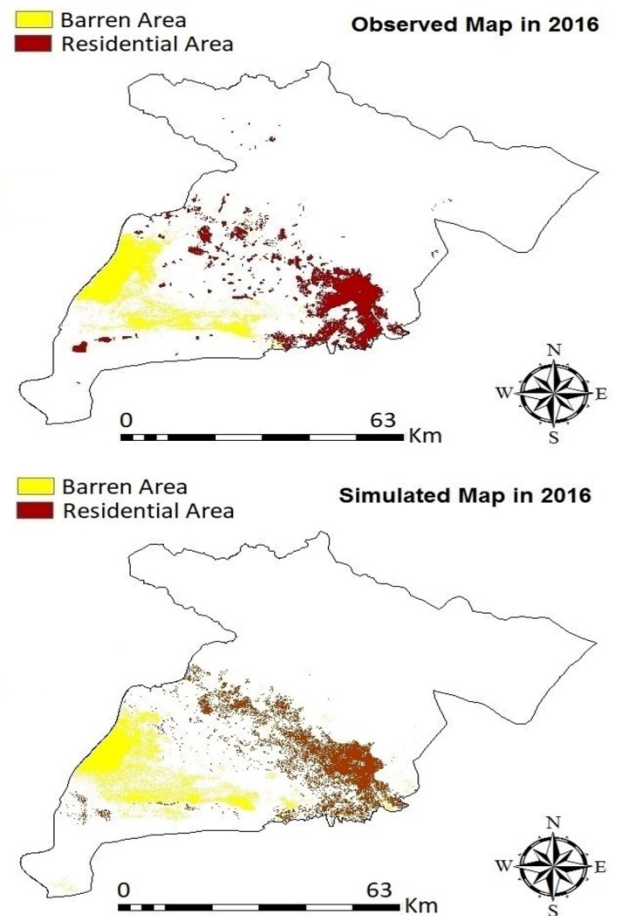

Figure 5. The observed and simulated land-use maps of Alborz province in 2016
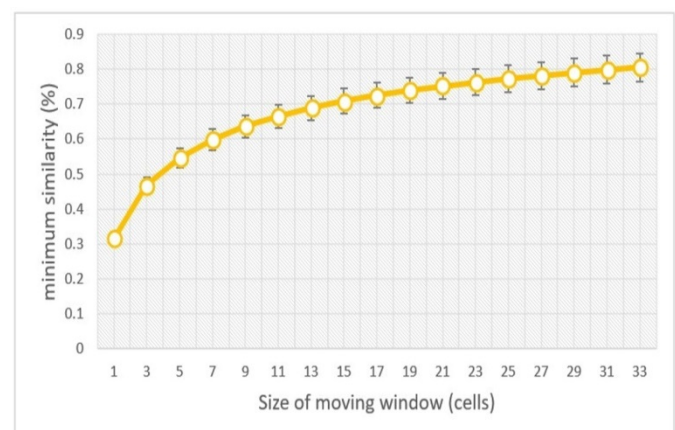

Figure 6. Similarity between observed and simulated land-use maps of Alborz province in 2016

As it can clearly be seen from Figure 6, the minimum similarity between compared maps grew and it was directly related to the size of the moving window. This increasing trend means that the model will give a more accurate result for an area with the bigger surface. In terms of ecology, it means that this model is more appropriate on landscape scales.

Because the model is sensitive to using independent variables, any changes in the number or type of these variables lead to variations in the accuracy. Therefore, in this study, no part of the model experienced any changes, except the initial land-use map. Thus, the final simulation was run from 2016 to 2031 to predict the new status of land-use classes. The result maps of 2024 and 2031 (as the sample of the outputs) are shown in Figure 7. Also, Table 5 shows the area of the land-use classes in the study area in the simulated years.
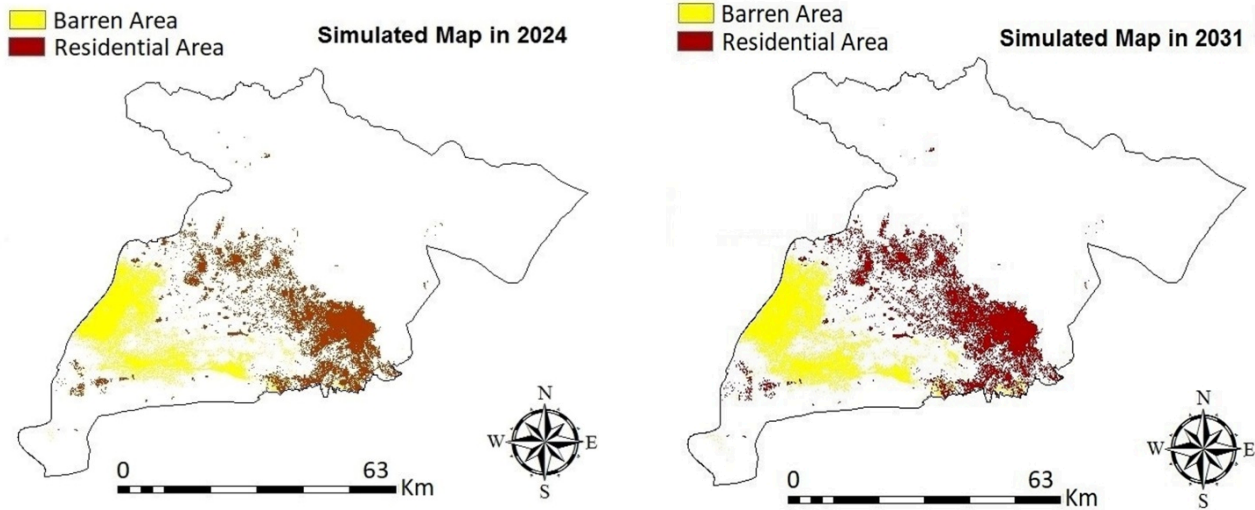
Figure 7. The simulated land-use maps of Alborz province in 2024 and 2031

Table 5. Area of the studied land-use classes in the simulated years in term of m^2

	Year			
	2001	**2016**	**2024**	**2031**
Barren area	150371100	254601900	302352300	341973000
Residential area	137493900	325665000	406314000	460677600

After finishing the simulation, the obtained areas had to investigate by considering the environmental conflicts. Because conserved areas were removed from all land-use maps in the data preparation process, there was not any environmental conflicts. Thus, the obtained land-use maps were used without any modification as the input for the optimization model.

In the following, due to making an MCDM model with WSM approach, the weight of objectives was determined using the DELPHI method. Based on the results of DELPHI method, the amount of power of the photovoltaic system was more significant than the cost of the system. Therefore, by calculating the proportions of answers, the weight of the first objective was considered as 0.73 (φ=0.73) and the weight of the second objective was determined as 0.27 (φ=0.27). Consequently, by considering the obtained weights and the area of land-use classes in 2031, the used optimization model (Equation 2) was modified as Equation 3.

Objectives:

$$\text{Max } 0.73 \times (250 \times x_1 + 250 \times 10^4 \times x_2)$$
$$- 0.27 \times (187.5 \times x_1 + 500000 \times x_2)$$

Constraints:

$$1.6335 \times x_1 \leq 0.3 \times 460677600$$
$$4047 \times x_2 \leq 0.3 \times 341973000$$
$$x_1, x_2 \geq 0 \qquad (3)$$

Finally, the optimization model was run by using LINGO. In this study, after 2 iterations, the model converged and the obtained results are represented in Table 6.

Table 6. The results of the optimization model

Variable	Optimized value	Description
x_1	84605620	The optimum number of distributed PV modules
x_2	25350.11	The optimum number of concentrated PV system

3.2. Discussion

In this study, to validate the simulation model, structural similarities between the observed and simulated data were analyzed using reciprocal fuzzy similarity method for the range from 900 square meters to 98 hectares (equals to 1 to 33 cells for the moving window). By considering Figure 6, it can be concluded that the results for the regions with an area of 900 square meters had about 30 % accuracy and it increased over 70 % for regions with an area of 29 hectares. It means that land-use simulation in the landscape scale resulted in more accurate result than the smaller scales. This finding is in compliance with some other similar studies [31]. Based on the results of simulation in 2031, the residential area will grow by approximately 2.3 times and in the same period, barren area will experience a growth by approximately 1.3 times. It seems

that these transitions occur because of population immigration. Also, from Table 3, the greatest value of the transition probability (0.006988) was related to the transition from the barren class to the residential class, and the lowest values (0.000061) were related to reverse transition. Clearly, it means that the study area will be faced with a high growth in the urban areas during the next years. Also, based on the validation results, a combination of cellular automata and Markov Chain was an effective approach to predicting the land-use changes and this result is similar to some other studies [32].

By considering the optimization results, the optimum scenario consists of using both concentrated and distributed photovoltaic systems in 2031. In this way, the best choice for the study area is to set up the distributed photovoltaic modules in 18.37 % of accessible residential area and to install the concentrated solar farms in 0.74 % of accessible barren area in 2031. It is noteworthy to say that this result is related to the assumption of using only 30 % of accessible areas and can change by modifying this assumption. Some similar studies denoted that concentrated photovoltaic systems were the best choice for the urban areas [33]. Some others indicated that distributed photovoltaic modules had the optimum performance in cities [34]. Also, the results of this study showed that selecting the optimum state for using the photovoltaic systems was completely dependent on land-use conditions. This finding is compatible with some other studies [35]. As a scenario for the future, the results of this study showed that if the process of land-use change continued as it is now, it is predicted that the study area needs to use both concentrated and distributed photovoltaic systems to meet lower cost and higher performance.

By combining the results of Table 6 and the data provided in Table 3, the optimum scenario shows that the study area needs to have about 52 million of the proposed distributed photovoltaic modules and about 7 concentrated photovoltaic systems. It is equivalently about 9.7 million dollars for the distributed photovoltaic modules and about 3.5 million dollars for concentrated photovoltaic systems. Also, the results showed that the distributed photovoltaic modules could generate about 13000 thousand kWh and for the concentrated photovoltaic systems, this amount is about 17.5 thousand kWh. It is obvious that the distributed photovoltaic system will have a greater share in supplying the solar electricity in the study area in 2031 by considering the proposed technology used in this study. By considering the average lifetime of the proposed photovoltaic systems about 20 years and the average price of sellback solar electricity about 0.8 dollar [36], the payback investment will be about 35 years. It means that if there will be no government financial support, the obtained scenario will not be efficient economically. On the other hand, as the technical feasible analysis, if the total power of the optimum scenario is provided only by the distributed photovoltaic modules, it needs about 10 million dollars and this value is about 2500 million dollars when the optimum scenario is performed only by the concentrated photovoltaic systems. Of note, although using the renewable energy systems is costly, they have many environmental and political benefits such as reduction of air pollutants, preventing the global warming, more energy safety, and providing new ecosystem services. Also, the invented technologies for renewable energy resources are enhanced and their performance will be increased, whereas their cost and size might be less. This means that the feasibility of this kind of

technology will increase day by day.

4. CONCLUSIONS

Installing photovoltaic systems needs spatial places. Studies show that barren area and rooftops of buildings are two appropriate types of places. Before planning for the usage of renewable energy systems, this question of whether the proposed technology is a sustainable choice for the study area during a specific period of time needs be answered. In this study, Alborz as one of crowded provinces in Iran was selected as the study area. At first, a GIS-based model was created by using cellular automata and Markov Chain. The status of two land-use classes including the barren and residential areas was simulated by this model until 2031. After that, an optimization model with two economic and performance objectives was defined. Then, two common types of distributed and concentrated photovoltaic systems were considered and the optimum scenario was investigated for the study area in 2031 by combining the results of the GIS-based model and the optimization model.

The obtained results showed that the study area would encounter population increase in both of residential and barren areas until 2031; however, the greater growth belongs to the transition from barren area to the residential area. Also, the optimization results indicated that the optimum scenario consists the usage of both concentrated and distributed systems, simultaneously. The optimum scenario recommends setting up the distributed photovoltaic modules in 18.37 % of accessible residential area and installing the concentrated photovoltaic systems in 0.74 % of accessible barren area in 2031 to achieve minimum cost and maximum generated power. Finally, although using the optimum scenario might have some environmental and political benefits such as more energy safety and reduction of air pollutants, if there is no government financial support, then the optimum scenario will not be efficient economically on the studied scale.

The main novelty of this study was related to use of the cellular automata for generating the required input data of the optimization model as an integrated method for future study of solar electricity. However, in this study, only two forms of technology were investigated. Therefore, it is recommended that in the similar studies, the possibility of using different technologies for solar electricity be discussed and the new results be compared with the results of this study. Also, it will be useful to investigate different percentages of accessible areas by considering different environmental and political considerations to achieve the optimum scenario.

5. ACKNOWLEDGEMENT

NOMENCLATURE

AHP	Analytic Hierarchy Process
CO_x	Carbon Oxides
ELECTRE	Elimination Et Choix Traduisant la REalite
GIS	Geographic Information System
LINGO	A linear optimization models solver tool
MCDM	Multi Criteria Decision Making
TOPSIS	Technique for Order Preference by Similarity to Ideal Solution

WSM	Weighted Summation Model

Greek letters

α_1	Area of the accessible residential regions
α_2	Area of the accessible barren regions
x_1	Number of distributed photovoltaic modules
x_2	Number of concentrated photovoltaic systems
φ	Weight of the first objective
ω	Weight of the second objective

Units

m^2	Squared meter
$\$$	USD
Wh	Watt-hour

REFERENCES

1. Brown, M.A., Levine, M.D., Short, W. and Koomey, J.G., "Scenarios for a clean energy future", *Energy Policy*, Vol. 29, No. 14 , (2001), 1179-1196. (https://doi.org/10.1016/S0301-4215(01)00066-0).

2. Lau, K.L., Lindberg, F., Johansson, E., Rasmussen, M.I. and Thorsson, S., "Investigating solar energy potential in tropical urban environment: A case study of Dar es Salaam, Tanzania", *Sustainable Cities and Society*, Vol. 30, (2017), 118-127. (https://doi.org/10.1016/J.SCS.2017.01.010).

3. Ibrahim, G.F., Ibrahim, F. and Rasul, G., "Urban land use land cover changes and their effect on land surface temperature: Case study using Dohuk city in the Kurdistan region of Iraq", *Climate*, Vol. 5, No. 1, (2017), 13. (https://doi.org/10.3390/cli5010013).

4. Mustafa, A., Cools, M., Saadi, I. and Teller, J., "Coupling agent-based, cellular automata and logistic regression into a hybrid urban expansion model (HUEM)", *Land Use Policy*, Vol. 69, (2017), 529-540. (https://doi.org/10.1016/J.LANDUSEPOL.2017.10.009).

5. Rimal, B., Zhang, L., Keshtkar, H., Haack, B., Rijal, S. and Zhang, P., "Land use/land cover dynamics and modeling of urban land expansion by the integration of cellular automata and Markov chain", *ISPRS International Journal of Geo-Information*, Vol. 7, No. 4, (2018), 154-163. (https://doi.org/10.3390/ijgi7040154).

6. Huang, J.P., Poh, K.L. and Ang, B.W., "Decision analysis in energy and environmental modeling", *Energy*, Vol. 20, No. 9, (1995), 843-855. (https://doi.org/10.1016/0360-5442(95)00036-G).

7. Mavromatakis, F., Makrides, G., Georghiou, G., Pothrakis, A., Franghiadakis, Y., Drakakis, E. and Koudoumas, E., "Modeling the photovoltaic potential of a site", *Renewable Energy*, Vol. 35, No. 7, (2010), 1387-1390. (https://doi.org/10.1016/J.RENENE.2009.11.010).

8. Janke, J.R., "Multicriteria GIS modeling of wind and solar farms in Colorado", *Renewable Energy*, Vol. 35, No. 10, (2010), 2228-2234. (https://doi.org/10.1016/J.RENENE.2010.03.014).

9. Wiginton, L.K., Nguyen, H.T. and Pearce, J.M., "Quantifying rooftop solar photovoltaic potential for regional renewable energy policy", *Computers, Environment and Urban Systems*, Vol. 34, No. 4, (2010), 345-357. (https://doi.org/10.1016/J.COMPENVURBSYS.2010.01.001).

10. Charabi, Y. and Gastli, A., "PV site suitability analysis using GIS-based spatial fuzzy multi-criteria evaluation", *Renewable Energy*, Vol. 36, No. 9, (2011), 2554-2561. (https://doi.org/10.1016/J.RENENE.2010.10.037).

11. Sánchez-Lozano, J.M., Teruel-Solano, J., Soto-Elvira, P.L. and Socorro García-Cascales, M., "Geographical information systems (GIS) and multi-criteria decision making (MCDM) methods for the evaluation of solar farms locations: Case study in south-eastern Spain", *Renewable and Sustainable Energy Reviews*, Vol. 24, (2013), 544-556. (https://doi.org/10.1016/J.RSER.2013.03.019).

12. Amaducci, S., Yin, X. and Colauzzi, M., "Agrivoltaic systems to optimise land use for electric energy production", *Applied Energy*, Vol. 220, (2018), 545-561. (https://doi.org/10.1016/J.APENERGY.2018.03.081).

13. Santoli, L.D., Mancini, F. and Astiaso Garcia, D., "A GIS-based model to assess electric energy consumptions and usable renewable energy potential in Lazio region at municipality scale", *Sustainable Cities and Society*, Vol. 46, (2019), 101413. (https://doi.org/10.1016/J.SCS.2018.12.041).

14. Ministry of Roads and Urban Development, "Strategic and structural planning for Karaj city", Tehran: Tehran province office; (2016). (https://www.mrud.ir/en/Home/ItemId/708).

15. Najafi, G., Ghobadian, B., Mamat, R., Yusaf, T. and Azmi, W.H., "Solar energy in Iran: Current state and outlook", *Renewable and Sustainable Energy Reviews*, Vol. 49, (2015), 931-942. (https://doi.org/10.1016/j.rser.2015.04.056).

16. Alamdari, P., Nematollahi, O. and Alemrajabi, A.A., "Solar energy potentials in Iran: A review", *Renewable and Sustainable Energy Reviews*, Vol. 21, (2013), 778-788. (https://doi.org/https://doi.org/10.1016/j.rser.2012.12.052).

17. Esslinger, P. and Witzmann, R., "Improving grid transmission capacity and voltage quality in low-voltage grids with a high proportion of distributed power plants", *Energy Procedia*, Vol. 12, (2011), 294-302. (https://doi.org/https://doi.org/10.1016/j.egypro.2011.10.040).

18. Chezgi, J., Pourghasemi, H.R., Naghibi, S.A., Moradi, H.R. and Kheirkhah Zarkesh, M., "Assessment of a spatial multi-criteria evaluation to site selection underground dams in the Alborz province, Iran", *Geocarto International*, Vol. 31, No. 6, (2016), 628-646. (https://doi.org/10.1080/10106049.2015.1073366).

19. Gueymard, C.A., "The sun's total and spectral irradiance for solar energy applications and solar radiation models", *Solar Energy*, Vol. 76, No. 4, (2004), 423-453. (https://doi.org/10.1016/j.solener.2003.08.039).

20. National Cartographic Center, (2019). (Available from: https://www.ncc.ir/en-us/NCCPortal/1/page/HomePage), (Accessed at 1/20/2019).

21. Zehtabian, G., Shakerian, N., Azarnivand, H. and Khosravi, H., "Hazard assessment of groundwater degradation using IMDPA model (Case study: Isfahan province, Iran)", *Proceedings of Conference of GeoInformation For Disaster Management 2011 (Gi4DM 2011)*, (2011). (https://www.isprs.org/proceedings/2011/gi4dm/pdf/OP76.pdf).

22. Hepu, D., "Multicriteria analysis with fuzzy pairwise comparison", *Proceedings of 1999 IEEE International Fuzzy Systems Conference (FUZZ-IEEE'99)*, Seoul, South Korea, (1999). (https://doi.org/10.1109/FUZZY.1999.793038).

23. Yousefi, M. and Ataei, F., "The lizards fauna of Alborz province: Distribution and conservation", *Payame Noor University*, Vol. 6, No. 3, (2018), 117-126. (http://eab.journals.pnu.ac.ir/article_4520_en.html).

24. Esnandeh, S. and Kaboli, M., "Using simulated annealing optimization algorithm for prioritizing protected areas in Alborz province, Iran", *Environmental Nanotechnology, Monitoring & Management* , Vol. 11, (2019), 100211. (https://doi.org/10.1016/J.ENMM.2019.100211).

25. Ye, B. and Bai, Z., "Simulating land use/cover changes of Nenjiang county based on CA-Markov model", *IFIP International Federation for Information Processing*, Vol. 258, (2008), 321-329. (https://doi.org/10.1007/978-0-387-77251-6_35).

26. Pradhan, B., Hagemann, U., Shafapour Tehrany, M. and Prechtel, N., "An easy to use ArcMap based texture analysis program for extraction of flooded areas from TerraSAR-X satellite image", *Computers & Geosciences*, Vol. 63, (2014), 34-43. (https://doi.org/https://doi.org/10.1016/j.cageo.2013.10.011).

27. Bhubaneswari, P., Iniyan, S. and Ranko, G., "A review of solar photovoltaic technologies", *Renewable and Sustainable Energy Reviews*, Vol. 15, No. 3, (2011), 1625-1636. (https://doi.org/10.1016/J.RSER.2010.11.032).

28. Solar Energy Industries Association (SEIA), (Available form: https://www.seia.org/). (Accessed at 1/20/2019).

29. Triantaphyllou E., Multi-criteria decision making methods, Boston: Springer, (2000). (https://doi.org/10.1007/978-1-4757-3157-6_2).

30. Schrage, L.E., Optimization modeling with LINGO, Lindo system, (2006). (https://www.lindo.com/downloads/Lingo_Textbook_5thEdition.pdf).

31. Sanzana, P., Gironás, J., Braud, I., Branger, F., Rodriguez, F., Vargas, X., Hitschfeld, N., Muñoz, J.F., Vicuña, S., Mejía, A. and Jankowfsky, S., "A GIS-based urban and peri-urban landscape representation toolbox for hydrological distributed modeling", *Environmental Modelling & Software*, Vol. 91, (2017), 168-185. (https://doi.org/10.1016/J.ENVSOFT.2017.01.022).

32. Ghosh, P., Mukhopadhyay, A., Chanda, A., Mondal, P., Akhand, A., Mukherjee, S., Nayak, S.K., Ghosh, S., Mitra, D. and Ghosh, T., "Application of cellular automata and Markov-chain model in geospatial environmental modeling - A review", *Remote Sensing Applications: Society and Environment*, Vol. 5, (2017), 64-77. (https://doi.org/10.1016/j.rsase.2017.01.005).

33. Zoghi, M., Ehsani, A.H., Sadat, M., Amiri, M.J. and Karimi, S., "Optimization solar site selection by fuzzy logic model and weighted linear combination method in arid and semi-arid region: A case study Isfahan-Iran", *Renewable and Sustainable Energy Reviews*, Vol. 68, (2017), 986-996. (https://doi.org/10.1016/J.RSER.2015.07.014).

34. Wang, D.D. and Sueyoshi, T., "Assessment of large commercial rooftop photovoltaic system installations: Evidence from California", *Applied Energy*, Vol. 188, (2017), 45-55. (https://doi.org/10.1016/J.APENERGY.2016.11.076).

35. Dias, L., Gouveia, J.P., Lourenço, P. and Seixas, J., "Interplay between the potential of photovoltaic systems and agricultural land use", *Land Use Policy*, Vol. 81, (2019), 725-735. (https://doi.org/10.1016/J.LANDUSEPOL.2018.11.036).

36. Hirbodi, K., Enjavi-Arsanjani, M. and Yaghoubi, M., "Techno-economic assessment and environmental impact of concentrating solar power plants in Iran", *Renewable and Sustainable Energy Reviews*, Vol. 120, (2020), 109642. (https://doi.org/https://doi.org/10.1016/j.rser.2019.109642).

ABSTRACTS

Estimation of Solar Radiation Energy in the Paraw Mountain of Kermanshah Province as a Rugged Topography

Somayeh Naserpour[a], Hasan Zolfaghari[a*], Parviz Zeaiean Firouzabadi[b]

[a] *Department of Geography, Razi University, P. O. Box: 67144-14971, Kermanshah, Kermanshah, Iran.*
[b] *Department of Remote Sensing and GIS, Faculty of Geographical Sciences, University of Kharazmi, P. O. Box: 15719-14911, Tehran, Tehran, Iran.*

PAPER INFO

ABSTRACT

One of the most important characteristics of site selection for solar energy system installations and optimum solar energy harvesting in the hilly or mountainous terrains is knowledge about the amount and duration of solar radiation within such topographic terrains. Solar radiation data are not readily available for most mountain terrains because of their rugged topography. For these areas, solar radiation data can be obtained through alternative methods such as the Hemispherical Viewshed Algorithm in which spatial and temporal variations of radiation are calculated in terms of elevation, slope, and terrain. In this study, this algorithm was used to estimate and model solar radiation in the Paraw Mountain in Kermanshah. The inputs for this method were ASTER Digital Elevation Model (DEM) with a spatial resolution of 30 m and meteorological parameters that affect solar radiation. The slope and aspect maps were created from ASTER DEM and layers for monthly direct, diffuse, global, and radiation periods were generated for the year 2016. The results showed that in the Paraw Mountain, the amount of solar radiation received was dependent on the slope orientation, as the north and northeast-facing slopes received the lowest and the south and southwest-facing slopes and the flat areas received the highest direct and global radiation (i.e., in terms of this factor, these landscapes can be recommended as the best site for solar energy system installations and optimum solar energy harvesting). The sum annual radiation period varies from 382.67 to 4310.9 hours, the total radiation received annually varies between 1005.56 and 7467.3 MJ/m^2, and the sum monthly solar radiation is the highest in July (181.49-842.26 MJ/m^2) and lowest in December (25.42-319.90 MJ/m^2). Statistical error comparisons between station-based measurements and model-based estimates were performed via R^2, measures. As a result, this model was recommended for solar radiation estimation with acceptable accuracy, especially in high areas with rugged topography where solar radiation data are not readily available.

چکیده

یکی از عوامل مهم برای ارزیابی مکان مناسب برای نصب سیستم‌های خورشیدی و بهره‌برداری از انرژی تابش خورشیدی در کوهستان، اطلاع از میزان تابش خورشیدی (با توجه به ویژگیهای توپوگرافی) می‌باشد. برای بهره‌برداری مطلوب از انرژی تابش خورشیدی در کوهستان، انتخاب بهترین موقعیت برای نصب تجهیزات خورشیدی ضروری است. از آنجا که اطلاعات دقیق در زمینه مقادیر تابش دریافتی با توجه به ویژگیهای توپوگرافی در دسترس نیست، می‌توان از طریق روشهای جایگزین به این اطلاعات دست یافت. یک روش جایگزین برای برآورد تابش خورشیدی در موقعیتهای مختلف کوهستان استفاده از الگوریتم Hemispherical Viewshed Algorithm برای تخمین میزان تابش است که در آن تغییرات مکانی و زمانی اجزای تابش با توجه به تغییر در ارتفاع ، شیب و جهت محاسبه می‌شود. در این مطالعه، با استفاده از این الگوریتم، اجزای تابش در کوهستان پراو مدلسازی شده است. به این منظور از تصاویر سنجنده ASTER با قدرت تفکیک مکانی ۳۰ متر و پارامترهای جغرافیایی و هواشناسیِ مؤثر در برآورد تابش بعنوان ورودی‌های مدل استفاده شد. بر این اساس ابتدا شیب و جهات آن با استفاده از مدل رقومی ارتفاع محاسبه و پس از آن تابش کل، مستقیم، پراکنده و زمان تابش بصورت ماهانه برای سال ۲۰۱۶ محاسبه گردید. نتایج نشان داد درکوهستان پراو وضعیت دریافت تابش با توجه به جهات شیب متفاوت است: دامنه های شمالی و شمال‌شرقی کمترین مقادیر و دامنه های جنوبی، جنوب‌غربی و مناطق هموار بیشترین مقادیر تابش مستقیم و تابش کل را دریافت می‌نماید (با توجه به این فاکتور این مناطق می‌توانند به عنوان بهترین مکان برای نصب سیستم‌های خورشیدی و بهره‌برداری مطلوب از انرژی آن توصیه شوند). بنا بر محاسبات صورت گرفته، مجموع مدت زمان تابش دریافتی سالانه در منطقه مورد مطالعه، بین ۳۸۲/۶۷ تا ۴۳۱۰/۹ ساعت متغیر است. مجموع تابش کل بین ۱۰۰۵/۵۶ تا ۷۴۶۷/۳ مگاژول بر متر مربع در سال می‌باشد. از نظر توزیع زمانی، بیشترین میزان تابش کل دریافتی مربوط به ماه جولای (از ۱۸۱/۴۹ تا ۸۴۲/۲۶ مگاژول) و کمترین مقدار آن در ماه دسامبر (بین ۲۵/۴۲ تا ۳۱۹/۹۰ مگاژول بر متر مربع) است. ارزیابی عملکرد این ابزار با استفاده از ضریب تعیین R^2 محاسبه شد که بر این اساس عملکرد آن مناسب است و با توجه به کمبود ایستگاههای تابش‌سنج درکشور، بویژه در مناطق مرتفع با توپوگرافی پیچیده، می‌توان از این ابزار برای برآورد تابش استفاده نمود.

Sensorless FCS-MPC-Based Speed Control of a Permanent Magnet Synchronous Motor Fed by 3-Level NPC

Sajad Saberi, Behrooz Rezaie*

Department of Computer and Electrical Enginnering, Babol Noshirvani Univercity of Technology, P. O. Box: 47148-71168, Babol, Mazandaran, Iran.

PAPER INFO

ABSTRACT

This paper presents a sensorless speed control algorithm based on Finite Control Set Model Predictive Control (FCS-MPC) for Permanent Magnet Synchronous Motor (PMSM) fed by a 3-level Neutral-Point Clamped (NPC) converter. The proposed scheme uses an anti-windup Proportional-Integral (PI) controller concept to generate the reference electromagnetic torque using the error of speed. Then, FCS-MPC uses this torque reference and other parameters such as a current limitation, neutral point voltage unbalance, and switching frequency to control the converter gate signals. Also, an Adaptive Nonsingular Fast Terminal Sliding Mode Observer (ANFTSMO) was employed to estimate rotor position precisely in positive (clockwise) and negative (counterclockwise) speed to eliminate the encoder. The proposed algorithm has fast dynamics and low steady-state error. Moreover, torque fluctuation and current distortion reduced compared with Space Vector Pulse Width Modulation (SVPWM) based speed control and Direct Predictive Speed Control (DPSC). Simulation results using MATLAB/SIMULINK® demonstrate the performance of the proposed scheme.

https://doi.org/10.30501/jree.2020.234039.1118

چکیده

در این مقاله، یک روش کنترل سرعت بر مبنای کنترل پیش‌بین با مجموعه کنترلی محدود (FCS-MPC) جهت کنترل یک موتور مغناطیس دائـم با مبدل سه سطحی NPC ارایه گردیده است. روش ارایه شده از مفهوم کنترل‌کننده تناسبی انتگرالی (PI) همراه با المان ضد پیچشی با اسـتفاده از خطای سرعت جهت تولید سیگنال مرجع گشتاور الکترومغناطیسی بهره می برد، سپس FCS-MPC با استفاده از مرجع گشتاور و سایر پارامترهای کنترلی مانند محدودیت جریان، نامتوازن بودن ولتاژ نقطه نوترال و فرکانس کلیدزنی سیگنال کنترل گیت‌هـای مبـدل را تولیـد مـی‌کنـد. همچنـین جهت حذف انکودر از یک رؤئیتگر تطبیقی غیرتکین مود لغزشی سریع جهت تخمین موقعیت روتور در سرعت های ساعتگرد و پادساعتگرد اسـتفاده شده است. روش ارایه از دینامیک سریع برخوردار بوده و خطای حالت ماندگار آن نیز بسیار کم اسـت. همچنـین نوسـانات گشـتاور و اعوجـاج هـای جریان در مقایسه با SVPWM و کنترل مستقیم سرعت (DPSC) کاهش چشمگیری داشـته اسـت. نتـایج شـبیه‌سـازی بـا اسـتفاده از نـرم‌افـزار MATLAB/SIMULINK® کارایی روش ارایه شده را نشان می‌دهد.

Comparative Analysis of Thermal Performance of a Solar Water Heating System Based on the Serpentine and Risers-Head Configurations

Selfa Johnson Zwalnan[a*], Nanchen Nimyel Caleb[b], Mahan Morgan Mangai[c], Nantim Yohanna Sanda[a]

[a] *Department of Metallurgical Engineering, Plateau State Polytechnic, Barkin-Ladi, Nigeria.*
[b] *Department of Computer Engineering, Plateau State Polytechnic, Barkin-Ladi, Nigeria.*
[c] *Department of Mechanical Engineering, University of Jos, Plateau State, P. O. Box: 930261, Jos, Nigeria.*

P A P E R   I N F O

A B S T R A C T

The effect of solar collector configurations on the thermal efficiency of an active solar water heater was investigated using TRNSYS in this study. Two versions of a solar heater were formulated on the basis of serpentine and riser-header flat plate configurations. Both models were simulated based on the same parameters and weather conditions. Besides, in accordance with clear sky and cloudy sky conditions, a parametric analysis was performed to determine the impact of varying parameters on the thermal efficiency of the two models. The results showed that the serpentine-based device model provided about 2.62 % more usable thermal energy than the riser-header configuration. In addition, both models demonstrated the same response and sensitivity to changes in the collector area and the volume of the tank. However, on a cloudy day, the efficiency of serpentine showed a significant improvement and sensitivity to flow variance with an efficiency gap of about 30 % to the riser header configuration.

چکیده

در این مقاله، بر روی تأثیرات پیکربندی جمع‌کننده (ذخیره‌کننده) خورشیدی بر روی بازده حرارتی یـک آبگـرمکن خورشـیدی فعـال بـا اسـتفاده از نرم‌افزار TRNSYS بررسی و مطالعه انجام شده است. دو نمونه از سیستم گرمایش خورشیدی بر اساس سرپانتین و صفحه تخت همراه با لوله هـای عمودی مخزن‌دار فرموله شده‌اند. هر دو مدل بر اساس پارامترها و شرایط آب و هوایی یکسان شبیه‌سازی شده‌اند. همچنین، مطابق با شرایط آسـمان صاف و آسمان ابری، تجزیه و تحلیل پارامتری برای تعیین تأثیر پارامترهای مختلف بر بازده حرارتی دو مدل انجـام شـد. نتـایج نشـان داد کـه مـدل دستگاه مبتنی بر سرپانتین حدود ۲/۶۲ ٪ انرژی گرمایی قابل استفاده بیشتری نسبت به پیکربندی صفحه تخت فراهم می‌کند. علاوه بـرایـن، هـر دو مدل واکنش و حساسیت یکسانی را به تغییرات منطقه جمع‌کننده و حجم مخزن نشان دادند. با این حال، در یک روز ابری، مدل سرپانتین، بهبـود و حساسیت قابل توجهی به واریانس جریان با فاصله کارایی حدود ۳۰ ٪ کارایی بهتری نسبت به پیکربندی صفحه تخت از خود نشان داد.

Building Energy Management Using Building Information Modeling: Evaluation of Building Components and Construction Materials

Nima Amani*, Abdul Amir Reza Soroush

Department of Civil Engineering, Chalous Branch, Islamic Azad University, P. O. Box: 46615-397, Chalous, Mazandaran, Iran.

ABSTRACT

Traditionally, building energy model is created in isolation from the architectural building information model and energy analyses have relied on a single analysis tool. The building energy model can be generated more quickly by leveraging existing data from the BIM. The impacts of energy consumption are significant in the building usage phase, which can last several decades. Due to the large share of the final energy consumption in the building sector, accurate analysis of thermal and cooling loads of a building and the efforts to reduce energy losses represent an effective way to reduce energy consumption. Therefore, it is essential to analyze the building energy performance in the design phase, which is when critical decisions are made. This study aims to investigate the impact of the building components and construction materials on building energy efficiency using Building Information Modeling (BIM) technology in a mild climate zone. After reviewing the proposed designs, the main building form was chosen for energy modeling and analysis. Then, building energy consumption analysis was performed based on the basic parameters of the building energy model. Eventually, the most optimal mode was selected by examining different energy consumption forms. This study showed that the building HVAC system always had the largest share of energy consumption. Finally, the results of parametric studies on alternative schemes of energy use intensity optimization showed that 22.59 % savings could be achieved as compared to the base building model in a 30-year time horizon.

https://doi.org/10.30501/jree.2020.236391.1120

چکیده

به طور سنتی، مدل انرژی ساختمان به طور جداگانه از مدل اطلاعات معماری ساختمان ایجاد می‌شود و تجزیه و تحلیل انرژی به یک ابـزار تجزیه و تحلیل واحد متکی است. با استفاده از داده های موجود از BIM، می توان مدل انرژی ساختمان را با سرعت بیشـتری ایجـاد کـرد. تـأثیرات مصـرف انرژی در مرحله استفاده از ساختمان که می‌تواند چندین دهه طول بکشد، قابل توجه می‌باشد. با توجه به سهم بالای مصرف نهایی انـرژی در بخـش ساختمان، تجزیه و تحلیل دقیق بارهای حرارتی و برودتی ساختمان و تلاش برای کاهش تلفات انرژی، راهی مؤثر در کاهش مصرف انرژی مـی‌باشـد. بنابراین، تجزیه و تحلیل عملکرد انرژی ساختمان در مرحله طراحی، یعنی زمانی که مهمترین تصمیمات گرفته می‌شوند، ضروری است. این مطالعه با هدف بررسی تأثیر مؤلفه‌های ساختمان و مصالح ساختمانی در بهره‌وری انرژی ساختمان با اسـتفاده از فنـاوری مـدل‌سـازی اطلاعـات سـاختمان در منطقه‌ای با آب و هوای معتدل انجام شده است. پس از بررسی طرح‌های پیشنهادی، فرم اصلی ساختمان برای مدل‌سازی و تجزیه و تحلیل انـرژی انتخاب شد. سپس، تجزیه، تجزیه و تحلیل مصرف انرژی ساختمان بر اساس پارامترهای اساسی مدل انرژی ساختمان انجام شد. سرانجام بـا بررسـی حـالات مختلف مصرف انرژی، بهینه‌ترین حالت انتخاب شد. این مطالعه نشان داد که سیستم HVAC ساختمان همیشه بیشترین سهم در مصرف انـرژی را به خود اختصاص داده است. در نهایت، نتایج مطالعات پارامتری در مورد طرح های جایگزین بهینه‌سازی شدت مصرف انرژی نشان داد کـه مـی‌تـوان ۲۲/۵۹ درصد صرفه جویی نسبت به مدل پایه ساختمان در یک افق زمانی ۳۰ ساله بدست آورد.

The Effect of Proton-Exchange Membrane Fuel Cell Configuration Changing from Straight to Cylindrical State on Performance and Mass Transport: Numerical Procedure

Tuhid Pashaee Golmarz[a], Sajad Rezazadeh[a*], Maryam Yaldagard[b], Narmin Bagherzadeh[a]

[a] Department of Renewable Energies, School of Mechanical Engineering, Urmia University of Technology, P. O. Box: 57166-17165, Urmia, West Azerbaijan, Iran.
[b] Department of Engineering, School of Chemical Engineering, Urmia University, P. O. Box: 57561-51818, Urmia, West Azerbaijan, Iran.

ABSTRACT

In the present work, a Proton-Exchange Membrane Fuel Cell (PEMFC) as a three-dimensional and single phase was studied. Computational fluid dynamics and finite volume technique were employed to discretize and solve a single set of flow fields and electricity governing equations. The obtained numerical results were validated with valid data in the literature and good agreement was observed between them. The main purpose of this paper is to investigate the effect of deformation of the geometric structure of a conventional cubic fuel cell into a cylindrical one. For this purpose, some important parameters indicating the operation of the fuel cell such as oxygen distribution, water, hydrogen, proton conductivity of the membrane, electric current density, and temperature distribution for two voltage differences between the anode and cathode and the proposed models were studied in detail. Numerical results showed that in the difference of voltages studied, the proposed new model had better performance than the conventional model and had a higher current density, in which at V = 0.4 [V], about a 10.35 % increase in the amount of electric current density was observed and the average increment in generated power was about 8 %, which could be a considerable value in a stack of cells. Finally, the discussion of critical parameters for both models was presented in more detail. The core idea of the results is that the Oxygen and Hydrogen utilization, water creation, and heat generation are greater in the new model.

https://doi.org/10.30501/jree.2020.253825.1152

چکیده

در کار حاضر، یک پیل سوختی با غشاء تبادل پروتون بصورت سه بعدی و تک‌فاز مطالعه شده است. مجموعه معادلات حاکم بر میدان جریان سیال و الکتریسیته با بهره‌گیری از تکنیک دینامیک سیالات محاسباتی و روش حجم محدود گسسته‌سازی و حل شده است. نتایج عددی به دست آمده با داده‌های معتبر موجود در ادبیات فن اعتبارسنجی گردیده و مطابقت مطلوب بین آنها مشاهده شده است. هدف اصلی در این مقاله، بررسی تأثیر تغییر شکل ساختار هندسی پیل سوختی مرسوم مکعبی به حالت استوانه ای می‌باشد. بدین منظور، برخی پارامترهای مهم نشان‌دهنده نحوه عملکرد پیل سوختی از قبیل توزیع اکسیژن، آب، هیدروژن، هدایت پروتونی غشاء، چگالی جریان الکتریکی و توزیع دما برای دو اختلاف ولتاژ بین آند و کاتد و مدل های ارائه شده با ذکر جزئیات بررسی گردیده است. نتایج عددی نشان می‌دهد که در اختلاف ولتاژهای بررسی شده، مدل جدید پیشنهادی نسبت به مدل مرسوم عملکرد بهتری داشته و تراکم جریان بالاتری دارد که در [V] 0.4 = V حدود ۱۰/۳۵ ٪ افزایش در مقدار تراکم جریان الکتریکی ملاحظه می‌گردد. مقدار متوسط افزایش توان تولیدی حدود ۸ ٪ می‌باشد که در یک استک سلولی می‌تواند مقدار قابل توجهی باشد. نهایتاً، بحث روی پارامترهای حیاتی برای هر دو مدل با جزئیات بیشتری ارائه گردیده است. خلاصه نتایج به دست آمده این است که در مدل جدید، مصرف اکسیژن و هیدروژن بیشتر بوده و در نتیجه تولید آب و گرما نیز بیشتر می‌باشد.

A Factorial Study of the Effect of Rhamnolipid and Stirring on the Electricity Production, Desalination, and Wastewater Treatment Efficiencies of a Five-Chamber Microbial Desalination Cell

Abubakari Zarouk Imoro[a*], Moses Mensah[b], Richard Buamah[c]

[a] Department of Environment, Water and Waste Engineering, University for Development Studies, P. O. Box: 1882, Nyankpala, Ghana.
[b] School of Graduate Studies, Regional Maritime University, P. O. Box: GP 1115, Accra, Ghana
[c] Department of Civil Engineering, Kwame Nkrumah University of Science and Technology, P. M. B. Kumasi, Ghana.

PAPER INFO	ABSTRACT
	This study was conducted to improve the voltage production, desalination, and COD removal efficiencies of a five-chamber Microbial Desalination Cell (MDC). To do this, rhamnolipid was added to anolytes only and catholytes stirred to determine the effects of these factors on the MDC activity. This was followed by a factorial study to investigate the effects of the interactions of rhamnolipid and stirring on the voltage production, desalination, and COD removal efficiencies of the MDC. Increasing the concentration of rhamnolipid to 240 mg/L improved the peak voltage produced from 164.50 ± 0.11 to 623.70 ± 1.32 mV. Also, the desalination efficiency increased from 20.16 ± 1.97 % when no rhamnolipid was added to 24.89 ± 0.50 % at a rhamnolipid concentration of 240 mg/L, and COD removal efficiency increased from 48.74 ± 8.06 % to 64.17 ± 5.00 % at a rhamnolipid concentration of 400 mg/L. In the stirring experiments, increasing the number of stirring events increased peak voltage from 164.50 ± 0.11 to 567.27 ± 18.06 mV. Similarly, desalination and COD removal efficiencies increased from 20.16 ± 1.97 % and 48.74 ± 8.06 % to 24.26 ± 0.97 % and 50.23 ± 1.60 %, respectively, when the number of stirring events was more than twice a day. In the factorial study, voltage production, desalination, and COD removal efficiencies were 647.07 mV, 25.50 %, and 68.15 %, respectively. However, the effect of the interaction between rhamnolipid and stirring was found to be insignificant ($p > 0.05$). Thus, the addition of only rhamnolipid or the stirring of catholytes only can improve the performance of the five-chamber MDC. https://doi.org/10.30501/jree.2020.243765.1137

چکیده

در این مطالعه، برای بهبود تولید ولتاژ از سیستم نمک‌زدایی و راندمان حذف COD، بر پنج محفظه سلولی نمک‌زدایی میکروبی (MDC) استفاده شده است. برای انجام این کار، رامنولیپید فقط به آنولیت‌ها اضافه شد و کاتولیت‌ها برای تعیین اثرات این عوامل بر فعالیت MDC هم زده شدند. در ادامه کار، مطالعه فاکتوری برای بررسی اثرات متقابل رامنولیپید و هم زدن بر روی تولید ولتاژ، نمک‌زدایی و بازده حذف COD از MDC انجام شد. افزایش غلظت رامنولیپید به ۲۴۰ میلی گرم در لیتر، اوج ولتاژ تولیدی را از ۰/۱۱ ± ۱۶۴/۵۰ به ۱/۳۲ ± ۶۲۳/۷۰ میلی ولت افزایش داد. همچنین، بدون اضافه شدن رامنولیپید، در غلظت رامنولیپید ۲۴۰ میلی گرم در لیتر، راندمان نمک‌زدایی از ۱/۹۷ ± ۲۰/۱۶ ٪. به ۰/۵۰ ± ۲۴/۸۹ ٪. افزایش یافت و راندمان حذف COD از ۸/۰۶ ± ۴۸/۷۴ ٪. به ۵/۰۰ ± ۶۴/۱۷ ٪. در غلظت رامنولیپید ۲۴۰ میلی گرم در لیتر افزایش یافت. در آزمایش‌های اختلاط، افزایش تعداد اختلاط، اوج ولتاژ را از ۰/۱۱ ± ۱۶۴/۵۰ به ۱۸/۰۶ ± ۵۶۷/۲۷ میلی ولت افزایش داد. به همین ترتیب، هنگامی که تعداد حوادث تکان‌دهنده بیش از دو بار در روز بود، بازدهی نمک‌زدایی و حذف COD به ترتیب از ۱/۹۷ ± ۲۰/۱۶ و ۸/۰۶ ± ۴۸/۷۴ ٪. به ۰/۹۷ ± ۲۴/۲۶ و ۱/۶۰ ± ۵۰/۲۳ ٪. افزایش یافت. در مطالعه طرح فاکتوریال، تولید ولتاژ، نمک‌زدایی و راندمان حذف COD به ترتیب ۶۴۷/۰۷ میلی ولت، ۲۵/۵۰ ٪. و ۶۸/۱۵ ٪. بود. با این حال، اثر متقابل رامنولیپید و هم زدن ناچیز بود (۰/۰۵ > p)، بنابراین، افزودن فقط رامنولیپید یا هم زدن کاتولیت‌ها می‌تواند عملکرد MDC پنج محفظه را بهبود بخشد.

Study of Long-Term Stability of Perovskite Solar Cells: Highly Stable Carbon-Based Versus Unstable Gold-Based PSCs

Mohammad Reza Shekari[a], Seyed Mohammad Sadeghzadeh[a], Mahdi Golriz[b*]

[a] *Department of Electrical Engineering, Shahed University, P. O. Box: 18155-159, Tehran, Tehran, Iran.*
[b] *Space Transportation Research Institute, Iranian Space Research Center, P. O. Box 13445-754, Tehran, Tehran, Iran.*

ABSTRACT

In recent decade, Perovskite Solar Cells (PSCs) have received considerable attention compared to other photovoltaic technologies. Despite the improvement of Power Conversion Efficiency (PCE) of PSCs, the chemical instability problem is still a matter of challenge. In this study, we have fabricated two kinds of PSCs based on gold and carbon electrodes with the optimal PCE of about 15 % and 10.2 %, respectively. We prepared a novel carbon electrode using carbon black nanopowder and natural graphite flaky powder for Hole Transport Material (HTM) free carbon-based PSC (C-PSC). Current density-voltage characteristics over time were measured to compare the stability of devices. Scanning Electron Microscope (SEM) and Energy-dispersive X-ray Spectroscopy (EDS) analyses were carried out to study applied materials, layer, and surface structures of the cells. The crystal structure of perovskite and its association with the stability of PSCs were analyzed using an obtained X-ray diffraction (XRD) pattern. As a result, the constructed HTM-free C-PSC demonstrated high stability against air, retaining up to 90 % of its optimal efficiency after 2000 h in the dark under ambient conditions (relative humidity of (50 ± 5); average room temperature of 25 °C) in comparison to constructed gold-based PSCs (Gold-PSC) which are not stable at times. The experimental results show that novel low-cost and low-temperature carbon electrode could represent a wider prospect of reaching better stability for PSCs in the future.

https://doi.org/10.30501/jree.2021.240562.1132

<div dir="rtl">

چکیده

در دهه‌های اخیر، توجه علمی بر روی سلول‌های خورشیدی پروسکایتی رشد قابل توجهی نسبت به سایر فناوری‌های فتولتاییک داشـته اسـت. بـازده این سلول‌ها از ۳/۸ ٪ در سال ۲۰۰۹ به ۲۵/۲ ٪ در سال ۲۰۱۹ بهبود یافته است. هرچند مشکل ناپایداری شیمیایی سلول‌های پروسکایتی هنوز یک موضوع چالش برانگیز است. در این تحقیق، ما دو نوع متفاوتی از سلول‌های پروسکایتی بر پایه الکترود طلا و کربن به ترتیب با بازده‌های بهینه ۱۵ ٪ و ۱۰/۲ ٪ ساختیم. ما یک الکترود کربنی جدید با استفاده از نانوپودر کربن سیاه و پودر گرافیت طبیعی برای سـلول پروسـکایتی کربنـی فاقـد مـاده انتقال‌دهنده حفره تهیه کردیم. مشخصات جریان- ولتاژ (J-V) سلول‌ها برای مقایسه پایداری اندازه‌گیری شد. برای مطالعه مواد به کار رفتـه، لایـه و سطوح ساختارهای سلول‌ها، آنالیزهای طیف‌سنجی پراش انرژی پرتو ایکس (EDS) و بلورشناسی پرتـو ایکـس (XRD) انجـام شـد. بـا اسـتفاده از الگوی XRD به دست آمده، ساختار بلوری پروسکایت و ارتباط آن با پایداری سلول آنالیز شد. در انتها، سلول دارای الکتـرود کربنـی در مقایسـه بـا سلول ساخته شده با الکترود طلا که ناپایدار بود، پایداری بالایی را در تاریکی در شرایط محیطی مورد نظر (رطوبت نسبی (۵ ± ۵۰ ٪) در دمای اتاق ۲۵ °C) از خود نشان داد که ۹۰ ٪ از بازده اولیه خود را بعد از ۲۰۰۰ ساعت حفظ کرد. نتایج آزمایشگاهی نشان داد که الکتـرود کربنـی کـم‌هزینـه ساخته شده با روشی در دمای کم، می‌تواند راه مناسبی را برای رسیدن به پایداری‌های بهتر برای سلول‌های خورشیدی پروسکایتی در آینده باز نگـاه دارد.

</div>

Evaluation a Hybrid Passive Cooling System for a Building Using Experimental and Commercial Software (Design Builder)

Mahnoosh Eghtedari[a], Abbas Mahravan[b*]

[a] *Department of Architecture, Kermanshah Branch, Islamic Azad University, Kermanshah, Kermanshah, Iran.*
[b] *Department of Architecture, Razi University, Kermanshah, Kermanshah, Iran.*

PAPER INFO

ABSTRACT

Increasing fossil fuel consumption in the building, especially in the air-conditioning sector, has increased environmental pollution and global warming. In this research, a zero-energy passive system was designed to ventilate the building and provide comfortable conditions for people in the summer. A hybrid passive system was designed for indoor cooling to minimize fossil energy use. This research was done experimentally- and analytically and by simulation. An experimental study comprising a test chamber and simulation using Builder Design software was carried out to evaluate the cooling and ventilation potential of a hybrid passive system functioning. In the experimental section, air temperature, humidity, and airflow for the outdoor environment and the output of the evaporative cooling channel were measured. These measurements were tested in August from 9:00 AM to 3:00 PM for six consecutive days. The obtained experimental data were given to Design Builder software as an input parameter, and then, the comfort conditions inside the chamber, the dimensions, and location of the air inlet valve into the chamber were examined. The findings showed that the proposed system could reduce the air temperature by an average of 10 ºC and increase the air humidity by 33 %. The findings showed that the air inside the chamber was comfortable during the hottest hours of the day. Raising the valve location, increasing the area, and increasing the volumetric flow rate of the air increased the percentage of dissatisfaction. The findings showed that in addition to wind speed and air temperature, the geometrical shape of the air inlet opening contributes to indoor air comfort conditions.

https://doi.org/10.30501/jree.2021.239940.1131

<div dir="rtl">

چکیده

افزایش مصرف سوخت‌های فسیلی در ساختمان به ویژه در بخش تهویه مطبوع، سهم بسزایی در افزایش آلودگی محیط‌زیست و گرم شدن کره زمین دارد. در این تحقیق، جهت تهویه ساختمان و تأمین نیازهای آسایش افراد، سیستم ایستای صفر انرژی در در تابستان طراحی شـد. سیسـتم ایسـتای هیبرید جهت سرمایش داخلی تا مصرف انرژی فسیلی را به حداقل برساند. یک مطالعه تجربی شامل اتاقک آزمایشی و نرم افزار شبیه سـازی دیـزاین بیلدر برای ارزیابی قابلیت خنک‌کننده و تهویه عملکرد سیستم ایستای ترکیبی انجام شد.این تحقیق به صورت تجربی - تحلیلی و شبیه‌سازی صورت گرفت. در قسمت تجربی، دمای هوا، رطوبت و سرعت جریان هوای محیط و دهانـه خروجـی کانـال خنک‌کننـده تبخیـری انـدازه‌گیـری شـد. ایـن اندازه‌گیری‌ها در گرمترین ماه سال (مرداد ماه) از ساعت ۹ صبح تا ۳ بعدازظهر در شش روز متوالی مورد آزمایش قرار گرفت. با اسـتفاده از داده‌هـای تجربی به دست آمده، به بررسی شرایط آسایش داخل اتاقک با استفاده از نرم افزار دیزاین بیلدر پرداخته شد و در نهایت محل، شکل هندسی و ابعـاد دریچه ورودی هوا به داخل اتاقک و تأثیرآن بر شرایط آسایش محیط داخل مورد بررسی قرار گرفت. داده‌های به دست آمده نشان داد که هوای داخل اتاقک در گرمترین ماه سال در شرایط آسایش قرار دارد. بالاتر بردن محل دریچه، افزایش مساحت و زیاد کردن دبی حجمی هوا باعث افزایش درصـد نارضایتی شد.

</div>

Spatial Study for Determining the Optimum Scenario for Generating Solar Electricity by Predicting the Land-Use Changes: Case of Alborz Province, Iran

Ali Khatibi, Mohammad Hossein Jahangir*, Fatemeh Razi Astaraei

Department of Renewable Energies and Environment, School of New Sciences and Technologies, University of Tehran, P. O. Box: 14399-57131, Tehran, Tehran, Iran.

PAPER INFO	*ABSTRACT*
	Land-use change is one of the most important spatial phenomena that can affect the usage of energy technologies. In this study, land-use change in barren and residential areas in Alborz province in Iran was modeled using the cellular automata combined with the Markov Chain from 2001 to 2031. Due to adaptability to the environmental considerations, all protected areas were removed from the study area. Then, an economical and performance-based optimization model was developed; then, by using the status of the two land-use classes in 2031, an optimum scenario was identified for generating solar electricity. Based on the results, the optimum scenario involves installing distributed photovoltaic modules in 18.37 % of residential areas and setting up concentrated solar systems in 0.74 % of barren areas, simultaneously. Economic investigation of the optimum scenario showed that although there were some environmental and political benefits for using the solar electricity such as reduction of air pollutants and more energy safety, the optimum scenario will be costly and non-economical without the government's financial supports.

چکیده

تغییرات کاربری سرزمین یکی از مهمترین پدیدههای مکانی میباشد که میتواند استفاده از فنـاوریهـای انـرژی را تحـت تـأثیر قـرار دهـد. در ایـن پژوهش، تغییرات کاربری سرزمین برای مناطق بیابانی و مسکونی در استان البرز در کشور ایران با استفاده از تلفیق اتوماتای سلولی و زنجیره مارکوف از سال ۲۰۰۱ تا ۲۰۳۱ مدلسازی گردید. با هدف سازگاری با ملاحظات محیطزیستی تمامی مناطق حفاظت شـده از منطقـه مـورد مطالعـه حـذف گردیدند. سپس یک مدل بهینهسازی عملکردی و اقتصادی با استفاده از وضعیت دو طبقه کاربری سرزمین در سـال ۲۰۳۱ توسـعه داده شـد و یـک سناریو بهینه برای تولید الکتریسیته خورشیدی معرفی گردید. براساس نتایج به دست آمده، سناریو بهینه مربوط بـه اسـتفاده همزمـان مـاژولهـای فتوولتائیک توزیع شده در ۱۸/۳۷ ٪ مناطق مسکونی و احداث سیستمهای متمرکز خورشیدی در ۰/۷۴ ٪ مناطق بیابانی میباشد. بررسـی اقتصـادی سناریو بهینه نشان داد که اگرچه مزیت های محیطزیستی و سیاسی برای استفاده از الکتریسیته خورشیدی وجود دارد (مانند کاهش آلایندگی هوا و امنیت انرژی بیشتر) اما اگر حمایتهای مالی توسط دولت وجود نداشته باشد، سناریوی بهینه، پرهزینه و غیراقتصادی میباشد.

CONTENTS